A trailing suction hopper dredge draghead production model

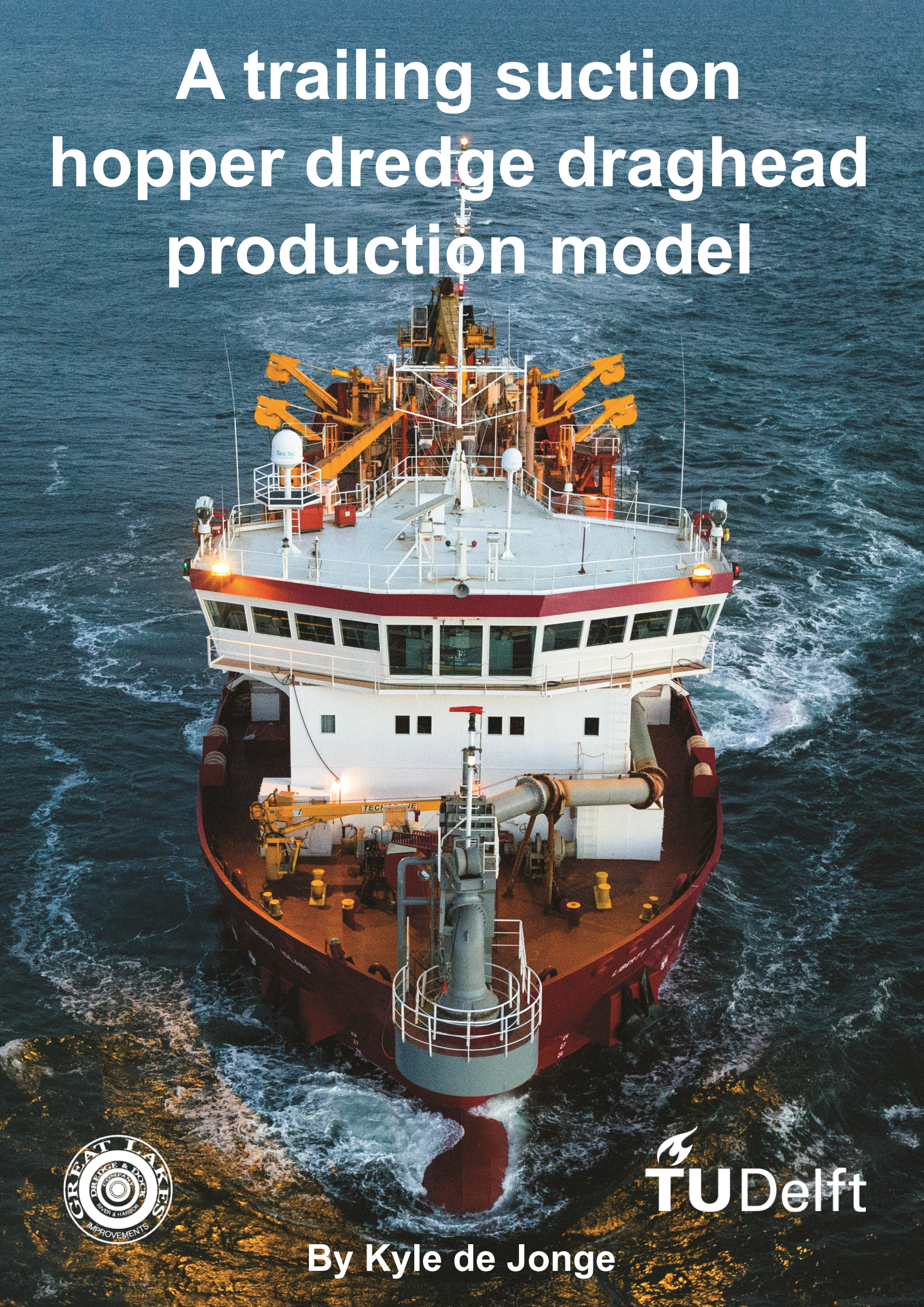

By Kyle de Jonge

A trailing suction hopper dredge draghead production model

by

Kyle de Jonge

to obtain the degree of Master of Science

at the Delft University of Technology,

to be defended publicly on Wednesday August 16, 2017 at 15:00 PM.

Student number:	4010124	
Supervisors:	Dr. ir. S. A. Miedema,	TU Delft
	R. C. Ramsdell,	Great Lakes Dredge & Dock Company
Thesis committee:	Prof. dr. ir. C. van Rhee,	TU Delft
	Dr. ir. S. A. Miedema,	TU Delft
	R. C. Ramsdell,	Great Lakes Dredge & Dock Company
	Dr. ir. R. L. J. Helmons ,	TU Delft

This thesis is confidential and cannot be made public until August 16, 2019.

TU Delft

GREAT LAKES DREDGE & DOCK COMPANY, LLC

Summary

One of the most important machines in the dredging industry is the trailing suction hopper dredge (TSHD). This ship-shaped dredge removes sediments (mainly sand) from the bottom using vacuum cleaner-like arms called drag arms and stores these sediments in its hopper. At the end of a drag arm the draghead is located. This part is responsible for cutting and taking in the sediments. With the sediments in its hopper a TSHD can then sail to a location to dispose these sediments.
One of the dredging companies using trailing suction hopper dredges is North America's largest dredging company: Great Lakes Dredge & Dock Company (GLDD). In order for GLDD to make an estimate of the duration and the costs of a certain project one of the things that must be known is the time it takes to fill the hopper of a TSHD. Great Lakes has models that can be used to find this time: a pump model and a hopper sedimentation model. Both of these models do however require the concentration of the sand-water mixture (slurry) as an input. Currently this input concentration is estimated based on data of previous comparable projects. Having a model that can calculate the slurry concentration could therefore aid in this estimating process and could possibly improve the estimates. Furthermore such a model might also be used for equipment performance evaluation or for operating performance improvement.
This thesis describes the development and evaluation of a model that aims to calculate the in situ production as well as the aforementioned slurry concentration. Together with the cut slice thickness the in situ production and the slurry concentration are the most important required outputs (as a function of the trailing speed) of this model. The inputs of the model are mainly soil mechanical properties, draghead geometry, application of jet water and the trailing speed. For the evaluation of the model the TSHD Liberty Island equipped with Wild Dragon dragheads is used. The Wild Dragon draghead has two rows of cutting teeth mounted in the visor and is furthermore equipped with water jets in the heel. What makes the Wild Dragon special is that the teeth also have water jets in them. These reduce the cutting force. The visor is pushed into the soil by a hydraulic cylinder that pushes with a constant force regardless of the visor angle.
The chosen approach for modeling the production and slurry concentration in this thesis is to only consider the draghead and to assume that it is fixed on the seabed for all translations. Furthermore the angle that the helmet makes with the horizon can only be varied as an input. This results in the fact that the only movable parts in this approach are the visor of the draghead and the hydraulic cylinder that is attached to the visor. Because the cutting teeth are mounted in the visor, rotating the visor changes the thickness of the layer that is cut.
Cutting with teeth is however not the only process that can remove a layer of the soil. The other process used in the model is the liquefaction of soil using the heel jets. This liquefied layer of soil is assumed to have no cutting force but does have to be in reach of the cutting teeth in order to be removed.
Because the in situ production is defined as the total cut layer thickness multiplied with the draghead width and the trailing speed, the in situ production is eventually dependent on the angle that the visor makes. This angle (for a given trailing speed) is the angle for which a balance between the moments acting around the visor hinge point exists.
Once the visor angle has been found the in situ production can be calculated. The slurry concentration is then calculated by assuming that all the cut sand is sucked in and that the flow in the drag arm can be described as a function of the slurry concentration.
The main challenge for this model is actually finding the angle for which the moment balance exists. Three moments were identified to be significant in this moment balance: The moment caused by the

hydraulic cylinder, the moment due to the submerged weight of the visor and the moment due to the cutting forces. The hydraulic cylinder moment and the submerged weight moment are also referred to as the actuator moments and push the visor into the soil. The cutting moment pushes the visor out of the soil and consists of two moments per row of cutting teeth. One moment due to the horizontal cutting force and one moment due to the vertical cutting force.
The moment of the hydraulic cylinder can be changed by changing the input value of the pressure of the hydraulic fluid. Using the diameter of the cylinder a force can be obtained which can then be used to calculate the cylinder moment by using the moment arms that are derived from the draghead geometry.
For the moment due to the submerged weight of the visor the mass of the visor must be known. By assuming that the visor is made entirely of steel then the submerged weight can be calculated. This weight can then be used with moment arms that are again derived from draghead geometry to calculate the moment.
The cutting moment is calculated using cutting forces and moment arms that are derived from the draghead geometry. For the calculation of the cutting forces the cutting model for water saturated sand of S.A. Miedema is used. This model assumes that the cutting forces are solely caused by the effects of dilatation. The shearing of the soil during cutting causes the pores between the sand particles to dilate which causes water to flow to the dilated zone. This results in the development of under pressures which eventually cause the cutting forces. The cutting model has been supplemented with another model of Miedema which allows cavitation to travel from the dilated zone up on the blade. This allows for greater cutting forces to be achieved.
An extension to the cutting model has been made to include the influence of the tooth jets of the Wild Dragon. In this extension the tooth jets are modeled as a pressure source that eventually provides water to the dilated zone. This partially counteracts the effects of dilatation and thus reduces the cutting force. A comparison has been made between the cutting force reduction achieved by using the tooth jet model and an approach based on specific cutting energy. This comparison has shown that the results of the two approaches match reasonably well for the cutting conditions used in this thesis.
Once the cutting forces have been calculated the cutting moments can be calculated using moment arms derived from the draghead geometry. The draghead geometry, which is also used to obtain inputs for the cutting model like the blade height and the blade angle, is described using polar coordinates. The origin of the polar coordinates lies in the center of the visor hinge. Using polar coordinates allows for easy modeling of the rotation of the visor and thus the cutting teeth. The points of the draghead geometry that are captured in the polar coordinates are: the attachment points of the hydraulic cylinder, the position of the center of gravity of the visor and the position of the tips and tops of the cutting teeth.
The actual visor angle for a given trailing speed for which the actuator moments and the cutting moments balance out is found through iteration. It can however be possible that no equilibrium can be found because the cutting moments are too small. In this case the visor will remain in the lowest possible position because it is pushed down by the actuators. Because the slice thickness in this position is the maximum slice thickness that can be achieved the production in this position can be considered the maximum production possible for that trailing speed and lower arm angle.
In order to evaluate the production model performance a sensitivity analysis was performed. For a given set of inputs the production and concentration were plotted for a range of trailing speeds while certain inputs were varied by plus and minus 20 percent.
What was found is that in all cases except for the case with a low angle of internal friction, the course of the production as a function of the trailing speed is characterized by a linear increase, which ends in a steep drop in production. After the drop the production slowly increases again for increasing trailing speeds but the rate of this increase never comes near the rate of the linear increase. In the case of the low angle of internal friction the production simply stayed linear with the trailing speed

over the entire plotted range. The general trend that is visible is that the linear production increase ends at higher trailing speeds (and is thus prolonged) when an input parameter is varied in a way that the cutting force is reduced with respect to the reference situation. The same was seen when the influence of the tooth jet model was tested because the tooth jets also reduce the cutting forces.
The steep drop in production usually occurs within the operational range of trailing speeds between 1 and 2 knots. In reality this large change in visor angle and production is not observed. What is also remarkable is that only productions that are part of the linear increase are of an order of magnitude that can be regarded as normal (between 36 m^3/min and 125 m^3/min for a single drag arm). Once the visor has moved the production usually stays below 36 m^3/min at operating speeds.
The cause of the large visor movement and thus the steep drop in production was investigated. It was found that the visor movement occurs when the cutting moment at the lowest possible visor position becomes larger than the actuator moment, thus the visor has to move. New equilibrium is then however only found after relative large visor rotations. This is caused by the shape of the cutting moment line as a function of the visor angle. Assuming that the cutting forces for a given visor angle are reasonably close to what they would be in reality leads to the conclusion that the shape of the cutting moment line is caused by the rapid decline of the vertical moment arms due to visor movement compared to the relatively small change of the horizontal moment arms. In the end this means that the large drop in production for increasing trailing speeds is caused by the geometry of the draghead.
Because the general shape of the production as a function of the trailing speed was not a smooth ever-increasing line but rather a line consisting of a linear and a non-linear regime, the production was measured in two points for each variation during the sensitivity analysis. The first point marks the end of the linear increase and the second point was set at 1.5 knots, which is in the middle of the operating range. Furthermore the model was evaluated without and with the tooth jet model. The four sets of data showed that the influence of the input parameters is significantly larger when observing in the linear regime compared to the non-linear regime. Adding the tooth jets also showed an increase of the influence in the non-linear regime of parameters directly used in the cutting force calculations (porosity and permeability). Having four sets of possible sensitivities raises the question which of those might be most applicable to reality. Because in reality the Wild Dragon does use the tooth jets it must be one of those two sets. This leaves the choice between the linear and the non-linear regime. A production in a normal order of magnitude has only been observed in the linear regime. Adding the influence of the tooth jets to the model prolonged the duration of the linear increase further into the operational range. Furthermore the steep drop in production is not observed in reality. These observations, together with the presumption that the cutting forces might be overestimated because a row of cutting teeth is modeled as a single blade, lead to the conclusion that the draghead production might actually be characterized as linearly increasing with the trailing speed. The steep drop in production might then not be observed because it would actually occur at higher trailing speeds outside of the operational range. Further research is required to find out if this is actually the case. Assuming that the draghead production can indeed be characterized as linear would mean that the influences found at the end of the linear increase with the tooth jet model active would be most applicable to reality. Based on this it would mean that the angle of internal friction has the largest influence on the production. Another parameter with a large influence is the permeability. Of the parameters that can be controlled the pressure in the hydraulic cylinder was found to have the largest influence on the production. The water depth and the lower arm angle also have a relatively large influence on the production in the model, however in reality these are not independent of each other and their effects would partially cancel out thus reducing their actual influence.
Finally, the proposed slurry concentration calculation method seems to work nicely because the concentrations for the calculated productions seem to be in the right order of magnitude. When using the method it must be kept in mind that the pump-slurry concentration relation can be altered in such a way that the model yields seemingly plausible concentrations for productions of any magnitude.

Preface

This thesis is the result of research that was aimed at producing a model capable of calculating production and slurry concentration for trailing suction hopper dredges. The thesis has been written as the completion of the master's programme of *Offshore & Dredging Engineering* at the faculty of 3mE at the Delft University of Technology.

The research, of which I had the great pleasure to be able to combine it with an internship, was carried out for and funded by *Great Lakes Dredge & Dock Company* in Oak Brook, Illinois, United States of America.

First of all, I would like to thank my parents for their help and support (and patience) during my eight year endeavour to become an engineer.

I would also like to thank my supervisors Sape Miedema (Delft University of Technology) and Robert Ramsdell (Great Lakes Dredge & Dock Company). In the first place for offering me this research internship, which has truly been a great experience. Furthermore I would like to thank them for their guidance and their support during the whole process and for the great discussions that we have had.

Finally I would like to thank my family and friends for being helpful and supportive during my study time in Delft.

Kyle de Jonge

Delft, August 6, 2017

Contents

1 Introduction

1.1 Context

Roughly 71 percent of the Earths' surface is covered with water. The major part of this water, roughly 98 percent, is salt water in oceans and seas, the remainder is fresh water in the form of rivers and lakes. Regardless of what type of water, humans have been living on the interface between land and water for almost as long as humanity exists. Nowadays that is not any different. It is estimated that about 44 percent of the worlds' population lives and works in coastal areas and roughly 90 percent of the worlds' trade is carried by sea through ports. Depending on the country, a significant amount of that trade is transported further inland through waterways.
These land-water interfaces are constantly changing: Waterways and ports silt up and beaches and dunes get eroded by wind and waves. In order to keep the ports and waterways accessible they have to be deepened, sometimes even deeper than their original depth to allow access to even larger ships. Beaches and dunes have to be re-nourished to ensure protection against the sea.
The land-water interfaces are not only changed by nature. Land is often reclaimed from the sea to provide new space to build ports, residential areas, airports or other things. Land reclamation, deepening of waterways and ports and re-nourishing beaches are all examples of dredging. In general dredging can be defined as excavating sediments under water with the aim to dispose them at another location. The three most commonly used types of equipment used in dredging are the cutter suction dredge, the clamshell dredge and the trailing suction hopper dredge (TSHD). The latter, the trailing suction hopper dredge, is a ship with a large hopper, a hold for the excavated sediments which are most commonly sand, clay or rock. The sediments are collected from the riverbed, seabed or harbor floor by using drag arms. Drag arms are giant vacuum cleaner-like arms. Driven by large centrifugal pumps they suck up the sediments. These sediments mixed with water form a slurry which is transported into the hopper through pumps and pipes. The most important part of the drag arms is the drag head. This is the part that actually excavates the sediment. Sometimes this is done solely by the flow caused by the suction of the centrifugal pumps (erosion) but often the drag head is also equipped with teeth and water jets which actually cut into the bed and help to increase production. Once the hopper is filled with sediment the TSHD sails to a disposal site where the sediments can either be unloaded through doors/valves in the hull or be pumped ashore as a slurry.
One of the dredging companies that uses TSHD's is America's largest dredging company: Great Lakes Dredge & Dock Company (GLDD or Great Lakes). An important aspect of estimating the duration and costs of a TSHD project is estimating the time it takes to load the hopper. At the moment of writing GLDD uses two well-understood models to estimate the loading time: A pump model and a hopper sedimentation model. The pump model calculates how a slurry of a certain density acts in the pumps and pipelines. The hopper sedimentation model calculates the sedimentation behavior in the hopper for a slurry of a certain density. As said, with a combination of both models a loading time estimate can be made given a certain loading density. This is where the problem is. Both the pump and hopper sedimentation model require the slurry concentration as an input, yet this concentration is estimated using data from previous comparable projects. Although this works well for most cases GLDD aims to develop a model that calculates the slurry concentration (or in situ production) because of several advantages. Such a production model might help to improve the estimates but also might explain differences between an estimate and the actual production. A production program can also be used to evaluate the performance of new or existing equipment and might even aid to improve

operating performance. This thesis will cover the development of a model that will be the foundation of such a production model. In the next paragraph the required inputs and outputs of the model are discussed.

1.2 Required inputs and outputs

As mentioned in the previous paragraph this thesis is about the development of a TSHD draghead production model. This model will provide the inputs, most importantly the slurry concentration, for the pump model and hopper sedimentation model. In order to calculate the required outputs the TSHD draghead production model needs a number of inputs. These inputs are listed below together with the required outputs in the way they were stated in the original assignment. The listed inputs are optional and more an indication of what data is available.

Inputs:

- Mechanical design of the dredge:
  - Propulsion power and efficiency
  - Draghead dimensions
  - Availability and application of jetwater
  - Presence of equipment such a turtle exclusion devices (TEDs) or screens due to environmental or contractual requirements
  - Pumping system
- The soil mechanical properties (for cohesive and non-cohesive materials)
- Dredging depth
- Trailing speed

Outputs:
Per material strength or trailing speed:

- Draghead cutting production in m^3/s
- Cut slice thickness
- Resultant slurry concentration for a given mixture flow and assumed mixing losses (spillage)
- Propulsion resistance
- Resulting/required downpressure (force)

After discussion with the supervisors the decision has been made to focus on draghead production for non-cohesive materials (sands) since these are most commonly encountered in the work field of TSHDs. This change of focus means that cohesive soil mechanical inputs are omitted for now. This also means that outputs are displayed per trailing speed since non-cohesive materials do not have a strength.

1.3 Starting points

In addition to the required inputs and outputs there are a couple of starting points for the model. The first is that the model must be made using either Excel or Python. This is required since the Great Lakes Production Department also uses (a combination of) these programs to make the production estimates. The choice has been made to develop the model using Python. The reason for this choice is not necessarily that Python is better than Excel (although Python might have a wider range of capabilities thanks to its open-source nature) but that the author wanted to learn Python.
The other starting point is that equipment parameters that are used to run the model are parameters of equipment that Great Lakes actually uses. A good model should be able to handle most TSHDs and dragheads. However, for validation purposes it is convenient to use parameters of GLDD equipment since there likely will be data available of these. These starting points lead to a TSHD and draghead to be selected that will be used to evaluate the model: The Liberty Island and the Wild Dragon draghead. Some general information about the Liberty Island and the Wild Dragon draghead will be given in the following sections.

1.3.1 Liberty Island

The Liberty Island was built in 2001 and is GLDD's second newest trailing suction hopper dredge (see figure 1.1). The Liberty Island has a length of 96.0 m a breadth of 18.0 m and a draft of 8.6 m. The hopper capacity is 5003 m^3 and the maximum dredging depth is 32.9 m. The total installed power is 11612 kW or 16566 hp. The Liberty Island is equipped with two drag arms with 800 mm piping that can load the hopper simultaneously. The sediments in the hopper can be discharged by using valves in the bottom of the ship or by pumping it through the discharge pipe at the bow of the ship.
The loaded sailing speed is 14 knots, however trailing speeds usually lie in the range of 0.25 to 2 knots depending on the material being cut, the equipment being used, the weather and other circumstances.

Figure 1.1: The trailing suction hopper dredge Liberty Island (shipspotting.com)

1.3.2 Wild Dragon draghead

The Wild Dragon draghead was originally developed as IHC's solution for cutting heavily compacted very fine sands in the Yangtze river [1]. The visor of the draghead is actuated by a hydraulic cylinder and is equipped with two rows of teeth. These teeth, which are usually chisel-shaped, have water jets

in them which help to loosen the sand. In addition to the tooth jets the Wild Dragon is also equipped with heel jets and jets in the visor. The heel jets liquefy the sand bed before it is cut. The jets in the visor dilute the sand-water mixture in the visor after it is cut.
Great Lakes uses two versions of Wild Dragon dragheads, the normal version and the extended version. The latter is equipped with a longer visor which can cut deeper into the bed material. On board of the Liberty Island the extended version mostly used, hence for calculations the data of the extended draghead will be used.

1.4 Approach

Earlier in this chapter a number of required outputs were shown. The two most important outputs of these are the in situ production and the slurry concentration because these outputs can eventually be used to estimate the loading time. However, to calculate these it must be known what the thickness of the removed layer is, thus actually the cut slice thickness might be the most important output.
Given the fact that the Wild Dragon draghead has a movable visor, a good approach to find the cut slice thickness might be to assume that the draghead is fixed at a certain distance above or even on the sea bed. This way the cut slice thickness is simply dependent on the angle that the visor makes because the cutting teeth are mounted in this visor. Assuming that the slice thickness and production are calculated for a situation in which all parameters are constant means that the visor also remains at a constant angle, which means that an equilibrium must exist between the moment acting on the visor around the point at which the visor is hinged. Thus, if for given conditions the angle of the visor can be found for which a moment balance exists then production can be calculated.
In order to model this process first it must be found out which moments around the visor hinge play a role. Two obvious moments are the moment due to the cutting of the sand and the moment of the hydraulic cylinder. For these a way must be found to model the force responsible for the moment. In the case of the moment due to the cutting of sand thus a way must be found to calculate the force that is required to cut the sand. Also the parameters of the soil that are needed for this must be identified.
Calculating a moment also requires a moment arm to be known. Hence, the parts of the draghead (the geometry) must be identified that can contribute to this. Furthermore a way must be found to obtain this geometry from a technical drawing and make it suitable for use in a numerical model.
As mentioned in the previous section the Wild Dragon is equipped with water jets at multiple locations. For these it must be found out if and how these contribute to the production process and if needed how this must be modeled.
Lastly, if all relevant moments can be calculated a way must be found to actually find the moment balance and a way must be found to calculate the slurry density based on the in situ production.
In the coming chapters of this thesis the steps required to make a draghead production model as described above have been taken and the findings of taking these steps have been written down. After completion of the model the model has also been tested by doing a sensitivity analysis. The findings of this analysis have also been written down.

2 Draghead Production

2.1 Introduction

As was mentioned in the introduction chapter, the draghead production model calculates the production by finding a moment balance around the visor hinge point. In this chapter the process of finding this moment balance as well as the process of calculating production and concentration when balance is found are described. In the next three paragraphs a small overview of the main components of the trailing suction hopper dredge (including the cutting tool) and their functions are given.
After this small overview it is shown what part of the TSHD is analyzed and actually modeled in the draghead production model. Having these system boundaries in mind, the processes of finding a moment balance and calculating the draghead production are described.
In the last paragraph a reference is given to the chapters describing the theories needed to model the aforementioned processes.

2.2 The trailing suction hopper dredge

In this paragraph a short description is given of the trailing suction hopper dredge and its main components.

2.2.1 General information

A trailing suction hopper dredge (TSHD) is a ship-shaped dredge that collects sand by using long arms (drag arms) on which a vacuum cleaner-like mouth is attached that sucks up the sediments from the bottom. The sediments are then stored in the hull of the the ship, the hopper. When the hopper has been filled the TSHD sails from the area where the sediments are collected (the borrowing area) to the area where the sediments are needed or have to be disposed.
Usually the sediments in the hopper can be unloaded in three ways. The sediments can be dumped below the TSHD through valves in the bottom of the ship, the sediments can be pumped ashore through a pipeline or the sediments can be pumped overboard through a nozzle (rainbowing). The process of rainbowing can be seen in figure 2.1.
Since a trailing suction hopper dredge is a ship, all systems that are present on normal ships are also present on a TSHD. This also means that the TSHD also uses propellers for propulsion during sailing as well as during trailing.
Besides the systems that a normal ships would also have, the trailing suction hopper dredge also has systems on board that are related to dredging. The most obvious of these systems are probably the drag arm and the draghead. These systems will however be discussed respectively in paragraph 2.3 and 2.4. Other important dredging related systems are the pump system and the davits and swell compensators. These systems will be discussed in the next sections.

Figure 2.1: The TSHD Northerly Island rainbowing (Original from: GLDD)

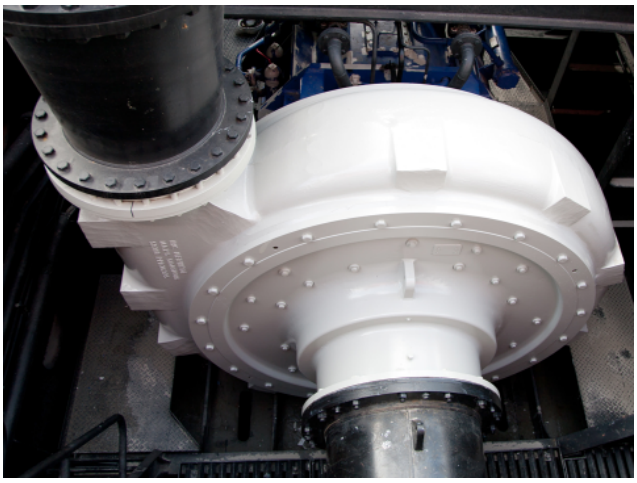

Figure 2.2: A centrifugal dredge pump (Original from: royalihc.com)

2.2.2 Pump system

The pump system of a TSHD can be divided into two systems. One system provides water to water jets. These water jets are used to liquefy sand on the seabed (heel jets and tooth jets) when trailing or in the hopper when discharging. The other system is used to pump slurry (a sand water mixture). Pumping slurry can happen in two directions, into the hopper and out of the hopper. When a TSHD is trailing the dredge pump system is mostly used for its suction in order to lift the slurry from the seabed into the ship and the hopper. When slurry is pumped out of the hopper the pump system is mostly used to push the slurry through pipelines.
Although both pump systems pump different materials, the systems consist of comparable components: pipes, valves and most importantly, one or multiple centrifugal pumps (see figure 2.2), albeit in different sizes and setups.

2.2.3 Davits and swell compensators

When a trailing suction hopper dredge is not trailing, the drag arm and draghead rest on a support on the deck of the ship. In order to start trailing the drag arm must be lifted from the deck, be moved to the side of the vessel and be lowered onto the seabed. This is done by a number of gantries (sometimes called davits) that are attached to the drag arm by steel cables. Usually two cables and gantries are used per drag arm. One cable attaches to the upper arm and one cable attaches to the lower arm (see paragraph 2.3), this can be seen in figure 2.3.
In order to prevent the draghead from smashing into the sea bed due to the heaving motions of the vessel, the TSHD is also equipped with swell compensators (see figure 2.4). Swell compensators are systems that consist of a number of winches and a hydraulic cylinder. The steel cable that is attached to the drag arm runs over these winches and the hydraulic cylinder. By changing the pressure in the hydraulic cylinder the amount of damping of the heave motions can be set. Changing the pressure in the hydraulic cylinder also changes the tension in the cable and hence the force that is pulling on the drag arm. This means that by changing the pressure in the hydraulic cylinder the weight of the drag arm and draghead that is acting on the seabed can be regulated.

Figure 2.3: Davits supporting the drag arm (Original from: products.damen.com)

Figure 2.4: A swell compensator with a davit in the background (dredgingmachinery.en.china.cn)

2.3 The suction arm

The suction arm (or drag arm) is the part that connects the ship and the draghead. The slurry that enters the suction mouth of the draghead travels through the suction arm to the dredge pump system on board of the ship. From there the slurry will eventually end up in the hopper of the ship.
Although a drag arm is a complex system six main components can be identified. These main components are numbered 1 through 6 in figure 2.5 and are described below.

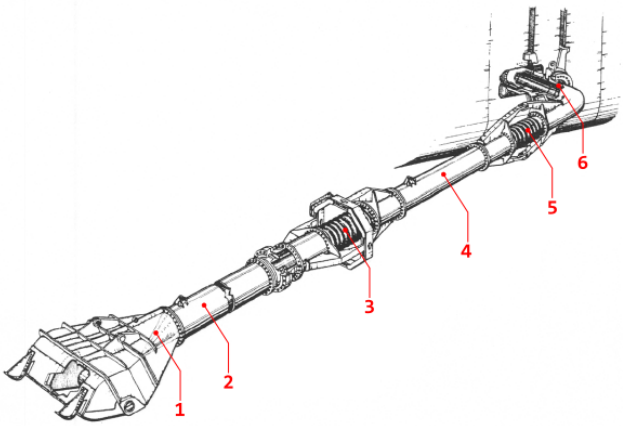

Figure 2.5: A TSHD suction arm (Original from: [2])

Number 1 is the draghead. The draghead is the part that is responsible for directing the sand from the seabed into the suction arm. The draghead is discussed in more detail in paragraph 2.4.
Number 2 is the lower suction arm. This is the part through which the slurry is transported from the draghead to the vessel. It is also the part to which the steel cable of the swell compensator is attached.
Number 3 is a gimbal joint. This joint allows the lower part of the suction arm to rotate in horizontal

and vertical direction with respect to the upper part of the suction arm. Since this joint connects the lower suction arm with the upper suction arm the slurry also passes through the joint.
Number 4 is the upper suction arm. As is the case with the lower suction arm the slury also passes through the upper suction arm. Also another steel cable of a swell compensator connects to this part.
Number 5 is another gimbal joint. This joint connects the upper suction arm with the corner tube that enters the ships hull. Contrary to the gimbal joint of number 3, this gimbal only allows horizontal motions. Again the slurry also passes through this joint.
Number 6 is the trunnion of the drag arm. The trunnion allows the drag arm to move up and down at the location where the drag arm enters the hull.

2.4 The Draghead

In this paragraph a small overview is given of the main parts of a draghead. In addition to the overview of the main parts also an overview is given of the production processes that are concerned with a draghead. Both overviews are key to understand the model working principle described in paragraph 2.6.

2.4.1 Main components

As was mentioned before, the draghead and the production related to the draghead are the main topic of this thesis. A draghead consists of many components, however a few main components can be identified. These components are numbered 1 through 5 in figure 2.6 and will be described in this section. In figure 2.7 a picture of a real draghead is shown in which these numbered components can also be seen. Other components whose function is not key to understanding the model working principle described in paragraph 2.6 might be described in paragraph 5.2.

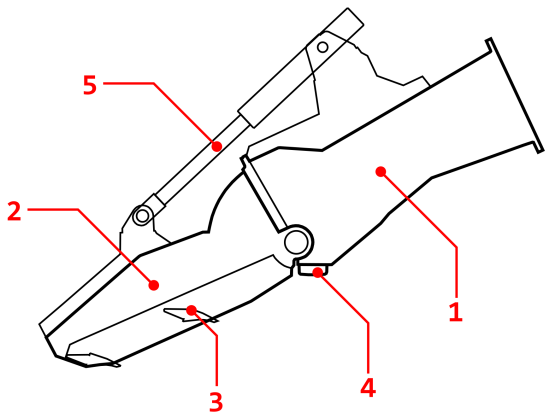

Figure 2.6: A schematic side view of a Wild Dragon draghead

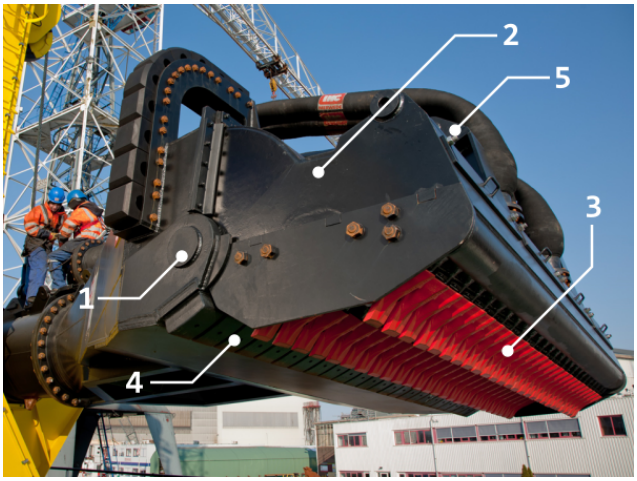

Figure 2.7: A real Wild Dragon draghead (Original from: royalihc.com)

Number 1 is the helmet of the draghead. This part connects to the lower suction arm and hence the entrance to the suction arm, the suction mouth, is located here. The helmet forms the basis of the draghead because all other components are directly or indirectly connected to it.

Number 2 is the visor. The visor closes off an area of the seabed from the surrounding water, making it easier for the sediments to be sucked up by the suction mouth. However, usually dragheads do not solely rely on suction for production. It is common for dragheads to have cutting teeth mounted in the visor. The visor hinges on the helmet, which makes the angle it makes with respect to the helmet adjustable.
Number 3 are the cutting teeth. As was already explained, modern dragheads do usually not solely rely on the flow caused by the suction of the pump (erosion) to remove a layer of sand. Modern dragheads are therefore usually equipped with cutting teeth that cut a layer of sand which makes the sand easier to be sucked up. Depending on the type of draghead one or two rows of teeth can be installed.
Number 4 are the heel jets. Some draghead have nozzles for water jets in the heel blocks. The water jets liquefy the soil which makes the soil easier to cut and suck up. Hence heel jets reduce the cutting force and the required trailing force.
Number 5 is the actuator. In the case of figures 2.6 and 2.7 the actuator is a hydraulic cylinder which will also be the standard for the production model. The actuator pushes the visor down and hence ensures contact between the visor and the seabed. When the visor is pushed down the cutting teeth are pushed deeper into the soil.
When a draghead is equipped with a hydraulic cylinder as an actuator the draghead is called an active draghead. Active dragheads enable the visor angle to be controlled by advanced control systems. Usually these control systems have different control programs to control the visor angle. Common control programs are a constant visor angle program, a constant cut slice thickness program (when the sea bed conditions are not constant) and a constant cylinder force program. The constant cylinder force program is what will be modeled in the production model.

2.4.2 Production processes

During trailing multiple processes contribute to the total in situ production. The in situ production is the volume of soil that is excavated from the seabed per unit of time. If no spillage to the surroundings is assumed then all of this volume of soil will enter the suction mouth and eventually end up in the hopper.
According to *P.M. van den Bergh* [3] three processes play an important role for excavation with a draghead equipped with cutting teeth and heel jets. These processes are: erosion caused by an incoming water flow from the back of the draghead, erosion due to the water jets in the heel and cutting the soil using the teeth. If in situ production (or simply production) is considered to be the volume of soil that is excavated from the seabed, only two of the three processes can be regarded production processes.
The first of these processes is the excavation by the heel jets. In the production model it is assumed that the jets liquefy the soil after which it is easily sucked up by the suction mouth. Another view on the working principle of the heel jets is that the jets loosen the soil which prevents any pore under pressures to build up during cutting, which makes the soil easy to cut. If it is assumed that soil without pore under pressures requires no cutting force to cut then there is no practical difference between the two views: the heel jets remove a layer of sand without requiring any cutting force.
The other process that can be regarded as a production process is cutting the soil with teeth. During this process a layer of sand is sheared, after which it travels up the blade and is taken into the suction mouth by a flow of water. Since an actual layer of sand is excavated, this process is seen as a production process. The flow of water that picks up the cut sand at the top of the blade can be provided water jets mounted in the visor or the water flowing from the back of the draghead (if the draghead setup allows for this). The source of the water flow does not matter for the production process and is therefore not an important topic in this thesis.

As was mentioned before, the erosion process due to the flow from the back of the draghead only transports sand that has already been removed from the seabed. Hence the flow does not remove a layer from the seabed and therefore this process cannot be seen as a production process.
How the production processes are used in the model is described in section 2.6.1.

2.5 System boundaries

In the previous paragraphs the main components of a trailing suction hopper dredge that help contribute to production have been highlighted. In reality many of these components influence each other or are influenced by external factors and hence they influence the production. However, modeling all the components (or many) and the internal and external influences in order to calculate production would lead to a very complex production model. Therefore a smaller system than the entire TSHD should be chosen to model.
For this production model the choice has been made to only consider the draghead (see figures 2.8 and 2.9). The draghead in this model is dragged over the seabed at a constant speed and is suspended in such a way that the heel barely touches the soil surface. Also, the lower arm does not change its angle during trailing. The production is calculated by finding balance between the cutting moments and the moments of the actuators, this is described in more detail in paragraph 2.6.
By only regarding the draghead and doing other assumptions in order to calculate production, various influences on the actual production are disregarded. This means that situations might arise in which although the model calculates the production, the assumptions made in order to make the calculation might not be valid anymore. Therefore also the limits of the validity of the model should be calculated. This is shown in paragraph 6.11.

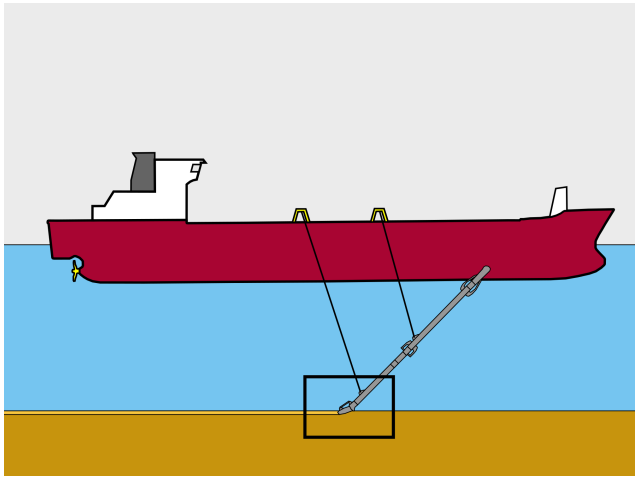

Figure 2.8: A trailing suction hopper dredge with its drag arm lowered onto the seabed

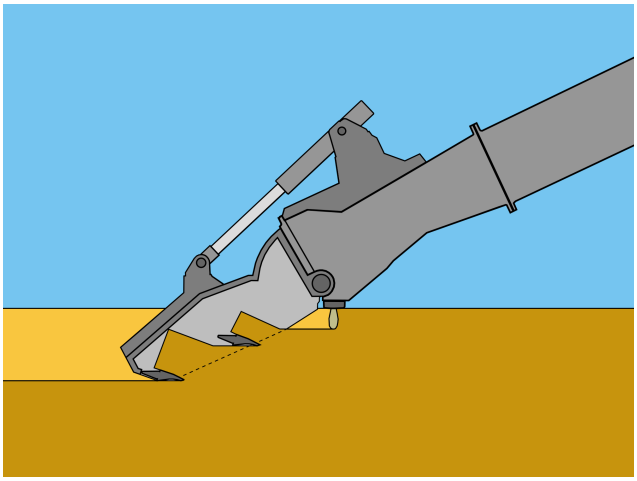

Figure 2.9: A draghead that is lowered onto the seabed

2.6 Model working principle

In this paragraph the theoretical approach in calculating the production and slurry concentration using a moment balance is covered.

2.6.1 Production

In section 2.4.2 it was established that for a draghead two processes remove layers of sand from the seabed and hence contribute to the in situ production. The first of these production processes is the excavation of soil by the heel jets. The second process is excavation of soil using cutting teeth. If a draghead is equipped with heel jets and two rows of teeth, like the Wild Dragon draghead, then three separate layers of sand are removed: $Layer_{Jet}$, $Layer_{Blade1}$ and $Layer_{Blade2}$. These layers are shown in figure 2.10. In dredging the SI units of production are cubic meters per second (m^3/s). However

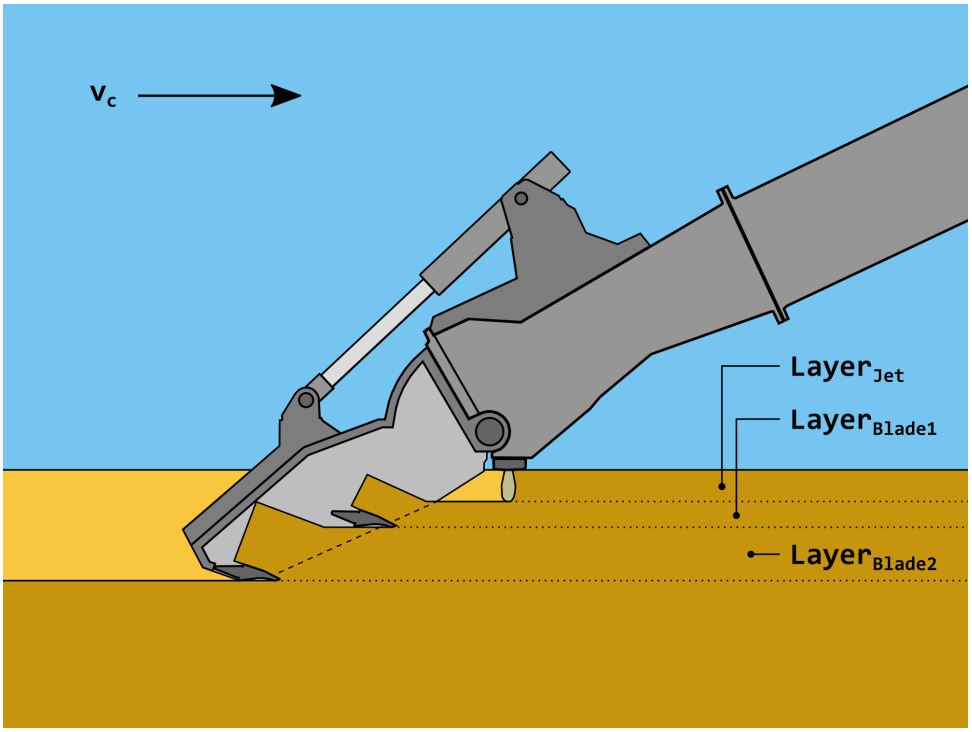

Figure 2.10: The different layers that contribute to the total in situ production

at Great Lakes more commonly used units are cubic yards per minute (yd^3/min) or cubic yard per hour (yd^3/hr). In general production is thus defined as a unit of volume per unit of time.
If the thickness of a layer that is removed is known then the production can be calculated by multiplying the thickness with the width over which this thickness is removed and the speed at which the layer is removed. For the production model the assumption is made that the width over which the layer is removed is the same for both rows of teeth as well as the layer removed by the heel jets and is equal to the width of the draghead W. The speed at which the layers are removed is the speed at which the draghead moves over the seabed, which is the trailing speed v_c. The production per layer can then be expressed as follows.

$$Production_{Jet} = Layer_{Jet} \cdot W \cdot v_c \tag{2.6.1}$$

$$Production_{Blade1} = Layer_{Blade1} \cdot W \cdot v_c \tag{2.6.2}$$

$$Production_{Blade2} = Layer_{Blade2} \cdot W \cdot v_c \tag{2.6.3}$$

Since all of the layers are multiplied with the same trailing speed and draghead width, the layers can be added together to $Layer_{Total}$. This layer can then be used to calculate the total in situ production.

$$Production_{Total} = (Layer_{Jet} + Layer_{Blade1} + Layer_{Blade2}) \cdot W \cdot v_c = Layer_{Total} \cdot W \cdot v_c \quad (2.6.4)$$

Equation (2.6.4) shows that when the layer thicknesses, the width of the draghead and the trailing speed are known the in situ production can be calculated. The width of a draghead is a parameter that can easily be obtained from technical drawings. The trailing speed is imposed since one of the required outputs is production per trailing speed. The layer thicknesses are not imposed and thus have to be calculated. This means that the layer thicknesses are dependent on various parameters: soil mechanical parameters like the angle of internal friction and the permeability, equipment parameters like the geometry of the draghead and dredging parameters like the water depth and trailing speed.
Only the layer removed by the heel jets can be directly calculated by using an equation. More precisely, a jet penetration equation. Several jet penetration equations exist and a number of them are described in chapter 4.
Calculating the layer(s) removed by the teeth is not so straightforward. In order to determine the thickness cut by the teeth the position of the teeth with respect to the soil surface must be known. This requires the angle of the visor (in which the teeth are mounted) to be known. This angle is determined by finding balance between the moments of an actuator and the moments caused by cutting forces of the teeth. This principle is described in section 2.6.2. The theory used to calculate the cutting forces is described in chapter 3.

2.6.2 Visor moment balance

In section 2.6.1 it was explained that the total in situ production of a draghead can be calculated if the layer thickness removed by water jets, the layer thickness(es) removed by the cutting teeth, the width of the draghead and the trailing speed are known. In this section it will be explained how the layer thicknesses removed by the cutting teeth can be found by using a moment balance around the visor hinge.
In order to get to the moment balance around the visor hinge, a number of assumptions have to be made. Since the effects of erosion are neglected it is assumed that the only way for sand to reach suction mouth of the draghead and hence end up in the hopper is for the sand to be directed to the suction mouth by the cutting teeth. In other words, the sand must be scooped up by the cutting teeth in order to be sucked up and contribute to the production. This assumption is valid for both sand that is liquefied by the water jets as for the sand that is cut by teeth. For the liquefied sand that is scooped up it is assumed that the scooping process does not contribute to any force on the cutting teeth. These assumptions lead to a situation in which the total in situ production is dictated by the depth of the tip of the lowest row of cutting teeth. Since the helmet is assumed to be fixed with respect to the soil surface, the position of the origin with respect to the soil surface will not change. Therefore it can be stated that the total in situ production is dictated by the vertical position of the tip of the lowest row of cutting teeth.
The cutting teeth are mounted in the visor and the visor is hinged on the helmet, which is fixed. Therefore the (vertical) position of the tips of the cutting teeth can only be changed by rotating the visor.
The whole cutting process is assumed to be continuous and stationary and the soil is assumed to be homogeneous. This means that the trailing speed does not change, the dredging depth does not change, the soil parameters do not change and the angles of the visor and the helmet do not change, which means that the production is constant. The only component that is allowed to rotate in this

system, the visor, is also at a constant angle, which means that the sum of the moments around the visor hinge must equal to zero. This can be expressed as follows:

$$\sum M_{visor} = 0 \tag{2.6.5}$$

It is assumed that the only forces that act on the visor and hence contribute to the moment balance, are the force of actuators and the cutting force(s) of one or more sets of teeth. These forces are shown in figure 2.11. Hence, friction forces of sand on the sides of the visor and drag forces of the flow of water on the visor are neglected. These assumptions lead to a moment balance that consists of two terms, a moment due to the cutting forces and a moment due to the force of actuators:

$$\sum M_{visor} = M_{cutting} + M_{actuator} = 0 \tag{2.6.6}$$

A cutting force that acts on a row of teeth consists of both a horizontal and a vertical component. For a draghead with two rows of teeth this means that four cutting force components act on the visor. As can also be seen in figure 2.11. Hence, the total cutting moment consists of four separate cutting moments.

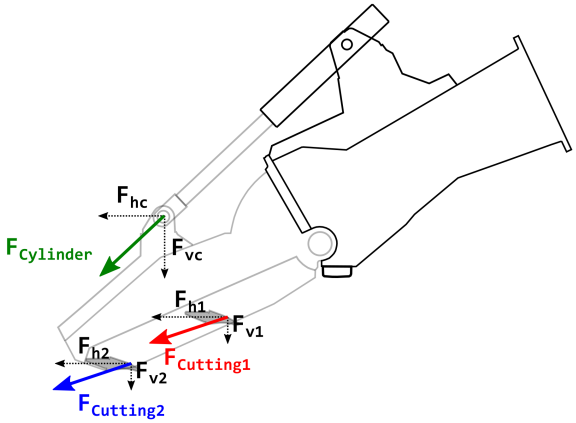

Figure 2.11: The actuator and cutting forces that cause a moment around the visor hinge

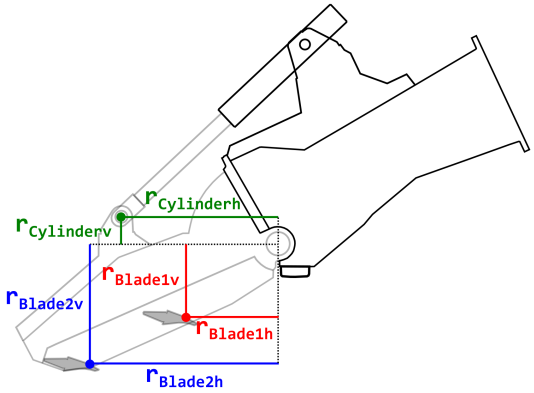

Figure 2.12: The moments arms on which the forces act to cause a moment around the visor hinge

If the row of cutting teeth closest to the visor hinge is denoted with *Blade1* and the other row of cutting teeth is denoted with *Blade2* then the following cutting moments can be identified.
The cutting moment due to the vertical cutting force component on blade 1:

$$M_{Blade1v} = F_{v1} \cdot r_{Blade1h} \tag{2.6.7}$$

The cutting moment due to the horizontal cutting force component on blade 1:

$$M_{Blade1h} = -F_{h1} \cdot r_{Blade1v} \tag{2.6.8}$$

The cutting moment due to the vertical cutting force component on blade 2:

$$M_{Blade2v} = F_{v2} \cdot r_{Blade2h} \tag{2.6.9}$$

The cutting moment due to the horizontal cutting force component on blade 2:

$$M_{Blade2h} = -F_{h2} \cdot r_{Blade2v} \tag{2.6.10}$$

In the equations above the moment arms $r_{Blade1h}$ and $r_{Blade2h}$ are respectively the horizontal distance from the force acting point on blade 1 to the origin and the horizontal distance from the force acting point on blade 2 to the origin. The moment arms $r_{Blade1v}$ and $r_{Blade2v}$ are respectively the vertical distance from the force acting point on blade 1 to the origin and the vertical distance from the force acting point on blade 2 to the origin. The aforementioned moments arms are shown in figure 2.12.
The cutting forces in the equations are calculated using the cutting theories described in chapter 3. In these cutting theories the positive direction for the horizontal cutting force is to the left and the positive direction for the vertical cutting force is downwards. Regarding the moments, a counterclockwise rotation of the visor is positive and a clockwise rotation is negative.
The total cutting moment is obtained by adding up all separate cutting moments:

$$M_{cutting} = M_{Blade1v} + M_{Blade2v} + M_{Blade1h} + M_{Blade2h} \tag{2.6.11}$$

How the actuator moment is calculated is dependent on the type of actuator. In the next section the actuator moment is described for four types of actuators.

2.6.3 Actuator moments

In the previous sections it was explained that in order to calculate the production of a draghead, the angle of the visor must be known since this defines how deep the teeth of the draghead will cut. It was also explained that this angle can be found by looking for the situation in which there is equilibrium between the moments caused by the cutting forces and the moments caused by a visor actuator. In this section, the actuator moments for four possible actuators will be derived. The first actuator is a hydraulic cylinder, the second a spring, the third the self-weight of the visor and the fourth the pressure difference between the inside and the outside of the visor.

A hydraulic cylinder is the actuator that is mounted on the Wild Dragon draghead. The force that a hydraulic cylinder exerts is dependent on the pressure in the cylinder and the area of the piston $A_{Cylinder}$. Since most hydraulic cylinders have a circular cross-section, the force of the cylinder can be defined as follows:

$$F_{Cylinder} = p_{Cylinder} \cdot A_{Cylinder} = p_{Cylinder} \cdot \frac{\pi}{4} \cdot D^2_{Cylinder} \tag{2.6.12}$$

This means that for a given cylinder, the force that is exerted can only by changed by changing the pressure of the hydraulic fluid.
The hydraulic cylinder attaches to both the visor and the helmet of the draghead. Usually the cylinder connects to the helmet and the piston connects to the visor. The position where the hydraulic cylinder connects to the visor can be defined with the coordinates x_1 and y_1. The position where the hydraulic cylinder connects to the helmet is defined with the coordinates x_2 and y_2. The origin of the coordinate system is defined as the center of the visor hinge. More on these coordinates and the position of the origin of the coordinate system can be found in chapter 5.
The horizontal distance between the two ends of the hydraulic cylinder is now defined as follows:

$$L_{Cylinderh} = x_1 - x_2 \tag{2.6.13}$$

The vertical distance between the two ends of the hydraulic cylinder can be calculated in a similar fashion:

$$L_{Cylinderv} = y_2 - y_1 \tag{2.6.14}$$

When the horizontal and vertical distances are known the angle that the hydraulic cylinder makes with a horizontal reference line can be calculated as follows:

$$\alpha_{Cylinder} = arctan\left(\frac{L_{Cylinderv}}{L_{Cylinderh}}\right) \tag{2.6.15}$$

The horizontal and vertical component of the force exerted by the hydraulic cylinder can now be calculated as follows:

$$F_{Cylinderh} = F_{Cylinder} \cdot cos(\alpha_{Cylinder}) = F_{Cylinder} \cdot cos\left(arctan\left(\frac{L_{Cylinderv}}{L_{Cylinderh}}\right)\right) \tag{2.6.16}$$

$$F_{Cylinderv} = F_{Cylinder} \cdot sin(\alpha_{Cylinder}) = F_{Cylinder} \cdot sin\left(arctan\left(\frac{L_{Cylinderv}}{L_{Cylinderh}}\right)\right) \tag{2.6.17}$$

In order to calculate moments, the moment arms of the forces acting on the visor have to be known. Because the origin of the coordinate system is defined in the center of the visor hinge and because the moment balance is around this point since the visor rotates around this point, the moment arms are equal to the distance between the origin and the attachment point of the hydraulic cylinder on the visor. This means that the horizontal moment arm $r_{Cylinderh}$ is equal to x_1 and the vertical moment arm $r_{Cylinderv}$ is equal to y_1. Since a moment is defined as a force multiplied with an arm, the moment caused by a hydraulic cylinder is defined as follows:

$$M_{Cylinder} = F_{Cylinderh} \cdot r_{Cylinderv} + F_{Cylinderv} \cdot r_{Cylinderh} = F_{Cylinderh} \cdot y_1 + F_{Cylinderv} \cdot x_1 \tag{2.6.18}$$

Another actuator that can be used on dragheads is a spring. A spring attaches to the helmet and the visor in a similar fashion as the hydraulic cylinder does. This means that for a spring also an attachment on the visor can be defined with coordinates x_1 and y_1. The same goes for an attachment point on the helmet, which is defined with coordinates x_2 and y_2.
In contrast with the hydraulic cylinder, the distance between the two attachment points does affect the force exerted by the spring since this distance defines the compression (or elongation) of the spring. Hence, in order to calculate the force for a given distance, the compression or elongation must be known. This means that a reference distance and force must be known. Since the helmet is assumed to be fixed, the position of spring attachment on the helmet is constant. This means that only a reference position of the spring attachment point on the visor and a reference force are needed. The reference position of the spring attachment point on the visor is denoted with x_0 and y_0 and is defined as the position of the visor attachment point when the visor is in the lowest possible position. When the visor is in this position, the spring might still be partially compressed. In that case a pretension F_0 is present. If the spring is uncompressed in this position the pretension is equal to zero.
The horizontal distance between the two spring attachment points in reference position is defined as follows:

$$L_{springh0} = x_0 - x_2 \tag{2.6.19}$$

Likewise, the vertical distance between the two spring attachment points in reference position is defined as follows:

$$L_{springv0} = y_2 - y_0 \tag{2.6.20}$$

Using the Pythagorean theorem the length of the spring in reference position can now be calculated:

$$L_{spring0} = \sqrt{L_{springh0}^2 + L_{springv0}^2} = \sqrt{(x_0 - x_2)^2 + (y_2 - y_0)^2} \tag{2.6.21}$$

Similar to equations (2.6.19) and (2.6.20), the horizontal and vertical distances between the spring attachment points when the visor is not in reference position can be calculated as follows:

$$L_{springh} = x_1 - x_2 \tag{2.6.22}$$

$$L_{springv1} = y_2 - y_1 \tag{2.6.23}$$

Again, the length of the spring can be calculated using the Pythagorean theorem:

$$L_{spring} = \sqrt{L_{springh}^2 + L_{springv}^2} = \sqrt{(x_1 - x_2)^2 + (y_2 - y_1)^2} \tag{2.6.24}$$

Assuming that the spring has a linear spring coefficient K_{spring}, the force that is exerted by the spring is defined as follows:

$$F_{spring} = F_0 + \Delta L \cdot K_{spring} \tag{2.6.25}$$

In which ΔL is defined as:

$$\Delta L = L_{spring0} - L_{spring} \tag{2.6.26}$$

The angle that the spring makes with a horizontal reference line can be calculated using the horizontal and vertical distances between the attachment points:

$$\alpha_{spring} = arctan\left(\frac{L_{springv}}{L_{springh}}\right) \tag{2.6.27}$$

The horizontal and vertical component of the force exerted by the spring can now be calculated as follows:

$$F_{springh} = F_{spring} \cdot cos(\alpha_{spring}) = F_{spring} \cdot cos\left(arctan\left(\frac{L_{springv}}{L_{springh}}\right)\right) \tag{2.6.28}$$

$$F_{springv} = F_{spring} \cdot sin(\alpha_{spring}) = F_{spring} \cdot sin\left(arctan\left(\frac{L_{springv}}{L_{springh}}\right)\right) \tag{2.6.29}$$

In order to calculate moments, the moment arms of the forces on the visor have to be known. Similar to a situation with a hydraulic cylinder, the origin of the coordinate system is defined in the center of

the visor hinge. Since the moment balance is around this point because the visor rotates around this point, the moment arms are equal to the distance between the origin and the attachment point of the hydraulic cylinder on the visor. This means that the horizontal moment arm $r_{springh}$ is equal to x_1 and the vertical moment arm $r_{springv}$ is equal to y_1. Since a moment is defined as a force multiplied with an arm, the moment caused by a hydraulic cylinder is defined as follows:

$$M_{spring} = F_{springh} \cdot r_{springv} + F_{springv} \cdot r_{springh} = F_{springh} \cdot y_1 + F_{springv} \cdot x_1 \tag{2.6.30}$$

The third actuator moment that will be described is the moment of a floating visor. In the case of a floating visor the visor is 'actuated' only by its own submerged weight (this includes possible extra weights added to the visor). Since every visor has an own submerged weight this moment can be added to every visor moment balance when another actuator is already present.
There are two forces contributing to the actuator moment of the floating visor, a gravity force and a buoyancy force. These two forces act in opposite directions, gravity acts downwards while buoyancy acts upwards. If the visor is assumed to be made entirely of one material, in this case steel, then the point on which these two forces act is the same point, the center of gravity. The location of the center of gravity can be defined with the coordinates x_g and y_g. As with the previous actuator moments, the origin is defined as the center of the visor hinge. Since the resulting force of he gravity and buoyancy only works in the vertical direction, only the horizontal moment arm r_{visorh} is needed to calculate the moments. Again this moment arm is equal to the distance between the origin (visor hinge) and the point where the force acts, hence r_{visorh} equals x_g.
Assuming that the visor is made entirely of steel, the resulting force can be defined as follows:

$$F_{float} = (\rho_{steel} - \rho_w) \cdot g \cdot V_{visor} \tag{2.6.31}$$

Where ρ_{steel} is the density of steel (roughly 7800 kg/m^3), ρ_w is the density of water (commonly 1025 kg/m^3 for seawater), g is the gravitational constant and V_{visor} is the volume of the visor.
However, in practice the volume of the visor might not readily be known but the mass of the visor might (because the mass of a visor must be known in order to lift it). Therefore, still assuming that the visor is made entirely of steel, an expression for the volume of the visor can be found:

$$V_{visor} = \frac{m_{visor}}{\rho_{steel}} \tag{2.6.32}$$

Substituting equation (2.6.32) in equation (2.6.31) yields an expression for the resulting visor force:

$$F_{float} = \frac{(\rho_{steel} - \rho_w)}{\rho_{steel}} \cdot g \cdot m_{visor} \tag{2.6.33}$$

The actuator moment due to the submerged weight of the visor can now be calculated by multiplying the moment arm with the resulting visor force:

$$M_{float} = F_{float} \cdot r_{visorh} = F_{float} \cdot x_g \tag{2.6.34}$$

The last actuator moment that will be described is the the moment due to a pressure difference between the inside and the outside of the visor. Since a draghead sucks in water and sand there is a lower pressure inside the the draghead than outside the draghead. This means that there is a resultant force acting on the outside of the visor acting inwards. The forces on the sides cancel each other out. Hence, the force of importance that is acting inward is the force on the top of the visor.

The pressure difference between the inside and outside the draghead is rarely measured and is difficult to precisely calculate. Therefore a simple approach on estimating this pressure difference is given below.
Usually an average flow Q_{dredge} into the draghead and suction arm is known. From technical drawings the the total area of openings underneath the visor A_{visor} can be derived. Using these two parameters an average flow speed can be calculated as follows.

$$v_{avg} = \frac{Q_{dredge}}{A_{visor}} \tag{2.6.35}$$

Using the Bernoulli equation and neglecting any height differences the pressure difference can be defined as follows.

$$\Delta p = \frac{1}{2} \cdot \rho_w \cdot v_{avg}^2 \tag{2.6.36}$$

To calculate a force using the pressure difference a surface area is needed. Simply taking the surface area of the top of the visor is however not sufficient. This is because the force due to a pressure acts perpendicular to the surface. Some visors are curved in such a way that the forces due to the pressure would point directly to the visor hinge point and would thus not generate a moment around this point. The parts of a visor that are curved in such a way should hence be disregarded when calculating the area of the visor top. For a draghead like the Wild Dragon this area can be simplified to the largest area that can be considered flat. When the area A_{top} is known the force acting on the visor can be calculated as follows.

$$F_{visor} = \Delta p \cdot A_{top} \tag{2.6.37}$$

Since pressure acts in all directions the force acting on the visor is independent of the angle of the visor and therefore constant as long as the pressure difference is considered constant. This means that the moment around the visor hinge due to the pressure is also constant.
If the point at which the pressure force acts on the top of the visor is known then the moment arm (which is perpendicular to the force) can be calculated. When the moment arm r_p has been calculated the moment around the visor hinge can be calculated as follows.

$$M_{pressure} = F_{visor} \cdot r_p = \Delta p \cdot A_{top} \cdot r_p \tag{2.6.38}$$

2.6.4 Concentration

In the required model outputs not only the in situ production and the cut slice thickness were listed. The other required outputs are the slurry concentration, the trailing force (or propulsion resistance) and the resulting downforce. Of these outputs the slurry concentration is the most important since it is an input for other models.
In reality the available pump head and hence the available pump flow is dependent on the slurry concentration in the pump. Likewise, the slurry concentration is dependent on the in situ production and the available pump flow and hence on the available pump head. This means that iteration cycles are required to find the slurry concentration that matches the pump head and flow and the in situ production. Furthermore this would require that the whole dredge pump system is modeled, which would lead to a rather complex model. To avoid adding complex flow calculation to the production model the assumption can be made that the dredge pump flow Q_{Dredge} is constant. This is a reasonable assumption since the dredge pump flow of a drag arm of the Liberty Island usually only varies slightly

for changing slurry concentrations (between 2.97 m^3/s for a density of 1100 kg/m^3 and 2.69 m^3/s for a density of 1500 kg/m^3). For a constant flow then the average of the two flows can then be chosen (2.83 m^3/s).
Spillage losses can be assumed to be a percentage of the in situ production and can be accounted for by multiplying the in situ production with $1 - C_{spillage}$. The coefficient $C_{spillage}$ should range between 0 and 1 and indicates the fraction of spillage losses.
Another option for spillage is to assume that there is no spillage as long as the following equation is true.

$$Q_{Dredge} \geq Q_{Jetwater} \tag{2.6.39}$$

In other words, as long as the flow of the dredge pump is greater than or equal to the total flow of jet water into the draghead there will be no spillage losses. In this situation the slurry concentration is defined as follows.

$$C_v = \frac{(1 - n_i) \cdot Production_{Total}}{Q_{Dredge}} \tag{2.6.40}$$

In equation (2.6.40) n_i is the porosity of the bed, which tells which fraction of the sea bed is pore (seawater). Hence, the numerator of the fraction in equation (2.6.40) calculates the total volume of the sand grains that are actually dug up by the draghead.
When the total jet water flow into the draghead is greater than the flow of the dredge pump, which is expressed by the following equation, spillage losses are introduced.

$$Q_{Dredge} \ngeq Q_{Jetwater} \tag{2.6.41}$$

The slurry concentration in this situation, assuming that a homogeneous mixture is made, is defined as follows.

$$C_v = \frac{(1 - n_i) \cdot Production_{Total}}{n_i \cdot Production_{Total} + Q_{Jetwater}} \tag{2.6.42}$$

The fraction of spillage losses $C_{spillage}$ is then expressed as follows.

$$C_{spillage} = 1 - \frac{Q_{Dredge}}{Production_{Total} + Q_{Jetwater}} \tag{2.6.43}$$

An alternative to assuming a constant flow for the concentration calculations is assuming that in the working range of the pump, the pump flow varies linearly with the slurry density. Using the range of flows and densities given earlier (2.97 m^3/s for a density of 1100 kg/m^3 and 2.69 m^3/s for a density of 1500 kg/m^3) the following linear equation can be made.

$$Q_{Dredge} = -7 \cdot 10^{-4} \cdot (\rho_m - 1100) + 2.97 \tag{2.6.44}$$

In equation (2.6.44) ρ_m is the slurry density. The relation between the slurry density and the volume concentration of the slurry C_v is defined as follows.

$$C_v = \frac{\rho_m - \rho_f}{\rho_s - \rho_f} \tag{2.6.45}$$

In equation(2.6.45) ρ_f is the density of the carrier fluid (1025 kg/m^3 for seawater) and ρ_s is the density of the solids (2650 kg/m^3 for quartz sands). Rewriting the equation and using the aforementioned densities leads to the following expression for the slurry density.

$$\rho_m = 1625 \cdot C_v + 1025 \tag{2.6.46}$$

Substituting the expression for ρ_m into equation (2.6.44) leads to the following expression.

$$Q_{Dredge} = -7 \cdot 10^{-4} \cdot (1625 \cdot C_v - 75) + 2.97 \tag{2.6.47}$$

If it now is assumed that the condition for no spillage of equation (2.6.39) is true then equation (2.6.40) can be rewritten in terms of the volume concentration.

$$Q_{dredge} = \frac{(1 - n_i) \cdot Production_{Total}}{C_v} \tag{2.6.48}$$

Now there are two equations which both have the same two unknowns, Q_{Dredge} and C_v, which is solvable. Hence, Q_{Dredge} can be eliminated as follows.

$$\frac{(1 - n_i) \cdot Production_{Total}}{C_v} = Q_{dredge} = -7 \cdot 10^{-4} \cdot (1625 \cdot C_v - 75) + 2.97 \tag{2.6.49}$$

Rewriting equation (2.6.49) eventually leads to the following equation.

$$-1.1375 \cdot C_v^2 + 3.0225 \cdot C_v - (1 - n_i) \cdot Production_{Total} = 0 \tag{2.6.50}$$

Equation (2.6.50) can then be solved by using the quadratic formula, as is shown in the next equation.

$$C_v = \frac{-b \pm \sqrt{b^2 - 4ac}}{2a} = \frac{-3.0225 \pm \sqrt{3.0225^2 - 4 \cdot -1.1375 \cdot (1 - n_i) \cdot Production_{Total}}}{2 \cdot -1.1375} \tag{2.6.51}$$

Logically the solution must be chosen that lies between zero and one since the solution is a concentration.
Instead of assuming a linear relation between the pump flow and the slurry density also a higher order relation like a quadratic relation can be assumed. If the linear relationship described above is extrapolated to a mixture density of pure water (1000 kg/m^3) then a pump flow is found of 3.04 m^3/s. If it is assumed that the parabolic relation will go through this point and has its vertex at the end of the known range of pump flow for slurry densities (2.69 m^3/s for 1500 kg/m^3) then Q_{dredge} is described by the following quadratic equation.

$$Q_{dredge} = 1.4 \cdot 10^{-6} \cdot (\rho_m - 1500)^2 + 2.69 \tag{2.6.52}$$

Now by applying the same step as before, substituting equation (2.6.46) for ρ_m in equation (2.6.52), setting this equal to equation (2.6.40) and rewriting the equation the following third order polynomial can be found.

$$3.696875 \cdot C_v^3 - 0.216118 \cdot C_v^2 + 3.005875 \cdot C_v - (1 - n_i) \cdot Production_{Total} = 0 \tag{2.6.53}$$

For the given coefficients equation (2.6.53) has only one real root. This root can be calculated using the following equation.

$$C_v = -\frac{1}{3a} \cdot (b + C + \frac{\Delta_0}{C}) \tag{2.6.54}$$

In equation (2.6.54) C is defined as follows.

$$C = \sqrt[3]{\frac{\Delta_1 + \sqrt{\Delta_1^2 - 4 \cdot \Delta_0^3}}{2}} \tag{2.6.55}$$

In equation (2.6.55) Δ_0 and Δ_1 are defined as follows.

$$\Delta_0 = b^2 - 3ac \tag{2.6.56}$$

$$\Delta_1 = 2b^3 - 9abc + 27a^2d \tag{2.6.57}$$

In the equation above a, b, c and d are the coefficients of the third order polynomial, which for equation (2.6.53) respectively are 3.696875, -0.216118, 3.005875 and $-(1 - n_i) \cdot Production_{Total}$.

2.6.5 Trailing force and downforce

As was mentioned before, two other outputs besides the production and the concentration are required of the production model. These two outputs are both forces, the trailing force and the downforce. However, this thesis mainly focuses on the calculation of the draghead production and the accompanying concentration, therefore only a rough approach on calculating the trailing and downforce will be given.
In general a trailing suction hopper dredge can be considered to only be propelled in directions in the horizontal plane. Any influences of waves on any angles of the ship and hence the propulsion direction are neglected in this consideration. Furthermore a TSHD usually trails in roughly a straight line. Therefore the direction of the propulsion force can be considered to be unidirectional. This would mean that in the trailing situation sketched in figure 2.8 the thrust of the propeller is acting on the hull (at the position of the propeller) and pointed to the right and can therefore be considered a horizontal force. Since horizontal forces to the left were considered to be positive the thrust of the ship is a negative force.
Since the production process (and hence the cutting process) is considered to be continuous and stationary. The sum of the horizontal forces acting on the TSHD must be zero. For this very simple approach the horizontal forces acting on the TSHD are considered to be the propulsion force (the thrust) T_{ship}, the horizontal cutting forces of the blades F_{h1} and F_h2 and the resistance of the ship (the drag) R_{ship}. Using these forces the following expression can be made.

$$\sum F_h = -T_{ship} + F_{h1} + F_{h2} + R_{ship} = 0 \tag{2.6.58}$$

Rewriting equation (2.6.58) leads to an expression for the required trailing (propulsive) force.

$$T_{ship} = F_{h1} + F_{h2} + R_{ship} \tag{2.6.59}$$

This approach does neglect a number of horizontal forces like the resistance of the draghead and the dragarm and the force required to accelerate the cut sand up to the trailing speed of the ship. A good overview of the horizontal forces acting on a TSHD is given by Vlasblom [2].
The last required output is the downforce. This force is interpreted to be the tension in the cable connected to the lower suction arm F_{cable}. If it is assumed that the drag arm is not supported by the sea bed then a simple approach to calculate the tension in the cable is to find a balance of moments around the lower gimbal joint (number 3 in figure 2.5). For a simple approach the forces generating a moment around the gimbal can be considered the cable tension, the cutting forces of blade 1 and 2 and the submerged weight of the lower suction arm filled with slurry and draghead. If these forces are multiplied with their respective moment arm with respect to the gimbal then the moments around around the gimbal M_{cable}, $M_{cutting1}$, $M_{cutting2}$ and $M_{gravity}$ are obtained. Note that

the cutting moments should not be confused with the cutting moments around the visor hinge. The moment balance is then defined as follows.

$$\sum M_{gimbal} = M_{cable} + M_{cutting1} + M_{cutting2} + M_{gravity} = 0 \tag{2.6.60}$$

The moment due to the cable tension can be defined as follows.

$$M_{cable} = F_{cable} \cdot r \tag{2.6.61}$$

Substituting the expression for the cable moment in equation (2.6.60) and rewriting the equation leads to the following equation.

$$F_{cable} \cdot r = -M_{cutting1} - M_{cutting2} - M_{gravity} \tag{2.6.62}$$

Using equation (2.6.62) an expression can be found for the force in the cable.

$$F_{cable} = \frac{-M_{cutting1} - M_{cutting2} - M_{gravity}}{r} \tag{2.6.63}$$

2.7 Reference to chapters

In this chapter a number of references to more detailed descriptions of theories in other chapters have been made. In the table in this paragraph the subjects and chapters that were mentioned in this chapter are summarized.

Table 2.1: A reference to the theory described in the coming chapters

Chapter	Relation to production model
Chapter 3	Theory to calculate the cutting forces for water saturated sand.
Chapter 4	Theory to calculate the penetration depth of the heel jets in sand.
Chapter 5	Description of the draghead and cutting tool geometry.
Chapter 6	Implementation of all theories in the production model.

3 Cutting Theory

3.1 Introduction

In this chapter the cutting theories used in the draghead production model are covered. These cutting theories can be found in in the book *The Delft Sand, Clay & Rock Cutting Model* by S.A. Miedema [4],[5].
The cutting theory is mainly used to calculate the horizontal and vertical cutting force. These forces can be used to calculate the required trailing force and power. But more importantly, the cutting forces are used in the moment balance which is the backbone of the production calculation, as will be shown in chapter 6.
Before the actual cutting theories are covered, first a brief overview of the soil and cutting parameter definitions is given in the next paragraph. The paragraph about saturated sand cutting holds the theory that is implemented in the production model.
In the numerical pore pressure paragraph the model behind the actual cutting force calculations for water saturated sands is discussed. In the two paragraphs that follow extensions to the existing numerical pore pressure code are discussed. The first of these describes the author his solution to modeling the tooth jets of the Wild Dragon draghead. The last paragraph describes how progression of cavitation onto the blade during cutting can be modeled. The theory behind this can also be found in *The Delft Sand, Clay & Rock Cutting Model*, however the implementation of the theory is done by the author.
For readers familiar with Miedema his cutting theory for water saturated sand, including the parallel resistor method, it is recommended to start reading at section 3.4.2 because the paragraphs before this are simply a short recap of the theory described in *The Delft Sand, Clay & Rock Cutting Model* and thus hold no new information.
Theory used to calculate the cutting forces of processes that have not been implemented in the Python code used to generate the results shown in chapter 7 can be found in appendix A.

3.2 General cutting model definitions

In this paragraph the definitions of parameters that are present in the main cutting model of the production model, the cutting model for water saturated sand, are discussed. The definitions are named general cutting model definitions because most of the parameters discussed here are also present in the other cutting models discussed in this chapter.

3.2.1 Soil parameter definitions

Below the definitions of a number soil parameters that are used in the different cutting theories are given together with the symbol that is used for the parameter in this thesis. Note that not all parameters are necessarily used in every theory.

Definitions:

ϕ: The angle of internal friction of sand. The angle of internal friction is a measure of the ability of the soil to withstand shear stresses.

δ: The angle of external friction. The angle of external friction is a measure of the ability of the soil to withstand shear stresses between the soil and in this case a steel surface.

n: Porosity. The porosity is a measure of voids in a soil. It is the fraction of the volume of the voids over the total volume of the soil.

k: Permeability. Permeability is a measure of a soils' ability to let fluids, in this case water, pass through.

3.2.2 Cutting parameter definitions

In this section the definitions for both the cutting model for dry sand and saturated sand are given since they are identical. The definitions for the cutting model for a saturated wedge is slightly different and will be presented in section A.2.1.
The definitions are shown in figure 3.1 and will be described below.

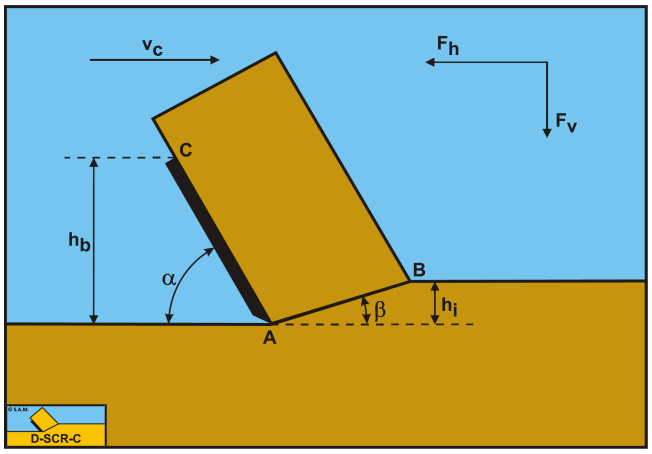

Figure 3.1: General definitions concerning the cutting process

Definitions:

A: Tip of the blade

B: End of the shear plane

C: Top of the blade

A-B: Shear plane

A-C: Blade surface

h_b: Blade height

h_i: Thickness of the layer cut

v_c: Cutting velocity or trailing speed

α: Blade angle

β: Shear angle

F_h: Horizontal force, positive in direction of arrow

F_v: Vertical force, positive in direction of arrow

3.3 Saturated sand cutting

The saturated sand cutting model is the main cutting model used in the production model. Opposed to the dry sand cutting model the effects of dilatation are taken into account in this model because the pores are saturated with water instead of air. This can lead to larger under pressures in the shear layer and on the blade which result in larger cutting forces.
Before the theory on how to calculate the cutting forces using a force equilibrium is shown it is important to explain what dilatation is, why it occurs and why this leads to large under pressures. This will be explained in sections 3.3.1 and 3.3.2. The section after that will explain the force equilibrium.

3.3.1 Dilatation

Cutting sand in essence is shearing layers of sand particles, or moving one layer of sand particles along another layer. In figure 3.2 a sand bed before shearing is simplified to a bed of densely-packed mono-sized spheres (circles in 2D). In the figure it is clear that in order to move a layer along another layer the particles of one layer have to move up since particles cannot move through each other. This upwards motion results in an increase of pore volume, as can be seen in the figure, indicated by 'after shearing'. This is what dilatation is: The increase of pore volume due to shear in the sand bed.

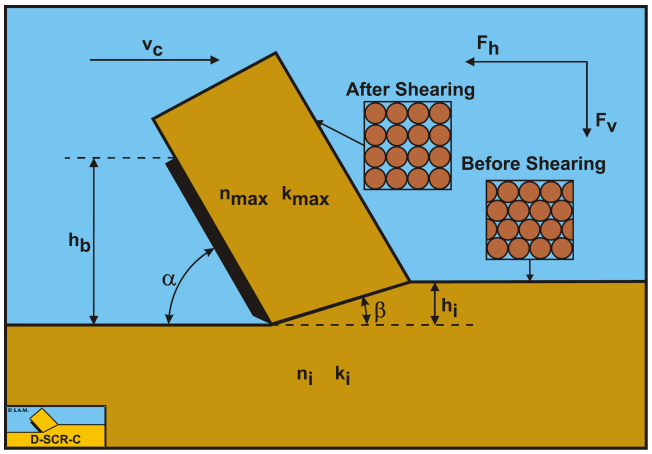

Figure 3.2: Dilatation demonstrated

The increase of the pore volume leads to a flow of water into the shear zone since the increase of pore volume has to be filled with water. This flow of water experiences a resistance due to the presence of the sand particles and this resistance causes the pressure in the pores to drop below the hydrostatic pressure. Due to the pressure difference the grain stresses increase and therefore the cutting forces increase. However, the pore under pressure knows a limit. When the pressure in the pores drops to the saturated water vapor limit bubbles of water vapor will form in the pores, this is known as cavitation. Since the saturated water vapor limit is the lowest pore pressure that can be reached there is also a maximum pressure difference that can be reached for a given hydrostatic pressure. This also means that the cutting forces have a maximum for a given hydrostatic pressure.
Once the shear layer is fully cavitating production can be increased by increasing the trailing speed

without increasing the cutting forces. However, the trailing speed will still be limited by the ship resistance and other forces, therefore production will also be limited.

3.3.2 Pore pressures

In the previous sections it was explained that for water saturated sand the cutting forces are governed by dilatation due to the drop in pore pressures. Hence, in order to calculate the cutting forces through a force equilibrium the forces caused by the pressure drop must be calculated.
As with the dry cutting model the assumption is that the cutting process is continuous and stationary. Furthermore it is assumed that deformations, or the change in volume (dilatation), only take place in the shear zone. These assumptions make the following equation applicable to the sand package around the blade:

$$\left|\frac{\partial^2 p}{\partial x^2}\right| + \left|\frac{\partial^2 p}{\partial y^2}\right| = 0 \tag{3.3.1}$$

Equation (3.3.1) is the two-dimensional storage equation. The equation basically states that if a quantity of anything flows into the element the same quantity must flow out of the element, hence nothing is stored in the element.
In this case it is a quantity of water, flowing due to the effects of dilatation.

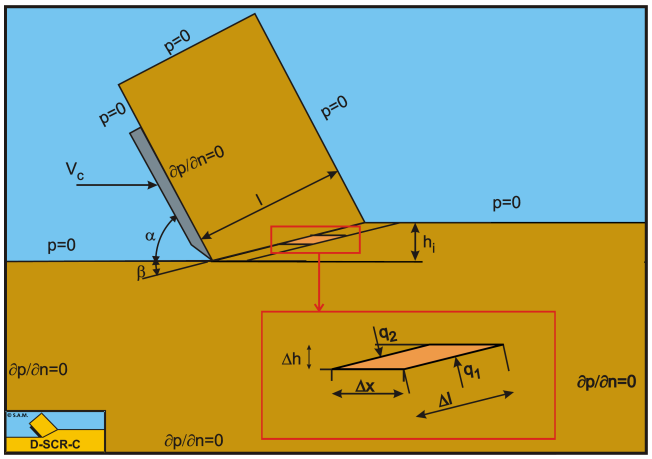

Figure 3.3: Dilatation demonstrated

Dilatation ϵ is a dimensionless number and a function of the initial porosity n_i and the maximum porosity after shearing n_{max}:

$$\epsilon = \frac{n_{max} - n_i}{1 - n_{max}} \tag{3.3.2}$$

Consider a sand element in the shear zone with dimensions Δx and Δl, see figure 3.3. Since the increase of the volume of the soil in the shear zone can entirely be addressed to the increase of pore volume the actual change of volume of the soil can be expressed as follows:

$$\Delta V = \epsilon \cdot \Delta A = \epsilon \cdot \Delta x \cdot \Delta h_i = \epsilon \cdot \Delta x \cdot \Delta l \cdot sin(\beta) \tag{3.3.3}$$

The volume flow rate of the water flowing to the sand element is defined as:

$$\Delta Q = \frac{\partial V}{\partial t} = \epsilon \cdot \frac{\partial x}{\partial t} \cdot \Delta l \cdot sin(\beta) = \epsilon \cdot v_c \cdot \Delta l \cdot sin(\beta) \tag{3.3.4}$$

Since all elements lie on the same line, the shear plane, and all elements are subject to the same dilatation no water will flow between elements. Hence water flowing into the elements will only flow perpendicular to the shear plane.
This leads to two flows entering an element; one flow through the non-dilated soil with permeability k_i and one flow through the dilated soil with permeability k_{max}. Using Darcy's Law expressions for these flows can be found:

$$q = \frac{\partial Q}{\partial l} = q_1 + q_2 = \frac{k_i}{\rho_w \cdot g} \cdot \left|\frac{\partial p}{\partial n}\right|_1 + \frac{k_{max}}{\rho_w \cdot g} \cdot \left|\frac{\partial p}{\partial n}\right|_2 = \epsilon \cdot v_c \cdot sin(\beta) \tag{3.3.5}$$

In equation (3.3.5) the partial derivative $\frac{\partial p}{\partial n}$ is the derivative of the water under-pressures perpendicular to the boundary on which the water under pressures are calculated, which in this case is the shear zone. The other boundary conditions on the sand package are shown in figure 3.3.
The length dimensions in equation (3.3.5) are normalized by dividing them by the cut layer thickness:

$$\frac{k_i}{k_{max}} \cdot \left|\frac{\partial p}{\partial n'}\right|_1 + \left|\frac{\partial p}{\partial n'}\right|_2 = \frac{\rho_w \cdot g \cdot v_c \cdot \epsilon \cdot h_i \cdot sin(\beta)}{k_{max}} \text{ with: } n' = \frac{n}{h_i} \tag{3.3.6}$$

After this step the equation can be made dimensionless with the following equation:

$$\left|\frac{\partial p}{\partial n}\right|' = \frac{\left|\frac{\partial p}{\partial n'}\right|}{\rho_w \cdot g \cdot v_c \cdot \epsilon \cdot h_i / k_{max}} \tag{3.3.7}$$

Making equation (3.3.6) dimensionless using (3.3.7) yields the following equation:

$$\frac{k_i}{k_{max}} \cdot \left|\frac{\partial p}{\partial n}\right|'_1 + \left|\frac{\partial p}{\partial n}\right|'_2 = sin(\beta) \tag{3.3.8}$$

The storage equation (equation (3.3.1)) also has to be made dimensionless:

$$\left|\frac{\partial^2 p}{\partial x^2}\right|' + \left|\frac{\partial^2 p}{\partial y^2}\right|' = 0 \tag{3.3.9}$$

Since equation (3.3.9) also equals zero the pore pressure distribution in the sand package can now be calculated using the storage equation and the boundary conditions.
The dimensionless pore water under-pressures can now be calculated by integrating the derivative of the water under pressure in the direction of a flow line, along a flow line:

$$P_{calc} = \int_{s'} \left|\frac{\partial p}{\partial s}\right|' \cdot ds' \text{ with: } s' = \frac{s}{h_i} \tag{3.3.10}$$

The calculated dimensionless water under pressure can now be transformed into the water under pressure as follows:

$$P_{real} = \int_s \left|\frac{\partial p}{\partial s}\right| \cdot ds = \int_{s'} \frac{\rho_w \cdot g \cdot v_c \cdot \epsilon \cdot h_i}{k_{max}} \cdot \left|\frac{\partial p}{\partial s}\right|' \cdot ds' \tag{3.3.11}$$

Equation (3.3.11) can be simplified to the following equation:

$$P_{real} = \frac{\rho_w \cdot g \cdot v_c \cdot \epsilon \cdot h_i}{k_{max}} \cdot P_{calc} \tag{3.3.12}$$

The equations that are described in this section are not yet suitable for use in calculation models, for that they will have to be discretized. How these equations are adapted for use in pressure calculations will be described in paragraph 3.4.

3.3.3 Equilibrium of forces

The cutting model for water saturated sand assumes that the cutting process is continuous and stationary. This means that all forces in the same direction, including the cutting forces, are in equilibrium.
As with the dry sand cutting model it is assumed that there is no adhesion nor cohesion since the material being cut is sand. Contributions of gravitational and inertial forces are omitted because their magnitude is negligible compared to the magnitude of the pore under pressure forces that are the result of dilatation.
The forces acting on the layer cut can be seen in figure 3.4 and are explained below.

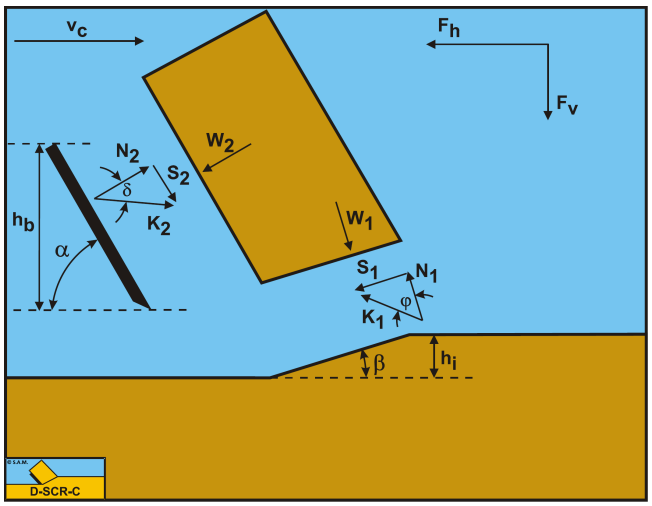

Figure 3.4: Forces acting on the saturated cut slice

Acting forces:

W_1: Force due to water under pressure in the shear zone

W_2: Force due to water under pressure on the blade

N_1: Normal force on shear surface, due to effective grain stresses

S_1: Shear force on shear plane, due to internal friction ($N_1 \cdot tan(\phi)$)

N_2: Normal force on blade surface, due to effective grain stresses

S_2: Shear force on blade surface, due to external friction between sand and steel ($N_2 \cdot tan(\delta)$)

It is important to notice that due to Newton's third law the forces acting on the blade are equal to N_2, S_2 and W_2 but in opposite direction.

The normal force N_1 and the shear force S_1 can be combined into a resulting force K_1:

$$K_1 = \sqrt{N_1^2 + S_1^2} \tag{3.3.13}$$

The same can be done with N_2 and S_2, resulting in K_2:

$$K_2 = \sqrt{N_2^2 + S_2^2} \tag{3.3.14}$$

Because the cutting process is assumed to be continuous and stationary there must be an equilibrium in both the horizontal and the vertical forces:

$$\sum F_h = K_1 \cdot sin(\beta + \phi) - W_1 \cdot sin(\beta) + W_2 \cdot sin(\alpha) - K_2 \cdot sin(\alpha + \delta) = 0 \tag{3.3.15}$$

$$\sum F_v = -K_1 \cdot cos(\beta + \phi) + W_1 \cdot cos(\beta) + W_2 \cdot cos(\alpha) - K_2 \cdot cos(\alpha + \delta) = 0 \tag{3.3.16}$$

Since equation (3.3.15) and equation (3.3.16) have the same two unknowns the system of equations is solvable. Solving the equations yields new expressions for K_1 and K_2:

$$K_1 = \frac{W_2 \cdot sin(\delta) + W_1 \cdot sin(\alpha + \beta + \delta)}{sin(\alpha + \beta + \delta + \phi)} \tag{3.3.17}$$

$$K_2 = \frac{W_2 \cdot sin(\alpha + \beta + \phi) + W_1 \cdot sin(\phi)}{sin(\alpha + \beta + \delta + \phi)} \tag{3.3.18}$$

Where W_1 and W_2 are the water pressure forces, which for the non-cavitating case, require the average pore pressure on the blade and in the shear zone p_{1m} and p_{2m}:

$$W_1 = \frac{p_{1m} \cdot \rho_w \cdot g \cdot v_c \cdot \epsilon \cdot h_i^2 \cdot w}{(a_1 \cdot k_i + a_2 \cdot k_{max}) \cdot sin(\beta)} \tag{3.3.19}$$

$$W_2 = \frac{p_{2m} \cdot \rho_w \cdot g \cdot v_c \cdot \epsilon \cdot h_i \cdot h_b \cdot w}{(a_1 \cdot k_i + a_2 \cdot k_{max}) \cdot sin(\alpha)} \tag{3.3.20}$$

For the cavitating case the formulas can be simplified since the under pressure will not drop any further for an increase of cutting speed. For the following equations it has been assumed that the pressure drop is equal to the hydrostatic pressure instead of the hydrostatic pressure minus the saturated

vapor pressure because the saturated water vapor pressure is of negligible magnitude compared to the pressure drop:

$$W_1 = \frac{\rho_w \cdot g \cdot (z+10) \cdot h_i \cdot w}{sin(\beta)} \tag{3.3.21}$$

$$W_2 = \frac{\rho_w \cdot g \cdot (z+10) \cdot h_b \cdot w}{sin(\alpha)} \tag{3.3.22}$$

The numerical model that is used to provide the average pore pressures p_{1m} and p_{2m} is made in such a way that the pore pressure drop is limited to the cavitation pressure $\rho_w \cdot g \cdot (z+10)$, see paragraph 3.4. This means that in the production model only equation (3.3.19) and equation (3.3.20) are used. When the water pressure forces are known the horizontal and vertical cutting force can be calculated using the following equations:

$$F_h = -W_2 \cdot sin(\alpha) + K_2 \cdot sin(\alpha + \delta) \tag{3.3.23}$$

$$F_v = -W_2 \cdot cos(\alpha) + K_2 \cdot cos(\alpha + \delta) \tag{3.3.24}$$

3.3.4 The shear angle

In the previous sections it was assumed that the shear angle β was just an input. However, the shear angle is actually calculated. This section explains how these calculations are done.

The method for calculating the shear angle is based on the assumption that nature always takes the path of least resistance. When translating this to the cutting process it means that β is 'chosen' in such a way that the cutting work is minimal. Since the draghead is only dragged horizontally only the horizontal cutting force contributes to the cutting work. Hence, the shear angle must be found for which the horizontal cutting force is minimal. The main assumption of this paragraph is still followed, the water under pressures are dominant in the cutting process and cohesion, adhesion, gravity, inertia, flow resistance and under pressures behind the blade are neglected. Now the horizontal cutting force can be expressed as follows:

$$F_h = \left\{ \begin{array}{l} -p_{2m} \cdot h_b \cdot \frac{sin(\alpha)}{sin(\alpha)} \\ +p_{2m} \cdot h_b \cdot \frac{sin(\alpha+\beta+\phi) \cdot sin(\alpha+\delta)}{sin(\alpha+\beta+\delta+\phi) \cdot sin(\alpha)} \\ +p_{1m} \cdot h_i \cdot \frac{sin(\phi) \cdot sin(\alpha+\delta)}{sin(\alpha+\beta+\delta+\phi) \cdot sin(\beta)} \end{array} \right\} \cdot \frac{\rho_w \cdot g \cdot v_c \cdot \epsilon \cdot h_i \cdot w}{(a_1 \cdot k_i + a_2 \cdot k_{max})} \tag{3.3.25}$$

The following simplification is added:

$$F_h' = \frac{F_h}{\frac{\rho_w \cdot g \cdot v_c \cdot \epsilon \cdot h_i \cdot w}{(a_1 \cdot k_i + a_2 \cdot k_{max})}} \tag{3.3.26}$$

The cutting work is minimal when the derivative of F'_h with respect to β is zero:

$$\begin{aligned}\frac{\partial F'_h}{\partial \beta} =& - p_{1m} \cdot h_i \cdot \frac{sin(\phi) \cdot sin(\alpha + 2 \cdot \beta + \delta + \phi) \cdot sin(\alpha + \delta)}{sin^2(\beta) \cdot sin(\alpha + \beta + \delta + \phi)^2} \\ &+ p_{2m} \cdot h_b \cdot \frac{sin(\delta) \cdot sin(\alpha + \delta)}{sin(\alpha) \cdot sin(\alpha + \beta + \delta + \phi)^2} \\ &+ \frac{\partial p_{1m}}{\partial \beta} \cdot h_i \cdot \frac{sin(\phi) \cdot sin(\alpha + \delta)}{sin(\beta) \cdot sin(\alpha + \beta + \delta + \phi)} \\ &+ \frac{\partial p_{2m}}{\partial \beta} \cdot h_b \cdot \left\{ \frac{sin(\alpha + \beta + \phi) \cdot sin(\alpha + \delta)}{sin(\alpha) \cdot sin(\alpha + \beta + \delta + \phi)} - 1 \right\} = 0\end{aligned} \tag{3.3.27}$$

Equation (3.3.27) can only be solved by iterative calculations since the shear angle will always be on both sides of the equation. Due to the fact that the pore pressures p_{1m} and p_{2m} are required and these pore pressures have to be calculated using the parallel resistor model (see section 3.4.1) solving the iteration might be very calculation intensive.
When the cutting process is fully cavitating, equation (3.3.27) can be simplified because the average pore pressure in the shear zone (p_{1m}) and on the blade (p_{2m}) are equal (both are the cavitation pressure). This simplification starts with the horizontal cutting force:

$$F_h = \left\{ \begin{array}{l} - \cdot h_b \cdot \frac{sin(\alpha)}{sin(\alpha)} \\ + \cdot h_b \cdot \frac{sin(\alpha+\beta+\phi) \cdot sin(\alpha+\delta)}{sin(\alpha+\beta+\delta+\phi) \cdot sin(\alpha)} \\ + \cdot h_i \cdot \frac{sin(\phi) \cdot sin(\alpha+\delta)}{sin(\alpha+\beta+\delta+\phi) \cdot sin(\beta)} \end{array} \right\} \cdot \rho_w \cdot g \cdot (z + 10) \cdot w \tag{3.3.28}$$

The following simplification is added:

$$F'_h = \frac{F_h}{\rho_w \cdot g \cdot (z + 10) \cdot w} \tag{3.3.29}$$

The derivative of the force F'_h with respect to shear angle β then becomes:

$$\begin{aligned}\frac{\partial F'_h}{\partial \beta} =& - h_i \cdot \frac{sin(\phi) \cdot sin(\alpha + 2 \cdot \beta + \delta + \phi) \cdot sin(\alpha + \delta)}{sin^2(\beta) \cdot sin(\alpha + \beta + \delta + \phi)^2} \\ &+ h_b \cdot \frac{sin(\delta) \cdot sin(\alpha + \delta)}{sin(\alpha) \cdot sin(\alpha + \beta + \delta + \phi)^2} = 0\end{aligned} \tag{3.3.30}$$

Equation (3.3.30) can only be solved by means of iteration. For more information on iteration functions see appendix C.
Alternatively the iterative results can be approximated by the following equation:

$$\beta = 61.29° + 0.345 \cdot \frac{h_b}{h_i} - 0.3068 \cdot \alpha - 0.4736 \cdot \delta - 0.248 \cdot \phi \tag{3.3.31}$$

3.4 Numerical pore pressure calculations

In this paragraph the different numerical pore pressure calculations will be discussed. However, all these methods are based on the same principle: the parallel resistor approach. In this approach

the flow resistance of soil is considered to be analogue to electrical resistance in an electrical circuit, pressure difference analogue to a voltage difference and flow analogue to electrical current. Hence, pore pressure calculations are solved in a similar fashion as voltage calculations for an electrical circuit. The first section will cover the parallel resistor method for cutting water saturated sand with a blade. The second section will cover the way the force acting point on the blade is calculated. The third section covers the parallel resistor method for cutting water saturated sand with a wedge.

3.4.1 Parallel resistor method

In section 3.3.2 it was established that water only flows perpendicularly into the shear zone. This leads to four possible ways for the water to flow into the shear zone. These four flow directions are shown in figure 3.5. Two of these flows go through soil that has not (yet) been deformed. Hence, the soil has a permeability k_i and a porosity n_i. The other two flow lines go through soil that has been deformed and thus the soil there has a permeability k_{max} and a porosity n_{max}.
The definitions of figure 3.5 are given below.

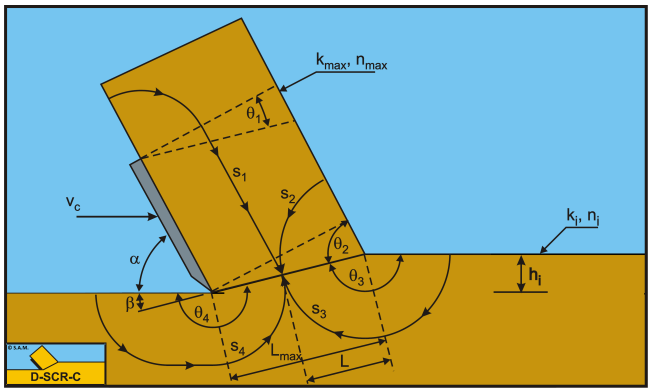

Figure 3.5: Flow lines in the analytical method

Definitions:

s_1: Flow line from top of blade through deformed sand package

s_2: Flow line from free surface through deformed sand package

s_3: Flow line from front of blade through initial sand package

s_4: Flow line from back of blade through initial sand package

θ_1: Angle between a line perpendicular to blade and the shear zone

θ_2: Angle between the free surface and the shear zone

θ_3: Angle between the initial sand bed and the shear zone

θ_4: Angle between the sand bed after cutting and the shear zone

L_{max}: Length of the shear zone, $h_i/sin(\beta)$

L: Variable distance between the free surface and the current soil element in the shear zone

h_b: Blade height

h_i: Thickness of the layer cut

v_c: Cutting velocity or trailing speed

α: Blade angle

β: Shear angle

In section 3.3.2 Darcy's Law was used to find the specific flow q in equation (3.3.5). This equation however, assumed infinitesimal small changes in pressure and distance. To make the equation suitable for numerical calculations the infinitesimal small pressure changes and distance changes are changed to pressure and distance differences:

$$q = k \cdot i = k \cdot \frac{\Delta p}{\rho_w \cdot g \cdot \Delta s} \tag{3.4.1}$$

Using equation (3.4.1) an expression for the total specific flow through the four flow lines as result of dilatation can be found:

$$\begin{aligned} q &= \epsilon \cdot v_c \cdot sin(\beta) \\ &= k_{max} \cdot \frac{\Delta p}{\rho_w \cdot g \cdot s_1} + k_{max} \cdot \frac{\Delta p}{\rho_w \cdot g \cdot s_2} + k_i \cdot \frac{\Delta p}{\rho_w \cdot g \cdot s_3} + k_i \cdot \frac{\Delta p}{\rho_w \cdot g \cdot s_4} \end{aligned} \tag{3.4.2}$$

In equation (3.4.2) the length of flow line s_1 is defined as:

$$\begin{aligned} &s_1 = (L_{max} - L) \cdot \left(\frac{\pi}{2} + \theta_1\right) + \frac{h_b}{sin(\alpha)} \\ &\text{With: } \theta_1 = \frac{\pi}{2} - (\alpha + \beta) \end{aligned} \tag{3.4.3}$$

The length of flow line s_2 is:

$$\begin{aligned} &s_2 = 0.8 \cdot L \cdot \theta_2 \\ &\text{With: } \theta_2 = \alpha + \beta \end{aligned} \tag{3.4.4}$$

The length of flow line s_3 is:

$$\begin{aligned} &s_3 = 0.8 \cdot L \cdot \theta_3 \\ &\text{With: } \theta_3 = \pi - \beta \end{aligned} \tag{3.4.5}$$

The length of flow line s_4 is:

$$\begin{aligned} &s_4 = (L_{max} - L) \cdot \theta_4 + 0.9 \cdot h_i \cdot \left(\frac{h_i}{h_b}\right)^{0.5} \cdot (1.85 \cdot \alpha)^2 \cdot \left(\frac{k_i}{k_{max}}\right)^{0.4} \\ &\text{With: } \theta_4 = \pi + \beta \end{aligned} \tag{3.4.6}$$

The factor of 0.8 for the lengths s_2 and s_3 is a correction factor and is calibrated on experiments. Equation (3.4.6) has been determined by calibrating the equation on experiments and finite element calculations. It is not a real flow line length but it more represents the influence of the flow of water around the tip of the blade.
The total specific flow can be rewritten as follows:

$$\begin{aligned} \rho_w \cdot g \cdot q &= \rho_w \cdot g \cdot \epsilon \cdot v_c \cdot sin(\beta) \\ &= \frac{\Delta p}{\left(\frac{s_1}{k_{max}}\right)} + \frac{\Delta p}{\left(\frac{s_2}{k_{max}}\right)} + \frac{\Delta p}{\left(\frac{s_3}{k_i}\right)} + \frac{\Delta p}{\left(\frac{s_4}{k_i}\right)} = \frac{\Delta p}{R_1} + \frac{\Delta p}{R_2} + \frac{\Delta p}{R_3} + \frac{\Delta p}{R_4} = \frac{\Delta p}{R_t} \end{aligned} \tag{3.4.7}$$

In equation (3.4.7) it can be seen that the resistance of a flow line is defined as the length of the flow line divided by the permeability of the soil in which the flow line is located. The equations for the resistance of the four flow lines are given below:

$$R_1 = \frac{s_1}{k_{max}} \tag{3.4.8}$$

$$R_2 = \frac{s_2}{k_{max}} \tag{3.4.9}$$

$$R_3 = \frac{s_3}{k_i} \tag{3.4.10}$$

$$R_4 = \frac{s_4}{k_i} \tag{3.4.11}$$

Since all four flow lines have the same pressure difference Δp they can be seen as four parallel resistors in an electrical circuit. In an electrical circuit the equivalent resistor R_t can be calculated for parallel resistors. Using the same equation this can also be done for the flow resistance in the soil:

$$\frac{1}{R_t} = \frac{1}{R_1} + \frac{1}{R_2} + \frac{1}{R_3} + \frac{1}{R_4} \tag{3.4.12}$$

Rewriting equation (3.4.7) now yields an equation for the pressure difference between a point (or element) in the shear zone and the hydrostatic pressure (pore vacuum pressure):

$$\Delta p = \rho_w \cdot g \cdot v_c \cdot \epsilon \cdot sin(\beta) \cdot R_t \tag{3.4.13}$$

The average pore vacuum pressure can be now be found by integration for infinitesimal small elements or by summation for a finite amount of elements, as is shown below:

$$p_{1m} = \frac{1}{n} \cdot \sum_{i=0}^{n} \Delta p_i \tag{3.4.14}$$

Now the average pore vacuum pressure on the blade has to be calculated. This is not done by assuming a linear pressure distribution from the tip to the top of the blade. This would lead to an average pore vacuum pressure of half that of the pore vacuum pressure at the tip of the blade. Instead, two flow lines are assumed. The first is a flow line along the blade from the top of the blade to a position on the blade. The resistance of this flow line is dependent on the length of the flow line and thus on the position of the element on the blade:

$$R_{1,i} = \frac{s_{1,i}}{k_{max}} \cdot \left(1 - \frac{i}{N}\right) \tag{3.4.15}$$

In equation (3.4.15) i is the counter and N is the number of elements in which the blade is divided. The second flow line is the result of entrainment of water from the sand package above the blade due to the pressure gradient. This entrainment is dependent on the ratio between the length of the shear

plane and the length of the blade. Hence, if the blade is divided into N elements then the entrainment per element will be $1/N$ times the total entrainment. The pore vacuum pressure calculations are however started with the constant flow resistance R_2:

$$R_2 = \frac{s_2}{k_{max}} \tag{3.4.16}$$

This flow resistance is compensated for the number of elements and the geometry:

$$R_2' = N \cdot 1.75 \cdot \left(\frac{h_i}{sin(\beta)} \cdot \frac{sin(\alpha)}{h_b} \right) \cdot R_2 \tag{3.4.17}$$

The total flow resistance is now defined as follows:

$$\frac{1}{R_{t,i}} = \frac{1}{R_{1,i}} + \frac{1}{R_2'} \tag{3.4.18}$$

Starting at the tip of the blade the initial flows can now be calculated:

$$q_0 = \frac{\Delta p_{tip}}{\rho_w \cdot g \cdot R_{t,0}},\ q_{1,0} = \frac{\Delta p_{tip}}{\rho_w \cdot g \cdot R_{1,0}},\ q_{2,0} = \frac{\Delta p_{tip}}{\rho_w \cdot g \cdot R_2'} \tag{3.4.19}$$

However, due to wear of the blade tip and under pressures behind the blade the pore pressures around the tip slightly change. This is accounted for in the first five percent of the steps ($Int(0.05 \cdot N \cdot \alpha)$) by increasing the total flow over the blade and by decreasing the total flow. The pressure difference is calculated as follows:

$$\begin{aligned} &q_i = q_{i-1} + q_{2,i-1},\ q_{1,i} = q_i \cdot \frac{R_{t,i}}{R_{1,i}},\ q_{2,i} = q_i \cdot \frac{R_{t,i}}{R_2'} \\ &\Delta p_i = \rho_w \cdot g \cdot q_i \cdot R_{t,i} \end{aligned} \tag{3.4.20}$$

After the first five percent of the steps the pressure difference is calculated as follows:

$$\begin{aligned} &q_i = q_{i-1} - q_{2,i-1},\ q_{1,i} = q_i \cdot \frac{R_{t,i}}{R_{1,i}},\ q_{2,i} = q_i \cdot \frac{R_{t,i}}{R_2'} \\ &\Delta p_i = \rho_w \cdot g \cdot q_i \cdot R_{t,i} \end{aligned} \tag{3.4.21}$$

Now the average pore pressure is calculated by integration for infinitesimal small elements and by summation for a finite amount of elements:

$$p_{2m} = \frac{1}{n} \cdot \sum_{i=0}^{n} \Delta p_i \tag{3.4.22}$$

When the pore pressure that is calculated for each step on the blade or shear plane, the pore pressure distribution made visible. This is done in figure 3.6 for a situation without cavitation and in figure 3.7 for a partially cavitating situation. On the x-axis the position on the blade or shear plane is expressed in the form of a percentage of the length of the blade or shear plane. Important to note is that 100% is the position at the tip of the blade for both the blade and the shear plane. On the y-axis the pore under pressure is displayed.
In figure 3.7 it can be seen that the pore under pressure in some parts of the shear plane is limited to the cavitation pressure.
When the average pore under pressures p_{1m} and p_{2m} are calculated they serve as inputs for the cutting force calculations, as is explained in section 3.3.3. How this method of calculating the pore pressures is applied in Python can be found in Appendix D.

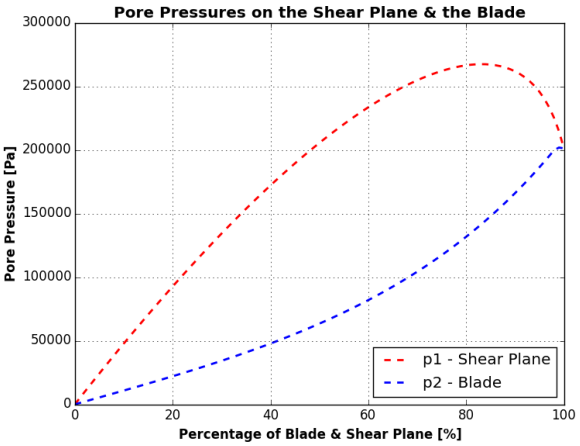

Figure 3.6: Pore pressures on the blade and the shear plane, $\alpha = 35°, \beta = 23.5°, k_i/k_{max} = 0.2, h_i/h_b = 0.5, \epsilon = 0.16, v_c = 0.5m/s, z = 20m$

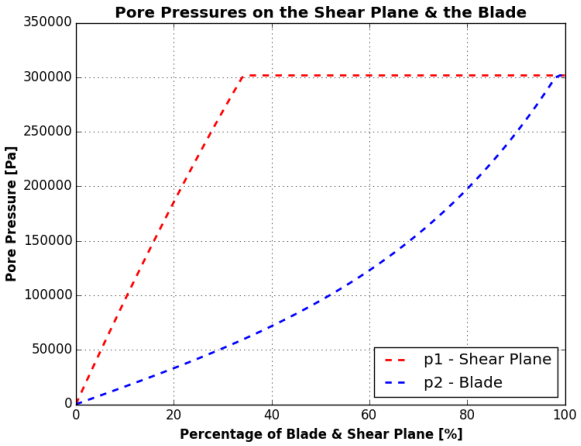

Figure 3.7: Pore pressures on the blade and the shear plane, $\alpha = 35°, \beta = 23.5°, k_i/k_{max} = 0.2, h_i/h_b = 0.5, \epsilon = 0.16, v_c = 1.0m/s, z = 20m$

3.4.2 Cutting force acting point

A cutting moment is calculated by multiplying a cutting force with a moment arm. The cutting force can be calculated using the theory described in this chapter. For the moment arm calculation, the percentage of the blade on which the point is located where all cutting forces act is needed. The position of the tip and the top of the blade are known, hence if the percentage of the force acting point is known then the position of the force acting point can be defined. When the position of the force acting point is known then the moment arms can be calculated.

Based on the pore pressure distribution on the blade, the force acting point is assumed to lie on the 'median' of the pore pressure distribution. Hence, fifty percent of the area under the distribution curve lies left of this point and fifty percent lies right of this point. The median line is indicated in figure 3.8. In this figure the force acting point X is at 0.247 or 24.7 percent of the blade length, starting from the blade tip. Note that the pore pressure distribution is plotted the same way as all other pore pressure distribution graphs, which means that 100 percent is the blade tip. Hence, the force acting point is indicated at 75.3% at the horizontal axis.

3.5 Cutting with tooth jets

In paragraph 1.3 it was explained that the Wild Dragon draghead was chosen as a starting point because GLDD uses it on the Liberty Island. Furthermore the Wild Dragon draghead is one of the most advanced dragheads on the market. Hence, if the production model works for this draghead it will likely also work for other dragheads.
The Wild Dragon draghead is equipped with tooth jets which, according to IHC, reduce the cutting force because the jetwater causes dilatation in the soil around the teeth [1].
The influence of the tooth jets on the cutting forces and production has to be incorporated into the production model. This can possibly be done by using the same or comparable jet penetration equations as described in chapter 4. However, this comes with multiple problems since the equations might not account for jets under an angle or jets submerged in the bed. Also, since the penetration

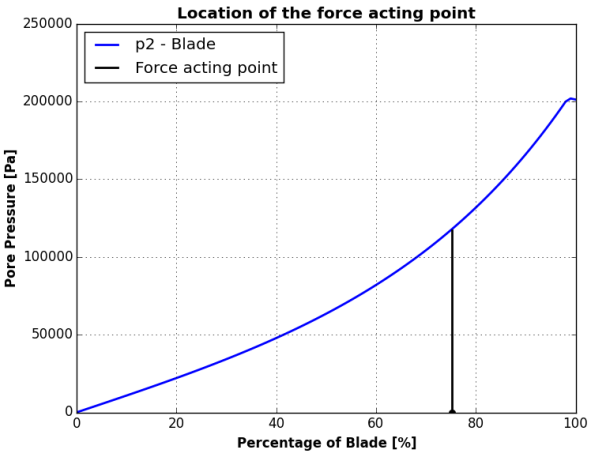

Figure 3.8: The force acting point at 24.7% from the blade tip

depth of a tooth jet varies with the visor angle it interferes with the moment balance which will probably lead to situations where no moment balance can be found. Another objection to using jet penetration equations is that these equations do not use dilatation as an input whilst dilatation is at the foundation of the cutting force calculations for water saturated sand.
Due to all the problems and objections against using water jet penetration equations to model the influence of the tooth jets the decision was made not to use these equations, hence there was need for another approach. This lead to the hypothesis that a tooth jet can be modeled as a pressure source, which adds a 'negative' resistor to the parallel resistor scheme that provides the water needed for dilatation hence reducing the pore under pressures and therefore the cutting forces.
The pressure source parallel resistor method for tooth jets is explained in the next to sections. The main difference between the two methods described in the sections is that the influence of the flow resistance of the soil on the total water flow is taken into account in the advanced method while the simple method neglects this.

3.5.1 Parallel resistor method for tooth jets - Simple

As said before the simple parallel resistor method for tooth jets does not take the influence of flow resistance of the soil on the total water flow into account. The simple method therefore requires only a few more inputs than the normal parallel resistor method. These inputs are: the percentage of the blade on which the nozzle is located (x), the jet pressure (Δp_{jet}) and the total flow of all the tooth jets in a row ($q_{jettotal}$). The pressure and total flow can be gained from spec sheets of the equipment manufacturer, flow simulation software like AFT Fathom or from actual measurements taken whilst dredging. Actual measurements probably yield the best results since this way the influence of flow resistance of the soil is automatically accounted for. The location of the nozzle usually is around 30 to 40 percent of the blade length, measured from the tip of the blade. This can be seen in figure 3.9. The percentage must be a nonzero number because a resistance of zero would lead to calculation problems.

The parallel resistor method for tooth jets starts the same way as the normal parallel resistor method. A short recap is given below, for a more detailed explanation and definitions see section 3.4.1.
The parallel resistor method starts with Darcy's Law, which defines a specific flow as follows:

$$q = k \cdot i = k \cdot \frac{\Delta p}{\rho_w \cdot g \cdot \Delta s} \tag{3.5.1}$$

Figure 3.9: Tooth jet nozzles in the teeth of a Wild Dragon draghead

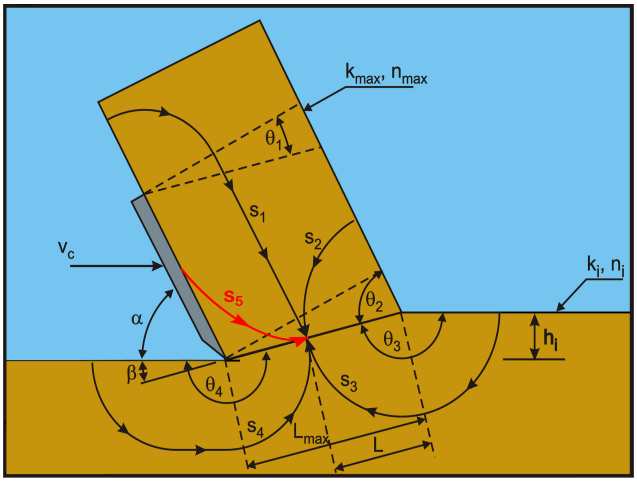

Figure 3.10: Flow lines in the analytical method for cutting with tooth jets. The new flow line of the jet is indicated in red

Equation (3.5.1) shows that the specific flow is related to a pressure difference by a factor that is a function of flow path length and permeability, the resistance. The resistance for each of the four flow lines in figure 3.10 can be defined by dividing the length of the flow line by the permeability of the soil it runs through:

$$R_1 = \frac{s_1}{k_{max}} \tag{3.5.2}$$

$$R_2 = \frac{s_2}{k_{max}} \tag{3.5.3}$$

$$R_3 = \frac{s_3}{k_i} \tag{3.5.4}$$

$$R_4 = \frac{s_4}{k_i} \tag{3.5.5}$$

The following equation is then used to calculate the equivalent resistor for the four parallel resistors:

$$\frac{1}{R_t} = \frac{1}{R_1} + \frac{1}{R_2} + \frac{1}{R_3} + \frac{1}{R_4} \tag{3.5.6}$$

Now the jet is introduced in the parallel resistor model as a pressure source, see figure 3.10. The distance from the tip of the blade to the pressure source is defined as follows:

$$L_{jet} = x \cdot L_1 = x \cdot \frac{h_b}{sin(\alpha)} \tag{3.5.7}$$

With: $0 < x \leq 1$

The flow line from the pressure source to a point in the shear zone is assumed to have the shape of a quarter ellipse with radii a and b. In which $a = L_{jet}$ and $b = L_{max} - L$.
The approximation of the circumference of an ellipse is given by Ramanujan [6]:

$$\begin{aligned} C &= \pi \cdot (a+b) \cdot \left(1 + \frac{3h}{10 + \sqrt{4-3h}}\right) \\ \text{With: } h &= \frac{(a-b)^2}{(a+b)^2} \end{aligned} \tag{3.5.8}$$

The length of flow line s_5 is now defined as follows:

$$s_5 = 0.25 \cdot C \tag{3.5.9}$$

Flow line s_5 runs through soil that has already been deformed, hence the permeability is k_{max}. This leads to the following resistance:

$$R_5 = \frac{s_5}{k_{max}} \tag{3.5.10}$$

Since both the jet pressure and the soil resistance are known the specific flow from the jet to a point in the shear zone can be calculated by using equation (3.5.1):

$$q_{tooth} = \frac{\Delta p_{jet}}{\rho_w \cdot g \cdot R_5} \tag{3.5.11}$$

The specific flow that is required to flow into the shear layer due to the effects of dilatation is defined as follows:

$$q_{req} = v_c \cdot \epsilon \cdot sin(\beta) \tag{3.5.12}$$

The specific jet flow is subtracted from the required specific flow to calculate the specific flow through the resistors R_1, R_2, R_3 and R_4:

$$q_{remainder} = q_{req} - q_{tooth} \tag{3.5.13}$$

In the situation that $q_{remainder}$ is negative liquefaction would occur due to the excess pore water pressure. However, in this model liquefaction is not directly accounted for and $q_{remainder}$ is set to zero. In the production model the cutting force of liquefied soil is assumed to be zero, as was explained in section 2.4.2. Since setting $q_{remainder}$ to zero leads to zero pore vacuum pressure for that element it does contribute to lowering the average pore pressure in the shear zone and on the blade. The lower average pore vacuum pressures in the shear zone and on the blade lead to a lower cutting force, resembling the situation of having partial liquefaction in the shear zone.
The pore vacuum pressure in the shear zone is calculated as follows:

$$\Delta p = \rho_w \cdot g \cdot R_t \cdot q_{remainder} \tag{3.5.14}$$

Now the average pore vacuum pressure in the shear zone can be calculated using the following equation:

$$p_{1m} = \frac{1}{n} \cdot \sum_{i=0}^{n} \Delta p_i \tag{3.5.15}$$

The calculation of the average pore vacuum pressure on the blade for the tooth jet model is identical to that of the normal parallel resistor model and is described in section 3.4.1. The method described above only works when the water jets can at least provide as much water as is required for the given combination of jet pressure and soil resistance or:

$$q_{real} = \sum_{i=0}^{n} q_{tooth} \cdot \frac{L_{max}}{n} \cdot W \leq q_{jettotal} \tag{3.5.16}$$

This might however not be the case and the calculation should be corrected in order to have to have the total discharged flow from the tooth nozzles match the maximum discharge of the tooth nozzles. This is done by using a correction factor:

$$f_{correction} = \frac{q_{jettotal}}{q_{real}} \tag{3.5.17}$$

After obtaining the correction factor the calculation should be done again whilst correcting the specific flow from the jet to a point in the shear zone:

$$q_{tooth} = f_{correction} \cdot \frac{\Delta p_{jet}}{\rho_w \cdot g \cdot R_5} \tag{3.5.18}$$

Note that the difference between the calculated discharge of the jets before correction and the maximum given discharge of the jets is a direct result of the lack of feedback of flow resistance of the soil. Two arbitrary values can be given for $q_{jettotal}$ and Δp_{jet} which in combination with the given soil data and geometry do not necessarily comply with Darcy's Law.
As was done for the normal pore pressure calculations described in section 3.4.1, pore pressure distribution graphs can also be made for the tooth jet resistor model. Again this is done by plotting the pore pressures for each step that is done on the blade or the shear plane. This is done in figure 3.11 for a situation where the tooth jets are off/blocked i.e. $\Delta p_{jet} = 0$ and in figure 3.12 for a situation where the jet pressure is 2.5 bar and sufficient jet water is present. On the x-axis the position on the blade or shear plane is expressed in the form of a percentage of the length of the blade or shear plane. Important to not is that 100% is the position at the tip of the blade for both the blade as the shear plane. On the y-axis the pore under pressure is displayed.

When figure 3.11 and 3.12 are compared it becomes clear that adding the influence of a tooth jet has a great impact on the pore pressure distributions. Both the pore under pressure in the shear plane and on the blade are considerably lower for the case of active tooth jets. The distributions of the pore pressures themselves also changes. In figure 3.12 it can be seen that the pore under pressure p_1 has been reduced throughout the entire shear plane. However, the shape change indicates that the pore pressure reduction has been the greatest in the area near the tip of the blade. This makes sense since this area is closest to the nozzle, hence the jet flow lines are short here and thus the flow resistance of the soil is low. This means that a large flow of jet water flows to the shear zone and thus only small pore under pressures develop. As with the normal parallel resistor model, the pore under pressure at the tip of the blade is the same on the shear zone and the blade and then gradually reduces along the blade. The reduction of the average pore under pressures p_{1m} and p_{2m} is what eventually leads to the reduction of the cutting force. In the situation of figure 3.11 the average pore under pressures p_{1m} and p_{2m} were respectively 179.6 kPa and 83.0 kPa. By adding the influence of the water jet with a Δp_{jet} of 2.5bar, the average pore under pressures p_{1m} and p_{2m} were respectively reduced to 62.6 kPa and 5.9 kPa. Theoretically both p_{1m} and p_{2m} can be reduced to zero by choosing a jet pressure that is high enough. Since the pore pressure calculations on the blade start with the value of the pore pressure at the tip of the blade, the average pore pressure on the blade becomes zero when the

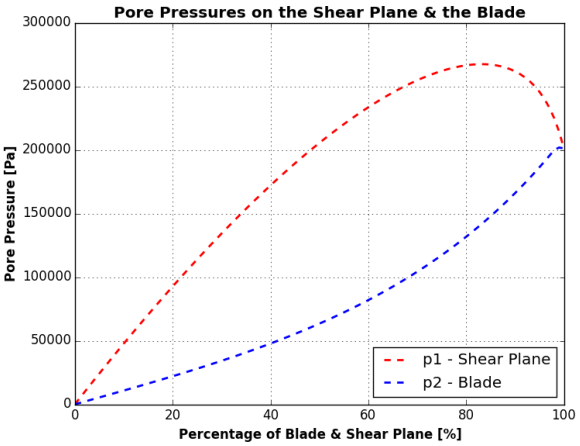

Figure 3.11: Pore pressures on the blade and the shear plane, $\alpha = 35°, \beta = 23.5°, k_i/k_{max} = 0.2, h_i/h_b = 0.5, \epsilon = 0.16, v_c = 0.5m/s, z = 20m, \Delta p_{jet} = 0bar$

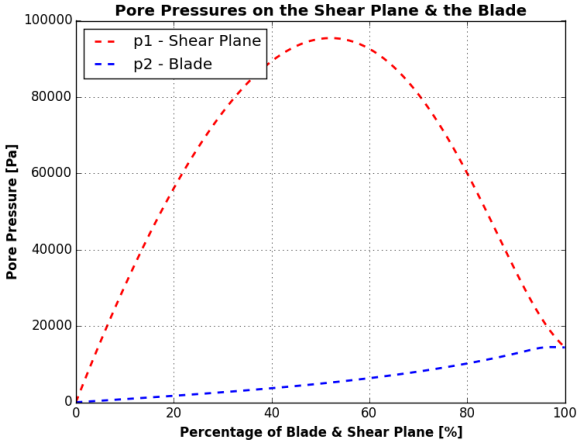

Figure 3.12: Pore pressures on the blade and the shear plane, $\alpha = 35°, \beta = 23.5°, k_i/k_{max} = 0.2, h_i/h_b = 0.5, \epsilon = 0.16, v_c = 0.5m/s, z = 20m, \Delta p_{jet} = 2.5bar$

pore pressure at the tip is zero. Therefore p_{2m} will always be the first average pore under pressure to become zero since the tip of the blade is the point closest to the jet nozzle. A situation where the average pore pressure is completely reduced to zero is shown in figure 3.14. The jet pressure chosen in this situation is $5.0bar$.

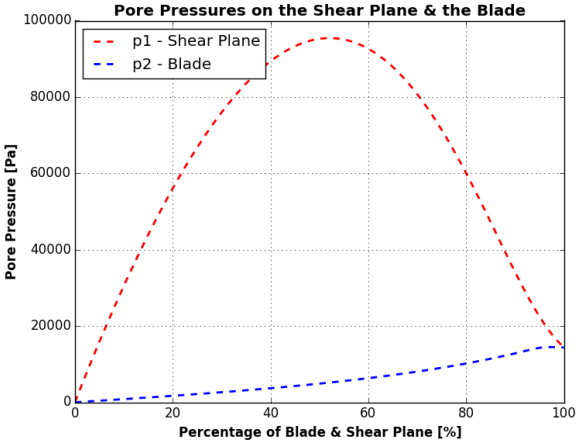

Figure 3.13: Pore pressures on the blade and the shear plane, $\alpha = 35°, \beta = 23.5°, k_i/k_{max} = 0.2, h_i/h_b = 0.5, \epsilon = 0.16, v_c = 0.5m/s, z = 20m, \Delta p_{jet} = 2.5bar$

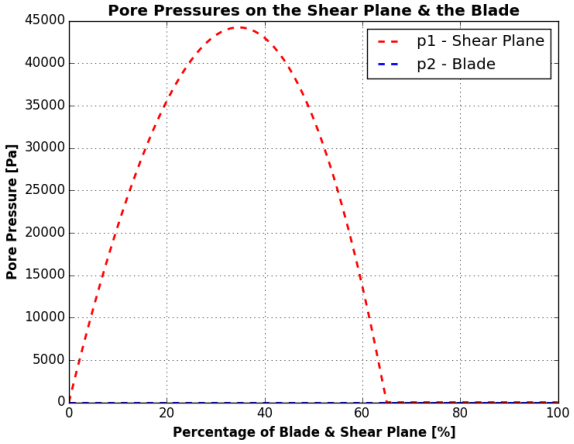

Figure 3.14: Pore pressures on the blade and the shear plane, $\alpha = 35°, \beta = 23.5°, k_i/k_{max} = 0.2, h_i/h_b = 0.5, \epsilon = 0.16, v_c = 0.5m/s, z = 20m, \Delta p_{jet} = 5.0bar$

Important to note is that in roughly one-third of the shear plane the pore under pressures also have been reduced to zero. Again this zone is close to the tip of the blade since this is closest to the jet nozzle. The average pore under pressures p_{1m} and p_{2m} in this situation are respectively 19.0 kPa and 0.0 kPa.
Including the tooth jet model in the pore pressure calculation will affect the magnitude of both the horizontal and vertical cutting force and therefore also the direction of the combined cutting force. Through the cutting forces the changed pore pressures will eventually affect the moment balance.

3.5.2 Parallel resistor method for tooth jets - Advanced

As was explained in the beginning of this paragraph the main difference between the simple and the advanced parallel resistor method for tooth jets is whether the soil flow resistance has influence on the total water flow and jet pressure or not. Not taking the influence into account can lead to situations where results do not comply with physics, as was explained in section 3.5.1. The advanced model does take the influence of soil flow resistance into account. This means that the jet and soil cannot be considered separately from the rest of the flow system. The whole jet water flow system must be considered: the pump, the piping, the free flowing visor jets, the heel jets and the tooth jets that are surrounded by soil. The whole aim of this method is to find a Δp_{jet} and a $q_{jettotal}$ for the tooth jets in such a way that they comply with the flow resistance in the soil according to Darcy's Law and that they comply with the pressure and flow characteristics of the rest of the system according to the Bernoulli Equation. The key to solving this problem is modeling the complex flow system as a set of parallel resistors. The total pressure loss for a given total flow in these parallel resistors must then be equal to the pressure and flow that the pump provides according to the pump curve. When Δp_{jet} and $q_{jettotal}$ are obtained they can be used in the system that is described in section 3.5.1. With the exception that there is no need for correction.
The first step in the advanced tooth jet model is to simplify the jet water system to a system of a number of 'building blocks', the parallel resistors. This starts at the centrifugal pump. The pump provides the pressure (head) and flow to the system and can therefore be seen as the battery or voltage source of the parallel resistor scheme, see figure 3.16. The relation between pressure and flow for centrifugal pumps is given in the form of a pump curve (see figure 3.15).

In the parallel resistor model the pump curve is replaced by a quadratic formula in which the

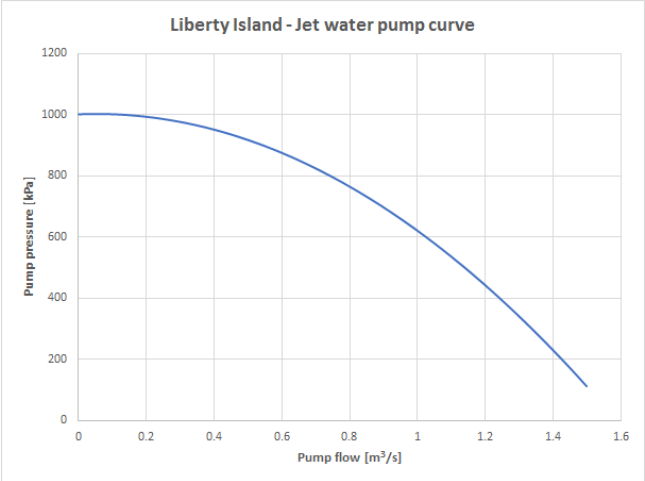

Figure 3.15: Pump curve of the jet water pump of the Liberty Island ($A = -425348$, $B = 44766$, $C = 1000000$)

coefficients A, B and C are obtained by doing a curve-fit on the pump curve:

$$\Delta p_{pump} = A \cdot Q_{total}^2 + B \cdot Q_{total} + C \tag{3.5.19}$$

The loss of pressure in piping is modeled as a resistor and can be split up in two parts: the major losses and the minor losses.
The major losses are the losses due to friction of the fluid with the pipe wall and can be calculated using the Darcy-Weisbach equation:

$$\Delta p_{major} = 0.5 \cdot \rho_w \cdot v^2 \cdot \frac{\lambda \cdot L}{D} \tag{3.5.20}$$

In equation (3.5.20) λ is the Darcy-Weisbach friction factor, which is a function of the relative roughness of the pipe wall and the Reynolds number and can be obtained using a Moody Diagram However, for the flow speeds and wall roughnesses in dredging it is reasonable to assume the friction factor to be constant and in the range of 0.015 to 0.020.
The flow velocity v can be expressed in terms of flow by dividing the flow by the cross-sectional area of the pipe:

$$v = \frac{Q}{A_{pipe}} \text{ with: } A_{pipe} = \frac{\pi}{4} D^2 \tag{3.5.21}$$

Now equation (3.5.20) can be rewritten in terms of the flow and pipe cross-sectional area:

$$\Delta p = 0.5 \cdot \rho_w \cdot \left(\frac{Q}{A_{pipe}} \right)^2 \cdot \frac{\lambda \cdot L}{D} \tag{3.5.22}$$

The minor losses are the pressure losses due to velocity changes in bends, fittings valves et cetera. The loss per bend, valve or fitting is expressed in a K factor which can be found in tables. The total minor loss can be found by adding all K factors and multiplying them with the dynamic pressure:

$$\Delta p_{minor} = \sum K \cdot 0.5 \cdot \rho_w \cdot v^2 \tag{3.5.23}$$

Using equation (3.5.21) again equation (3.5.23) can be expressed as follows:

$$\Delta p_{minor} = \sum K \cdot 0.5 \cdot \rho_w \cdot \left(\frac{Q}{A_{pipe}} \right)^2 \tag{3.5.24}$$

Combining equation (3.5.22) and (3.5.24) yields the following equation:

$$\Delta p_{pipe} = \left(\sum K + \frac{\lambda \cdot L}{D} \right) \cdot 0.5 \cdot \rho_w \cdot \left(\frac{Q}{A_{pipe}} \right)^2 \tag{3.5.25}$$

The loss factor K can also be replaced by an extra section of pipe with the same loss. This is the equivalent length method. The equivalent length can be calculated using the following equation:

$$L_{eq} = \frac{K \cdot D}{\lambda} \tag{3.5.26}$$

Using equation (3.5.26) equation (3.5.25) can be rewritten as follows:

$$\Delta p_{pipe} = \frac{\lambda \cdot (L + L_{eq})}{D} \cdot 0.5 \cdot \rho_w \cdot \left(\frac{Q}{A_{pipe}} \right)^2 \tag{3.5.27}$$

Another pressure loss, or resistor that can be identified is the pressure loss due to the free flowing jets. These are the heel jets, the jets in the visor and tooth jets that are not in the sand. The pressure loss is expressed as follows:

$$\Delta p_{jet} = 0.5 \cdot \rho_w \left(\frac{Q}{\alpha \cdot A_{jet}} \right)^2 \tag{3.5.28}$$

In equation (3.5.28) α is a contraction coefficient that is in the order of magnitude of 0.82. The cross-sectional area A_{jet} is the combined area of all jets in a row.
For the tooth jets that penetrate the sand bed a modified version of Darcy's Law is used to calculate the pressure loss:

$$\Delta p = \frac{Q \cdot R_{total} \cdot \rho_w \cdot g}{A_{soil}} \tag{3.5.29}$$

In equation (3.5.29) A_{soil} is defined as follows:

$$A_{soil} = \frac{h_i}{sin(\beta)} \cdot W = L_{max} \cdot W \tag{3.5.30}$$

The resistor R_{total} is the equivalent resistor for all parallel flow lines from the pressure source (jet nozzle) to points in the shear zone (see figure 3.10) and is defined as follows:

$$\frac{1}{R_{total}} = \frac{1}{R_{5,1}} + \frac{1}{R_{5,2}} \ \ldots \ \frac{1}{R_{5,n}} \tag{3.5.31}$$

Now that all building blocks that are needed are defined a simplified flow scheme of the jet water system can be made. In reality a number of main components can be identified for the jet water system: the pump, the piping from the pump to the draghead, the piping to the heel jets, the heel jets, two times piping in the visor, two times visor jets and two times tooth jets. These main components are used to make the parallel resistor scheme in figure 3.16.
Note that certain resistors can be combined so that the parallel resistor scheme in its simplest form

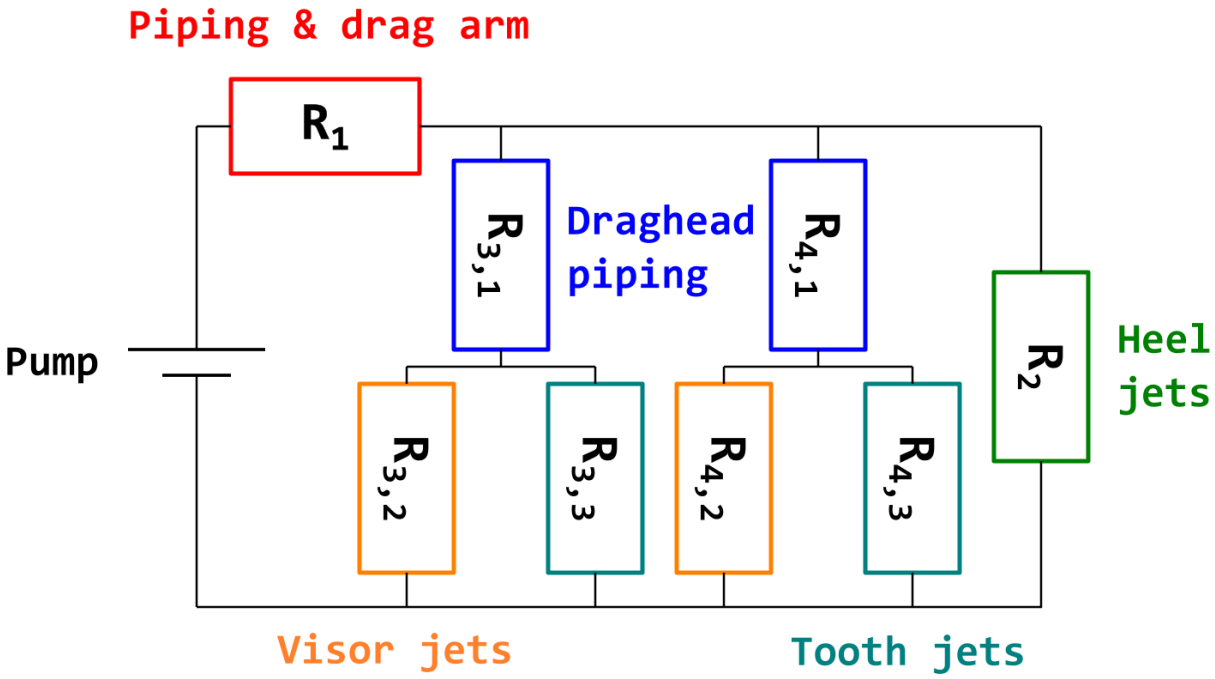

Figure 3.16: Parallel resistor scheme of the jet water system of the Liberty Island

consist of four resistors R_1, R_2, R_3 and R_4. The resistors R_3 and R_4 in figure 3.16 are split up in their

respective sub-resistors. For this example it is assumed that R_3 and R_4 are the same. This is however almost never the case since the rows of teeth almost never cut the same slice thickness. It can also happen that only one of the two rows of teeth is actually cutting sand. In that case the tooth jets of the other row must be modeled as free flowing jets. Nevertheless it is assumed that both rows of tooth jets are in the sand and that they are cutting slices of equal thickness.
The goal of solving the scheme is to find the pressure and flow of the tooth jet or the Δp and Q belonging to $R_{3,3}$ (or $R_{4,3}$ since they are assumed to be the same). This pressure and flow will then be the input for the simple tooth jet cutting model described in section 3.5.1.
Solving the scheme starts with a volume balance:

$$Q_{pump} = Q_{total} = Q_1 = Q_2 + Q_3 + Q_4 = Q_2 + 2 \cdot Q_3 \tag{3.5.32}$$

In equation (3.5.32) the subscripts of the flows correspond with the resistor they flow through. The total flow provided by the pump will flow through R_1 and is then distributed among R_2, R_3 and R_4. The pump curve is known and is described by equation (3.5.19), hence when a Q_{total} is known the pressure provided by the pump Δp_{pump} can be calculated. Since the total flow provided by the pump flows through R_1 the pressure drop Δp_1 over the resistor can be calculated using equation (3.5.25). Since the total pressure provided by the pump was calculated and the pressure drop over resistor R_1 is calculated the remaining pressure drop over the resistors R_2, R_3 and R_4 can be calculated:

$$\Delta p_2 = \Delta p_{pump} - \Delta p_1 \tag{3.5.33}$$

Now that the pressure drop over R_2 is known the flow through R_2 can be calculated. However, R_2 consist of two resistors. One for the pressure loss in the piping and one for the pressure loss due to the free flowing jets, hence:

$$\Delta p_2 = \Delta p_{pipe} + \Delta p_{jet} \tag{3.5.34}$$

Using equation (3.5.25) and (3.5.28) in equation (3.5.34) yields the following expression for Δp_2:

$$\Delta p_2 = \frac{\lambda \cdot (L + L_{eq})}{D} \cdot 0.5 \cdot \rho_w \cdot \left(\frac{Q_2}{A_{pipe}} \right)^2 + 0.5 \cdot \rho_w \left(\frac{Q_2}{\alpha \cdot A_{jet}} \right)^2 \tag{3.5.35}$$

Rewriting equation (3.5.35) yields an expression for the flow through resistor R_2:

$$Q_2 = \sqrt{\frac{\Delta p_2}{\left(0.5 \cdot \rho_w \left(\frac{\lambda \cdot (L+L_{eq})}{D} \cdot \left(\frac{1}{A_{pipe}} \right)^2 + \left(\frac{1}{\alpha \cdot A_{jet}} \right)^2 \right) \right)}} \tag{3.5.36}$$

Now Q_2 is known Q_3 can be found by rewriting the last part of equation (3.5.32):

$$Q_3 = \frac{Q_{total} - Q_2}{2} \tag{3.5.37}$$

Resistor R_3 and R_4 both consist of three smaller resistors. Two of these, the free flowing jet and the tooth jet are parallel to each other and in series with the pipe resistor (see figure 3.16). Since Q_3, the flow through resistor R_3 is known the pressure drop $\Delta p_{3,1}$ over resistor $R_{3,1}$ can be calculated using equation (3.5.25):

$$\Delta p_{3,1} = \left(\sum K + \frac{\lambda \cdot L}{D} \right) \cdot 0.5 \cdot \rho_w \cdot \left(\frac{Q_3}{A_{pipe}} \right)^2 \tag{3.5.38}$$

Now the pressure drop over resistors $R_{3,2}$ and $R_{3,3}$ can be calculated:

$$\Delta p_{3,2} = \Delta p_2 - \Delta p_{3,1} \tag{3.5.39}$$

The flow through the free flowing jets in the visor can now be calculated by rewriting equation (3.5.28):

$$Q_{3,2} = \sqrt{\frac{\Delta p_{3,2}}{\left(0.5 \cdot \rho_w \cdot \left(\frac{1}{\alpha \cdot A_{jet}}\right)^2\right)}} \tag{3.5.40}$$

The flow through the tooth jets can now be calculated as follows:

$$Q_{3,3} = Q_3 - Q_{3,2} \tag{3.5.41}$$

However, since the pressure difference $\Delta p_{3,2}$ and the flow resistance R_{total} were already known, it is also possible to calculate the flow by rewriting equation (3.5.29). This leads to the following expression:

$$Q_{tooth} = \frac{\Delta p_{3,2} \cdot A_{soil}}{\rho_w \cdot g \cdot R_{total}} \tag{3.5.42}$$

Although there are two different ways to calculate the flow through the tooth jets it does not necessarily mean that both equations yield the same result. This is because the system is over defined. Iterations are needed where Q_{pump} is varied (and hence Δp_{pump}) until $Q_{3,3} = Q_{tooth}$ or:

$$Q_{3,3} - Q_{tooth} = 0 \tag{3.5.43}$$

Problems can occur during iterations due the fact that in some situations the calculated flow through a free flowing jet is larger then the flow provided by the pump. This then leads to other flows becoming negative which will lead to negative pressures. These negative pressures lead to errors when the square root is taken. Measures should therefore be taken to prevent pressures and flows from becoming negative during iteration.
Once the condition in equation (3.5.43) has been met the correct Δp_{jet} (and Q_{jet}) can be obtained. The pore pressure calculations are then continued as described in section 3.5.1 with the exception of the correction proposed in equations (3.5.16) to (3.5.18).

3.6 Cavitation cloud

In the previous paragraphs that described the theory of cutting water saturated sand it was assumed that deformation only takes place in the shear zone. This means that dilatation also only is assumed to take place in the shear zone, and thus cavitation would also only take place in the shear zone. This might be a reasonable assumption for situations where the cutting speed is low, the slice thickness is normal or the permeability is high, i.e. in situations where only a small part of the shear zone is cavitating. In situations where this is not the case like cutting soil at high velocities, cutting large slice thicknesses and/or cutting soil with a low permeability the water vapor bubbles might not have dissolved after leaving the shear zone. This leads to a 'cloud' or 'spot' of water vapor traveling up the blade. The presence of this cloud above the blade inhibits the flow of water to the soil that is in

direct contact with the blade. Therefore the pore vacuum pressure is not reduced going up on the blade until the cloud is gone. The pore vacuum pressure that is on the blade while the cloud is there is the cavitation pressure ($\rho_w \cdot g \cdot (z + 10)$) since there is no pressure gradient due to the lack of water flow. Because of this the presence of a cavitation cloud can have a great influence on the average pore vacuum pressure on the blade since the pore vacuum pressure stays constant along the blade as long as the cloud is there while, without the cloud, it would almost immediately start dropping. The change in average pore vacuum pressure on the blade has an influence on the cutting force, the direction of the cutting force and the location of the acting point on the blade, all of which influence the moment balance. It is therefore important to incorporate the influence of the cavitation cloud in the production model. In the next sections two models for the cavitation cloud are given. In the first model actual equations from *The Delft Sand, Clay & Rock Cutting Model* are used to calculate how far the cavitation cloud progresses up the blade. The second model is an alteration of the normal pore pressure calculations (see paragraph 3.4) which simply mimics the 'behavior' of the cavitation cloud. Therefore this model is named the quasi cavitation cloud model or in short the quasi-cloud model.

3.6.1 The cavitation cloud model

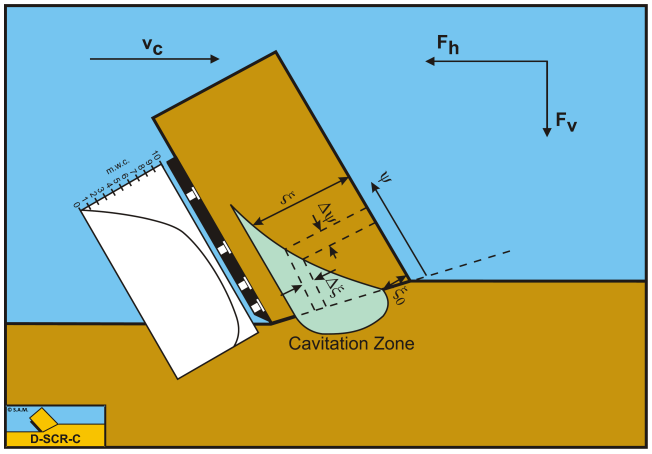

Figure 3.17: The cavitation cloud during the cutting process

Calculating the pore vacuum pressure on the blade under influence of a cavitation cloud starts by finding the distance of the cloud to the free sand surface ξ_0, see figure 3.17. This is done by assuming that this point is close to the free sand surface. Therefore the flow lines s_2 and s_3 (see figure 3.5) are very short compared to flow lines s_1 and s_4. Respectively resistances R_2 and R_3 are very small compared to R_1 and R_4. It is therefore assumed that all water needed in the shear zone ($v_c \cdot \epsilon \cdot sin(\beta)$) will flow through flow lines s_2 and s_3. Since the pressure is known (cavitation pressure), the required flow is known and the expressions for the flow line lengths are known an equation for the distance ξ_0 can be found:

$$\xi_0 = \frac{(z + 10)}{v_c \cdot \epsilon \cdot sin(\beta)} \cdot \left(\frac{k_{max}}{\alpha + \beta} + \frac{k_i}{\pi - \beta} \right) \cdot sin(\alpha + \beta) \tag{3.6.1}$$

However, equation (3.6.1) is based on the flow line lengths s_2 and s_3 described in Miedema his dissertation from 1987. In an updated version of the theory a factor of 0.8 has been added to both flow line length, this can also be seen in equation (3.4.4) and equation (3.4.5). The factor of 0.8 is based on finite-element calculations. In order to get an expression for ξ_0 for the updated flow line lengths,

equation (3.6.1) should be multiplied with a factor of $\frac{1}{0.8}$ or 1.25. This is shown in the following equation.

$$\xi_0 = 1.25 \cdot \frac{(z+10)}{v_c \cdot \epsilon \cdot sin(\beta)} \cdot \left(\frac{k_{max}}{\alpha+\beta} + \frac{k_i}{\pi-\beta} \right) \cdot sin(\alpha+\beta) \tag{3.6.2}$$

Alternatively the point can be found by looking into the results of the pore vacuum pressure calculation in the shear zone. The pore vacuum pressure calculations in the shear zone are discussed in section 3.4.1. Starting in the point where the shear zone meets the free surface, the break point, it should be the first point where cavitation occurs when moving towards the tip of the blade. Since the shear zone is divided into a finite amount of elements the first point at which cavitation occurs can be seen as the first element for which the pore pressures reach cavitation pressure. The number of the element in which cavitation starts $i_{cavitation}$ is then used in the following equation to calculate ξ_0.

$$\xi_0 = \frac{i_{cavitation}}{N} \cdot L_{max} \cdot cos(\theta_1) \tag{3.6.3}$$

In equation (3.6.3) N is the number of elements, L_{max} is the length of the shear zone and $cos(\theta_1)$ converts the distance along the shear plane to a distance perpendicular to the free surface.
Even when the updated equation (3.6.2) is used, the calculated distance ξ_0 will be different than the ξ_0 calculated with equation (3.6.3). These differences are caused by neglecting the flow line lengths s_1 and s_4 in equation (3.6.2) whilst the method of equation (3.6.3) does take them into account. If the flow line lengths s_1 and s_4 would go to infinity then their respective resistances R_1 and R_4 would also go to infinity. This means that no flow will pass through s_1 and s_4. In this situation the calculated ξ_0 is the same for both equations.
After having calculated ξ_0 it is assumed that the flow that fills the cavitation cloud with water flows into the cloud in a straight line perpendicular to the free sand surface. The length of this flow line is ξ, this leads to the following resistance:

$$R_\xi = \frac{\xi}{k_{max}} \tag{3.6.4}$$

Since the pressure difference is known to be the cavitation pressure ($\rho_w \cdot g \cdot (z+10)$) the specific flow into the cavitation cloud can be calculated using Darcy's Law:

$$q = k \cdot i = \frac{\Delta p}{\rho_w \cdot g \cdot R_\xi} = \frac{k_{max} \cdot (z+10)}{\xi} \tag{3.6.5}$$

If it is assumed that the specific flow of the cavitation bubbles is equal to that required by dilatation the following equation can be made:

$$q = v_c \cdot \epsilon \cdot \frac{sin(\beta)}{sin(\alpha+\beta)} \tag{3.6.6}$$

In equation (3.6.6) the term $1/sin(\alpha+\beta)$ is compensation for the angle since flow lines perpendicular to the free surface are considered. Now assuming that an infinitesimal small step up the blade $d\psi$ leads to an infinitesimal small increase of flow line length $d\xi$ will lead to the following equation:

$$\frac{k_{max} \cdot (z+10)}{\xi} \cdot d\psi = v_c \cdot \epsilon \cdot \frac{sin(\beta)}{sin(\alpha+\beta)} \cdot d\xi \tag{3.6.7}$$

Integration of equation (3.6.7) and rewriting the result leads to an expression for the distance between the free surface and the cavitation cloud:

$$\xi = \sqrt{\xi_0^2 + 2 \cdot \frac{k_{max} \cdot (z + 10)}{\left(v_c \cdot \frac{sin(\beta)}{sin(\alpha+\beta)} \cdot \epsilon \right)} \cdot \psi} \tag{3.6.8}$$

Now starting in the break point the last point in the shear zone that is cavitating has to be found. This is done by looking into the results of the pore vacuum pressure calculations in the shear zone. The distance between this point and the free surface (in this situation the break point) then has to be compensated for the difference in angle and is denoted as ξ_{max}.
To incorporate the effect of the cavitation cloud in the standard pore pressure calculations the free surface is divided into $n + 1$ sections, where n is equal to the amount of sections in which the blade is divided. Furthermore, n of the free surface sections align with the sections of the blade, this way there is one section of free surface left with a different length. This section is denoted ψ_0 and is calculated using the following equation:

$$\psi_0 = L_{max} \cdot sin(\frac{\pi}{2} - \alpha - \beta) \tag{3.6.9}$$

For every step on the blade and hence the free surface there is a check if the cavitation cloud is still present. If so, the pore vacuum pressure on that point on the blade is equal to the cavitation pressure. This is visualized in the following expression:

$$\text{If } \xi_{max} - \xi_i > 0 \text{ then: } p_{2,i} = \rho_w \cdot g \cdot (z + 10) \tag{3.6.10}$$

In equation (3.6.10) ξ_i is defined as follows:

$$\xi_i = \sqrt{\xi_0^2 + 2 \cdot \frac{k_{max} \cdot (z + 10)}{\left(v_c \cdot \frac{sin(\beta)}{sin(\alpha+\beta)} \cdot \epsilon \right)} \cdot (i \cdot \frac{h_b}{n \cdot sin(\alpha)} + \psi_0)} \tag{3.6.11}$$

When the condition in equation (3.6.10) is no longer valid the pore vacuum pressure on the blade has to decrease to zero over the remaining length of the blade. This can be done in many ways, but according to Miedema a linear decrease is in line with the measurements. Other types of curves can also be used, as long as the pressure is always decreasing.
In the production model the decrease is not fully linear. Instead the decrease of pore vacuum pressure on the blade is calculated using a smoothstep function (see appendix E). Important to note is that this does not have any real physical meaning but since the smoothstep function is used, large parts of the curve are almost linear. In addition to the almost linear decrease, this way of pressure decrease is also chosen because it gives a smooth course of the average pore pressure on the blade. This is important since a smooth course of average pore pressures means a smooth course of cutting forces and hence a smooth course of cutting moments. A smooth course of cutting moments is important because some iteration functions cannot handle discontinuities (see appendix C).
As was done for the normal pore pressure calculations described in section 3.4.1, pore pressure distribution graphs can also be made in the case of the cavitation cloud. Again this is done by plotting the pore pressures for each step that is done on the blade or the shear plane. This is done in figure 3.18 for a cavitating situation without modeling the cavitation cloud and in figure 3.19 for a cavitating situation where the effects of the cavitation cloud are modeled. On the x-axis the position on the blade or shear plane is expressed in the form of a percentage of the length of the blade or shear plane.

Important to note is that 100% is the position at the tip of the blade for both the blade as the shear plane. On the y-axis the pore under pressure is displayed.
When figure 3.18 and 3.19 are compared it should be noted that the pressure distributions in the the shear plane are identical. This is correct since the cavitation cloud only influences the pore under pressures on the blade. The effect of the cavitation cloud on the pore under pressure on the blade is also clearly visible. The pore under pressure in figure 3.18 starts dropping below the cavitation pressure at around 95%. However, when the effect of the cavitation cloud is modeled, the pore under pressure only starts dropping below the cavitation pressure at around 45%, as can be seen in figure 3.19. The difference in shape of the slopes of p_2 (convex and concave) can be explained by the way the pressures are calculated. The p_2 in figure 3.18 is calculated using the parallel resistor model while the p_2 in figure 3.19 is simply the result of a smoothstep function.
Modeling the effect of the cavitation cloud using the theory described above and the smoothstep function contributes to a higher average pore pressure on the blade in two ways. The prolonged cavitation pressure on the blade raises the average pore pressure and when the pressure does start dropping, the concave shape causes the pressure in a point on the blade to still be higher than in the normal parallel resistor situation. Including the effects of the cavitation cloud in the pore pressure calculations hence makes the effects of the pore under pressures on the blade more dominant with respect to the pore under pressures on the shear plane. This leads to a change in cutting forces and the directions of the cutting forces (with respect to the normal parallel resistor model), which eventually leads to a change in moments.

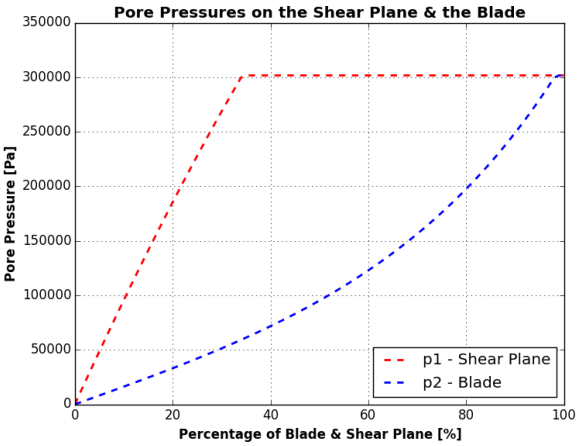

Figure 3.18: Pore pressures on the blade and the shear plane, $\alpha = 35°, \beta = 23.5°, k_i/k_{max} = 0.2, h_i/h_b = 0.5, \epsilon = 0.16, v_c = 1.0m/s, z = 20m$

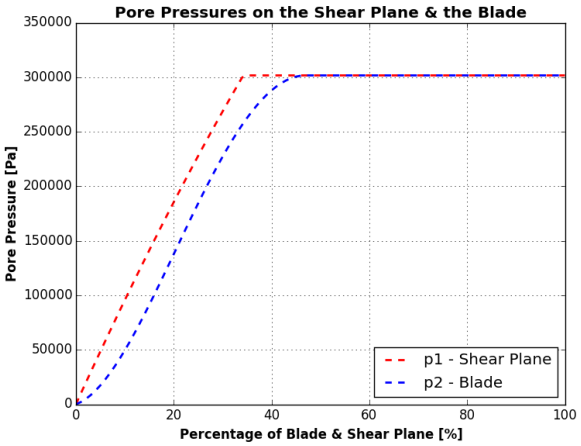

Figure 3.19: Pore pressures on the blade and the shear plane, $\alpha = 35°, \beta = 23.5°, k_i/k_{max} = 0.2, h_i/h_b = 0.5, \epsilon = 0.16, v_c = 1.0m/s, z = 20m$

How this method of calculating the pore pressures under the influence of a cavitation cloud is applied in Python can be found in Appendix D.

3.6.2 The quasi cavitation cloud model

As was stated in the beginning of this paragraph, the quasi cavitation cloud model is simply an alteration of the normal pore pressure model and only mimics the behavior of a cavitation cloud.
The alteration starts at the end of the pore under pressure calculations in the shear zone. The last under pressure calculated in the shear zone is the under pressure at the tip of the blade. In the normal pore pressure calculations the under pressure at the tip (and all other under pressures) is limited to

the cavitation pressure. However, for the quasi cloud model the pressure at the tip is not limited since it is the input for the pore pressure calculations on the blade. For the calculation of the average pore under pressure in the shear zone still the limited pressure is used.
The unlimited pressure at the tip of the blade Δp_{tip} is then used to calculate the initial flows using equation 3.4.19. Since in the case of cavitation at the tip the unlimited Δp_{tip} is greater than or equal to the cavitation pressure and since Δp_{tip} is in the numerators of equation 3.4.19, the initial flows that are calculated are also greater than or equal to the flows in the normal pore pressure calculations. These greater than normal (or equal) flows are then used to calculate the pore under pressure for the next step on the blade using equation 3.4.21. Again, the pressure should not be limited for the calculation. Which can again lead to flows that might eventually lead to pore under pressures greater than the cavitation pressure. This process will go on until either the end of the blade is reached and the calculations are ended or until the under pressure falls below the cavitation pressure and the pressure starts decreasing like in the normal calculations. Important to note is that the calculated pressures should still be limited to the cavitation pressure when summing them up in order to calculate the average pore under pressure on the blade (as shown in equation (3.4.22)).
When figure 3.21 is compared with figure 3.20 the difference between no cavitation cloud model and the quasi cloud model can be seen. As with the normal cavitation cloud model there is no difference between the pore pressures in the shear zone since these are not influenced by the presence of a cavitation cloud model.

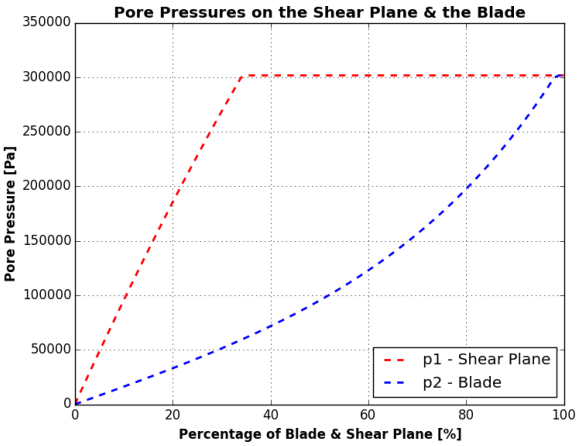

Figure 3.20: Pore pressures on the blade and the shear plane, $\alpha = 35°, \beta = 23.5°, k_i/k_{max} = 0.2, h_i/h_b = 0.5, \epsilon = 0.16, v_c = 1.0m/s, z = 20m$

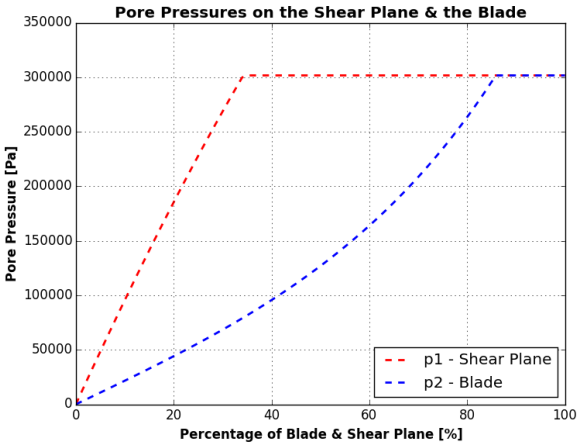

Figure 3.21: Pore pressures on the blade and the shear plane, $\alpha = 35°, \beta = 23.5°, k_i/k_{max} = 0.2, h_i/h_b = 0.5, \epsilon = 0.16, v_c = 1.0m/s, z = 20m$

As can been seen in figure 3.21 the pore pressure on the blade starts dropping at roughly 85% (when starting at 100%). This means that between roughly 85% and 100% the unlimited pore pressure was higher than the cavitation pressure. These pressures are then however capped at the cavitation for the results since a pore pressure higher than the cavitation pressure would have no physical meaning. However, as explained before the calculation between in this case 85% and 100% use the unlimited pressure.

3.6.3 Comparison between the cavitation models

Upon inspection of figures 3.19 and 3.21 it can be seen that the cavitation cloud model and the quasi cavitation cloud model yield fairly different results for the same inputs. The main difference is the

percentage at which the pore pressure starts dropping. The other difference is the type of slope at which the pressure drops. However, in both cases replacing the slope with a linear slope will not make much of a difference for the average pore pressure that is calculated.
As as explained before, the difference between the two cloud models is that the normal cloud model is actually based on physics while the quasi cloud model just mimics the effect of the cavitation cloud model. However, stating that the quasi cloud model is not dependent on the cutting parameters would be incorrect since cutting parameters are used to calculate the pore pressures and flows (as discussed in the previous section). Also, simply stating that the two models work in different ways does not automatically explain the differences in the results that were shown in figures 3.19 and 3.21. This difference can partially be explained by looking when the cloud models are used.
The normal cavitation cloud model is used as soon as there is cavitation at any point in the shear zone. Then calculations are done to see if, or up to which point above the blade the cloud is present. This point is dependent on many cutting parameters like the slice thickness, the maximum permeability and the blade angle. This means that for certain combinations of parameters the cloud might be present above the entire blade and that for other combinations the cloud might not reach the blade at all.
The quasi cavitation cloud model is only used from the moment when there is cavitation at the tip of the blade. Compared to the normal cloud model, this model lacks a check whether the cloud actually reaches the blade. As soon as there is cavitation at the tip of the blade a cloud will develop above the blade for increasing trailing speeds.
Since cavitation generally starts somewhere in the middle of the shear zone and then expands to the free soil surface and the tip of the blade it would be logical to think that the position of the cloud above the blade for the quasi cloud model always lags behind the position of the cloud in the normal cloud model. However, this assumption does not take into account that cutting conditions might exist for which the cloud in the normal cloud model does not reach the blade for lower speeds and hence would lag behind the position of the cloud of the quasi cloud model. Since it is dependent on the cutting parameters which of these scenarios will happen and since some of these cutting parameters change for changing trailing speeds during the production calculations it is difficult to predict how close the results of both models lie to each other. Therefore it is not possible to immediately tell which cloud model would work better in the production model and hence both can be used in the production model.
Both models do have their advantages. The advantage of the quasi cavitation cloud model is that it has a smooth increase from no cavitation on the blade to cavitation on the blade. For the normal cloud model this is very dependent on how the progression of the cloud is modeled. This is a disadvantage of the normal cloud model because the progression of the cloud, once on the blade, can occur rather quickly. This leads to jumps in the average pore pressure for increase of the trailing speed. These jumps, or discontinuities, might eventually lead to convergence errors in the moment balance calculations because the iterative methods used require a continuous function (see appendix C). The advantage of the normal cloud model is that it is based on actual physical processes.

4 Jetting Theory

4.1 Introduction

This chapter covers the jetting theories that can be used in the production model. With 'jetting' the process of liquefying water saturated sand by using water jets is meant. In the production model the jetting theory is used to model the heel jets. The heel jets are assumed to liquefy a layer of the sea bed making the bed easier to cut (no cutting force). The thickness of the liquefied layer is what the theories in this chapter aim to predict. How the theories described in this chapter are implemented can be found in chapter 6. The effects of the tooth jets and visor jets are not described by the theories in this chapter.
Water jets are applied in many fields of engineering like mechanical engineering, hydraulic engineering and dredging engineering. Therefore many theories exist that aim to predict jet scour or jet penetration. However, not all of these theories are suitable for application in the production model. The next paragraph will explain why some theories have been chosen and others not.
The four paragraphs after this cover the theories that have been found suitable for use in the production model. Not all four theories are used at the same time in the production model. They are substitutes for each other and should be chosen based on user preference and experience. However, the comparison in the last paragraph of this chapter might help with this choice.

4.2 Suitability of jet scour equations

In literature many papers can be found of researches that aim to predict or describe jet scour in non-cohesive materials. These researches have been carried out in many fields of study including dredging engineering, hydraulic engineering and chemical engineering. However, in the paragraphs that follow it can be seen that only jet production equations from researches in the dredging field have been applied in the production model. This paragraph will explain the most common arguments on why equations/results from jet scour studies were eventually found not suitable for application in the production model. This is done with examples based on a number of papers.
One of these papers was written by Aderibigbe and Rajaratnam [7] and presents the results of a laboratory study on the erosion of loose sand beds by submerged circular impinging vertical turbulent jets. For the draghead production model the modeled sand does not necessarily have to be a loose sand, however the theories from the paper might still give insight in the order of magnitude of the penetration depth of the heel jets. Therefore it was still interesting to see if the theories could be used to predict jet penetration.
In the paper of Aderibigbe and Rajaratnam the final scour depth $\epsilon_{m\infty}$ is presented as a function of the erosion parameter E_c. This function can be seen in equation (4.2.1).

$$\frac{\epsilon_{m\infty}}{H} = 1.26 \cdot E_c^{0.11} - 1 \tag{4.2.1}$$

Where the erosion parameter E_c is defined as follows.

$$E_c = \frac{u_0 \cdot \frac{D_n}{H}}{\sqrt{g \cdot \Delta \cdot d}} \tag{4.2.2}$$

In equation (4.2.2) u_0 is the exit velocity of the jet, D_n is the nozzle diameter of the jet, H is the height at which the jet is positioned above the sand bed, g is the gravitational constant, Δ is the specific density of sand and d is the particle diameter.
The final scour depth $\epsilon_{m\infty}$ in equation (4.2.1) is made dimensionless by dividing by dividing by the jet suspension height H. The jet suspension height is also present in the equation of the erosion parameter. This poses a problem when the equations are applied to a situation with heel jets since the heel in the production model is assumed to be at the same height as the sand bed. This would mean that the jet suspension height is equal to zero and hence the erosion parameter would go to infinity. Therefore the final scour depth cannot be calculated.
In reality situation might occur in which the heel is suspended above the sand bed. However, choosing this suspension height for the model would be very arbitrarily and could lead to a wide variation of final scour depths. Furthermore, the opposite situation also occurs in reality. The heel can also be plowed through the sand bed. In this case the suspension height would still be zero since the distance between the heel jet and the sand is still zero. Hence the final scour depth in this situation cannot be calculated.
Besides the fact that the final scour depth cannot be calculated it would also questionable how representative the results would be if the depth could be calculated. This is because the final scour depth is the depth that is reached after a water jet has stationary been scouring for a number of minutes. This does not say much about what volume of sand is liquefied per second, which is what reduces the cutting force. Furthermore the heel jets in the draghead are not stationary since the draghead is always moving and even if the draghead is moving slowly, these trailing speeds are still too high to even consider the jet to be near stationary.
Experiments on the final scour depth by moving circular jets were done by Yeh et al [8]. Since the jet is moving the influence of a trailing speed is accounted for. However, again the jet suspension height H is present in both expressions for the erosion parameter and the final scour depth, again making the equations unsuitable for use in a heel jet model. Also still the same is that a final scour depth does not necessarily say anything about the liquefied volume of soil. Furthermore, the jet exit velocity during the experiments is considerably lower than the jet exit velocity of the heel jets of the Wild Dragon draghead (respectively 2.05 m/s and 25 m/s).
A study similar to the one of Aderibigbe and Rajaratnam was conducted by Deghani et al [9]. Again the same erosion parameter described in in equation (4.2.2) was used and again the final scour depth was made dimensionless by diving by the jet suspension height thus making the results not applicable for the heel jet model. However, in the paper also a dynamic scour depth is described. The dynamic scour depth is the scour depth caused by the jet when the final scour depth has not yet been reached. This means that the dynamic scour depth is a function of time. In equation (4.2.3), in which t is in minutes, such a function is given for a jet exit velocity of 9.07 m/s.

$$d_{dyn} = 26.3159 \cdot (1 - \mathrm{e}^{-0.1873 \cdot t}) \tag{4.2.3}$$

The paper also mentions the dynamic scour diameter. If the derivative with respect to time would be taken for equation (4.2.3) and an equation for the dynamic scour diameter then an expression for the rate of change of the scour hole volume could be found. This rate of change of scour hole volume can be regarded the volume of soil that is liquefied per unit of time, which eventually by using the draghead width and trailing speed could be turned into a penetration depth. However, no equation is given for the dynamic scour diameter so this is not possible. Also, equation (4.2.3) is given for a single jet exit velocity which would make it difficult to apply the results to situations with other jet velocities. It would also be questionable if the equation could be applied due to the fact that the application range of the equation only starts at a t equal to one minute whilst for jet penetration probably a t in the order of magnitude of a second or less would be preferred.
It seems difficult to directly calculate the jet penetration for heel jets based solely on jet and soil

properties. In the three papers that were discussed this is mainly due to the fact that the jet suspension height is present in the equations, which is zero in the case of heel jets. Also, some jet parameters in the experiments seem to be in different orders of magnitude than the jet parameters of the heel jets. Even if it were possible to directly calculate the jet penetration it would still be questionable if this depth could be applied over the entire width of the draghead since this would be dependent on the shape (width) of the jet cone. When this is assumed to be the case this might lead to an overestimation of the jetted (produced) volume of soil. Therefore, a more conservative approach would be to calculate the liquefied (or produced) volume of soil based on the soil and jet properties and to divide this by the draghead width and trailing speed. This basically is what is done with the jetting equations described in the next paragraphs.

4.3 Vlasblom

This method of calculating jet penetration is derived from W.J. Vlasblom's jet production equation. The equation has never been published by Vlasblom in any official papers and can only be found in the lecture notes of his course *Designing Dredging Equipment* at *Delft University of Technology* [2]. Vlasblom's jet production equation assumes that the jet production is proportional with the total momentum of the jet system and is independent of the trailing velocity. The momentum for a water jet is defined as follows:

$$I = \rho_w \cdot Q_{jet} \cdot u \tag{4.3.1}$$

In equation (4.3.1) Q_{jet} is the flow of a jet and u is the exit flow velocity of the jet. The exit velocity can be approached by using a simplified Bernoulli equation in which the pressure due elevation is neglected:

$$p_{jet} = \frac{\rho_w \cdot (u_{out}^2 - u_{in}^2)}{2} \tag{4.3.2}$$

One of the properties of a jet is that the exit velocity is considerably bigger than the entry velocity. This means that for the square of the velocity the difference is even bigger or: $u_{out}^2 \gg u_{in}^2$. This leads to the following assumption:

$$u_{out}^2 - u_{in}^2 \approx u_{out}^2 \tag{4.3.3}$$

Substituting equation (4.3.3) in equation (4.3.2) yields the following equation:

$$p_{jet} \approx \frac{\rho_w \cdot (u_{out}^2)}{2} \tag{4.3.4}$$

Rewriting equation (4.3.4) yields an approximation for the jet exit velocity:

$$u_{out} \approx \sqrt{\frac{2 \cdot p_{jet}}{\rho_w}} \tag{4.3.5}$$

Since the assumption is that jet production (mass flux) is proportional with the jet momentum substituting equation (4.3.4) in equation (4.3.1) yields the following equation:

$$\dot{M}_{sand} = \alpha \cdot I = \alpha \cdot \rho_w \cdot Q_{jet} \cdot u = \alpha \cdot \rho_w \cdot Q_{jet} \cdot \sqrt{\frac{2 \cdot p_{jet}}{\rho_w}} \tag{4.3.6}$$

In equation (4.3.6) $\dot{M}_{sand}$ is the mass flux of sand and α is a coefficient that is dependent on the part particle size, jet pressure, jet flow and trailing velocity. However, a reasonable assumption for α is 0.1 according to Vlasblom. The coefficient is presumably the result of regression analysis among data sets of jet production at various particle diameters, jet pressures, jet flows and trailing velocities.
The calculated mass flux is the mass flux for one jet. However, dragheads have a row of jets in the heel. To calculate the total mass flux the mass flux of one jet is multiplied by the number of jets n_{jet}:

$$\dot{M}_{total} = n_{jet} \cdot \dot{M}_{sand} \tag{4.3.7}$$

This is under the assumption that all jets are the same, that the jets do not influence each other and that the jets are wide enough together to liquefy the body of sand over the whole width of the draghead. Once the total mass flux has been calculated the jet penetration can be calculated using the following equation:

$$y_{jet} = \frac{\dot{M}_{total}}{\rho_{quartz} \cdot (1 - n_i) \cdot W \cdot v_c} \tag{4.3.8}$$

In equation (4.3.8) ρ_{quartz} is the density of the particles (usually $2650 kg/m^3$ for sand), n_i is the porosity of the sand bed, W is the width of the draghead and v_c is the trailing speed.
The elegance of this equation is that it based on a very elementary law in physics: the law of conservation of momentum. However, the equation lacks soil mechanical inputs, hence it basically ignores all flow aspects of water through soil. The in situ porosity is used, but only after the jet production in kg/s is already calculated. Stating that there is no influence of soil mechanical parameters in the equation would be incorrect however since the coefficient α is generated using data sets that also include particle size. Through this particle size data, or more accurately the particle size distribution, the influence of the permeability is hidden in α. There are various equations that describe a relation between the particle size distribution and the permeability. Well-known equations are the Kozeny-Carman equation [10],[11],[12] and the equations of Shepherd [13]. These equations can be found in appendix F.

4.4 Weegenaar

In 2014 research was done on sand erosion by a traversing circular jet by R.A. Weegenaar as part of his Msc thesis [14]. In this research, commissioned by *Damen Dredging Equipment*, experiments were carried out with various nozzle diameters, jet pressures, trailing speeds and two different sands (different permeabilities and D_{50}'s). During the experiments the scour hole was analyzed to find out what volume of sand was liquefied by the jet.
A regression analysis was performed on the results, which showed that there is a linear relation between jet momentum and jet production and hence confirms Vlasblom's statement. The equation for jet production is therefore the same as Vlasblom's:

$$\dot{M}_{sand} = \alpha \cdot I = \alpha \cdot \rho_w \cdot Q_{jet} \cdot u = \alpha \cdot \rho_w \cdot Q_{jet} \cdot \sqrt{\frac{2 \cdot p_{jet}}{\rho_w}} \tag{4.4.1}$$

A detailed explanation of equation (4.4.1) can be found in paragraph 4.3. The difference between Vlasblom's production calculation and Weegenaar's is the coefficient α. Where Vlasblom proposes α is 0.1 as a reasonable assumption, Weegenaar finds on average that α is 0.13 through his experiments. According to Weegenaar this factor of 1.3 difference might suggest that Vlasblom overestimates

the specific cutting energy. Another possibility is that the factor difference is caused by a different choice of reference window. Weegenaar assumes a square reference window ($A_{square} = D^2$) while Vlasblom might have chosen a circular reference window ($A_{circle} = \frac{\pi}{4} \cdot D^2$). This leads to a factor of $A_{square}/A_{circle} = \frac{4}{\pi} \approx 1.27$ difference.
When the mass flux of a jet has been calculated the total mass flux for all heel jets can be calculated by multiplying the mass flux with the number of jets:

$$\dot{M}_{total} = n_{jet} \cdot \dot{M}_{sand} \tag{4.4.2}$$

This is again under the assumption that all jets are the same, that the jets do not influence each other and that the jets are wide enough together to liquefy the body of sand over the whole width of the draghead. Once the total mass flux has been calculated the jet penetration can be calculated using the following equation:

$$y_{jet} = \frac{\dot{M}_{total}}{\rho_{quartz} \cdot (1 - n_i) \cdot W \cdot v_c} \tag{4.4.3}$$

In equation (4.4.3) ρ_{quartz} is the density of the particles (usually $2650 kg/m^3$ for sand), n_i is the porosity of the sand bed, W is the width of the draghead and v_c is the trailing speed.
As with Vlasblom's equation, there is no visible direct link between any soil mechanical parameters and the production since this link is hidden in the coefficient α.

4.5 C.S.B.

The C.S.B. equation is the result of a regression analysis performed on results of jetting experiments done with various nozzle diameters, jet pressures, permeabilities and trailing speeds. These experiments were commissioned by *Combinatie Speurwerk Baggertechniek* (C.S.B.), a combination of several Dutch dredging companies with the aim of doing research into dredging processes.

$$y_{jet} = C \cdot p_1^{0.59} \cdot d^{0.49} \cdot k^{0.369} \cdot v_c^{-1} \tag{4.5.1}$$

In equation (4.5.1) y_{jet} itself is in millimeters, p_1 is the jet pressure (MPa), d the nozzle diameter (mm), k the permeability (cm/s) and v_c the trailing speed (m/s). The coefficient C is part of the result of the regression analysis and is mostly dependent on the compaction of the sand. Multiple versions of the C.S.B. equation exist but for the version described in the thesis of *de Jong* [15], C is equal to 291.
The advantage of the C.S.B. equation is that both jet properties as well as an important soil mechanical property (the permeability) are used to predict the jet penetration. A disadvantage of the equation is that it predicts penetration for a single jet whilst in reality multiple jets are mounted next to each other in the heel of the draghead. This raises the question on how to use the jet penetration for a single jet in the situation of a draghead where multiple jets are in line. The simplest way is probably assuming that the spacing between the jets is done in such a way that the jet cones liquefy the body of sand up to the penetration depth over the entire width of the draghead. In that case, the liquefied volume of soil or, the in situ jet production, can easily be calculated using the following equation:

$$Q_{situ} = y_{jet} \cdot W \cdot v_c \tag{4.5.2}$$

For the shape of the liquefied body of sand the general rule is, the deeper the penetration the narrower the shape. Hence, for deeper penetration depths it might happen that the the liquefied bodies of sand of the separate jets are so narrow that they do not touch each other anymore. In this situation 'columns' of undisturbed soil will exist, as is demonstrated in figure 4.1. These columns have to be cut and hence there will be a cutting force. This also means that there can be situations in which the jet penetration is far beyond the reach of the blade but where still a relatively large cutting force is required.

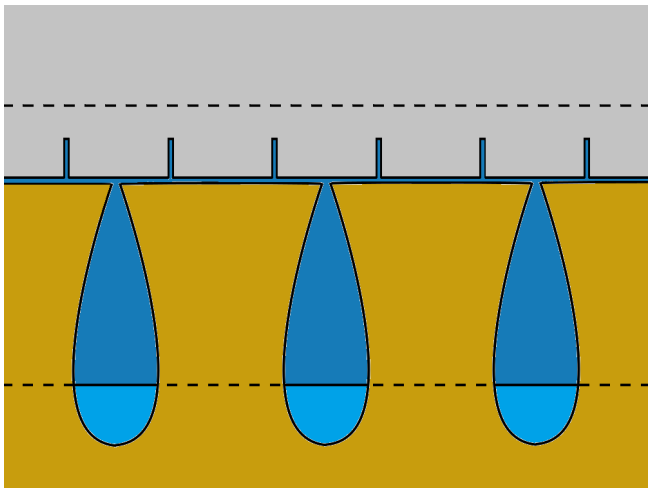

Figure 4.1: The occurrence of sand columns due to limited jet width. The dashed lines mark the position of the blade

During the occurrence of sand columns the cutting force can be calculated in several ways. One approach is to change the width W in the cutting force calculations. Normally W is the width of the draghead but this can be replaced by the cumulative width of the sand column. The cumulative width of the sand columns cannot be larger than the width of the draghead.
Another approach is to find out what percentage of the area $y_{jet} \cdot W$ has been liquefied and then to evenly distribute this percentage over the width of the draghead. This means that when α percent of the area is liquefied then the adjusted penetration depth is simply $\alpha \cdot y_{jet}$.
A disadvantage of both approaches is that information on the shape and size of the liquefied areas is needed.

4.6 Specific energy method

The two methods of calculating jet penetration described in paragraph 4.3 and paragraph 4.4 were based on the law of conservation of momentum. The method described in this paragraph use the law of conservation of energy to calculate jet penetration. This is done by assuming that all the energy per unit of time of a water jet, hence jet power, is used to cut a certain volume of in situ soil per unit of time.
When cutting with blades, the relation between the cutting power and the volume of the produced soil is given by the specific cutting energy. The specific cutting energy or E_{sp} with units kN/m^2 or kPa is defined in *The Delft Sand, Clay & Rock Cutting Model* [4], [5] as follows: The amount of energy , that has to be added to a volume unit of soil (e.g. sand, clay or rock) to excavate the soil. The amount of energy that per unit of time is added to a volume unit of soil, or the cutting power, is defined as

follows for cutting with a blade:

$$P_{cut} = F_h \cdot v_c \tag{4.6.1}$$

The volume unit of soil that is cut per unit of time, or the situ production, is defined as follows:

$$Q_{situ} = h_i \cdot W \cdot v_c \tag{4.6.2}$$

Combining equation (4.6.1) and equation (4.6.2) yields an expression for the specific cutting energy:

$$E_{sp} = \frac{P_{cut}}{Q_{situ}} = \frac{F_h \cdot v_c}{h_i \cdot W \cdot v_c} = \frac{F_h}{h_i \cdot W} \tag{4.6.3}$$

Rewriting equation (4.6.3)yields an expression for the cutting production in terms of cutting power and specific cutting energy of the soil:

$$Q_{situ} = \frac{P_{cut}}{E_{sp}} \tag{4.6.4}$$

By replacing the cutting power by the jet power, equation (4.6.4) can now be used to calculate jet production. A factor of η is added in front of E_{sp}, where η is usually somewhere in the range of 0.5 to 1. This is because in general the process of cutting sand with water jets is more efficient than cutting cutting the sand with blades. The production equation for water jets now looks as follows:

$$Q_{situ} = \frac{P_{jet}}{\eta \cdot E_{sp}} \tag{4.6.5}$$

In equation 4.6.5 Q_{situ} is the production of in situ soil. Important to note is that E_{sp} is still the specific energy for cutting sand instead of a specific energy for jetting sand since this is accounted for in the factor η. The jet power P_{jet} can be obtained by using data sheets provided by the manufacturer of the jet water system. Alternatively it can be calculated by using the parallel resistor model which is described in section 3.5.2. The pressure drop over the resistor that represents the heel jet nozzles should be calculated as well as the flow through this resistor. The jet power can then be calculated by using equation 4.6.10.
Once Q_{situ} has been calculated using equation (4.6.5), the jet penetration y_{jet} can be calculated by using the following equation:

$$y_{jet} = \frac{Q_{situ}}{v_c \cdot W} \tag{4.6.6}$$

In equation 4.6.6 v_c is the trailing speed and W the width of the blade (or draghead).
In its current form equation (4.6.5) has a very limited applicability because the specific energy of the soil that is being jetted has to be known. This means that the specific cutting energy probably will be estimated by using data from previous dredging jobs. However, by combining equation (4.6.5) with several other equations an expression can be found for jet penetration in terms of jet properties and soil properties.
This alternative starts with an equation of Miedema [16] that is used to calculate the specific cutting energy for non-cavitating situations:

$$E_{sp} = \frac{c_1 \cdot \rho_w \cdot g \cdot h_i \cdot \epsilon \cdot v_c}{k_m} \tag{4.6.7}$$

In equation (4.6.7) ρ_w is the density of water, g is the gravitational constant, h_i is the initial cut height, ϵ is the dilatation, v_c is the trailing speed and k_m is the average permeability of the soil. The coefficient c_1 can normally be calculated or found in tables. However both methods require a blade height and angle of external friction and since these are not present when jetting. This poses a slight problem. The range in which c_1 varies in the tables of *The Delft Sand, Clay & Rock Cutting Model* is roughly 0.1 to 1.7 but most values seem to be in the order of magnitude of 0.45. Therefore it is assumed that c_1 simply is equal to 0.45.
When the jet production equation (4.6.5) is substituted in jet penetration equation (4.6.6) the following expression for jet penetration is found:

$$y_{jet} = \frac{Q_{situ}}{v_c \cdot W} = \frac{P_{jet}}{\eta \cdot E_{sp} \cdot v_c \cdot W} \tag{4.6.8}$$

Substituting equation (4.6.7) in equation (4.6.8) yields the following equation:

$$y_{jet} = \frac{P_{jet} \cdot k_m}{\eta \cdot c_1 \cdot \rho_w \cdot g \cdot h_i \cdot \epsilon \cdot v_c \cdot v_c \cdot W} = \frac{P_{jet} \cdot k_m}{\eta \cdot c_1 \cdot \rho_w \cdot g \cdot h_i \cdot \epsilon \cdot v_c^2 \cdot W} \tag{4.6.9}$$

The power of a water jet is defined as the jet pressure times the jet flow, or:

$$P_{jet} = p_{jet} \cdot Q_{jet} \tag{4.6.10}$$

The jet flow can be defined as follows:

$$Q_{jet} = \alpha \cdot n_{jet} \cdot A_{jet} \cdot u_{out} \tag{4.6.11}$$

In equation (4.6.11) α is the contraction coefficient, n_{jet} is the number of heel jets, A_{jet} is the area of a nozzle (usually $\frac{\pi}{4} \cdot D^2$) and u_{out} is the exit velocity of the jet water.
In paragraph 4.3 it was shown that the jet exit velocity can be approximated as follows:

$$u_{out} \approx \sqrt{\frac{2 \cdot p_{jet}}{\rho_w}} \tag{4.6.12}$$

Substituting equation (4.6.12) in equation (4.6.11) yields the following expression:

$$Q_{jet} = \alpha \cdot n_{jet} \cdot A_{jet} \cdot \sqrt{\frac{2 \cdot p_{jet}}{\rho_w}} \tag{4.6.13}$$

Equation (4.6.13) is now substituted in equation (4.6.10):

$$P_{jet} = p_{jet} \cdot \alpha \cdot n_{jet} \cdot A_{jet} \cdot \sqrt{\frac{2 \cdot p_{jet}}{\rho_w}} \tag{4.6.14}$$

Now equation (4.6.14) can be substituted in equation (4.6.9) to get a new expression for y_{jet}:

$$y_{jet} = \frac{p_{jet} \cdot \alpha \cdot n_{jet} \cdot A_{jet} \cdot \sqrt{\frac{2 \cdot p_{jet}}{\rho_w}} \cdot k_m}{\eta \cdot c_1 \cdot \rho_w \cdot g \cdot h_i \cdot \epsilon \cdot v_c^2 \cdot W} \tag{4.6.15}$$

Assuming that the initial cut height in equation (4.6.15) is equal to the jet penetration yields the following equation:

$$y_{jet} = \frac{p_{jet} \cdot \alpha \cdot n_{jet} \cdot A_{jet} \cdot \sqrt{\frac{2 \cdot p_{jet}}{\rho_w}} \cdot k_m}{\eta \cdot c_1 \cdot \rho_w \cdot g \cdot y_{jet} \cdot \epsilon \cdot v_c^2 \cdot W} \tag{4.6.16}$$

This can be rewritten as follows:

$$y_{jet}^2 = \frac{p_{jet} \cdot \alpha \cdot n_{jet} \cdot A_{jet} \cdot \sqrt{\frac{2 \cdot p_{jet}}{\rho_w}} \cdot k_m}{\eta \cdot c_1 \cdot \rho_w \cdot g \cdot \epsilon \cdot v_c^2 \cdot W} \tag{4.6.17}$$

Now taking the square root of equation (4.6.17) yields the final equation for jet penetration based on specific energy:

$$y_{jet} = \sqrt{\frac{p_{jet} \cdot \alpha \cdot n_{jet} \cdot A_{jet} \cdot \sqrt{\frac{2 \cdot p_{jet}}{\rho_w}} \cdot k_m}{\eta \cdot c_1 \cdot \rho_w \cdot g \cdot \epsilon \cdot v_c^2 \cdot W}} \tag{4.6.18}$$

The advantage of this equation is that there are multiple inputs regarding the jets as well as soil mechanical inputs. Hence, the influences of these inputs on the jet penetration are clearly visible. Both an advantage and a disadvantage is the great amount of parameters in the equation. On one hand this gives the user the freedom to specify the inputs to preference, on the other hand one might actually prefer as few inputs as possible for the sake of simplicity.
In an attempt to further simplify equation (4.6.18) certain parameters can be replaced by a coefficient by assuming standard values for these parameters. The two most obvious standard values are the one for the gravitational constant g ($9.81 m/s^2$) and the density of seawater ρ_w ($1025 kg/m^3$). Standard values can also be assumed for the contraction coefficient α (0.82), the factor for converting the specific cutting energy to specific jetting energy η (order of magnitude is 0.7) and the dilatation ϵ (order of magnitude is 0.16). The Wild Dragon draghead has a width of $2.7m$ and 10 heel jets. This leads to a ratio of jets per meter of roughly 3.7. The last step is to assume that all jets are circular so that A_{jet} can be replaced by $\frac{\pi}{4} \cdot D^2$. The replacing coefficient is now calculated as follows:

$$C = \frac{\alpha \cdot n_{jet} \cdot \frac{\pi}{4} \cdot \sqrt{\frac{2}{\rho_w}}}{\eta \cdot c_1 \cdot \rho_w \cdot g \cdot \epsilon \cdot W} = \frac{0.82 \cdot 3.7 \cdot \frac{\pi}{4} \cdot \sqrt{\frac{2}{1025}}}{0.7 \cdot 0.45 \cdot 1025 \cdot 9.81 \cdot 0.16} = 2.079 \cdot 10^{-4} \tag{4.6.19}$$

Applying the coefficient from (4.6.19) to equation (4.6.18) leads to the following expression for the jet penetration y_{jet}:

$$y_{jet} = \sqrt{2.079 \cdot 10^{-4} \frac{p_{jet} \cdot D_{jet}^2 \cdot \sqrt{p_{jet}} \cdot k_m}{v_c^2}} = (2.079 \cdot 10^{-4} \cdot p_{jet} \cdot D_{jet}^2 \cdot p_{jet}^{\frac{1}{2}} \cdot v_c^{-2})^{\frac{1}{2}} \tag{4.6.20}$$

Equation (4.6.20) can be further simplified to the following equation:

$$y_{jet} = 0.0144 \cdot p_{jet}^{0.75} \cdot D_{jet} \cdot k_m^{0.5} \cdot v_c^{-1} \tag{4.6.21}$$

Equation (4.6.21) greatly resembles the C.S.B. equation (4.5.1). Both consist of a coefficient, a jet pressure, a nozzle diameter and a trailing speed. The powers of the pressure are 0.75 for the specific energy method and 0.59 for the C.S.B. equation, hence they are in the same order of magnitude. The same holds for the powers of the permeability with 0.5 for the specific energy method and 0.369 for the C.S.B. equation. The powers of the trailing speed are identical with -1. The biggest difference in power is seen at the nozzle diameters with 1 for the specific energy method and 0.49 for the C.S.B. equation, which is roughly the difference between D and $\sqrt{D}$. At first sight it looks if the coefficient in front of the equations also differs greatly with 0.0144 for the specific energy method and 291 for the C.S.B. equation. However, the specific energy method uses SI units whereas the C.S.B. equation

mostly uses non-SI metric units (respectively $MPa, mm, cm/s$ and m/s). When the coefficient of the C.S.B. equation is compensated for the difference in units, including the one of y_{jet}, the coefficient is 0.0215 whereas the coefficient of the specific energy method is 0.0144. Which makes them of the same order of magnitude. The difference might (partially) be explained by the fact that the C.S.B. equation is developed to predict jet penetration for a single jet while the specific energy method predicts jet penetration for a row of equally spaced jets.

4.7 Comparison of Vlasblom, C.S.B. and specific energy equations

At first sight the jet penetration equations of Vlasblom, C.S.B and the specific energy method might look quite different. However, when the Vlasblom equation (equation (4.3.8)) is slightly altered, many similarities can be found. For this comparison the equation of Weegenaar is just considered to be the Vlasblom equation with another coefficient.
From paragraph 4.3 it can be found that the jet penetration depth can be defined as follows.

$$y_{jet} = \frac{\alpha \cdot n_{jet} \cdot \rho_w \cdot Q_{jet} \cdot \sqrt{\frac{2 \cdot p_{jet}}{\rho_w}}}{\rho_{quartz} \cdot (1 - n_i) \cdot W \cdot v_c} \tag{4.7.1}$$

In this equation Q_{jet} can also be written as follows.

$$Q_{jet} = A_{jet} \cdot u_0 = \frac{\pi}{4} \cdot D_n^2 \cdot u_0 = \frac{\pi}{4} \cdot D_n^2 \cdot \sqrt{\frac{2 \cdot p_{jet}}{\rho_w}} \tag{4.7.2}$$

Substituting equation (4.7.2) in equation (4.7.1) will yield the following equation.

$$y_{jet} = \frac{\alpha \cdot n_{jet} \cdot \rho_w \cdot \frac{\pi}{4} \cdot D_n^2 \cdot \sqrt{\frac{2 \cdot p_{jet}}{\rho_w}} \cdot \sqrt{\frac{2 \cdot p_{jet}}{\rho_w}}}{\rho_{quartz} \cdot (1 - n_i) \cdot W \cdot v_c} = \frac{2 \cdot \alpha \cdot n_{jet} \cdot \frac{\pi}{4} \cdot D_n^2 \cdot p_{jet}}{\rho_{quartz} \cdot (1 - n_i) \cdot W \cdot v_c} \tag{4.7.3}$$

Now if all parameters except for the nozzle diameter D_n, the jet pressure p_{jet} and the trailing speed v_c would be combined into a coefficient C then equation (4.7.3) would look as follows.

$$y_{jet} = C \cdot p_{jet} \cdot D_n^2 \cdot v_c^{-1} \tag{4.7.4}$$

The equation of C.S.B. from paragraph 4.5 is written in the following form.

$$y_{jet} = C \cdot p_{jet}^{0.59} \cdot D_n^{0.49} \cdot k^{0.369} \cdot v_c^{-1} \tag{4.7.5}$$

The specific energy jet penetration equation from paragraph 4.6 is written in the following form.

$$y_{jet} = C \cdot p_{jet}^{0.75} \cdot D_n \cdot k^{0.5} \cdot v_c^{-1} \tag{4.7.6}$$

The most obvious difference between equations (4.7.4) to (4.7.6) is that the Vlasblom equations seems to lack a permeability term. In paragraph 4.3 it was however discussed that the influence of permeability was already incorporated in coefficient α, which is now incorporated in coefficient C.
The other differences that can be found are the differences in power for the parameters p_{jet}, k and D_n. The powers of the jet pressure and the permeability differ in a relatively small range, respectively

between 0.59 and 1 and 0.369 and 0.5. However, the power of the nozzle diameter ranges from 0.49 to 2 or almost $\sqrt{D_n}$ to D_n^2. This looks if especially the C.S.B. and the Vlasblom equation contradict each other. It can however be shown that this is not necessarily the case.
The process of fluidizing a sand bed using water jets can be seen as forcing the sand bed to dilate using water jets. Dilatation is the increase of pore volume of soil and can be expressed as a factor of increase in terms of initial and maximum porosities.

$$\epsilon = \frac{n_{max} - n_i}{1 - n_{max}} \tag{4.7.7}$$

To increase a certain volume of soil V with ϵ times that volume means that a volume of water of $V \cdot \epsilon$ has to flow into the volume of soil. This means that for a moving jet the flow of the jet can be defined as follows.

$$Q_{jet} = W \cdot y_{jet} \cdot v_c \cdot \epsilon \tag{4.7.8}$$

In equation 4.7.8 W is the width of the liquefied volume, y_{jet} is the height of the liquefied volume and v_c is the speed at which the jet is moving.
Since it was shown in equation (4.3.5) that the jet exit velocity can be regarded as only dependent on the jet pressure (and the density of water) it can be shown that jet flow is linearly dependent on the jet nozzle area, which can be written as follows.

$$Q_{jet} = A_{jet} \cdot u_{out} = \frac{\pi}{4} \cdot D_n^2 \cdot u_{out} \tag{4.7.9}$$

Now assuming that the jet pressure and water density are constant means that the jet exit velocity is constant which means that the jet flow is solely dependent on the nozzle diameter D_n. In other words, the jet flow Q_{jet} is proportionate to D_n^2.

$$Q_{jet} \propto D_n^2 \tag{4.7.10}$$

Alternatively this can be written as follows.

$$D_n^2 \propto W \cdot y_{jet} \cdot v_c \cdot \epsilon \tag{4.7.11}$$

Since v_c and ϵ are assumed to be constant it means that D_n^2 is proportionate to $W \cdot y_{jet}$. This can be expressed as follows.

$$y_{jet} \propto D_n^{\alpha_1} \tag{4.7.12}$$

$$W \propto D_n^{\alpha_2} \tag{4.7.13}$$

In which the sum of the exponents α_1 and α_2 must equal the exponent of D_n.

$$\alpha_1 + \alpha_2 = 2 \tag{4.7.14}$$

In equation (4.7.5), the C.S.B. equation, it can be seen that y_{jet} is proportional to $D_n^{0.49}$ hence α_1 is equal to 0.49. This means that α_2 is equal to 1.51. What this physically means is that an increase in jet flow would lead to a greater increase of the width of the jetted area than to the depth of the jetted

area.
In the Vlasblom equation, equation (4.7.4), y_{jet} is proportional to D_n^2. Hence, α_1 is equal to 2 and α_2 is equal to zero. Physically this means that an increase in jet flow would only lead to an increase of the depth of the jetted area.
In equation (4.7.6), the specific energy equation, y_{jet} is proportional to D_n hence both α_1 and α_2 are equal to 1. Physically this means that an increase in jet flow leads to an equal increase of depth and width of the jetted area.
All three equations describe a different development of the jetted area. Especially the two extreme cases, the C.S.B. and the Vlasblom equation do not seem to describe the same jetting process at all. This does however not mean that one of the two equations is wrong. It must be kept in mind that the C.S.B. equation describes jet penetration for a single jet, whilst the Vlasblom equation describes jet penetration for a row of jets.
It might very well be possible that the jetted area increases more sideways that downwards for an increasing jet flow. This might even be true for jets placed in a row, as long as the jetted areas of the jets do not touch each other. When the jetted areas start to touch each other it becomes impossible for the jetted areas to expand sideways (with exception of the two outer jets, but this is neglected), which means that the expansion can only go in one way, which is downwards. This is the situation as described by the Vlasblom equation.
The C.S.B equation and the Vlasblom equation describe jet penetration for two different situations. The first situation is when the jetted areas do not touch each other whilst the other situation is when the jetted areas do touch each other. Which equation describes the jet penetration best for a given set of parameters is hence dependent on whether the jetted areas touch each other, which is dependent on the spacing of the jets. If the spacing is such that the jetted areas do not touch, then the C.S.B. equation might described jet penetration best. If the spacing is so close that the jetted areas do touch, then the Vlasblom equation might describe the jet penetration best. When it is not known whether the jetted areas do or do not touch for a certain spacing then the specific energy equation might give a reasonable estimate of the jet penetration. However, dependent on whether the jetted areas do or do not touch the use of the specific energy equation always underestimates or overestimates the jet penetration.

5 Modeling the Draghead

5.1 Introduction

In this chapter the way the draghead is modeled in the production model is described. To do this, first the main features of the Wild Dragon draghead are discussed. Not all of these features have eventually been modeled though.
The next paragraph will cover the simplifications that have been made to some of the draghead components in order to model them. After this it is described which draghead geometry is actually needed and how this is modeled in the production model.
The paragraph after this describes how the draghead geometry is converted to a suitable input for the cutting model.
The last paragraph explains how the geometry data can be obtained from technical drawings.

5.2 Draghead features

In this paragraph the most important parts of a draghead are discussed. The function of each part is discussed as well as whether the function or properties of the part have to be modeled in the production model. As was mentioned before, the Wild Dragon draghead is used as an example.

5.2.1 Helmet

The helmet (see figure 2.7) can be considered the basis of the draghead. It is the part that connects to the lower suction arm and hence holds the opening where the slurry will enter the dredge pump system. The helmet is also the part on which the visor hinges and one of two parts to which a visor actuator (a hydraulic cylinder in the case of the Wild Dragon) is connected. Furthermore the heel jets are mounted underneath the helmet.
As mentioned before the helmet is a kind of basis on which (moving) parts are mounted. In the production model the helmet has a similar function. On the helmet the origin of a coordinate system will be defined. All positions of other parts, like the heel jets and the visor actuator will be related to this origin, as will be explained in section 5.4.1. The actual geometry of the helmet does however not matter that much with the exception of the lower arm angle since an other than default lower arm angle changes the orientation of the draghead.
The other exception is the vertical distance between the lower part of the heel pads and the origin. Since it is assumed that the bottom of the heel pads coincides with the soil surface, the vertical distance between the bottom of the heel and the origin also relates the position of the soil surface to the origin.

5.2.2 Visor

The visor (see figure 5.1 and 2.7) is the part of the draghead in which the cutting teeth are mounted. It is attached to the helmet using hinges, meaning that the visor can rotate with respect to the helmet.

The force to rotate the visor can be provided by several kinds of actuators: The weight of the visor, a spring or as with the Wild Dragon draghead a hydraulic cylinder. Rotating the visor changes the blade angle and slice thickness and hence the required cutting force. However, the visor can also be fixed to the helmet.
Important points in the geometry of the visor are the point where an actuator attaches to the visor and the point(s) where the teeth are mounted. Furthermore there are vents for water and nozzles for water jets present in the visor. However, both of these provide water to create a slurry and are assumed not to take part in the actual cutting process (see 2.6.4 for more information) hence their actual position is not important. When the visor is actuated by its self-weight, the position of the center of gravity of the visor is also important to know.

Figure 5.1: A side view of a real Wild Dragon extended visor

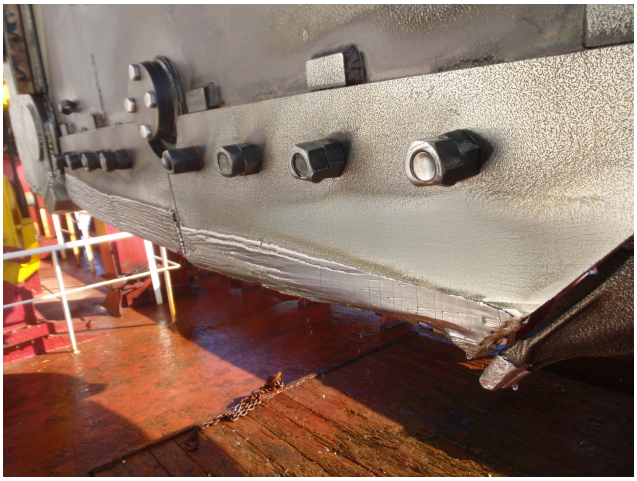

Figure 5.2: The side plates of a draghead with wear due to sand clearly visible

5.2.3 Teeth

As was mentioned in the previous section, the teeth are mounted in the visor and are used to cut the soil. The teeth of a draghead are usually changeable and come in different shapes and sizes. When cutting sand, flared chisels are usually used (see figure 5.3). In the case of the Wild Dragon draghead the flared chisels are equipped with jet nozzles.
In figure 5.3 it can be seen that a tooth has a rather complex shape. It is therefore needed to simplify the geometry. The simplifications are described in paragraph 5.3. After simplification only the position of the tip and the position of the top of the tooth with respect to a reference point are needed to define inputs for the production model like blade height and blade angle. Other important properties of the teeth are the number of teeth and the width of a tooth or alternatively only the combined width of the teeth.

5.2.4 Heel jets

The heel jet nozzles are incorporated in the heel pads, which are mounted underneath the helmet (see figure 5.4). The water jets from these nozzles shoot down into the soil. This liquefies the soil, making it easier to cut for the blades.
The position of the heel jets on the helmet can be important since rotating the helmet decreases the effective penetration depth of the jet. The penetration depth of the heel jets is calculated using the

Figure 5.3: The inside of a visor equipped with MEC screening. Behind the MEC screening a water port is visible. Furthermore the visor jets and tooth jets are clearly visible

Figure 5.4: The heel jet blocks of a Wild Dragon draghead

theories described in chapter 4. To use these theories other properties of the heel jets are important like: the nozzle diameter, the number of nozzles, the jet pressure and the jet flow.

5.2.5 Tooth jets

The nozzles of the tooth jets are incorporated in the chisel-shaped teeth of the Wild Dragon draghead. The tooth jets were designed to reduce the required cutting force during the cutting of very densely packed sands and stiff clays.
The influence of the tooth jets on the cutting forces are calculated using the model described in paragraph 3.5. Important input properties for this model are the position of the nozzle with respect to the tip of the blade, the nozzle diameter, the number of nozzles, the jet pressure and the jet flow.

5.2.6 Visor jets

The nozzles of the visor jets are mounted inside the visor and are aimed at the position where the cut soil slice is during cutting (see figure 5.3). The visor jets do not directly take part in the cutting process. Instead they help slurryfying the cut soil slice and dilute the sand-water mixture making it easier to transport.

Since the visor jets do not directly take part in the cutting process their position is not of much importance for the model. However, data of the visor jets is used during tooth jet pressure calculations since their flow contributed to the total jet flow of the system. Hence, the nozzle diameter is of importance as well as the number of nozzles, the jet pressure and the jet flow. The latter is also of importance for the slurry concentration calculations.

5.2.7 Water ports

Visor vents are located in the back of the visor (see figure 5.3). They can manually be (partially) opened or closed to regulate the flow of water into the draghead. The visor vents basically have the same function as the visor jets: eroding the cut soil slice into a slurry and diluting the sand-water mixture. Furthermore the water ports help to regulate the pressure in the visor.
Just like the visor jets, visor vents do not directly take part in the cutting process. Therefore their actual position is not of importance for the production calculation. The size of the vents (area) is important since this is needed to calculate the total flow into the draghead, which is needed for the slurry concentration calculations. This is if the vents are assumed to be open.

5.2.8 Visor actuator

Actuators are installed on dragheads to counteract the part of the cutting forces that try to push the cutting teeth out of the soil. This is done to ensure a more or less constant production per trailing speed. The actuator pushes against the visor since this is where the cutting teeth are mounted in.
The dragheads that Great Lakes uses are equipped with different actuators: hydraulic cylinders, springs, (self-) weight, fixed. As mentioned before the Wild Dragon draghead is equipped with a hydraulic cylinder. Also mentioned before is that it is important to know the position where the actuator attaches to the visor and the helmet. Furthermore the operating pressure of the cylinder and the diameter of the cylinder are important to calculate the force of the cylinder.
For dragheads that have a spring as actuator it is also important to know the positions where the spring is attached to the visor and the helmet. To calculate the spring force the spring constant and pre-tension must be known.
A visor that is actuated by its own weight is called a floating visor. With a floating visor the visor is free to rotate during cutting. Sometimes weight is added to the visor for a greater reaction force. For this actuation mechanism there is no real actuator, hence there are no attachment positions. For a floating visor it is important to know the center of gravity of the visor (possibly combined with weights) as well as the mass of the visor (and weights).
For all aforementioned actuators it is important to find out what limits the visor rotation angles. This could be just the maximum rotation angle of the visor but the rotation could also be limited by a maximum stroke of the cylinder in case of a hydraulic cylinder. Floating visors are sometimes restricted in rotation angle by using a buffer bar. Using this bar the highest and lowest rotation angle of the visor can be set. In such a case the visor is called a fixed-float visor.
A visor that is fixed at a certain angle is not really actuated. Therefore no information is needed except for the angle at which the visor is fixed.

5.2.9 Turtle exclusion device

When sea turtles, an endangered species, are present near a job site the use of a turtle exclusion device (TED) may be required to prevent the draghead from sucking in the turtles. The TED is mounted

on the front of the draghead and acts as a plow that pushes a layer of soil sideways (both to the left and right). These sand waves push any sea turtles that might be on the bottom to the side, out of the dragheads way. Hence, there is no direct contact between the draghead and the turtle.
When the draghead is modeled with a TED the cutting force of the TED is calculated by using the theory described in paragraph A.2. Therefore information about the geometry of the TED like the tilt angle, the wedge angle, the width and the penetration depth are needed. However, the TED cutting does still not directly take place in the 'production' cutting process since it is assumed that it does not interfere with the moment balance. Therefore the actual position of the TED with respect to the origin is not of importance and is not modeled.

5.2.10 MEC screening

When dredging in an area where there is a risk to dredge up ammunition or explosives MEC (Munitions and Explosives of Concern) screens are installed in the visor. These screens are grate-like structures with slots of usually 1.25 by 6 inches, which prevent ammunition or explosives from entering the draghead. The screening does also prevent other objects, like pebbles or shells, from entering the draghead. These objects can get stuck in the screening, hence regular flushing and clearing of the screening is required. The MEC screening does not take part in the cutting process but might take part in the slurry concentration calculation since the screening reduces the inflow area of the visor. This area is reduced even more when the screening is clogged up with objects, which might has to be taken into account when doing the slurry concentration calculations.

5.3 Simplifications

In the previous paragraph the most important features and functions of parts of a draghead were discussed. Some of these parts are somehow incorporated in the production model. This also means that a draghead already has been simplified to a small group of components with certain functions. However, for these components even more assumptions and simplification have to be made in order to have a draghead model that is simple enough to incorporate in the production model.
In the following sections the assumptions and simplifications are listed per main component.

5.3.1 Blade

One of the most important simplifications in the production model is that the cutting teeth are not modeled separately. Instead a whole row of teeth is modeled as a single blade. In the case of the Wild Dragon draghead this means that a row of 19 teeth is modeled as a blade with a blade length equal to the tooth length and a width which is equal to the width of the inside of the draghead. The latter is also a simplification since the spacing between the teeth and the spacing between the teeth and the sides of the visor are included in this width. The two aforementioned simplification likely contribute to an overestimation of the cutting force because of two reasons. The first reason is that the width of the blade is bigger than the combined width of the teeth. The second reason is that the spacing between the teeth allows water to flow to the dilatation zone which reduced the pore pressures and hence the cutting force. Since this is not modeled, the calculated cutting force is likely too large.
The blade is assumed to be flat, smooth and without wear. In reality a cutting tooth has a different shape at the top compared to the bottom and possibly has a jet nozzle built-in. Cutting teeth are restored by having a wear-layer welded onto them, which is typically not very smooth. Furthermore the tip of a tooth is usually rounded instead of sharp, due to wear.

5.3.2 Nozzles

All water jet nozzles are assumed to be without wear and are assumed to have the same contraction coefficient. In reality the nozzles can wear out due to abrasive particles in the jet water or due to cavitation. However, not all nozzles (of one type) wear out at the same rate. This leads to nozzles having different 'diameters' and contraction coefficients which leads to different flows per nozzle of the same type. The different flows per jet, especially for the tooth and heel jets, can lead to an uneven production over the width of the draghead. However, since the nozzles are assumed to be without wear this is not taken into account in the production model.

5.3.3 Heel

In figures of dragheads (like figure 2.6) it can be seen that when the heel is horizontal both lower edges of the heel are in one line. Since it is assumed that the horizontal heel is in contact with the soil surface this means that the vertical distance between either of the edges and a horizontal reference line is equal to the distance between the soil surface and that reference line.
This changes when the heel is no longer horizontal due to a rotation of the helmet. The distance between one of the edges and the reference line has increased while the distance between the other edge and the reference line has decreased. This makes it unclear what the distance between the soil surface and the reference line now is. Therefore the heel is simplified to a point that lies at a certain distance directly below the visor hinge when the heel is horizontal. This point is assumed to coincide with the soil surface even if the helmet rotates.

5.3.4 Moving parts

All moving parts of the draghead, including the draghead itself (through the water) are assumed to be frictionless. This means that the visor hinges are assumed to be frictionless, the hinges of actuators are frictionless and the actuators themselves are also frictionless. The friction of water running past the draghead is also neglected since the drag force due to this phenomenon is negligible compared to the cutting forces. The only exceptions concerning friction are the teeth and the helmet when cutting (or bulldozing) the soil since there the friction is used in the cutting force calculations. The friction on the side cutting plates (see figure 5.2) is neglected. Nor are these parts taken into account when doing cutting force calculation. This is because their width is very small compare to the total draghead width.

5.4 Draghead geometry

In this paragraph the way the draghead geometry is captured and used in the production model is discussed. With the term 'draghead geometry', the important points of the blades and the actuators that where identified in paragraph 5.2 are meant. To do this first the frame of reference and important angles are discussed.

5.4.1 Frame of reference

Before the position of any important point can be defined and calculations can be done there is a need for a frame of reference. The frame of reference for the draghead geometry is a two-dimensional

Cartesian coordinate system or rectangular coordinate system. The origin of this coordinate system is located in the center of the hinge point of the visor and the helmet and hence moves with the same speed (the trailing speed) in the same horizontal direction as the draghead (assuming that there is no draghead movement in vertical direction). Although the origin moves along with the helmet, it is not fully fixed to the helmet. When the angle of the helmet changes by changing the lower arm angle (see section 5.4.3), the orgin does not follow the rotation of the helmet but stays at the same angle. Hence, rotation-wise the origin is fixed to the reference system of the surroundings (earth). The positive x-direction is chosen to be on the left of the origin. The reason for this is that the majority of important points lie on the left of the origin in technical drawings since in most drawings the visor is drawn left of the helmet. The positive y-direction is upwards because the visor moving up corresponds with a positive visor angle (see section 5.4.4).

5.4.2 Polar coordinates

In the previous section it was explained that the frame of reference for draghead geometry is a Cartesian coordinate system. Such a coordinate system makes it easy to calculate horizontal and vertical distances between points and hence makes it very suitable for moment arm calculations and slice thickness calculations (see chapter 6). However, all important points that were identified in paragraph 5.2 can move with respect to the origin in a rotational fashion during the production calculation. This rotational movement of the important points is hard to describe using Cartesian coordinates. Therefore another coordinate system is used when the geometry is loaded in the model and when the rotational movements are applied: polar coordinates.

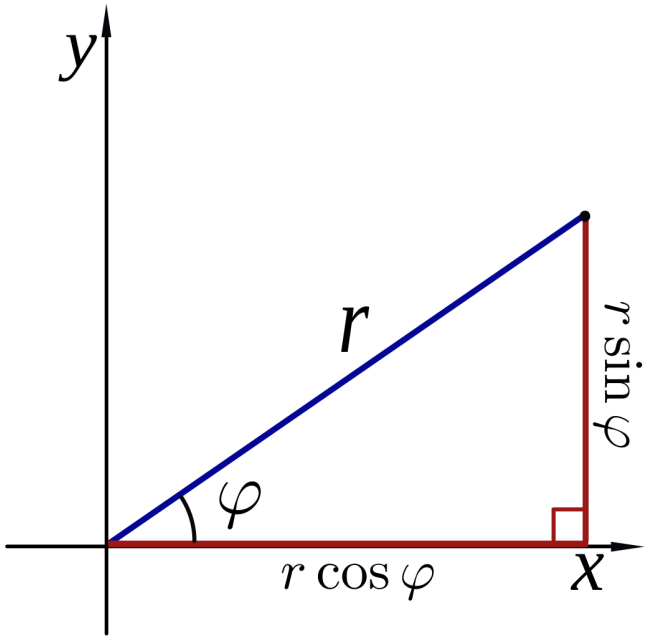

Figure 5.5: Conversion of polar coordinates to Cartesian coordinates (wikimedia.org)

In the polar coordinate system the 'origin' is called a pole. The pole is located at the same position as the origin of the Cartesian system: the hinge point of the visor and the helmet. A point in the coordinate system is defined by two coordinates, a radius (r) and an azimuth (ϕ) as is shown in figure 5.5. The radius is the distance between the pole and a point in a straight line. The azimuth is the angle between this line and a reference line. For the production model this reference line is always a horizontal or vertical line and is usually chosen in such a way that the azimuth is an acute angle. An

acute angle is preferred because these angles are usually easier to measure when using CAD software. Since he main reference system of the production model is a Cartesian coordinate system, polar coordinates have to be converted to Cartesian coordinates. This is done by the following equations:

$$x = r \cdot cos(\phi) \tag{5.4.1}$$

$$y = r \cdot sin(\phi) \tag{5.4.2}$$

The main advantage of using polar coordinates to describe the position of important points is that since all points rotate around the pole, a change of position is described by a change in the azimuth. When a point with radius r and azimuth ϕ rotates over an angle $\Delta\phi$ in positive direction, the new Cartesian coordinates are simply defined as follows:

$$x_{new} = r \cdot cos(\phi + \Delta\phi) \tag{5.4.3}$$

$$y_{new} = r \cdot sin(\phi + \Delta\phi) \tag{5.4.4}$$

It might seem that during the development of the draghead model the choice was made to place the pole of the polar coordinate system at the same location as the origin of the Cartesian coordinate system. It is however the other way around. Placing the pole of the polar coordinate system in the visor hinge point has the advantage that all important points can be described using polar coordinates since their movement is purely rotational around this point. It therefore makes sense to also place the origin of the Cartesian coordinate system in this point so that after conversion, described by equations (5.4.1) to (5.4.4), there is no need for another translation step.

5.4.3 Lower arm angle

In the draghead production model the lower arm angle is **not** the angle that the lower part of the drag arm makes with the horizontal plane. Instead it is the angle over which the lower arm has rotated from the standard position (see figure 5.6). Since the lower arm is rigidly connected to the helmet, the helmet will have rotated over the same angle. Therefore the standard position is defined as the position of the helmet for which the heel pads are 'flat on the ground' or the position of the helmet for which the heel jets shoot straight down. This position is usually, but not always, the position in which the helmet is drawn in technical drawings.
The definition of the lower arm angle might be confusing at first but it is defined this way in order to standardize the geometry inputs of different dragheads. This is because a lower arm angle (Γ) of zero now means the standard position of the helmet. The standard position of the helmet together with the standard angle of the visor (see section 5.4.4) is the position of the draghead that is used as input position of the draghead. This means that the polar coordinates of important points are measured in this position when the input data for the production model is gathered.
To know how much the lower arm has rotated from the standard or in other words, to know the lower arm angle, there is still need for a reference. This reference lower arm angle, denoted with Γ_0, is the angle that the lower arm makes with the horizontal plane when the draghead is in standard position. In reality the lower arm angle changes with dredging depth, but since a drag arm consists of two parts that both can rotate, the lower arm and the upper arm, it is hard to predict the lower arm angle based

on the dredging depth. Furthermore, the lower arm angle is also dependent on the draft of the ship. For these reasons the lower arm angle has to be assumed and hence is still an input in the production model instead of being directly calculated based on the dredging depth. A situation for which the lower arm angle does not have to be assumed is when a TED is used during dredging because then the lower arm is fixed at a certain (prescribed) angle.

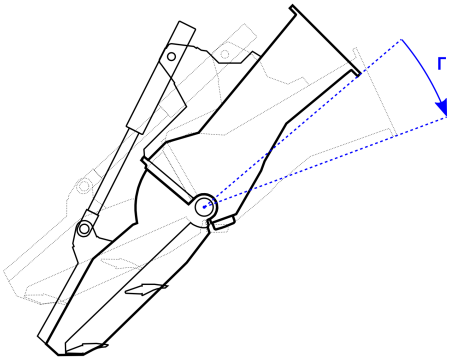

Figure 5.6: Draghead with nonzero lower arm angle. The standard position is indicated in grey and the positive rotational direction is indicated by the blue arrow

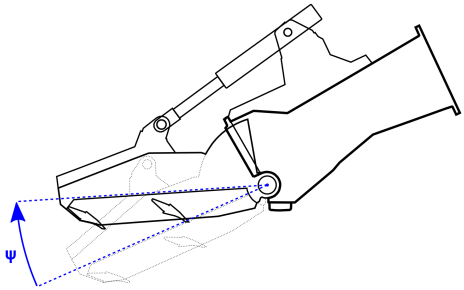

Figure 5.7: Draghead with nonzero visor angle. The standard position is indicated in grey and the positive rotational direction is indicated by the blue arrow

5.4.4 Visor angle

The visor angle is one of the most important concepts in the production model. Many of the important points that were defined in paragraph 5.2 are located on the visor. Hence, when the visor rotates, these points will rotate with it and thus change position. Change in position of the important points means a change in a lot of things including change in blade angle, blade height and slice thickness. This means that the cutting force and production will change.
In the production model the visor angle is denoted with Ψ and is defined as the angle over which the visor has rotated from the lowest possible visor orientation (see figure 5.7). The lowest possible visor orientation is defined as the orientation for which the visor is mechanically limited in downward movement. When the visor is in this orientation and the helmet (or lower arm) is in the standard position, then the visor angle Ψ is equal to zero.
In upward movement the visor is also mechanically limited. The maximum angle over which the visor can rotate, starting from the lowest orientation, is denoted Ψ_{max}.
With respect to the helmet the visor can rotate in a range of 0 to Ψ_{max} degrees, this is the standard visor angle range. The visor angle does however not necessarily have to lie within this range since this is dependent on the lower arm angle. If the lower arm angle is not equal to zero then the standard visor angle range has to be compensated.
When the lower arm angle is Γ degrees (or radians) and positive, meaning that the helmet has rotated over Γ degrees (or radians) in the same direction as what is positive for the visor then the compensated visor range becomes as follows.

$$\begin{aligned} &\text{Standard: } 0 \text{ to } \Psi_{max} \\ &\text{Compensated: } 0 + \Gamma \text{ to } \Psi_{max} + \Gamma = \Gamma \text{ to } \Psi_{max} + \Gamma \end{aligned} \tag{5.4.5}$$

When the lower arm angle is Γ degrees (or radians) and negative, meaning that the helmet has rotated over Γ degrees (or radians) in the opposite direction as what is positive for the visor then the compensated visor range becomes as follows.

$$\begin{aligned} &\text{Standard: } 0 \text{ to } \Psi_{max} \\ &\text{Compensated: } 0-\Gamma \text{ to } \Psi_{max}-\Gamma = -\Gamma \text{ to } \Psi_{max}-\Gamma \end{aligned} \tag{5.4.6}$$

Equations (5.4.5) and (5.4.6) show that the magnitude of the visor angle range does not change but that the boundaries of the range simply shift. Theoretically this means that the maximum slice thickness possible is dependent on the lower arm angle since the lower boundary of the visor angle range can only be controlled by changing the lower arm angle.

5.4.5 Actuator points

From the important points that were identified in paragraph 5.2 three points can be regarded actuator points. These points are the actuator attachment points on the visor, the helmet and the center of gravity of the visor, since the weight of the visor can also actuate the visor.
In this section it is shown how the polar coordinates of the actuator points are defined. Important to note is that the draghead is in standard position ($\Psi = 0$ and $\Gamma = 0$), hence the polar coordinates defined in this section are the inputs for the production model. The first point is the point where the

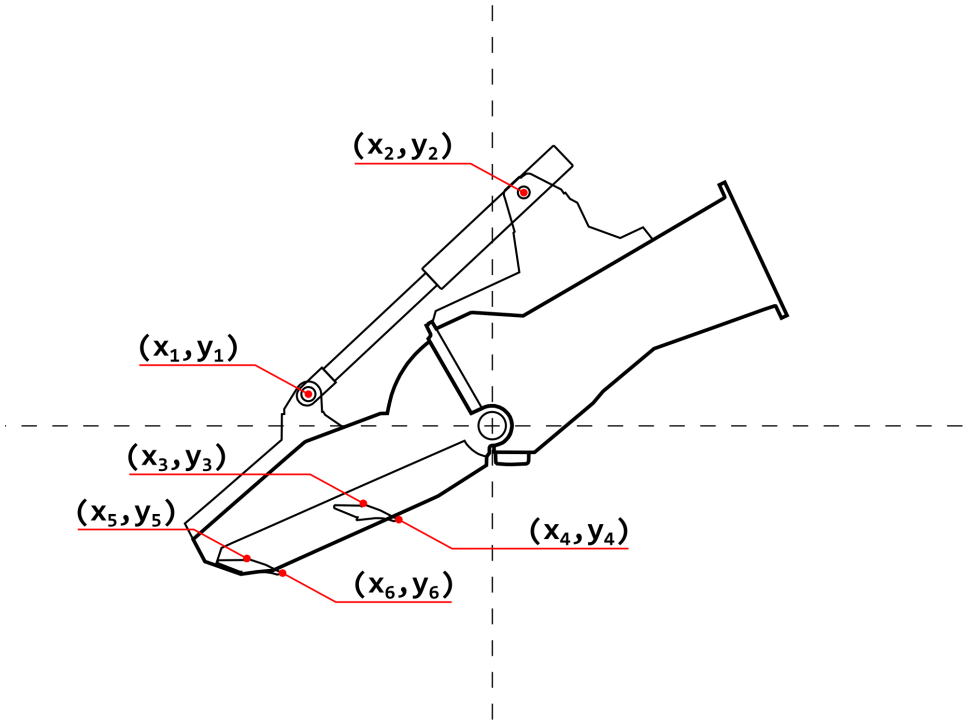

Figure 5.8: The important points of a draghead in Cartesian coordinates

actuator attaches to the visor (x_1,y_1), see figure 5.8. The radius r_1 is defined as the distance between the center of the visor hinge (the origin or pole) and the center of the actuator attachment point of the visor (since this point is also a hinge). Since an acute angle is preferred (see section 5.4.2) the reference line is chosen to be the horizontal line and the positive rotation direction is counterclockwise. This definition makes the azimuth $\angle r_1$ negative for this draghead but that is not a problem.

Using the polar coordinate conversion equations (5.4.1) to (5.4.4) the Cartesian coordinates of the visor actuator attachment point can be defined.

$$x_1 = r_1 \cdot cos(-\angle r_1 + \Psi) \tag{5.4.7}$$

$$y_1 = r_1 \cdot sin(-\angle r_1 + \Psi) \tag{5.4.8}$$

The minus sign of $\angle r_1$ is due to the definition of the positive angle. The Ψ accounts for the movement of the visor out of standard position.
The second point is the point where the actuator attaches to the helmet, see figure 5.8. The radius r_2 is defined as the distance between the pole (the center of the visor hinge) and the center of the actuator attachment point of the helmet, which is also a hinge. Again an acute angle is preferred, therefore the reference line is chosen to be a vertical line through the origin and the positive rotation direction is counterclockwise. This definition makes the azimuth $\angle r_2$ negative for the Wild Dragon draghead, but this is not an issue.
Using the polar coordinate conversion equations the Cartesian coordinates of the actuator attachment point of the helmet are defined as follows.

$$x_2 = r_2 \cdot sin(\angle r_2 + \Gamma) \tag{5.4.9}$$

$$y_2 = r_2 \cdot cos(\angle r_2 + \Gamma) \tag{5.4.10}$$

Since this point is not located on the visor it is not dependent on the visor angle Ψ. However, since this point is located on the helmet, which is attached to the lower part of the suction arm, it is dependent on the lower arm angle Γ. Which is the movement of the helmet/lower suction arm out of the standard position.
The last actuator point is the center of gravity of the visor. The polar coordinates of the center of gravity are defined in the same way as the polar coordinates of the visor actuator attachment point. The reference line is again a horizontal line through the origin and the positive angle for the azimuth $\angle r_g$ is counterclockwise. The radius is named r_g and is defined as the distance between the center of the visor hinge and the center of gravity of the visor. The center of gravity of the visor might often not be indicated in drawings and might have to be located using 3D CAD software.
Using the polar coordinate conversion equations the Cartesian coordinates of the visor center of gravity are defined as follows.

$$x_g = r_g \cdot cos(-\angle r_g + \Psi) \tag{5.4.11}$$

$$y_g = r_g \cdot sin(-\angle r_g + \Psi) \tag{5.4.12}$$

Again,the minus sign of $\angle r_g$ is due to the definition of the positive angle and the Ψ accounts for the movement of the visor out of standard position.
How the actuator points are used to calculate the actuator moments is explained in paragraph 2.6.3. How these calculations are done in Python can be found in Appendix D.

5.4.6 Blade points

The important points that were identified in paragraph 5.2 which are not related to actuator attachments are all related to the blades of the draghead. These points are the tips and tops of the blades. In this section it is shown how the polar coordinates of the tips and tops of the blade are defined. Important to note is that the draghead is in standard position ($\Psi = 0$ and $\Gamma = 0$), hence the polar coordinates defined in this section are the inputs for the production model.

For all blade points the same reference line for the azimuth is used, a horizontal line through the center of the visor hinge. In case of two blades blade 1 is the blade closest to the visor hinge and blade 2 the furthest from the visor hinge. The radius of the top of blade 1, r_3, is defined as the distance between the center of the visor hinge and the top of blade 1. The radius of the tip of blade 1 r_4 is similarly defined, the distance between the center of the visor hinge and the tip of blade 1. For both azimuths holds that the positive rotation direction is counterclockwise. Using the polar coordinate equations the Cartesian coordinates of the top of blade 1 can be defined.

$$x_3 = r_3 \cdot cos(\angle r_3 - \Psi) \tag{5.4.13}$$

$$y_3 = r_3 \cdot sin(\angle r_3 - \Psi) \tag{5.4.14}$$

The same can be done for the tip of blade 1.

$$x_4 = r_4 \cdot cos(\angle r_4 - \Psi) \tag{5.4.15}$$

$$y_4 = r_4 \cdot sin(\angle r_4 - \Psi) \tag{5.4.16}$$

If a second blade is present the radii and azimuths are defined in the same way as for blade 1. The Cartesian coordinates for the top of blade 2 are then defined as follows.

$$x_5 = r_5 \cdot cos(\angle r_5 - \Psi) \tag{5.4.17}$$

$$y_5 = r_5 \cdot sin(\angle r_5 - \Psi) \tag{5.4.18}$$

The same can be done for the tip of blade 2.

$$x_6 = r_6 \cdot cos(\angle r_6 - \Psi) \tag{5.4.19}$$

$$y_6 = r_6 \cdot sin(\angle r_6 - \Psi) \tag{5.4.20}$$

5.4.7 Blade width, cylinder diameter & heel distance

Aside from the important actuator and blade points described in the previous sections there are a number of other geometry parameters that are vital for the production model to operate.
The first of these parameters is the blade width W. As was explained in section 5.3.1 the blade width is chosen to be equal to the width of the draghead since the difference between the width of a row of cutting teeth and the width of the draghead is small. This might lead to situations where the words blade width and draghead width are used interchangeably.
The second parameter is the diameter of the hydraulic cylinder $D_{Cylinder}$. With the name 'cylinder diameter' actually the internal diameter of the hydraulic cylinder is meant. However, the diameter of the piston rod is nearly the same and and is usually easier to measure, therefore it could also be used for $D_{Cylinder}$.
The previous two parameters can be measured in drawings regardless of the position the draghead is drawn in. For the last parameter, the heel distance r_{heel}, it is required that the draghead is drawn in the standard position since it would change for changing lower arm angles. The standard position was explained in section 5.4.3. As was mentioned before, the heel distance is defined as the vertical distance between the horizontal axis and the bottom of the heel pad.

5.5 Cutting model inputs

In order to calculate cutting forces using the theory described in chapter 3 a number of inputs are needed that are related to the geometry of the draghead, or more specifically the geometry of the blade. Of these inputs, the blade width is straightforward since it was assumed to be equal to the width of the draghead. Other inputs are the blade height, the blade length and the blade angle. These inputs are not directly measured but are calculated using the blade points that are described in section 5.4.6.
The blade height is simply defined as the difference in vertical position between the tip and the top of the blade. This is described for blade 1 and blade 2 as follows.

$$h_{b1} = y_4 - y_3 = r_4 \cdot sin(\angle r_4 - \Psi) - r_3 \cdot sin(\angle r_3 - \Psi) \tag{5.5.1}$$

$$h_{b2} = y_6 - y_5 = r_6 \cdot sin(\angle r_6 - \Psi) - r_5 \cdot sin(\angle r_5 - \Psi) \tag{5.5.2}$$

The blade length L_{Blade} can be calculated using the Pythagorean theorem. The differences in vertical and horizontal position between the tip and top of a blade are squared, then added together and then the square root is taken. This is demonstrated for both blades in the following equations.

$$\begin{aligned} L_{Blade1} &= \sqrt{(x_3 - x_4)^2 + (y_4 - y_3)^2} \\ &= \sqrt{(r_3 \cdot cos(\angle r_3 - \Psi) - r_4 \cdot cos(\angle r_4 - \Psi))^2 + (r_4 \cdot sin(\angle r_4 - \Psi) - r_3 \cdot sin(\angle r_3 - \Psi))^2} \end{aligned} \tag{5.5.3}$$

$$\begin{aligned} L_{Blade2} &= \sqrt{(x_5 - x_6)^2 + (y_6 - y_5)^2} \\ &= \sqrt{(r_5 \cdot cos(\angle r_5 - \Psi) - r_6 \cdot cos(\angle r_6 - \Psi))^2 + (r_6 \cdot sin(\angle r_6 - \Psi) - r_5 \cdot sin(\angle r_5 - \Psi))^2} \end{aligned} \tag{5.5.4}$$

The blade angle α is calculated by dividing the vertical distance between the tip and the top of a blade by the horizontal distance between the tip and tip and then taking the arc tangent of that division.

$$\alpha_{Blade1} = arctan\left(\frac{y_4 - y_3}{x_3 - x_4}\right) = arctan\left(\frac{r_4 \cdot sin(\angle r_4 - \Psi) - r_3 \cdot sin(\angle r_3 - \Psi)}{r_3 \cdot cos(\angle r_3 - \Psi) - r_4 \cdot cos(\angle r_4 - \Psi)}\right) \tag{5.5.5}$$

$$\alpha_{Blade2} = arctan\left(\frac{y_6 - y_5}{x_5 - x_6}\right) = arctan\left(\frac{r_6 \cdot sin(\angle r_6 - \Psi) - r_5 \cdot sin(\angle r_5 - \Psi)}{r_5 \cdot cos(\angle r_5 - \Psi) - r_6 \cdot cos(\angle r_6 - \Psi)}\right) \tag{5.5.6}$$

5.6 Obtaining the draghead geometry

In paragraph 5.4 it was explained that in order to model a draghead in the production model, a number of geometry parameters are required. These parameters are azimuths and radii of the blade and actuator points, the heel distance and the cylinder diameter.
At the moment of writing the easiest and probably only method to obtain these parameters is to measure them in a drawing. This drawing can simply be a 2D (CAD) drawing or a 3D CAD drawing. However, taking the measurements from a 2D drawing is probably the preferred method since this eliminates the risk of measurement errors due to accidentally measuring distances in three instead of two dimensions.
When measuring the azimuths it must be kept in mind that all but the azimuth $\angle r_2$ use the horizontal axis as the reference line. The aforementioned azimuth uses the vertical line as a reference line. It must also be noted that an angle in counterclockwise direction is regarded positive and that an angle in clockwise direction is negative.
When measuring the radii, the cylinder diameter or the heel distance it must be kept in mind that all are distances and that their position with respect to the origin does not matter. This means that all these parameters are positive.
The last important note for taking measurements is that the draghead in the drawing is in standard position. This means that the visor must be in the lowest possible position ($\Psi = 0$) and that the lower arm angle is zero ($\Gamma = 0$).
All the required geometry inputs are shown in figure 5.9, as well as the coordinate axes.

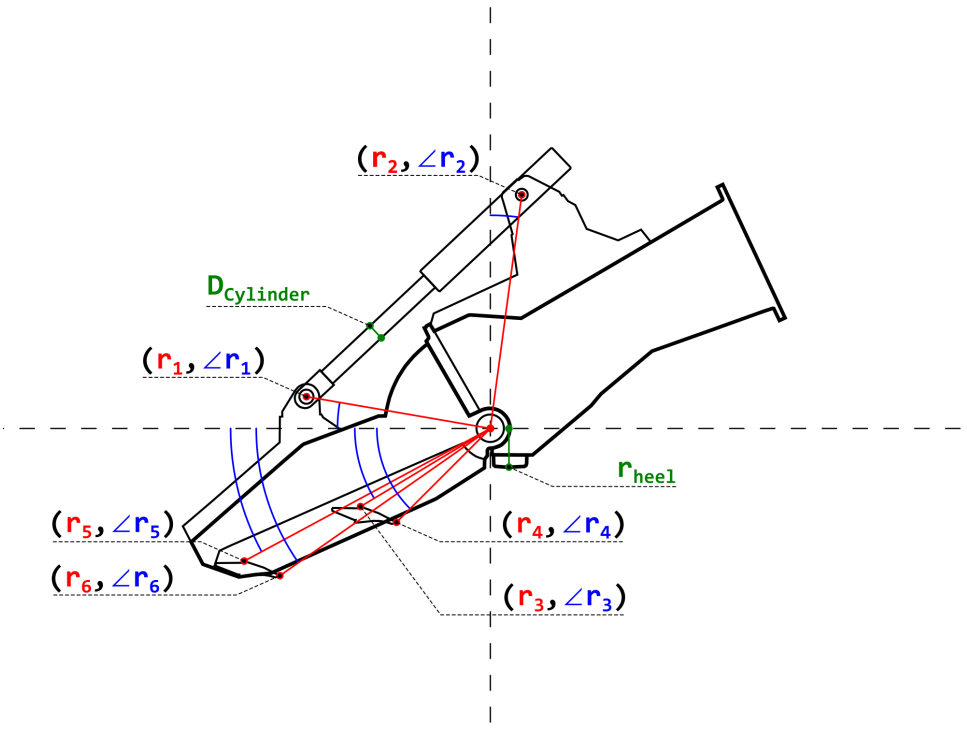

Figure 5.9: The radii (red), azimuths (blue) and distances (green) that are required to model a draghead

6 Implementation of the Theory

6.1 Introduction

In this chapter the implementation of the previously discussed theories into the draghead production model is covered. First it is discussed which actuator moments are actually required to be implemented into the model. After this the controls that can alter the behavior of the production model are discussed.
The seven paragraphs that follow describe the actual steps that the production model in Python follows to come to a production and a concentration. Regarding these steps, a visual aid is provided in the form of a flowchart in appendix G. The last paragraph discusses the possible limits to the production, these have however not been implemented.
Possible ways of implementing the bulldozing effect and cutting with a turtle exclusion device have also been described. Both of these have however not been implemented in the Python code that has been used to generate the results shown in chapter 7. Therefore the possible implementation of the bulldozing effect and cutting with a TED can be found in appendix H.

6.2 Selection of actuator moments

In section 2.6.3 it was shown that there are four possible moments that oppose the moment caused by the cutting forces: a moment of a hydraulic cylinder, a moment caused by a spring, a moment due to the weight of the visor and a moment due to the pressure difference between the inside and the outside of the visor.
In the production model the Wild Dragon draghead is modeled. This draghead does not have a spring actuator and thus that moment is not modeled. Instead the Wild Dragon has a hydraulic cylinder and thus this moment will be modeled. Whether the moment due to the visor weight and the moment due to the pressure difference will also be taken into account dependents on the order of magnitude compared to the moment of the hydraulic cylinder. As a reference the cylinder moment is calculated at a visor angle and a lower arm angle of zero degrees ($\Psi = 0$ and $\Gamma = 0$). The geometry used is the geometry of the Wild Dragon draghead with extended visor and is summarized in section 7.3.3. The pressure used is $25 \cdot 10^5 Pa$. Using the aforementioned conditions and the equations of section 2.6.3 lead to a calculated moment of the hydraulic cylinder of $31416 Nm$.
For the moment due to the visor weight the mass of the visor must be known. This mass was found in a technical drawing and is $5575 kg$. The location of the center of gravity was not found an is therefore estimated to lie on the polar coordinates (1.10, 20.0°). Assuming the same visor angle and lower arm angle and using the equations described in section 2.6.3 leads to a calculated visor weight moment of $21324 Nm$. Since this moment is in the same order of magnitude as the moment of the hydraulic cylinder it cannot be neglected and must therefore be present in the moment balance.
For the moment due to the pressure difference an average suction arm flow of $2.83 m^3/s$ was chosen. An open area below the visor of $2.64 m^2$ was found in technical drawings. Using the equations of section 2.6.3 this lead to an average flow speed of $1.07 m/s$ which leads to a rather small pressure difference of $587 Pa$. Judging by technical drawings the area on which the pressure acts is roughly 2.629 by 1.5 meters which lead to an A_{top} of $3.94 m^2$. This leads to a force of roughly $2313 N$. Assuming a moment arm of 1.5 meters then leads to a moment of roughly $3470 Nm$. This moment is about 6.5

percent of that of the cylinder moment and the weight moment combined. Due to the geometry in the equations in the cylinder moment and the weight moment both moments will only increase for visor angles greater then zero. Meanwhile the pressure difference moment is assumed to be constant. This means that the influence of the pressure moment with respect to the other two moments will only decrease for increasing visor angles. For this reason, together with the fact that the contribution of the pressure moment is roughly 6.1 percent of the total moment at a visor angle of zero degrees, the influence of the pressure difference will be neglected in the moment balance.
The moments that play a role in the moment balance are thus the hydraulic cylinder moment, the visor weight moment and the cutting moment.

6.3 Calculation controls

Since the production will be plotted for a range of trailing speeds, the starting velocity v_{start}, the end velocity v_{end} and the size of the trailing speed increment v_{step} must be defined. These three parameters are the inputs for the for-loop in which all production calculations are performed. The unit of the trailing speed is meters per second (m/s).
Two other important inputs to control the calculations are the starting angle of the visor *StartAngle* and the option whether the visor angle resets to *StartAngle* for every increment of the trailing speed. The starting angle of the visor must be a number between 0 and Ψ_{max} (see section 5.4.4 for more information on the visor angle). The option to reset the visor angle after a trailing speed increment is called *ResetAngle* and can be either *True* or *False*. Both $VisorAngle$ and *ResetAngle* were added to the calculation controls because for certain combinations of trailing speed, soil parameters and equipment parameters multiple visor angles and hence multiple productions can be found for which equilibrium exists between the actuator moment and the cutting moment. This means that the visor angle, or production, calculated at a certain trailing speed can be dependent on the visor angle of the previous trailing speed. In other words, the production can be dependent on the history of the visor angle. The angle *StartAngle* hence defines the visor angle at the beginning of the trailing speed loop. If *ResetAngle* is *True*, then the visor angle is reset to *StartAngle* for every increment of the trailing speed and thus the new calculations start at this angle again. When *ResetAngle* is *False* then the new calculations will start at the visor angle of the previous trailing speed. What toggling *ResetAngle* basically does is switching between two different operational approaches. When *ResetAngle* is *True*, the graphs show the production per trailing speed as if the TSHD would trail at that speed and then lower the dragheads (with a certain visor angle) onto the seabed. When *ResetAngle* is *False*, the graphs show the course of the production when the TSHD lowers the dragheads (with a certain angle) onto the seabed at a low trailing speed and then very slowly increases the trailing speed.
The remaining two important inputs are $Heel\_ON$ and $Tooth\_ON$. These two inputs can be either *True* or *False* and can toggle the heel jets and tooth jets active or inactive.

6.4 Preparatory calculations

Before a loop can be started in which the production per trailing speed is calculated first a number of parameters must be calculated which will remain constant in the loop. Some of these calculations are conversions from degrees to radians. The other calculations are the hydraulic force of the cylinder and the dilatation of the sand package.

6.4.1 Convert degrees to radians

The angles that are inputs for the production model are in degrees. The reason for this is simply that angles in degrees tend to appeal more to the imagination than angles expressed in radians. However, the trigonometric functions in Python only function with angles in radians. Hence there is need for a conversion. This conversion is simply multiplying the number in degrees with $2\pi/360$ but can also be done in Python by using the *radians()* function.
The angles that have to be converted can be split up in three categories, the soil parameters, draghead geometry and operational parameters. The soil parameters are the angle of internal friction ϕ and the angle of external friction δ. The draghead geometry angles are all azimuths of the polar coordinates (see paragraph 5.4) with the exception of the maximum visor angle Ψ_{max}. For a draghead with two rows of teeth these azimuths are $\angle r_1$, $\angle r_2$, $\angle r_3$, $\angle r_4$, $\angle r_5$, $\angle r_6$ and $\angle r_g$. The operational parameter that has to be converted is the lower arm angle Γ.

6.4.2 Calculate the dilatation

The cutting forces in the production model are calculated using the cutting model for water saturated sand of Miedema (see paragraph 3.3). One of the inputs for this cutting model is the dilatation of the sand package ϵ. In the production model the dilatation is calculated using the initial porosity n_i and the maximum porosity n_{max} in the following equation.

$$\epsilon = \frac{n_{max} - n_i}{1 - n_{max}} \tag{6.4.1}$$

6.4.3 Calculate the hydraulic cylinder force

In the production model one of the actuators of the modeled draghead is a hydraulic cylinder. Hence the force exerted by the hydraulic cylinder must be calculated in order to calculate the contribution of the hydraulic cylinder to the total actuator moment.
As was explained in section 2.6.3 the force of the hydraulic cylinder is calculated by multiplying the pressure in the hydraulic cylinder with the area of the piston. This can be written as follows.

$$F_{cylinder} = p_{cylinder} \cdot A_{cylinder} = p_{cylinder} \cdot \frac{\pi}{4} \cdot D^2_{cylinder} \tag{6.4.2}$$

In equation (6.4.2) the pressure in the cylinder $P_{cylinder}$ is in Pascals (Pa) and the piston diameter $D_{cylinder}$ is in meters (m).

The hydraulic cylinder force is the last input that is calculated before the for-loop is started in which the trailing speed is varied between v_{start} and v_{end} with a step size of v_{step}, as was explained in paragraph 6.3. All upcoming calculations will therefore take place in the trailing speed loop unless stated otherwise. This means that all upcoming calculations are shown for a single trailing speed.

6.5 Calculate jet penetration

Since the jet penetration is inversely proportional to the trailing speed, the jet penetration has to be calculated again for every increment of trailing speed. This is done using one of the equations described in chapter 4. In the model in Python the equation of Weegenaar is arbitrarily used. When the model is going to be used, research must be done to find out which jet penetration equation yields

the most realistic results.
The Weegenaar equation is defined as follows.

$$y_{jet} = \frac{\dot{M}_{total}}{\rho_{quartz} \cdot (1 - n_i) \cdot W \cdot v_c} \tag{6.5.1}$$

The assumption is made that the jet penetration is the same over the entire width W of the draghead. Another assumption is that the liquefied sand has no cutting force. Since the cutting force is needed in the moment balance this means that the jet penetration has to be known before the moments are calculated. This is why the jet penetration is the first thing calculated for every trailing speed increment.

6.6 Finding the right moment balance

In chapter 2 it was explained that the production is calculated by finding a moment balance around the visor hinge between the cutting moments and the actuator moments. When the visor angle Ψ for which a moment balance exists has been calculated then this angle Ψ can be used, in combination with the draghead geometry described in chapter 5, to calculate the total removed slice thickness and hence the production.
Mathematically this moment balance can be represented as follows.

$$\sum M_{visor} = M_{cutting} + M_{actuator} = 0 \tag{6.6.1}$$

In the production model the actuators that are used are the hydraulic cylinder and the weight of the visor. Also, for a single trailing speed both the actuator moment and the cutting moment can be expressed as a function of the visor angle Ψ. Hence, equation 6.6.1 can be rewritten as follows.

$$\sum M_{visor} = M_{cutting}(\Psi) + M_{cylinder}(\Psi) + M_{float}(\Psi) = 0 \tag{6.6.2}$$

The moment calculations, which will be described in more detail in paragraphs 6.7 and 6.8, are done multiple times for a single trailing speed because of two reasons. The first reason is that finding a moment equilibrium around the visor hinge is an iterative process. Hence, the moments are evaluated several times with (slightly) different visor angles in order to find the visor angle for which equilibrium exists.
The second reason is that under certain conditions, especially when cutting with a single blade, multiple points can be found for which equilibrium exists. This means that before the visor angle is calculated by means of iteration first the correct equilibrium point must be selected based on the conditions of *StartAngle* and *ResetAngle*.
How this is done can be explained based on the graphs of figures 6.1 and 6.2. In figure 6.1 the cutting and actuator moments at one trailing speed are plotted for a range of visor angles. Note that the cutting moment is multiplied by -1 in order to compare the magnitudes of the moments. It can be seen that the actuator moment curve and the cutting moment curve only intersect once at roughly 1.87°. However, for different cutting conditions it is possible that the curves intersect twice. Which point should be chosen then is dependent on *StartAngle*. If *StartAngle* lies right of the right-most intersection then $M_{actuator} > M_{cutting}$. This means that the hydraulic cylinder and the weight of the visor will push the visor downwards until there is a moment balance. This is also true for graphs with a single intersection like the one in figure 6.1 Hence, in that situation the point around 1.87° should be chosen.

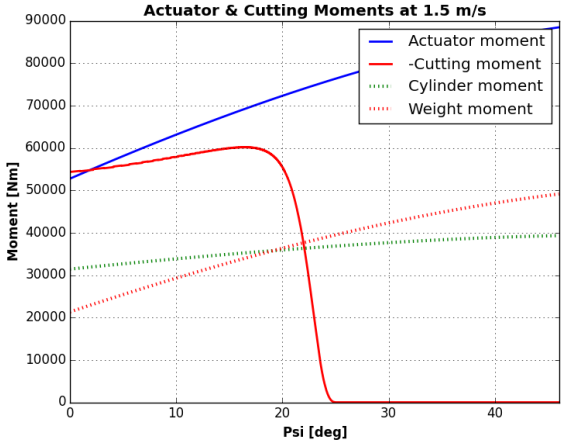

Figure 6.1: An example of cutting and actuator moments as a function of the visor angle for a draghead with a single row of teeth

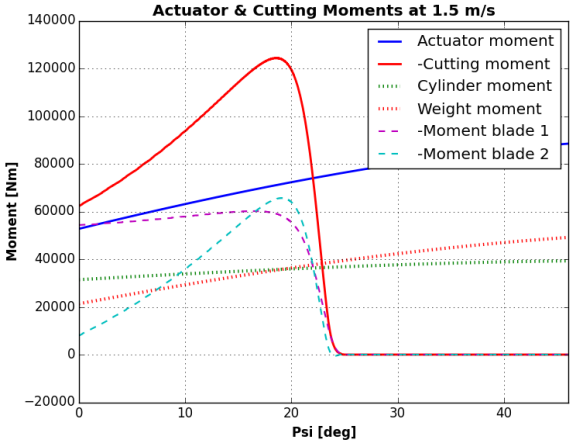

Figure 6.2: An example of cutting and actuator moments as a function of the visor angle for a draghead with a two rows of teeth

If $StartAngle$ lies between two intersections or just left of the only intersection, like in figure 6.1 it can be seen that $M_{cutting} > M_{actuator}$, which means that the visor is pushed out of the soil due to the cutting forces. In this situation again the point around 1.87° should be chosen.
If $StartAngle$ lies left of the left-most intersection in the case of two intersections then again $M_{actuator} > M_{cutting}$. This means that the hydraulic cylinder and the weight of the visor push the visor to the lowest possible visor angle. This is the angle where the visor is mechanically limited in movement (most likely due to the maximum stroke of the cylinder). In this situation the lowest possible visor angle should be chosen, which is 0° if the lower arm angle is 0°. Also, no further iteration is needed since no equilibrium between the cutting and cylinder moment would be found. What is also interesting to note is that conditions exist for which the cutting moment at low visor angles (usually $< 1°$) is negative. Since the cutting moment was multiplied by -1 this means that the real cutting moment is positive. This implies that for those conditions for small visor angles the cutting moments help the actuators to push the visor down.
In figure 6.2 it can be seen that for the shown situation there is also only one intersection of both curves. Therefore it again seems not necessary to select the right intersection. However, since different combinations of input parameters might lead to moments curves with two intersections, the process of selecting the right intersection is still maintained.
Important to note is that the cutting moment curve in figure 6.1 is identical to the moment curve of blade 1 in figure 6.2 (the purple dashed line) since both curves are plotted using the same input parameters including the same geometry of blade 1. Furthermore it can be seen in figure 6.2 that the moment curves of blade 1 and blade 2 are not much alike. This is odd since at a trailing speed of $1.5m/s$ the layer removed by the heel jets is very small. Therefore the layer thickness cut by blade 1 is more or less the same as the layer cut by blade 2. Since the blade height and blade angle of the two blades are nearly the same, more or less the same horizontal and vertical cutting force should be expected. Cutting force-wise it is therefore odd that the two moment curves are that different. However, the explanation for this can be found in the moment arms. At a visor angle of zero degrees the horizontal moment arm of blade 2 can be considered to be twice the length of the moment arm of blade 1. Hence, if the vertical cutting forces are considered to be equal then the moment due to the vertical cutting force of blade 2 is twice that of blade 1. Now if the same is considered to be true for the vertical moment arm then for identical horizontal cutting forces the cutting moment of blade 2 would be twice the cutting moment of blade 1. The cutting moment of blade 1 and 2 should then

roughly have the same shape but only with different heights. Judging from figure 6.2 this seems far from true. Part of this is because the horizontal and vertical forces of both blades are only close but not identical. The same goes for the horizontal moment arm. The difference in vertical moment arm is greater because the difference between the vertical moment arm of blade 1 and blade 2 is about one blade height. The moment arm of blade 1 is however one blade height plus the distance between the visor hinge and the seabed. Another important reason for the apparent great difference is the way the cutting moment of a blade is calculated. For positive horizontal and vertical cutting forces for one blade the two moments generated are in opposite directions. Therefore the moment due to the horizontal force is subtracted from the moment due to the vertical force as is shown in the following equation.

$$M_{Blade} = M_{vertical} - M_{horizontal} \tag{6.6.3}$$

This gives a kind of distorted view of the calculated cutting moments per blade because a horizontal and vertical moment component can be in the order of 300 kNm while the cutting moment of the blade is only about -9 kNm (300 - 309 = -9 kNm, for example). Therefore the difference between the excepted factor 2 difference between the two moments at $\Psi = 0$ and the observed difference seems worse then it actually is. Apart from the distorted view there is another and probably more important cause for the difference in shape between the graphs which is also related to the moment arms. If a line was drawn through both force acting points of the blades and the origin then the angle between that line and the horizon would be in the order of magnitude of 35°. Now if the visor angle is increased this angle gets smaller until it is zero, then both force acting points lie on the horizon. The force acting point of blade 2 lies at twice the distance from the horizon as the force acting point of blade 1, in other words, the vertical moment arm of blade 2 is twice as long as that of blade 1. Since both force acting points end up on the horizon at a visor angle of 35°, on average the decrease of the vertical moment arm of blade 2 is twice that of blade 1. However, for certain angles the decrease is even more than that of blade 1 because it is proportional to the sine of the angle. In the meanwhile the factor of 2 difference between the horizontal moment arms stays more or less the same for an increase of visor angle. For these reasons the difference between the vertical moment component and the horizontal moment component (see equation (6.6.3)) of blade 2 and thus the cutting moment of blade 2 is not twice as big as the cutting moment of blade 1 and thus the graphs do not have a similar shape.
What is also important to note is that in a situation with two intersections the visor will never move to the equilibrium at the left-most intersection. This is because when the visor starts at a visor angle left of that intersection, the actuator moment is larger than the cutting moment and hence the visor will be pushed to 0° or whatever the lowest visor angle possible might be. When the visor starts at an angle right of the intersection the cutting moment is larger than the actuator moment and hence the visor will move upwards to the angle of the right-most intersection. The only way to reach a left-most intersection is thus to start at this angle, since the visor will not move because there is equilibrium. Usually the calculations start with the visor at the lowest possible angle. This means that in practice only two visor angles are possible: the lowest possible visor angle (usually 0°) or the visor angle of the right-most intersection. This means that in practice calculations with two intersections will behave the same as calculations with one intersection.
In practice (not to be confused with reality) the visor will be in the lowest possible position starting at trailing speeds for which the entire cutting moment line is below the actuator moment line until the cutting moment at the lowest possible visor angle becomes larger than the actuator moment. Then the visor will move to the angle of the right-most intersection. Using figure 6.2 as an example, this would mean that if the visor angle was 0° for a trailing speed of $1.49 m/s$ and the red line would be below the blue line at that angle of 0° then for the increase of the speed to $1.5 m/s$ (as in the figure) the visor angle would jump to roughly 22.0°.
Logically, a change in visor angle leads to a change in cut slice thicknesses which leads to a change

in production. Since a visor in the lowest possible position yields maximum production for a given trailing speed the production at another visor angle for that same trailing speed will always be less. This means that at the trailing speed at which the transition is made from the lowest possible visor angle to another angle always a change in production increase rate (how much the in situ production increases for increasing trailing speed) can be noted. Depending on the difference between the lowest possible visor angle and the angle of equilibrium this rate can become slightly lower (small difference) to negative (large difference). A negative rate means that production actually drops for increasing trailing speed. More information on the calculation of the production increase rate can be found in Appendix I.
When the rough location of the correct intersection has been found a more precise location is found by means of iteration as was described earlier in this section.

6.7 Actuator moment calculations

As was explained before, the production model uses the Wild Dragon draghead as an example. Hence, in this case the actuators are a hydraulic cylinder and the weight of the visor as was discussed in paragraph 6.2. In the following two sections the implementation of both actuators will be discussed, starting with the hydraulic cylinder.

6.7.1 Cylinder moment calculations

In section 2.6.3 a description was given on how the moment of a hydraulic cylinder must be calculated. There the positions of the end points of the cylinder were given by the coordinates (x_1, y_1) and (x_2, y_2). In section 5.4.5 it was explained how these coordinates are described using a polar coordinate description. Below the equations from both sections are combined which will yield the equations that are actually used in the production model in Python.
First the coordinates of the attachment point of the hydraulic cylinder on the visor are calculated. Because these coordinates are also the moment arms of the actuator moments, they are denoted with r_{1h} and r_{1v} instead of x_1 and y_1.

$$r_{1h} = r_1 \cdot cos(-\angle r_1 + \Psi) \tag{6.7.1}$$

$$r_{1v} = r_1 \cdot sin(-\angle r_1 + \Psi) \tag{6.7.2}$$

The coordinates of the attachment point of the hydraulic cylinder on the helmet. These coordinates are not used for moment arms. They are however still denoted with r_{2h} and r_{2v} instead of x_2 and y_2 for the sake of uniformity.

$$r_{2h} = r_2 \cdot sin(\angle r_2 + \Gamma) \tag{6.7.3}$$

$$r_{2v} = r_2 \cdot cos(\angle r_2 + \Gamma) \tag{6.7.4}$$

The next step is to calculate the angle that the hydraulic cylinder makes with the x-axis. To do this first the distances between the horizontal and vertical coordinates are calculated.

$$L_{cylinderh} = r_{1h} - r_{2h} \tag{6.7.5}$$

$$L_{cylinderv} = r_{2v} - r_{1v} \tag{6.7.6}$$

The angle is calculated by dividing the vertical distance by the horizontal distance and taking the arc tangent of the result.

$$\alpha_{cylinder} = arctan\left(\frac{L_{cylinderv}}{L_{cylinderh}}\right) \tag{6.7.7}$$

The angle which the hydraulic cylinder makes is used to split the force of the hydraulic cylinder $F_{cylinder}$ up into a horizontal and a vertical component. The calculation of $F_{cylinder}$ is described in section 6.4.3.

$$F_{cylinderh} = F_{cylinder} \cdot cos(\alpha_{cylinder}) = F_{cylinder} \cdot cos\left(arctan\left(\frac{L_{cylinderv}}{L_{cylinderh}}\right)\right) \tag{6.7.8}$$

$$F_{cylinderv} = F_{cylinder} \cdot sin(\alpha_{cylinder}) = F_{cylinder} \cdot sin\left(arctan\left(\frac{L_{cylinderv}}{L_{cylinderh}}\right)\right) \tag{6.7.9}$$

Since the force of the cylinder is split up into two components, the total cylinder moment also consists of two moments. One moment is obtained by multiplying the vertical component of the cylinder force with the horizontal moment arm. The other moment is obtained by multiplying the horizontal component of the cylinder force with the vertical moment arm. The total cylinder moment will then look as follows.

$$M_{cylinder} = F_{cylinderv} \cdot r_{1h} + F_{cylinderh} \cdot r_{1v} \tag{6.7.10}$$

Since the moment of the hydraulic cylinder is dependent on the visor angle through equations (6.7.1) and (6.7.2), it is possible that the moment is calculated several times for a single trailing speed.

6.7.2 Visor weight moment calculations

In section 2.6.3 it was discussed how the moment due to the submerged weight of the visor can be calculated. For these calculations the mass of the visor m_{visor} must be known and the horizontal position of the center of gravity x_g (when the draghead is in the standard position, see section 5.4.3) with respect to the origin must be known. The horizontal position of the center of gravity is the horizontal and only moment arm r_{visorh} since the submerged weight is always acting downwards.
In the production model the standard position of the center of gravity is defined with the polar coordinates (r_g,$\angle r_g$). However, since the position of the center of gravity is dependent on the visor angle Ψ the expression of the horizontal position of the center of gravity and thus the horizontal moment arm is defined as follows.

$$r_{visorh} = r_g \cdot cos(\angle r_g - \Psi) \tag{6.7.11}$$

The submerged weight F_{float} (named after the floating visor) is then calculated as follows.

$$F_{float} = \frac{(\rho_{steel-\rho_w})}{\rho_{steel}} \cdot g \cdot m_{visor} \tag{6.7.12}$$

Now the moment of the visor weight can be calculated using the following equation.

$$M_{float} = F_{float} \cdot r_{visorh} \tag{6.7.13}$$

Like the moment of the hydraulic cylinder the visor weight moment is also dependent on the visor angle. Therefore it is possible that the moment is calculated several times for a single trailing speed.

6.8 Cutting moment calculations

In this paragraph the way the cutting moments are calculated in the production model are discussed. First it is discussed how the cutting calculations change as the visor moves up. After this it is discussed how the inputs needed to calculate the cutting forces are calculated. This is followed by a description of the calculation of the moment arms. Finally the calculation of the cutting moments is described.

6.8.1 Possible cutting scenarios

In paragraph 6.5 it was explained that the jet penetration varies with trailing speed and that it is assumed that there is no force required to cut liquefied sand. It has also been explained that the thickness of the slice that is cut is dependent on the visor angle. This means that for varying jet penetration and visor angles combinations exist in which a blade might not have a cutting force and hence not a cutting moment because it is only cutting liquefied sand. For a draghead with two sets of teeth, like the Wild Dragon, five different scenarios are theoretically possible. In the production model in Python these scenarios are distinguished in an if-statement. The right scenario is selected by looking at the depth of the teeth with respect to the jet penetration and by looking at the depth of the teeth with respect to each other. The first step in this process is calculating the depths of the blades $Layer_{Blade1}$ and $Layer_{Blade2}$ and the jet penetration $Layer_{jet}$.
Note that $Layer_{jet}$ is not necessarily equal to the jet penetration y_{jet}. This is because y_{jet} is perpendicular to the heel, which is part of the helmet. When the heel itself is not perpendicular to the sand bed due to a variation in the lower arm angle Γ then the jet is not perpendicular to the sand bed either and thus has to be compensated.

$$Layer_{jet} = y_{jet} \cdot cos(\Gamma) \tag{6.8.1}$$

For $Layer_{Blade1}$ and $Layer_{Blade2}$ two scenarios are possible. The first scenario is that the position of the tip of blade 1 y_4, the blade closest to the visor hinge, is lower than or as low as the position of the tip of blade 2 y_6. Using the polar coordinate description of these points from section 5.4.6 this can mathematically be expressed as follows.

$$r_4 \cdot sin(\angle r_4 - \Psi) \geq r_6 \cdot sin(\angle r_6 - \Psi) \tag{6.8.2}$$

In this scenario blade 2 is 'overshadowed' by blade 1. Hence, blade 2 is not cutting and $Layer_{Blade2}$ is set to zero.

$$Layer_{Blade2} = 0 \tag{6.8.3}$$

The layer removed by blade 1 can now be defined as follows.

$$Layer_{Blade1} = r_4 \cdot sin(\angle r_4 - \Psi) - r_{heel} \cdot cos(\Gamma) - Layer_{jet} \tag{6.8.4}$$

Note that the distance between the visor hinge (the origin) and the seabed is also dependent on the lower arm angle and hence has to be compensated for variations in the lower arm angle. The total layer thickness that is removed from the sand bed can now also be calculated since this is the distance between the heel and the tip of the lowest blade.

$$Layer_{Total} = r_4 \cdot sin(\angle r_4 - \Psi) - r_{heel} \cdot cos(\Gamma) \tag{6.8.5}$$

The other possible scenario for the blade thicknesses is that the position of the tip of blade 1 y_4, is not lower than or as low as the position of the tip of blade 2 y_6. This is mathematically expressed as follows.

$$r_4 \cdot sin(\angle r_4 - \Psi) \not\geq r_6 \cdot sin(\angle r_6 - \Psi) \tag{6.8.6}$$

In this scenario the tip of blade 2 is lower then the tip of blade one, hence the thickness of the layer removed by blade 1 can be defined as follows.

$$Layer_{Blade1} = r_4 \cdot sin(\angle r_4 - \Psi) - r_{heel} \cdot cos(\Gamma) - Layer_{jet} \tag{6.8.7}$$

Again the total layer thickness that is removed from the sand bed is defined as the distance between the heel and the tip of the lowest blade.

$$Layer_{Total} = r_6 \cdot sin(\angle r_6 - \Psi) - r_{heel} \cdot cos(\Gamma) \tag{6.8.8}$$

The layer thickness of blade 2 is now the difference between the total layer and the layer removed by blade 1 and the jet.

$$Layer_{Blade2} = Layer_{Total} - Layer_{Blade1} - Layer_{jet} \tag{6.8.9}$$

When all the layers are calculated the five different cutting scenarios can be described.

The first scenario is the scenario in which $Layer_{Total}$ is smaller than or equal to zero. In equation (6.8.5) and equation (6.8.8) it can be seen that this scenario would happen if the depth of the tip of the lowest blade (y_4 or y_6) is smaller than or equal to the distance between the sand bed and the visor hinge ($r_{heel} \cdot cos(\Gamma)$). This would mean that the blades do not penetrate the (liquefied) sand bed as is shown in figure 6.3.

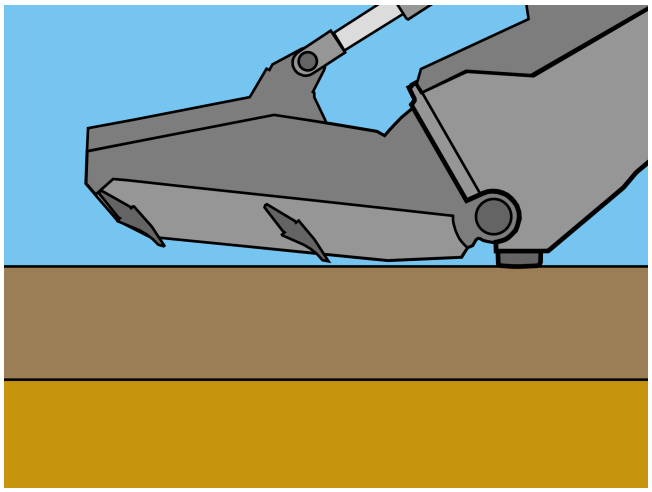

Figure 6.3: The blades of the draghead do not penetrate the liquefied layer (dark brown) nor the undisturbed soil layer (light brown)

Since both blades are not cutting any soil the horizontal and vertical cutting force for both blades is zero. This also means that the horizontal and vertical cutting moment for both blades is zero, which results in the cutting moment per blade and the total cutting moment also being zero. Below the cutting forces and moments are summarized.

- $F_{h1} = 0$
- $F_{v1} = 0$
- $F_{h2} = 0$
- $F_{v2} = 0$
- $M_{Blade1h} = 0$
- $M_{Blade1v} = 0$
- $M_{Blade2h} = 0$
- $M_{Blade2v} = 0$
- $M_{Blade1} = 0$
- $M_{Blade2} = 0$

In the second scenario $Layer_{Total}$ is smaller than or equal to $Layer_{jet}$. This means that the layer that is liquefied by the heel jets is deeper than or as deep as the tip of the lowest blade. This is shown in figure 6.4.

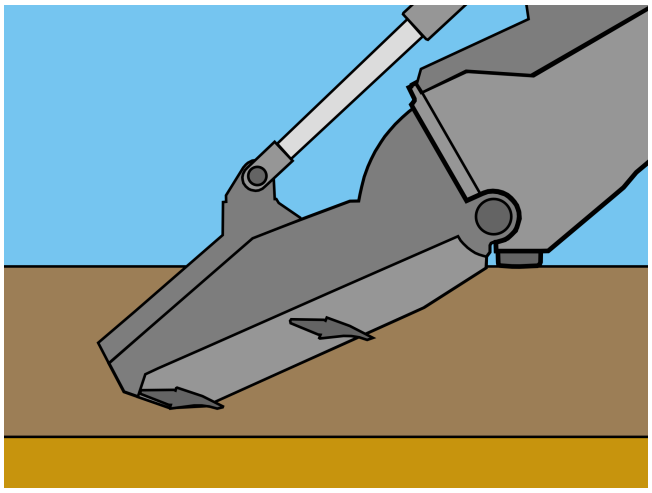

Figure 6.4: The blades of the draghead both only penetrate the liquefied layer (dark brown) and not the undisturbed soil layer (light brown)

In this scenario both blades are cutting liquefied soil. Since it was assumed that liquefied soil has no cutting force this means that all cutting forces and hence all cutting moments are zero. This is summarized again below.

- $F_{h1} = 0$
- $F_{v1} = 0$
- $F_{h2} = 0$
- $F_{v2} = 0$
- $M_{Blade1h} = 0$
- $M_{Blade1v} = 0$
- $M_{Blade2h} = 0$

- $M_{Blade2v} = 0$
- $M_{Blade1} = 0$
- $M_{Blade2} = 0$

The third scenario is the scenario in which $Layer_{Total}$ is greater than $Layer_{jet}$ and $Layer_{Blade2}$ is equal to zero. In equation (6.8.3) it was shown that $Layer_{Blade2}$ is set to zero when blade 2 is 'overshadowed' by blade 1, hence scenario 3 is the scenario in which blade 2 is overshadowed by blade 1 and blade 1 is doing all the cutting. To make sure that blade 1 is actually cutting and not only scooping up liquefied soil, the extra check of $Layer_{Total}$ being greater than $Layer_{jet}$ is added.
In figure 6.5 scenario 3 is shown. Note that the figure only demonstrates the position of the blades with respect to the layers of liquefied and undisturbed soil and not the actual cutting process since blade 2 (the left blade) would not be cutting any soil in this scenario. Since blade 2 is overshadowed,

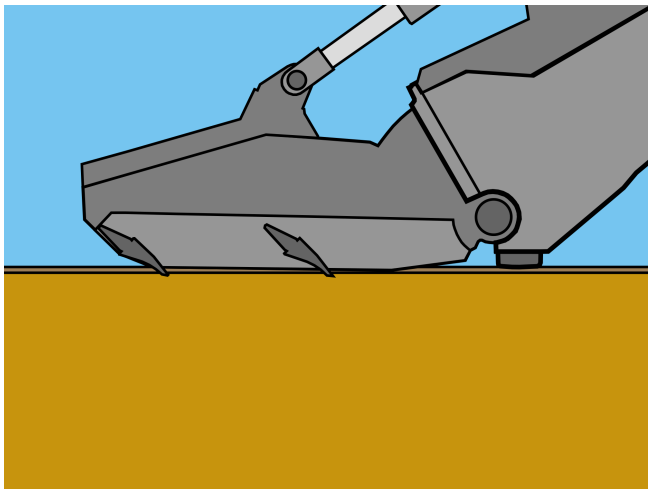

Figure 6.5: Blade 2 (left) is overshadowed by blade 1, hence only blade 1 is cutting undisturbed soil (light brown)

it has no cutting forces and no cutting moments, hence the total cutting moment of blade 2 is equal to zero. Blade 1 however is cutting undisturbed soil, hence there are cutting forces and cutting moments which makes the total cutting moment for blade 2 not equal to zero. How these cutting forces and moments are calculated is explained in the remaining sections of this paragraph. A summary of which cutting forces and moments are calculated is given below.

- $F_{h1} = Calculated$
- $F_{v1} = Calculated$
- $F_{h2} = 0$
- $F_{v2} = 0$
- $M_{Blade1h} = Calculated$
- $M_{Blade1v} = Calculated$
- $M_{Blade2h} = 0$
- $M_{Blade2v} = 0$
- $M_{Blade1} = Calculated$

- $M_{Blade2} = 0$

The fourth scenario is defined by $Layer_{Total}$ being greater than $Layer_{jet}$ and $r_4 \cdot sin(\angle r_4 - \Psi)$ being smaller than or equal to $Layer_{jet} + r_{heel} \cdot cos(\Gamma)$. The first part of this definition simply states that at least one blade is cutting undisturbed soil. The other part of the definition states that blade 1 is not cutting undisturbed soil. Together the definitions state that only blade 2 is cutting undisturbed soil. This is demonstrated in figure 6.6.

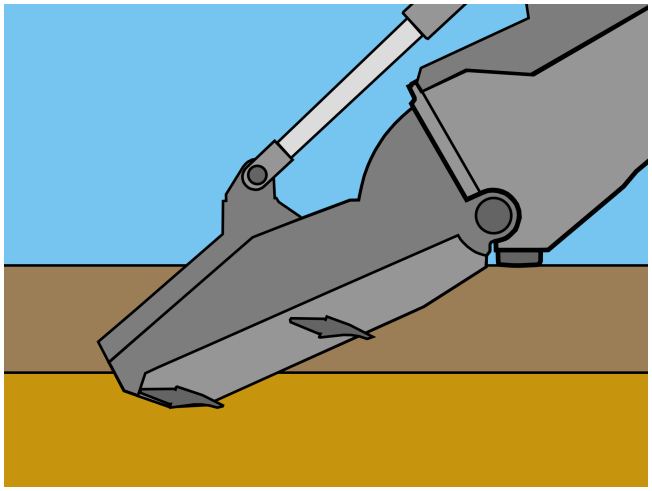

Figure 6.6: Blade 2 (left) is cutting undisturbed soil whilst blade 1 is only scooping up liquefied soil

Since blade 2 is cutting undisturbed soil, blade 2 will have a cutting force and hence cutting moments. Blade 1 is scooping up liquefied soil and hence does not have a cutting force nor cutting moments. Again this is summarized below.

- $F_{h1} = 0$
- $F_{v1} = 0$
- $F_{h2} = Calculated$
- $F_{v2} = Calculated$
- $M_{Blade1h} = 0$
- $M_{Blade1v} = 0$
- $M_{Blade2h} = Calculated$
- $M_{Blade2v} = Calculated$
- $M_{Blade1} = 0$
- $M_{Blade2} = Calculated$

The last scenario is the only possible scenario that is left. This is the scenario in which both blades are cutting undisturbed soil. This is demonstrated in figure 6.7. Since both blades are cutting undisturbed soil, both blades have cutting forces and cutting moments, these are summarized below.

- $F_{h1} = Calculated$
- $F_{v1} = Calculated$
- $F_{h2} = Calculated$

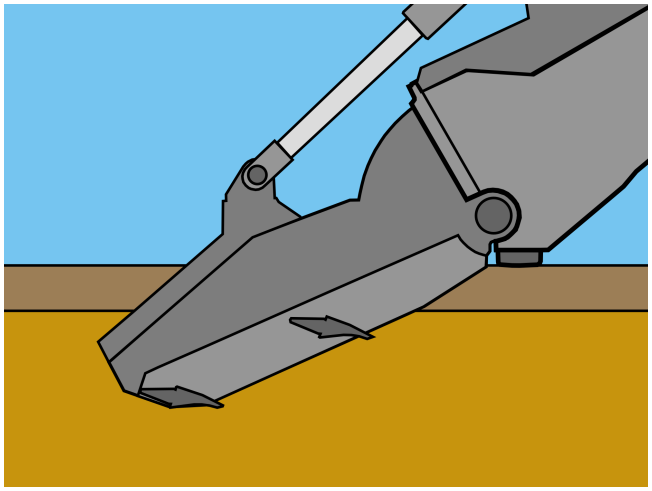

Figure 6.7: Both blades penetrate the undisturbed soil layer (light brown)

- $F_{v2} = Calculated$
- $M_{Blade1h} = Calculated$
- $M_{Blade1v} = Calculated$
- $M_{Blade2h} = Calculated$
- $M_{Blade2v} = Calculated$
- $M_{Blade1} = Calculated$
- $M_{Blade2} = Calculated$

6.8.2 Calculating cutting force inputs

In the previous section it has been established which cutting forces in which scenario have to be calculated. To calculate the cutting forces a number of inputs are needed. For the saturated cutting model and the underlying pore pressure model a number of inputs are required. These inputs are the blade angle α, the angle of external friction δ, the angle of internal friction ϕ, the initial porosity n_i, the maximum porosity n_{max}, the initial permeability k_i, the maximum permeability k_{max}, the initial cut slice thickness h_i, the blade height h_b, the water depth z and the trailing speed v_c. Of these inputs the soil parameters and the water depth remain constant during all calculations. The trailing speed is the variable that changes in the production loop since the production will be plotted per trailing speed. However, for a single production calculation, the trailing speed is constant. During a single production calculation the visor angle Ψ is varied until an equilibrium between the actuator and the cutting moments is found. Since the blades are mounted in the visor, varying the visor angle means that blade related parameters will also vary. Hence, for every variation in visor angle the blade angle α, the blade height h_b and the initial cut height h_i must be calculated. In paragraph 5.5 it was explained that the blade geometry is defined by two points, the top of the blade and the tip of the blade. For a draghead with two blades the top of the first blade has the coordinates (x_3, y_3) and the tip of the first blade has the coordinates (x_4, y_4). For the second blade the coordinates of the top and tip are respectively (x_5, y_5) and (x_6, y_6). In general the blade angle can be calculated as follows.

$$\alpha = arctan\left(\frac{y_{tip} - y_{top}}{x_{top} - x_{tip}}\right) \tag{6.8.10}$$

In the production model the coordinates of the geometry are defined in polar coordinates. Substituting the polar coordinates of the tip and the top of blade 1 for the coordinates in equation 6.8.10 will yield an expression for the angle of blade 1.

$$\alpha_{Blade1} = arctan\left(\frac{r_4 \cdot sin(\angle r_4 - \Psi) - r_3 \cdot sin(\angle r_3 - \Psi)}{r_3 \cdot cos(\angle r_3 - \Psi) - r_4 \cdot cos(\angle r_4 - \Psi)}\right) \tag{6.8.11}$$

The same can be done for blade 2, this yields the following equation.

$$\alpha_{Blade2} = arctan\left(\frac{r_6 \cdot sin(\angle r_6 - \Psi) - r_5 \cdot sin(\angle r_5 - \Psi)}{r_5 \cdot cos(\angle r_5 - \Psi) - r_6 \cdot cos(\angle r_6 - \Psi)}\right) \tag{6.8.12}$$

The blade height can simply be defined as the vertical distance between the tip and the top of the blade.

$$h_b = y_{tip} - y_{top} \tag{6.8.13}$$

Using the polar coordinates of blade 1 and 2 the blade heights are expressed as follows.

$$h_{b1} = r_4 \cdot sin(\angle r_4 - \Psi) - r_3 \cdot sin(\angle r_3 - \Psi) \tag{6.8.14}$$

$$h_{b2} = r_6 \cdot sin(\angle r_6 - \Psi) - r_5 \cdot sin(\angle r_5 - \Psi) \tag{6.8.15}$$

The initial cut heights depend on the cutting scenario. When a blade is not cutting any undisturbed soil because it is either above the soil surface or only scooping up liquefied soil, the initial cut height is zero. This means that only in scenarios 3, 4 and 5 (see section 6.8.1) the initial cut heights are non-zero.
The initial cut heights have already been calculated in order to select the right cutting scenario. These initial cut height were named $Layer_{Blade1}$ and $Layer_{Blade2}$ and their calculation can be found in the beginning of section 6.8.1. To summarize, this means that if a blade is cutting then the initial cut height for that blade is defined as follows.

$$h_{i1} = Layer_{Blade1} \tag{6.8.16}$$

$$h_{i2} = Layer_{Blade2} \tag{6.8.17}$$

When all inputs have been calculated the cutting forces can be calculated. This is described in the next section.

6.8.3 Calculating the cutting forces

The cutting forces are calculated using the theory described in paragraph 3.3. For which blade the cutting forces are required to be calculated is dependent on the cutting scenario.
The first step in all cutting force calculations is calculating the shear angle β. In the production model the equation for β in a fully cavitational situation is always used. Although cutting might not always be a (fully) cavitational process, the cavitational equation is used because it does not requires the average pore pressures p_{1m} and p_{2m}. This greatly simplifies and speeds up the iterative calculation of the shear angle since p_{1m} and p_{2m} do not have to be calculated for every iteration step. Hence, for every cutting force calculation the shear angle is found by solving the following equation.

$$\begin{aligned}\frac{\partial F_h'}{\partial \beta} =& - h_i \cdot \frac{sin(\phi) \cdot sin(\alpha + 2 \cdot \beta + \delta + \phi) \cdot sin(\alpha + \delta)}{sin^2(\beta) \cdot sin(\alpha + \beta + \delta + \phi)^2} \\ &+ h_b \cdot \frac{sin(\delta) \cdot sin(\alpha + \delta)}{sin(\alpha) \cdot sin(\alpha + \beta + \delta + \phi)^2} = 0\end{aligned} \tag{6.8.18}$$

The next step is to calculate the average pore under pressures in the shear plane and on the blade p_{1m} and p_{2m}. These calculations are described in great detail in paragraphs 3.4 to 3.6 and are therefore not repeated here. A side note to this is that if the normal cloud model is used in the production model then ξ_0 is calculated using the following equation.

$$\xi_0 = \frac{i_{cavitation}}{N} \cdot L_{max} \cdot cos(\theta_1) \tag{6.8.19}$$

In general the required inputs for these calculations are the blade angle α, the shear angle β, the initial porosity n_i, the maximum porosity n_{max}, the initial permeability k_i, the maximum permeability k_{max}, the blade height h_b, the initial cut height h_i, the water depth z and the trailing speed v_c.

Once the average pore under pressures p_{1m} and p_{2m} have been calculated the water pressure forces on the shear plane (W_1) and the blade (W_2) are calculated using the following equations.

$$W_1 = \frac{p_{1m} \cdot h_i \cdot W}{sin(\beta)} \tag{6.8.20}$$

$$W_2 = \frac{p_{2m} \cdot h_b \cdot W}{sin(\alpha)} \tag{6.8.21}$$

The resulting force on the blade is now calculated using the following equation.

$$K_2 = \frac{W_2 \cdot sin(\alpha + \beta + \phi) + W_1 \cdot sin(\phi)}{sin(\alpha + \beta + \delta + \phi)} \tag{6.8.22}$$

The resulting force K_2 is then used in the following equations to calculate the horizontal and vertical cutting forces.

$$F_h = -W_2 \cdot sin(\alpha) + K_2 \cdot sin(\alpha + \delta) \tag{6.8.23}$$

$$F_v = -W_2 \cdot cos(\alpha) + K_2 \cdot cos(\alpha + \delta) \tag{6.8.24}$$

When the cutting forces of each blade are calculated, the moment arms must be calculated in order to calculate the moments. This is described in the next section.

6.8.4 Calculating the moment arms

The moment arms that are needed to calculate the cutting moments are defined as the horizontal and vertical distances between the visor hinge (the origin) and the point on a blade on which the cutting forces act. The position of the force acting point of the blade is indicated by a fraction X_1 for blade 1 and X_2 for blade 2. Starting from the tip of the blade a force acting point lies at a distance of X times the blade length. The fractions X_1 and X_2 are calculated during the numerical pore pressure calculations, this is described in section 3.4.2.
How the horizontal and vertical moment arms are calculated is dependent on the cutting scenario. If in a certain scenario the cutting force is set to zero then the moment arm is not calculated. This means that for scenario 1 and 2 (see section 6.8.1) no moment arms are calculated. In scenario 3, only blade 1 is cutting since blade 2 is 'overshadowed'. The horizontal and vertical moment arm in this scenario can then be defined as follows.

$$r_{Blade1h} = r_4 \cdot cos(\angle r_4 - \Psi) + X_1 \cdot \frac{h_{b1}}{tan(\alpha_{Blade1})} \tag{6.8.25}$$

$$r_{Blade1v} = Layer_{Total} + r_{heel} \cdot cos(\Gamma) - X_1 \cdot h_{b1} \tag{6.8.26}$$

Note that horizontal and vertical indicate the direction of the moment arm and not the direction of the force that acts on the moment arm (these are always perpendicular in the production model).

In scenario 4, only blade 2 is cutting since blade 1 is only scooping up liquefied soil. In this scenario the horizontal and vertical moment arm can be defined as follows.

$$r_{Blade2h} = r_6 \cdot cos(\angle r_6 - \Psi) + X_2 \cdot \frac{h_{b2}}{tan(\alpha_{Blade2})} \tag{6.8.27}$$

$$r_{Blade2v} = Layer_{Total} + r_{heel} \cdot cos(\Gamma) - X_2 \cdot h_{b2} \tag{6.8.28}$$

In scenario 5, both blades are cutting. The moment arms for blade 1 are defined as follows.

$$r_{Blade1h} = r_4 \cdot cos(\angle r_4 - \Psi) + X_1 \cdot \frac{h_{b1}}{tan(\alpha_{Blade1})} \tag{6.8.29}$$

$$r_{Blade1v} = r_4 \cdot cos(\angle r_4 - \Psi) - X_1 \cdot h_{b1} \tag{6.8.30}$$

The horizontal and vertical moment arms for blade 2 are defined as follows.

$$r_{Blade2h} = r_6 \cdot cos(\angle r_6 - \Psi) + X_2 \cdot \frac{h_{b2}}{tan(\alpha_{Blade2})} \tag{6.8.31}$$

$$r_{Blade2v} = Layer_{Total} + r_{heel} \cdot cos(\Gamma) - X_2 \cdot h_{b2} \tag{6.8.32}$$

The next section will describe how the cutting moments are calculated.

6.8.5 Calculating the moments

When the cutting forces and moment arms are calculated the cutting moments can be calculated. This might happen multiple times per trailing speed since an equilibrium between the cutting moments and the actuator moment is found through iteration. Logically, the same goes for the calculation of the cutting forces and moment arms.
In section 2.6.2 the equations for the different cutting moments due to the cutting force components of blade 1 and 2 were already given but they are listed below again.
The moments due to the vertical and horizontal force components of blade 1.

$$M_{Blade1v} = F_{v1} \cdot r_{Blade1h} \tag{6.8.33}$$

$$M_{Blade1h} = -F_{h1} \cdot r_{Blade1v} \tag{6.8.34}$$

The moments due to the vertical and horizontal force components of blade 2.

$$M_{Blade2v} = F_{v2} \cdot r_{Blade2h} \tag{6.8.35}$$

$$M_{Blade2h} = -F_{h2} \cdot r_{Blade2v} \tag{6.8.36}$$

Note that the forces in equations (6.8.34) and (6.8.36) have a minus sign in front of them due to the fact that a downwards force in the cutting model is positive but a downwards movement of the visor is regarded negative.
The cutting moment per blade can now simply be calculated by adding up the two moments of a blade.

$$M_{Blade1} = M_{Blade1v} + M_{Blade1h} = F_{v1} \cdot r_{Blade1h} - F_{h1} \cdot r_{Blade1v} \tag{6.8.37}$$

$$M_{Blade2} = M_{Blade2v} + M_{Blade2h} = F_{v2} \cdot r_{Blade2h} - F_{h2} \cdot r_{Blade2v} \tag{6.8.38}$$

The total cutting moment $M_{Cutting}$ is calculated by adding the cutting moments of blade 1 and 2.

$$M_{Cutting} = M_{Blade1} + M_{Blade2} = F_{v1} \cdot r_{Blade1h} - F_{h1} \cdot r_{Blade1v} + F_{v2} \cdot r_{Blade2h} - F_{h2} \cdot r_{Blade2v} \tag{6.8.39}$$

6.9 Layer thicknesses

When the angle Ψ has been found for which there is an equilibrium between the cutting moments and the actuator moments at a certain trailing speed then the layer thicknesses that are cut must be found in order to calculate production.
Since the moment balance iteration stops at the angle for which equilibrium exists, all parameters that were used to calculate the moments for that visor angle, including layer thicknesses, have already been calculated. This means that the total layer thickness that has been cut is equal to $Layer_{Total}$, the layer thickness cut by blade 1 is equal to h_{i1} and the layer thickness cut by blade 2 is equal to h_{i2}. The layer thickness of the liquefied soil that is removed by the draghead is equal to $Layer_{Jet}$. Note that this layer is not necessarily equal to the penetration depth of the heel jets since $Layer_{Jet}$ is dependent on the blades to scoop up the liquefied soil.

6.10 Production calculations

In paragraph 1.2 the required outputs of the production model were listed. The three most important outputs are the in situ draghead production, the cut slice thickness and the resultant slurry concentration for a given mixture flow and assumed spillage. In the previous paragraph the cut slice thickness was already given. This paragraph will focus on the in situ draghead production and the resultant slurry concentration, which are also the last things calculated in the production model before the trailing speed is increased.

6.10.1 In situ production

In general the in situ production can be calculated by multiplying a cut slice thickness with a width of the cut slice and a trailing speed. In the production model the width of the cut slice is assumed to be the width of the draghead W.
The total in situ production can then be calculated as follows.

$$Production_{Total} = Layer_{Total} \cdot W \cdot v_c \tag{6.10.1}$$

Since the layer thicknesses that make up $Layer_{Total}$ are also known, partial in situ productions can also be calculated. The productions per blade for blade 1 and blade 2 are defined as follows.

$$Production_{Blade1} = h_{i1} \cdot W \cdot v_c \tag{6.10.2}$$

$$Production_{Blade2} = h_{i2} \cdot W \cdot v_c \tag{6.10.3}$$

Another partial production is the 'production' by the heel jets. This is the production due to the liquefied layer that is removed.

$$Production_{Jet} = Layer_{Jet} \cdot W \cdot v_c \tag{6.10.4}$$

As was stated before $Layer_{Jet}$ is not necessarily equal to the jet penetration. Therefore $Production_{Jet}$ is not necessarily equal to the liquefied volume of soil. This liquefied volume is calculated as follows.

$$Liquefaction_{Jet} = y_{jet} \cdot W \cdot v_c \tag{6.10.5}$$

The difference between $Production_{Jet}$ and $Liquefaction_{Jet}$ usually only exists at low trailing speeds.

6.10.2 Slurry concentration

When the total in situ production has been calculated the concentration of the slurry in the drag arm can be calculated. In section 2.6.4 multiple approaches to calculating this concentration were discussed. The approach that is implemented in the production model in Python is the approach in which a quadratic equation is solved to obtain the slurry concentration.
The quadratic equation approach assumes that there is no spillage because the flow of the dredge

pump is greater than or equal to the total flow of jet water into the draghead. This was shown with the following expression.

$$Q_{Dredge} \geq Q_{Jetwater} \tag{6.10.6}$$

In the case of the Wild Dragon draghead, the total jet water flow consists of the heel jet flows, the tooth jet flows and the visor jet flows. Hence, equation (6.10.6) can also be written as follows.

$$Q_{Dredge} \geq Q_{heel} + Q_{teeth} + Q_{visor} \tag{6.10.7}$$

In section 2.6.4 it was shown that since a range of dredge pump flows is known for a range of densities (2.97 m^3/s for a density of 1100 kg/m^3 and 2.69 m^3/s for a density of 1500 kg/m^3) the following cubic equation could be derived.

$$3.696875 \cdot C_v^3 - 0.216118 \cdot C_v^2 + 3.005875 \cdot C_v - (1 - n_i) \cdot Production_{Total} = 0 \tag{6.10.8}$$

In order to obtain the slurry concentration equation (6.10.8) must be solved. For the given coefficients only one real root exists. This root can be found by using the following third order root finding equation.

$$C_v = -\frac{1}{3a} \cdot (b + C + \frac{\Delta_0}{C}) \tag{6.10.9}$$

The equation above has been explained in section 2.6.4 and thus it will not be repeated. What is important to note is that in equation (6.10.8) $Production_{Total}$ is in SI units (m^3/s) and that it is for a single draghead.

6.11 Production limits

The production model can be run for a wide range of input parameters and trailing speeds and as long as it is mathematically possible it will yield results. However, mathematically possible does not mean that the results physically still make sense or that the operation conditions are safe.
In this paragraph some of the factors that limit the production will be discussed. None of the limits are implemented in the Python code of the model. Nevertheless the production limits are discussed in the implementation chapter so they might serve as a future reference.

6.11.1 Trailing speed

The trailing speed can be a limiting factor in a situation in which the increase of the trailing speed would lead to an increase of production. This is not always the case as will be demonstrated in chapter 7.
However, if an increase of trailing speed would lead to an increase of production and the trailing speed is not limited by the thrust of propulsion power then the trailing speed might still be limited by the operator of the dredge. This is out of safety concerns. Hitting objects (like boulders) at the sea bottom at high speeds might seriously damage the draghead or drag arm which might lead to long down times due to repair works.
For the Liberty Island the typical range of trailing speeds is between 1 and 2 knots or roughly 0.5 and 1.0 meters per second. In this report usually a larger range of trailing speeds will be shown. This is only to show a wider course of the production graph. For production estimation purposes it is more practical to set the range of trailing speeds of the model closer to the actual operation range of the dredge.

6.11.2 Thrust

In the previous section a situation was sketched in which an increase of trailing speed would lead to an increase of production but where the trailing speed and thus production were limited because of safety reasons. In this section a situation is sketched in which production would increase for increasing trailing speed but where the trailing speed cannot be increased because the thrust is already at a maximum. The production model assumes a stationary cutting process. Hence, all forces and moments are in equilibrium. Since the thrust of the dredge is a horizontal force the following equation must be true.

$$\sum F_h = 0 \tag{6.11.1}$$

In section 2.6.5 the most important horizontal forces acting on the TSHD were already identified. These forces are the thrust of the propeller T_{ship}, the horizontal cutting forces F_{h1} and F_{h2} and the resistance of the ship R_{ship}. If the draghead is bulldozing or trailing with a TED then respectively a $F_{hBulldoze}$ or F_{hTED} should also be included to the sum of the horizontal forces. Hence in the case of a bulldozing draghead the sum of the horizontal forces would be as follows.

$$\sum F_h = -T_{ship} + F_{h1} + F_{h2} + F_{hBulldoze} + R_{ship} = 0 \tag{6.11.2}$$

Equation (6.11.2) can then be rewritten as follows.

$$T_{ship} = F_{h1} + F_{h2} + F_{hBulldoze} + R_{ship} \tag{6.11.3}$$

Production at a given velocity can only exist if the trailing speed can actually be reached. In other words, the maximum deliverable thrust must be greater than or equal to the sum of the other horizontal forces. This is shown in the following equation.

$$T_{ship-max} \geq F_{h1} + F_{h2} + F_{hBulldoze} + R_{ship} \tag{6.11.4}$$

As long as equation (6.11.4) is true, production at that trailing speed can exist, given that it is not limited by another factor.

6.11.3 Propulsion power

Another thrust-related limit is a production limit due to propulsion power. In this case the trailing speed and hence the production cannot be increased because the power output of the ships engine is at a maximum. The power output of the propeller shaft is lower due to losses. If the efficiency of the propeller and the drive train is defined as η, then the power that the engine delivers can be defined as follows.

$$P_{engine} = \frac{T_{ship} \cdot v_c}{\eta} \tag{6.11.5}$$

Production at a given velocity can only exist if the trailing speed can be reached. In other words, the maximum deliverable engine power must be greater than or equal to the required engine power. This is shown in the following equation.

$$P_{engine-max} \geq \frac{T_{ship} \cdot v_c}{\eta} \tag{6.11.6}$$

For a trailing situation in which the draghead is bulldozing equation (6.11.6) can also be written as follows.

$$P_{engine-max} \geq \frac{(F_{h1} + F_{h2} + F_{hBulldoze} + R_{ship}) \cdot v_c}{\eta} \tag{6.11.7}$$

In general, as long as equation (6.11.6) is true, production at that trailing speed can exist, given that it is not limited by another factor.

6.11.4 Drag arm moment

In the production model it is assumed that the cutting process is continuous an stationary. This implies that forces and moment are in equilibrium. One of these moment equilibria is the moment equilibrium around the gimbal of the lower arm. If a moment equilibrium around this joint would not exist then in reality the lower arm angle would change until equilibrium does exist. Changing the lower arm angle changes the angle of the draghead and its position with respect to the seabed which will likely change the production. Therefore in order for production to exist for given parameters a moment balance around the gimbal joint must exist.
In section 2.6.5 the most important moments around the gimbal were defined. These moments are the moment due to the cable tension M_{cable}, the moments due to the cutting forces $M_{cutting1}$ and $M_{cutting2}$ and the moment due to the submerged weight of the draghead, drag arm and the slurry inside $M_{gravity}$. The cutting moments should not be confused with the cutting moments around the visor hinge. The moment balance is defined as follows.

$$\sum M_{gimbal} = M_{cable} + M_{cutting1} + M_{cutting2} + M_{gravity} = 0 \tag{6.11.8}$$

If the moment balance of equation (6.11.8) exists then the calculated production is valid. This is as long a no other limits are violated.

6.11.5 Cable tension

The cable tension of the cable that supports the lower suction arm can limit the production in two ways. The first way is that the tension in the cable reaches a maximum. Dependent on how this maximum is defined the cable will either snap or the operations will be stopped out of safety concerns. The other way is that a negative cable tension is calculated, which means that the cable is pushing, which is not possible.
In section 2.6.5 a rough approach was given on how to calculate the cable tension. This approach is shown in the following equation. In this equation r is the moment arm between the cable force and the gimbal.

$$F_{cable} = \frac{-M_{cutting1} - M_{cutting2} - M_{gravity}}{r} \tag{6.11.9}$$

From equation (6.11.9) the following two conditions that must be met in order to have a valid production can be defined.

$$F_{cable-max} \geq \frac{-M_{cutting1} - M_{cutting2} - M_{gravity}}{r} \tag{6.11.10}$$

$$F_{cable} > 0 \tag{6.11.11}$$

If both conditions have been met and no other limits are violated then the calculated production is valid.

6.11.6 Concentration

If it is assumed that the concentration calculated for an in situ production matches reality reasonably well then based on the concentration certain production limits can be found.
First it can be established that volume concentrations greater than one make no sense. Mathematically there might be no reasons why this cannot be calculated but physically it does not make sense. Hence, productions that result in concentrations greater than one can be considered not valid.
However, a concentration equal to one would imply that the slurry is basically pure quartz, which still does not make sense. A more reasonable approach would be to set the maximum production possible to the production associated with a concentration equal to the concentration of the bed. Since this is still a high concentration (around 60%) the best approach is to set the limit to a maximum concentration that is actually observed.

7 Results

7.1 Introduction

In this chapter the results of the draghead production model are shown in the form of a sensitivity analysis. This sensitivity analysis is roughly done in two parts. First for a Wild Dragon draghead without tooth jets and then for the same draghead with tooth jets. After both analyses the results are summarized.
In the next paragraph however, first the cutting forces calculated by the model are verified. Before the sensitivity analysis with tooth jets starts first the cutting forces with application of the tooth jets are validated.

7.2 Verification of pore pressure calculations

Before the production model is run it must be verified whether the pore pressures calculated by the pore pressure module in Python (see appendix D) are the same as the pore pressures calculated by Miedema his pore pressure model in excel. Since the cutting force calculations in the production model are dominated by the pore pressures, verifying that the calculated pore pressures are correct shows that the major part of the cutting force calculations is done correctly. Any errors in the calculated cutting force and cutting moments would then likely be caused by trigonometric errors.
The excel file of Miedema calculates the average pore pressures in the shear layer and on the blade using the same theory as is used in the pore pressure module of the production model. In the model in excel the influences of a quasi cavitation cloud are also modeled.
For the verification pore pressures will be calculated for three situations: non-cavitational cutting, cavitation in the shear layer and cavitational cutting. Non-cavitational cutting is when nowhere in the shear zone and on the blade the cavitation pressure is reached. Cavitation in the shear plane is when only in parts of the shear plane the cavitation pressure is reached. Cavitational cutting is when both in the shear plane and on the blade the cavitation pressure is reached.
The input parameters are chosen in such a way that the previously described situations will be achieved.

7.2.1 Non-cavitational cutting

The input parameters that were used to calculate the average pore pressures for a non-cavitational situation are listed below.

- $\alpha = 35.0°$
- $\beta = 23.5°$
- $h_i = 0.1m$
- $h_b = 0.2m$
- $k_i = 0.000025m/s$

- $k_{max} = 0.000125 m/s$
- $\epsilon = 0.16$
- $v_c = 0.2 m/s$
- $z = 20 m$

The average pore pressures in the shear plane and on the blade for both the pore pressure module and the excel sheet are listed in table 7.1. The pore pressure distributions for the pore pressure model and the excel sheet are respectively shown in figure 7.1 and 7.2.

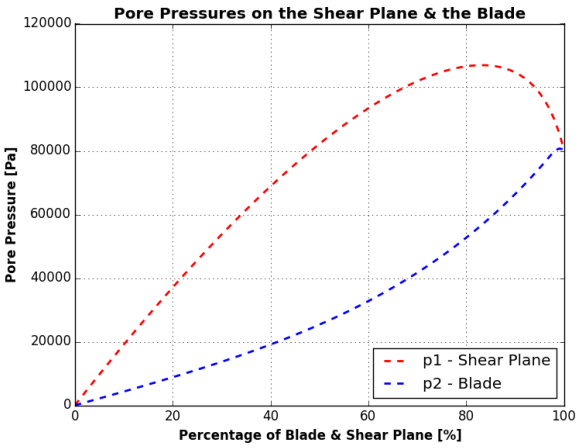

Figure 7.1: Pore pressure graph produced by pore pressure module of the production model

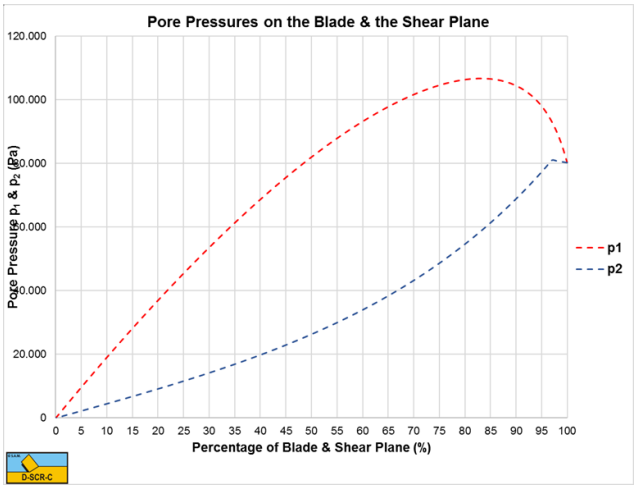

Figure 7.2: Pore pressure graph produced by excel sheet of Miedema

Table 7.1: The average pore pressures of the production model and the excel sheet

Pressure	Production model	Excel Miedema	Unit
p_{1m}	71783.0	71541.5	Pa
p_{2m}	30920.0	31964.6	Pa

The shape of the graphs in both figures as well as the order of magnitude seem to be the same. The only apparent difference is the difference in shape of the p_2 graph in the 100% region. This can be explained by the fact that the pore pressure module of the production model uses a smoothstep function to account for the tip effect while Miedema his excel does not do this.
The numbers in table 7.1 confirm that the differences between the average pore pressures calculated by the model are negligible. The small differences that can be noted can be explained by the aforementioned smoothstep function, rounding numbers between calculations and differences in calculating the average.

7.2.2 Cavitation in the shear layer

The input parameters that were used to calculate the average pore pressures for a cavitation in the shear layer situation are listed below.

- $\alpha = 35.0°$

- $\beta = 23.5°$
- $h_i = 0.2m$
- $h_b = 0.2m$
- $k_i = 0.000025m/s$
- $k_{max} = 0.000125m/s$
- $\epsilon = 0.16$
- $v_c = 0.4m/s$
- $z = 20m$

The average pore pressures in the shear plane and on the blade for both the pore pressure module and the excel sheet are listed in table 7.2. The pore pressure distributions for the pore pressure model and the excel sheet are respectively shown in figure 7.3 and 7.4.

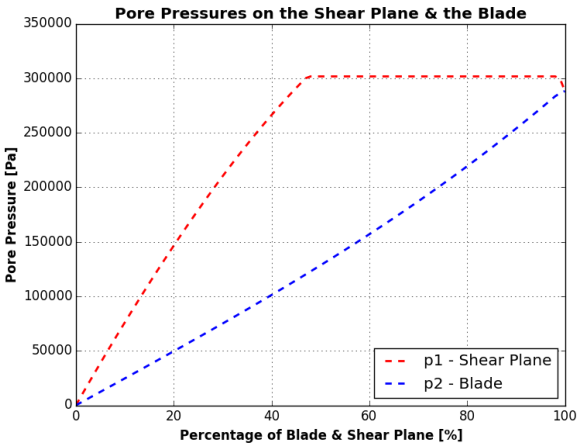

Figure 7.3: Pore pressure graph produced by pore pressure module of the production model

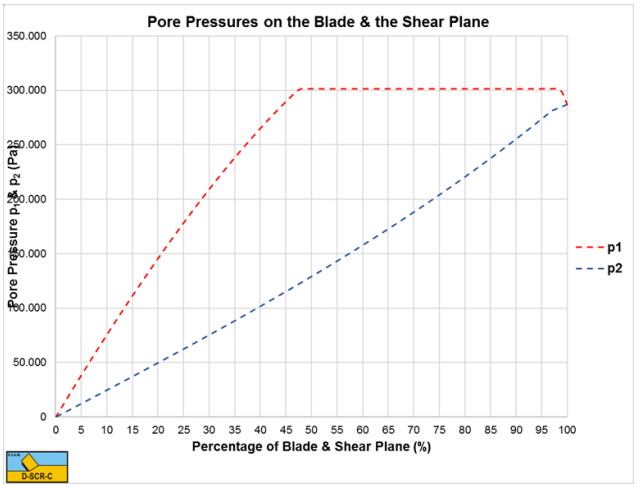

Figure 7.4: Pore pressure graph produced by excel sheet of Miedema

Table 7.2: The average pore pressures of the production model and the excel sheet

Pressure	Production model	Excel Miedema	Unit
p_{1m}	237826.0	237543.4	Pa
p_{2m}	135423.0	136237.4	Pa

The shape of the graphs in both figures as well as the order of magnitude seem to be the same. The only difference is a small difference in shape of the p_2 graph in the 100% region. Again this can be explained by the fact that the pore pressure module of the production model uses a smoothstep function to account for the tip effect while Miedema his excel does not do this.
The numbers in table 7.2 confirm that the differences between the average pore pressures calculated by the model are negligible. The small differences that can be noted can be explained by the aforementioned smoothstep function, rounding numbers between calculations and differences in calculating the average.

7.2.3 Cavitational cutting

The input parameters that were used to calculate the average pore pressures for a cavitational situation are listed below.

- $\alpha = 55.0°$
- $\beta = 20.0°$
- $h_i = 0.2m$
- $h_b = 0.2m$
- $k_i = 0.000025m/s$
- $k_{max} = 0.0001m/s$
- $\epsilon = 0.16$
- $v_c = 0.7m/s$
- $z = 20m$

The average pore pressures in the shear plane and on the blade for both the pore pressure module and the excel sheet are listed in table 7.3. The pore pressure distributions for the pore pressure model and the excel sheet are respectively shown in figure 7.5 and 7.6.

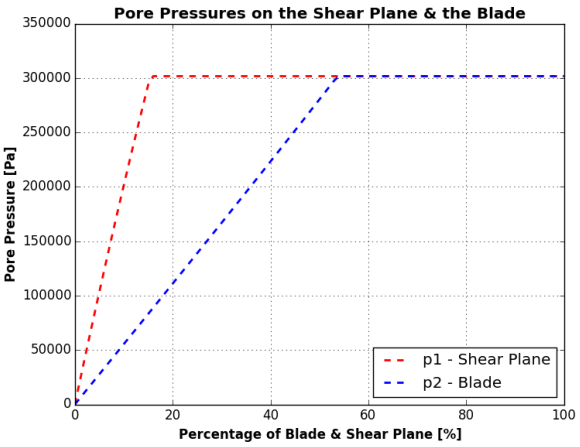

Figure 7.5: Pore pressure graph produced by pore pressure module of the production model

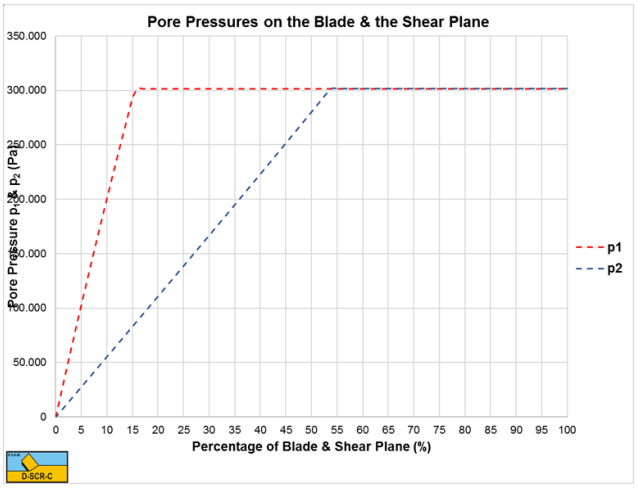

Figure 7.6: Pore pressure graph produced by excel sheet of Miedema

Table 7.3: The average pore pressures of the production model and the excel sheet

Pressure	Production model	Excel Miedema	Unit
p_{1m}	280531.0	280450.4	Pa
p_{2m}	221584.0	220209.0	Pa

The shape of the graphs in both figures as well as the order of magnitude seem to be the same. In contrast to the previous situations no apparent differences can be found between the graphs. This can be explained by the fact that the pore pressure module of the production model does not use the smoothstep function anymore as soon as cavitation reaches the blade.

The numbers in table 7.1 confirm that the differences between the average pore pressures calculated by the model are negligible. The small differences that can be noted can be explained by rounding numbers between calculations and differences in calculating the average.

7.3 Sensitivity analysis

In the coming paragraphs a sensitivity analysis will be performed in order to find out which input parameters have the greatest influence on the production magnitude and how the production changes for changing these parameters. This sensitivity analysis is done with the quasi-cloud model providing the pore under pressures for the cutting force calculations. First a set of parameters is chosen that is used to calculate a reference production. This reference production will be shown in paragraph 7.4 along with the reference parameters. In the paragraphs that follow per paragraph a certain parameter is varied by 20 percent (20 percent more and 20 percent less) and new productions are calculated. In the last paragraph of the sensitivity analysis (paragraph 7.12) the results of the analysis are summarized.
The input parameters of the production model can roughly be split up into three groups, the soil parameters, the dredging parameters and the equipment parameters. The equipment parameters, or the geometry of the draghead, will not be changed during the sensitivity analysis since the production is calculated for a certain type of draghead (in this case the Wild Dragon draghead).
The parameters that will be varied in the sensitivity analysis are described in the following sections.

7.3.1 Soil mechanical parameters

The soil mechanical inputs that will be varied for the analysis are the angle of internal friction ϕ, the dilatation ϵ and the permeabilities k_i and k_{max}.
The first soil mechanical input that will be varied is the angle of internal friction ϕ. Changing the angle of internal friction does however also change the angle of external friction since it is generally assumed that the latter is proportional to the angle of internal friction by about two-thirds. This is shown in the following equation.

$$\delta = \frac{2}{3} \cdot \phi \tag{7.3.1}$$

Since the relation between ϕ and δ is linear, the angle of external friction will be varied by the same percentage as the angle of internal friction.
The second soil parameter that will be varied is the dilatation ϵ. The dilatation is a function of the initial porosity n_i and the maximum porosity n_{max} and is calculated as follows.

$$\epsilon = \frac{n_{max} - n_i}{1 - n_{max}} \tag{7.3.2}$$

The initial porosity is not only used to calculate the dilatation or the pore under pressures but is also used to calculate the jet penetration depth y_{jet} (see paragraph 6.5). Since the aim of the sensitivity analysis is not to find the influence of the jet penetration depth it is preferred that y_{jet} remains constant. To achieve this, the initial porosity is kept constant. This means that varying the dilatation can only be done by changing the maximum porosity.
When the porosity of a sand package changes so does the permeability. Hence, because the maximum porosity changes the maximum permeability also changes. The proportionality of the change in permeability as a function of the change in porosity can be found using the Kozeny Carman equation (see appendix F) and can be written as follows.

$$k_{max} = k_i \cdot \frac{\frac{n_{max}^3}{(1-n_{max})^2}}{\frac{n_i^3}{(1-n_i)^2}} \tag{7.3.3}$$

Although the maximum permeability changes for a changing dilatation, the permeabilities (initial and maximum) are also changed whilst keeping the dilatation constant. This means that the magnitude of both permeabilities changes by 20 percent but the factor between k_i and k_{max} stays the same.
The difference between these two situations can be seen as changing the density of a sand package versus changing the type (coarseness) of granular material.

7.3.2 Dredging parameters

The four dredging parameters that will be varied are the dredging depth z, the hydraulic pressure in the cylinder $p_{Cylinder}$, the flow of the heel jets Q_{heel} and the lower arm angle Γ.
In the production model changing these parameters does not influence other inputs. In reality changing the dredging depth might change the lower arm angle and hence the maximum possible slice thickness. Also, in reality changes of the dredging depth would lead to changes in pressure which influences the jet water pump and hence the jet flow.
It can also be noted that changing the jet flow for the same equipment (the same amount of nozzles and the same nozzle diameters) requires the jet pressure to be changed. In paragraph 4.3 it has been established that the jet flow is proportional to the jet pressure squared. This can be written as follows.

$$Q_{heel} \propto p_{heel}^2 \tag{7.3.4}$$

This means that an increase of 20 percent of the jet flow would require an increase of 44 percent of the jet pressure.
The standard angle for what is called the lower arm angle Γ is zero degrees. This makes it impossible to add or subtract 20 percent. To solve this the angle that the lower arm actually makes with the horizontal in standard position must be used.

7.3.3 Equipment parameters

As has been stated before, the draghead in the production model will be modeled after the Wild Dragon draghead and will not be varied during the sensitivity analysis. In table 7.4 the geometry data of the Wild Dragon is listed. In addition to the geometry of the draghead there are a number of miscellaneous parameters that are needed in order to run the model. These parameters are the mass of the visor, the number of heel jet nozzles and the diameter of the heel jet nozzles. The data of these parameters is listed in table 7.5.

Table 7.4: Wild Dragon draghead extended visor geometry data

Distances	m	Python variable
Blade width	2.629	W
Cylinder diameter	0.120	$D_{Cylinder}$
Visor hinge to heel	0.288	r_{heel}
Visor hinge to cylinder attachment on visor	1.394	r_1
Visor hinge to cylinder attachment on helmet	1.760	r_2
Visor hinge to top of blade 1	1.133	r_3
Visor hinge to tip of blade 1	0.994	r_4
Visor hinge to top of blade 2	2.093	r_5
Visor hinge to tip of blade 2	1.920	r_6
Visor hinge to center of gravity of visor	1.10	r_g
Angles	degrees	Python variable
Maximum visor rotation	46.0	Ψ_{max}
Angle between r_1 and the horizontal axis	-9.75	$\angle r_1$
Angle between r_2 and the vertical axis	-7.75	$\angle r_2$
Angle between r_3 and the horizontal axis	31.21	$\angle r_3$
Angle between r_4 and the horizontal axis	45.10	$\angle r_4$
Angle between r_5 and the horizontal axis	28.35	$\angle r_5$
Angle between r_6 and the horizontal axis	35.07	$\angle r_6$
Angle between r_g and the horizontal axis	20.0	$\angle r_g$

Table 7.5: Miscellaneous draghead parameters

Miscellaneous parameter	magnitude	unit	Python variable
Visor mass	5575	kg	m_{visor}
Heel jet nozzle diameter	0.022	m	D_n
Number of heel jet nozzles	10	-	n_{nozzle}

7.4 Reference parameters and production

7.4.1 Reference parameters

In paragraph 7.3 it was stated that the parameters that will be varied in the sensitivity analysis are the angle of internal friction ϕ, the dilatation ϵ, the permeability k, the dredging depth z , the pressure in the hydraulic cylinder $p_{Cylinder}$, the flow of the heel jets Q_{heel} and the lower arm angle Γ.
It has also been stated that the variation of a parameter will be plus and minus 20 percent. This percentage is chosen because for many of the chosen parameters this will yield values that are close to the maximum and minimum values that are possible (or observed). The great exception is the permeability since it ranges between several orders of magnitude. Having the values of a varied parameter lie close to the maximum and minimum possible value requires that the reference value is chosen in the middle of the range of possible values. The reference values of the parameters that were mentioned before are listed below.

- $\phi = 36^{\circ}$
- $\epsilon = 0.16$
- $k_i = 0.000025 m/s$
- $k_{max} = 0.0000591 m/s$
- $z = 15m$
- $p_{Cylinder} = 25 \cdot 10^5 Pa$
- $Q_{heel} = 0.010468 m^3/s$
- $\Gamma = 0^{\circ}$

It has been explained that when certain parameters are changed (varied) other parameters would be changed as well. In the next tables an overview is given of which parameters change for what reference parameter and by how much.

Table 7.6: The parameters changing when the internal friction angle is changed

Parameter	-20%	Reference	+20%	Unit
ϕ	28.8	36.0	43.2	°
δ	19.2	24.0	28.8	°

In table 7.6 the changing parameters for a changing angle of internal friction are shown. For all these tables the upper parameter is the main parameter, or the parameter being changed, for the sensitivity analysis. In the third column of every table the reference value is listed. This value is used to produce the reference results that are shown in the next sections.
The columns left and right of the reference column show the values if the main parameter is varied by 20 percent. Good to note is that for non-main parameters the change between the reference value and the values in the plus and minus 20 percent columns does not necessarily have to be 20 percent due to the non-linearities explained in section 7.3.1 and section 7.3.2.

Table 7.7: The parameters changing when the dilatation is changed

Parameter	-20%	Reference	+20%	Unit
ϵ	0.128	0.16	0.192	-
n_i	0.4	0.4	0.4	-
n_{max}	0.468	0.483	0.497	-
k_i	0.000025	0.000025	0.000025	m/s
k_{max}	0.0000510	0.0000591	0.0000680	m/s

In table 7.7 the changing parameters for a changing dilatation are shown. Note that the initial porosity n_i and initial permeability k_i remain constant, as is explained in section 7.3.1.

Table 7.8: The parameters changing when the permeabilities are changed

Parameter	-20%	Reference	+20%	Unit
k_i	0.000020	0.000025	0.000030	m/s
k_{max}	0.0000473	0.0000591	0.0000710	m/s

In table 7.8 the values of changing permeabilities are shown. Note that the factor between k_i and k_{max} does not change per column since the dilatation remains constant.

Table 7.9: The parameters changing when the dredging depth is changed

Parameter	-20%	Reference	+20%	Unit
z	12.0	15.0	18.0	m

In table 7.9 it can be seen that for a changing dredging depth no additional parameters change.

Table 7.10: The parameters changing when the hydraulic pressure is changed

Parameter	-20%	Reference	+20%	Unit
$p_{Cylinder}$	$20.0 \cdot 10^5$	$25.0 \cdot 10^5$	$30.0 \cdot 10^5$	Pa

In table 7.10 it can be seen that for a changing pressure in the hydraulic cylinder no additional parameters change.

Table 7.11: The parameters changing when the flow of the heel jets is changed

Parameter	-20%	Reference	+20%	Unit
Q_{heel}	0.008374	0.010468	0.012562	m^3/s
p_{heel}	$2.49 \cdot 10^5$	$3.89 \cdot 10^5$	$5.60 \cdot 10^5$	Pa

In table 7.11 the corresponding jet pressure for the changing flows can be seen. The reference value of the flow was obtained by performing a flow analysis in AFT Fathom for the jet system of the Wild Dragon and Liberty Island and is the flow per jet (10 nozzles per draghead). The corresponding jet pressure was calculated using the relationships described in paragraph 4.3.
In section 7.3.2 it was explained that for the 20 percent increase and decrease of the lower arm angle the actual angle between the lower arm and the horizontal axis must be used since normally Γ is zero. For the Wild dragon this angle is 25 degrees when Γ is zero. Therefore the changes of the lower arm angle will be plus and minus 5 degrees. The increase follows the definition of the positive direction for Γ. This means that the positive rotational direction is the same direction as the positive direction

for the visor. This sign convention does lead to a situation in which an increase of Γ actually reduces the angle between the lower arm and the horizontal axis.

Table 7.12: The parameters changing when the lower arm angle is changed

Parameter	-20%	Reference	+20%	Unit
Γ	-5.0	0.0	5.0	$^\circ$

7.4.2 General model settings and graphs

Besides the input parameters, the model also has other parameters or settings that influence the way the model is run, which thus influence the results of the model. These settings were discussed in paragraph 6.3.
The first of these settings are v_{start}, v_{end} and v_{step}. With these settings the minimum and maximum trailing speed between which the model is run are set. Logically, these settings also set the range for which the production is plotted. For the results the calculations have been done for trailing speeds starting at 0.1 m/s and ending at 2.0 m/s. A step size of 0.01 m/s is chosen to ensure smooth graphs. Although 2.0 m/s (roughly 4 knots) is too fast to be a realistic trailing speed, the calculations are done in this range to show a larger portion of the course of the production as a function of the trailing speed. For the Liberty Island trailing speeds typically lie between 1 and 2 knots or roughly 0.5 and 1 meters per second.
Next is the setting *StartAngle*, which is set to zero and the setting *ResetAngle*, which is set to *False*. The combination of these two settings means that the visor is only guaranteed to start in the lowest possible position at v_{start}. This resembles a TSHD that starts dredging at low speed with the visor in the lowest position and then very slowly increases the trailing speed.
The results are normally plotted in five sets of graphs, the production breakdown, the concentration graph, the moment breakdown, the moment components and the cutting parameters. Of these sets the production breakdown is the most important graph because it shows the total in situ production, the production done by the heel jets and the production per blade for a single draghead. Another important graph is the concentration graph. This graph shows how the dredge pump reacts to the in situ production. The other sets of graphs serve to check whether the underlying calculations of the production calculation are correct.
With exception of the graphs in this paragraph, the moment breakdown, the moment components and cutting parameters graphs are not shown. The parameters used for the calculations that produced the graphs in this section are shown below.

- $\phi = 36^\circ$
- $\delta = 24^\circ$
- $\epsilon = 0.16$
- $n_i = 0.4$
- $n_{max} = 0.483$
- $k_i = 0.000025 m/s$
- $k_{max} = 0.0000591 m/s$
- $z = 15m$

- $p_{Cylinder} = 25 \cdot 10^5 Pa$
- $Q_{heel} = 0.010468 m^3/s$
- $p_{heel} = 3.89 \cdot 10^5 Pa$
- $\Gamma = 0°$

7.4.3 Reference production - No cloud model

Although the sensitivity analysis will only be done using the quasi-cloud model, a reference production for a production model with no cloud model will be shown in this section. This way also the influence of having a cloud model versus having no cloud model can be shown. In this section all graphs mentioned in the previous section will be shown.

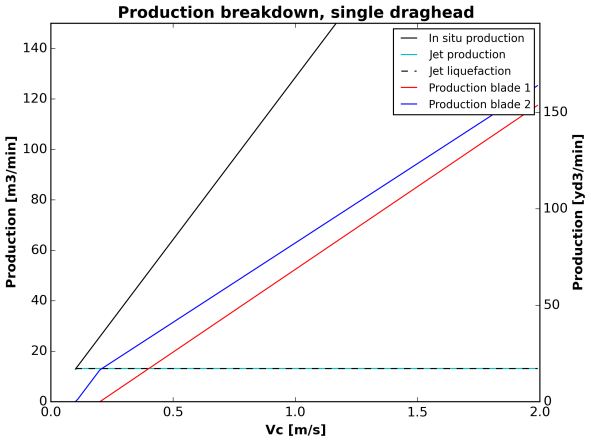

Figure 7.7: The production breakdown of the reference production with no cavitation cloud model

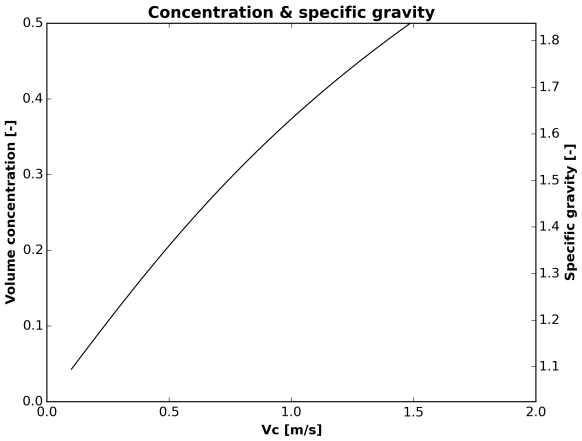

Figure 7.8: The concentration graph of the reference production with no cavitation cloud model

In figure 7.7 it can be seen that the in situ production increases seemingly linear at a fast rate. This linear increase can also be seen in the top graph of figure 7.9. The in situ production for a single draghead in the normal trailing range of 0.5 to 1.0 m/s seems to be very reasonably in accordance with the in situ production range found by GLDD of 36 to 125 m^3/min (15th-85th percentile, with 15 percent assumed overflow losses, see appendix J). However, the linear increase with increasing trailing speed means that the total cut layer thickness and hence the visor angle Ψ remain unchanged. This can be seen in the second and third graph of figure 7.10. Since the visor angle started at zero and remained unchanged for all increases of trailing speed the combined cutting moment was never large enough or in the right direction the move the visor up. This is confirmed by the second graph of figure 7.11. In this graph it can be seen that for most trailing speeds the largest moment is the cutting moment of blade 2. It should also be noted that this moment is negative, which means that it is actually helping the actuator. In figure 7.7 it can be seen that at the starting speed only the heel jets and blade 2 contribute to the total production. The penetration depth of the heel jets decreases with increasing trailing speed. At about 0.2 m/s blade 1 also starts cutting because the penetration depth of the heel jets is less then the depth of the tip of blade 1.

The advantage of seeing the production with a constant visor angle is that certain processes of the production model, that are also present in the models with cavitation clouds, become clearly visible.

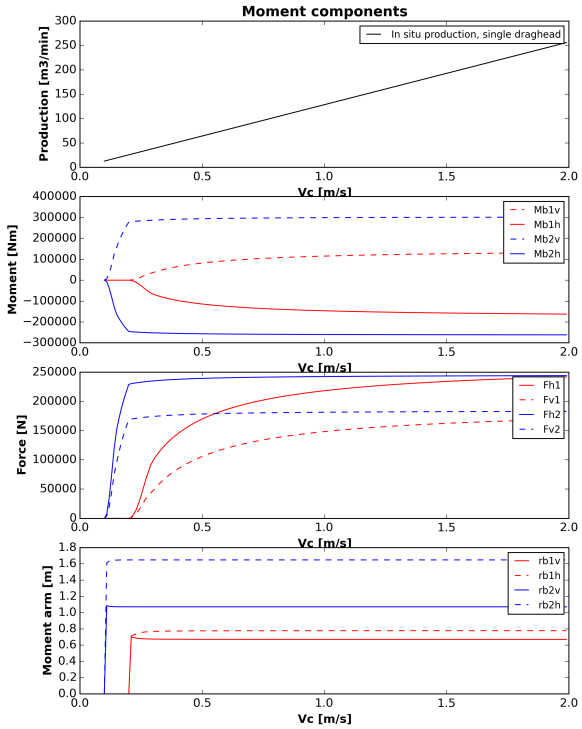

Figure 7.9: The moment components of the reference production with no cavitation cloud model

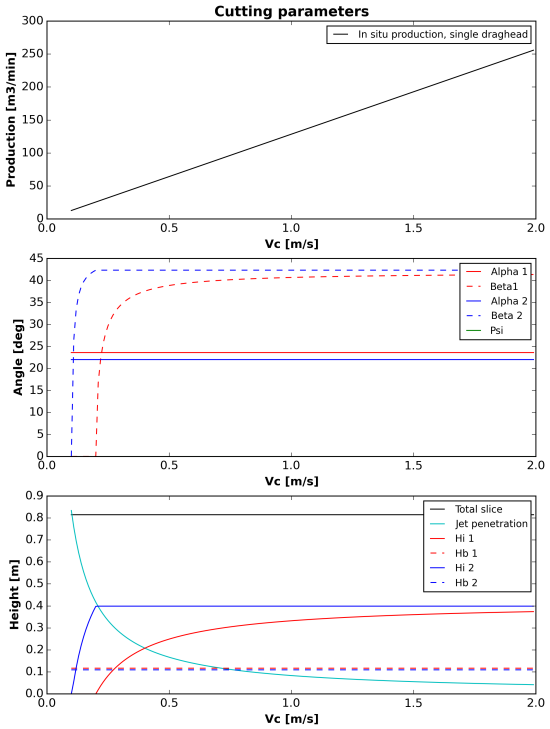

Figure 7.10: The cutting parameters of the reference production with no cavitation cloud model

It can for instance be seen in figure 7.10 that the blade angles and thus the blade heights slightly differ. This is not an error of the model. The difference can actually be found in the technical drawings of the draghead as well.

Another thing that can be noted is that the moment arms of the cutting forces are not constant at the lower trailing speeds, even though the visor angle does not change. This can be explained by the force acting point that shifts due to changing pore pressures on the blade. This implies that as long as the moment arm is not constant, the pore pressure on the blade has not reached its maximum.

In the third graph of figure 7.9 it can be seen that the horizontal and vertical cutting force of blade 2 become constant for the higher trailing speeds. This means that at those speeds fully cavitational cutting is achieved and that the pore pressures do not change anymore. This is only possible in situations where the visor angle (and hence the blade angle etc.) remains constant. It should also be noted that in case of a constant visor angle the cutting forces of blade 1 will never become fully constant since the initial cut height of blade one will always increase due to an ever decreasing jet penetration depth.

For the operation range of trailing speeds the concentration lies mostly within the commonly observed range (0.046 to 0.3 or about 1.1 to 1.5 specific gravity). Especially for 1.0 m/s the concentration is higher than commonly observed however, concentrations as high as 0.45 have been reported which makes the concentrations at this speed still plausible. The influence of the cubic relationship between the concentration and the dredge pump flow can clearly been seen in the graph. What can also be noted that if a linear relationship would have been used which would have the same steepness as the curve at the low trailing speeds then for the higher trailing speeds the predicted concentration would clearly be of an impossible magnitude.

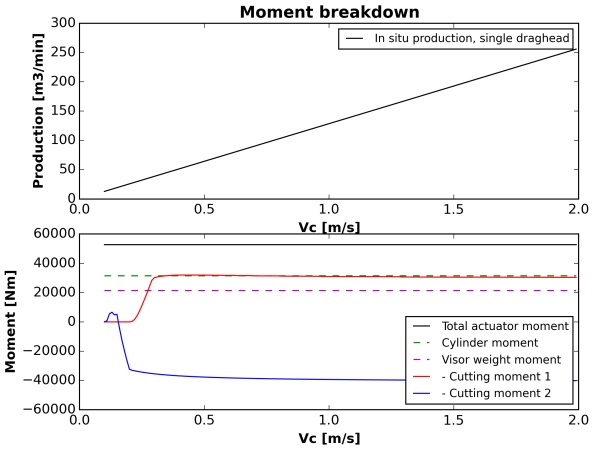

Figure 7.11: The moment breakdown of the reference production with no cavitation cloud model

7.4.4 Reference production - Quasi cloud model

In this section the reference production and concentration for the production model with the quasi-cloud model are discussed. Since the course of the in situ production for the increasing trailing speed is generally the same for all variations of the sensitivity analysis, the general features are only discussed in this section. Hence, in the coming paragraphs only features that stand out will be discussed.

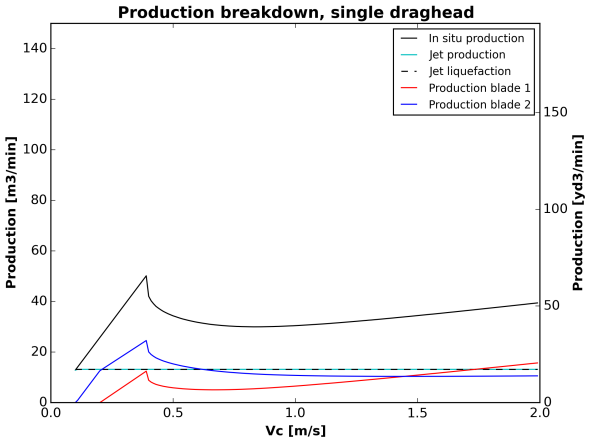

Figure 7.12: The production breakdown of the reference production with the quasi-cloud model

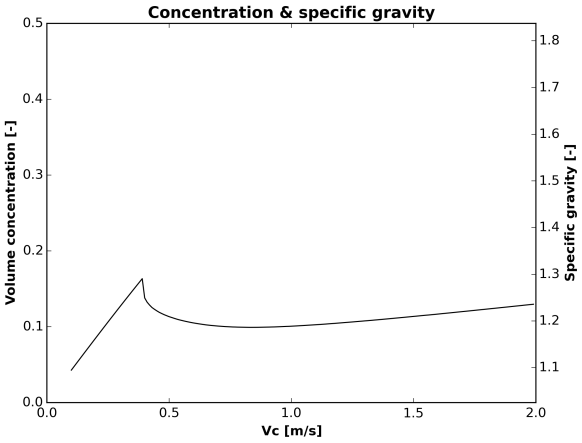

Figure 7.13: The concentrations and specific gravity of the reference production with the quasi-cloud model

The description of the course of the in situ production graph of figure 7.12 starts at the lower speeds on the left and will move to the higher speeds on the right.
At first a linear increase of the production can be seen. A linear increase means that the visor angle remains constant, in this case at the lowest position ($\Psi = 0°$). This can be seen in the second graph of figure 7.16. In the beginning of this graph it can be seen that Ψ remains zero until roughly 0.4 m/s. Likewise, the total slice thickness in the height graph of figure 7.16 remains constant until roughly 0.4 m/s. Since both the total slice thickness and the blade width are constant, the linear increase of

the trailing speed leads to a linear increase of production. When the visor is in the lowest possible position this means that the combined moment of the hydraulic cylinder and the visor weight is larger than the combined cutting moment as can be seen in the second graph of figure 7.14. The build-up of the separate cutting moments can be found in figure 7.15. The actuator moment being greater than the combined cutting moment can be caused by the fact that the draghead is only cutting liquefied sand, which is assumed to have no cutting force, or simply by the cutting forces being too small (due to small cut slice thicknesses which are caused by large heel jet penetration) a last option is that a cutting moment is actually helping the actuator moment. This last option can be seen at the blue line at roughly 0.2 m/s in the second graph of figure 7.14.

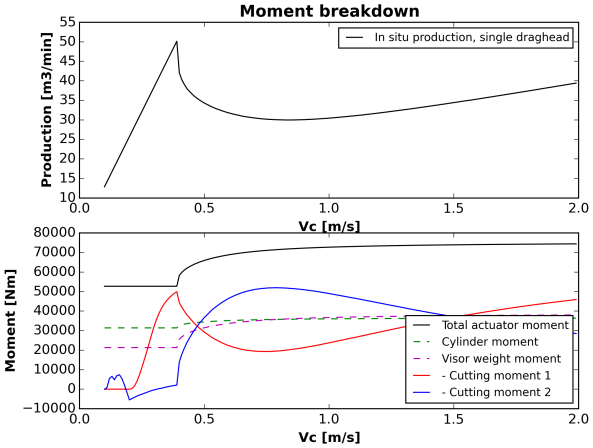

Figure 7.14: The moment breakdown of the reference production with the quasi-cloud model

When the trailing speed increases the cutting moment becomes larger than the actuator moment at the lowest visor angle and hence the visor will move up to find a new moment equilibrium. This new equilibrium is found at a visor angle of about six degrees, as can be seen in the second graph of figure 7.16. Apparently this change of six degrees for an increment of 0.01 m/s trailing speed is enough to cause a steep drop in production. More information on the allowable change in visor angle to ensure rising production can be found in appendix I.
After the initial steep drop in production the production will first continue to decrease until about 0.8 m/s. After this, the production starts to rise again. This increase of production seems to be linear, but it is not and cannot be. A linear increase would imply that the visor angle is constant and a constant visor angle implies that the cutting forces are constant. For blade 2 this could be the case if the cutting process already would be fully cavitational. However, for blade 1 this is not possible because the cut slice thickness of blade 1 increases for every increment of speed regardless of whether the visor angle changes or not. This is due to the ever decreasing penetration depth of the heel jets. Since the decrease of the penetration depth is non-linear and the increase of actuator moment for increasing visor angle is non-linear, the increase of the production must also be non-linear. However, the changes in visor angle for an increment in trailing speed are so small that for the plotted range of trailing speeds the increase does seem linear.
Noteworthy is the intersection of the horizontal cutting forces of both blades in the third graph of figure 7.15 at about 1.4 m/s. The horizontal cutting force of blade 1 increases while the horizontal cutting force of blade 2 decreases. This is due to an increasing visor angle and a decreasing jet penetration. For an increasing visor angle the cut slice thickness will decrease for both blades. The cut slice thickness of blade 2 does decrease faster since it is slowly being overshadowed by blade 1. Furthermore the cut slice thickness of blade 1 decreases slower due to the decreasing heel jet penetration.

Eventually blade 2 will stop cutting and thus the cutting force will go to zero. The cutting force of blade 1 will never become constant due to the ever decreasing jet penetration.

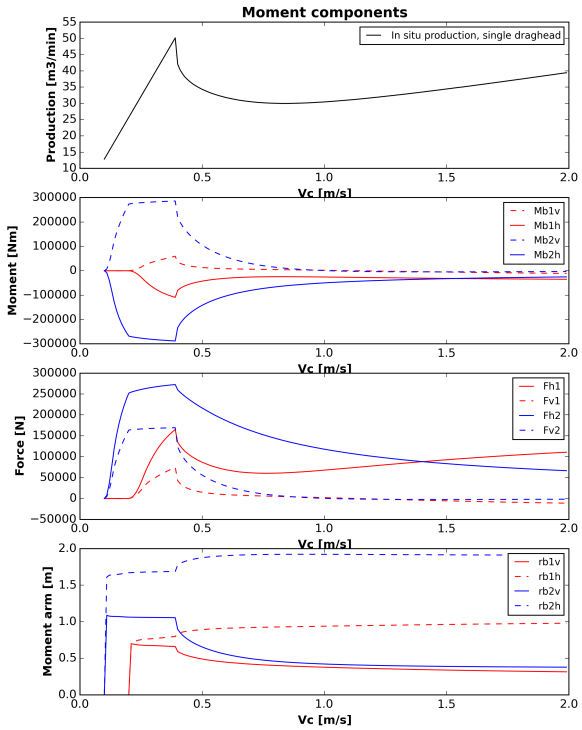

Figure 7.15: The moment components of the reference production with the quasi-cloud model

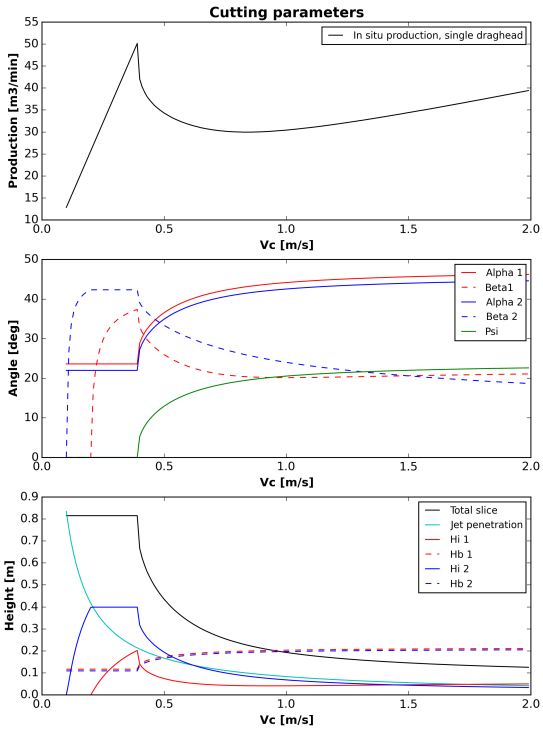

Figure 7.16: The cutting parameters of the reference production with the quasi-cloud model

When looking at the overall magnitude of the in situ production per draghead it is obvious that the production mostly lies on the lower side of the typical range of 36 to 125 m^3/min. The calculated concentrations do lie within the typical range of 0.046 (1.1 specific gravity) and 0.30 (1.5 specific gravity), albeit on the lower side of this range. This can be seen in figure 7.13. Since the concentrations are not calculated using a constant suction pipe flow but are rather calculated by solving a third order polynomial equation, the shape of the concentration graph does not fully match the in situ production graph (at the same scales). If a constant flow would be used then the concentrations would be spread over a wider range.
For the sensitivity analysis two reference points will be recorded. The first point is the in situ production at 1.5 knots or 0.77 m/s. This trailing speed is chosen because it lies in the middle of the range of typical trailing speeds. The second point is the point at the end of the linear production increase since this point indicates the trailing speed for which the visor starts moving. At which speed this point lies differs per graph an therefore both the trailing speed as the production are recorded.
Both points and the trailing speeds are shown in table 7.13.

Table 7.13: The trailing speed and production for the reference points with the quasi cloud model

Point	Trailing speed $[m/s]$	Production $[m^3/min]$
1.5 Knots	0.77	29.99
End linear increase	0.39	50.15

7.4.5 Reference production - Cloud model

In this section the reference production and concentration for the production model with the normal cavitation cloud model are discussed. Although the sensitivity analysis is done for the production model with the quasi-cloud model a reference production for the cloud model is still shown in order to show any differences between the performance of both cloud models.

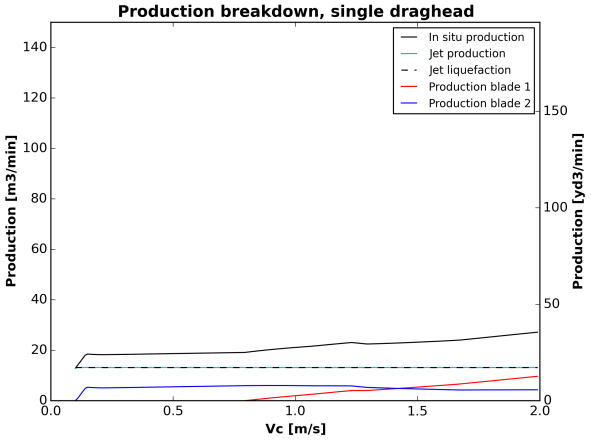

Figure 7.17: The production breakdown of the reference production with the cloud model

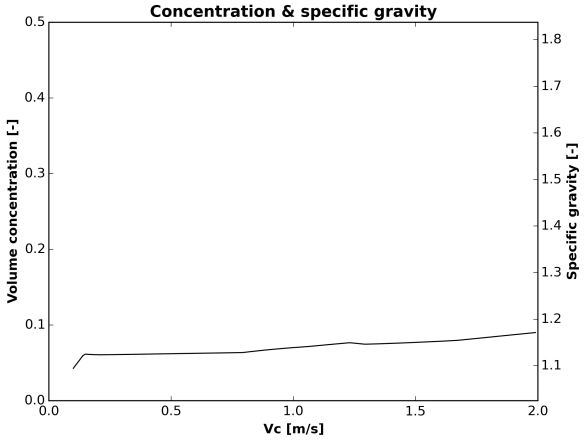

Figure 7.18: The concentration and specific gravity of the reference production with the cloud model

The description of the course of the in situ production graph of figure 7.17 starts at the lower speeds on the left and moves to the higher speeds on the right.
Starting at 0.1 m/s a short linear increase of the in situ production can be seen. This linear increase indicates that the visor angle remains constant, in this case at the lowest possible angle ($\Psi = 0°$). A constant visor angle means that the total cut slice thickness is also constant. This can be observed in the third graph of figure 7.20. The constant visor angle can be seen in the second graph of the figure. The visor angle remains constant until roughly 0.15 m/s.
After already 0.15 m/s a strong increase of the visor angle and logically a strong decrease of cut slice thickness can be seen. This causes the in situ production to be nearly constant despite the increase of the trailing speed. More information on the maximum allowable visor angle change to ensure a rising production can be found in appendix I. The strong increase of the visor angle is caused by a strong increase of the cutting moment of blade 2, this can be seen in figure 7.21. In its turn, the sudden increase of the cutting moment is caused by a relatively larger increase of the horizontal cutting force of blade 2 with respect to the increase of the vertical cutting force. This can be seen when the third graph of figure 7.19 is compared to the third graph of figure 7.15. Since the cutting forces are calculated using the pore pressures in the shear zone and on the blade, the cause of this sudden increase of the visor angle can be found in the way the pore pressures are calculated and thus

in the cloud model. In section 3.6.1 it was explained that slight changes in the cutting conditions can already have a large effect on how far the cavitation cloud travels up the blade. This manifests itself as a jump in the average pore pressure on the blade and thus as a jump in cutting forces. Another jump in cutting forces can also be seen for blade 1 at around 1.25 m/s in the third graph of figure 7.19. This also leads to a jump in the cutting moment, which can be seen in figure 7.21.

After the linear increase until 0.15 m/s the production still slightly increases. At about 1.2 m/s a

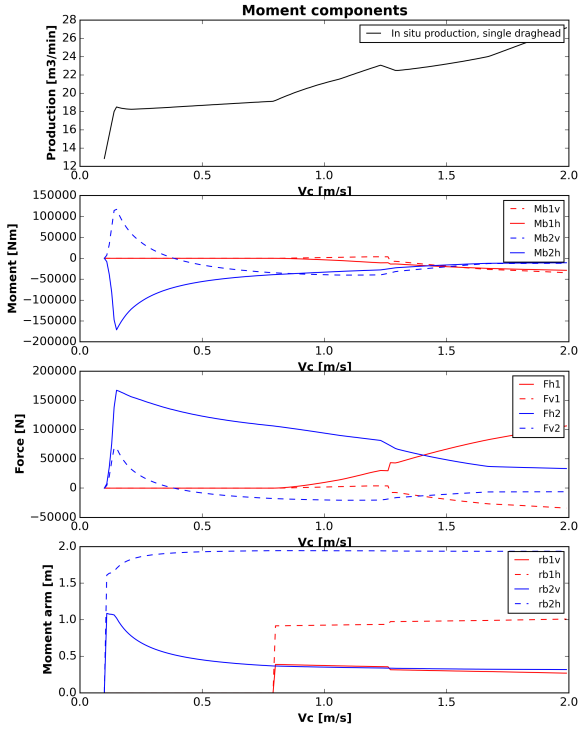

Figure 7.19: The moment components of the reference production with the cloud model

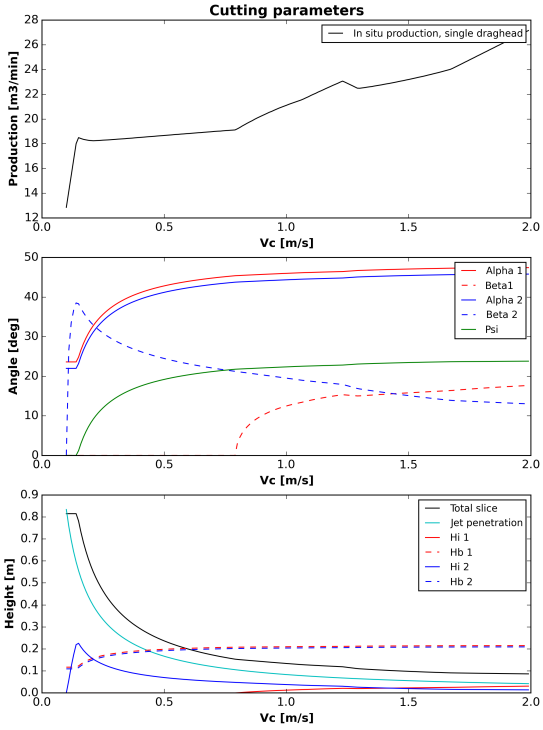

Figure 7.20: The cutting parameters of the reference production with the cloud model

local maximum in production is reached. This can be seen more clearly in the first graph of figure 7.21. After the local maximum the production slightly drops and then rises again.

When looking at the overall magnitude of the in situ production per draghead it is clear that over the entire plotted range the production is below the lower boundary of the common production range. The concentrations are also on the low side, however this is to be expected with the low in situ production.

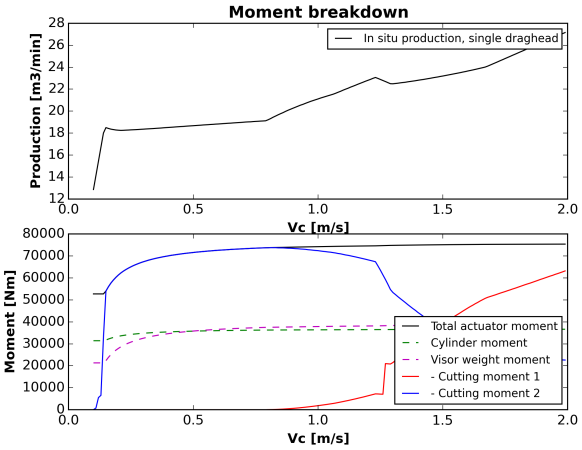

Figure 7.21: The moment breakdown of the reference production with the cloud model

7.5 Angle of internal friction

In this paragraph the results of the sensitivity analysis for the variations in angle of internal friction are shown. Since the general course of the production graph has already been discussed in for the reference production, only notable differences will be discussed.

7.5.1 Production for $\phi = 28.8°$

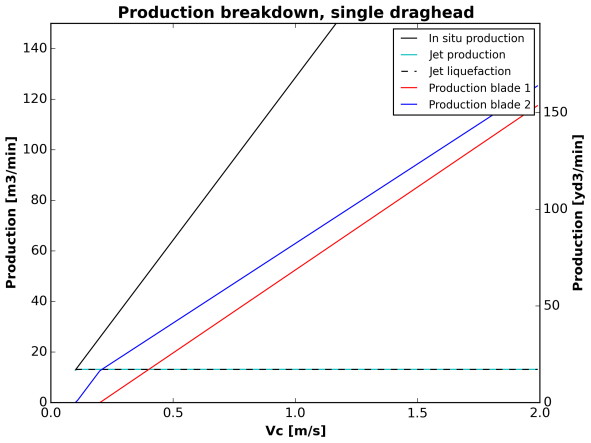

Figure 7.22: The production breakdown for a production with a reduced angle of internal friction

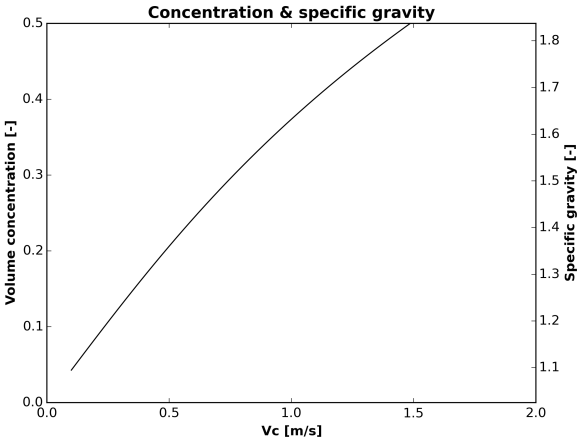

Figure 7.23: The concentrations and specific gravity for a production with a reduced angle of internal friction

As can be seen in figure 7.22 a 20 percent reduction of the angle of internal friction leads to linear production course over the entire plotted range. This means that for the plotted range of trailing speeds the combined cutting moment at the lowest visor angle is never larger than the actuator moment. Since there is no end visible of the linear increase no data is shown for this point in table 7.14.
For the operation range of 1 to 2 knots (roughly 0.5 to 1.0 m/s) the calculated in situ production does lie nicely within the common range of production (36 to 125 m^3/min). The same is true for the concentrations in figure 7.23 although the concentration at the end of the operational range might be somewhat on the higher side.

Table 7.14: The trailing speed and production for the reference points with the quasi cloud model

Point	Trailing speed $[m/s]$	Production $[m^3/min]$
1.5 Knots	0.77	98.92
End linear increase	-	-

7.5.2 Production for $\phi = 43.2°$

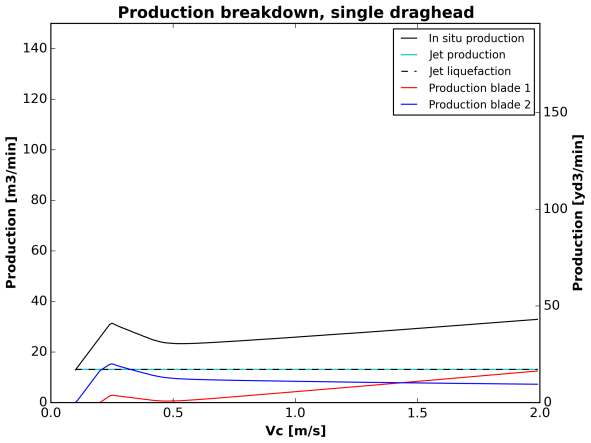

Figure 7.24: The production breakdown for a production with an increased angle of internal friction

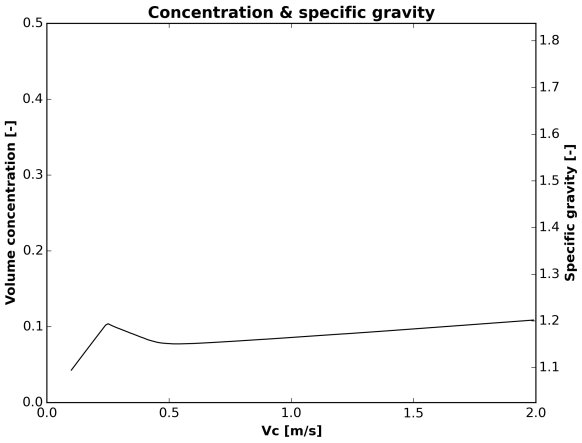

Figure 7.25: The concentrations and specific gravity for a production with an increased angle of internal friction

In contrary to a reduction of the angle of internal friction a 20 percent increase does lead to a production shape that is quite similar to the reference production. The most striking difference is that the drop after the linear increase is not as steep as for the reference production. This indicates that the change of the visor angle for an increment of the trailing speed at the end of the linear increase is less than it is for the reference production. The overall production is lower than that of the reference production and below the common range of production. The linear increase for this situation ends sooner than that of the reference production. This can be seen when the data in table 7.15 is compared with the reference data.

Table 7.15: The trailing speed and production for the reference points with the quasi cloud model

Point	Trailing speed $[m/s]$	Production $[m^3/min]$
1.5 Knots	0.77	24.38
End linear increase	0.24	30.86

7.6 Dilatation

In this paragraph the results of the sensitivity analysis for the variations in dilatation are shown. Since the general course of the production graph has already been discussed in for the reference production, only notable differences will be discussed.

7.6.1 Production for $\epsilon = 0.128$

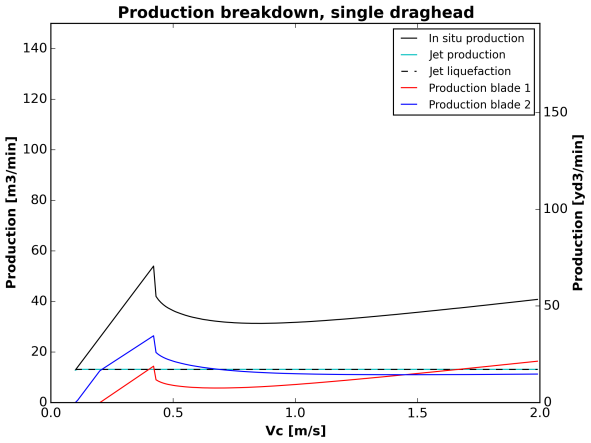

Figure 7.26: The production breakdown for a production with a reduced dilatation

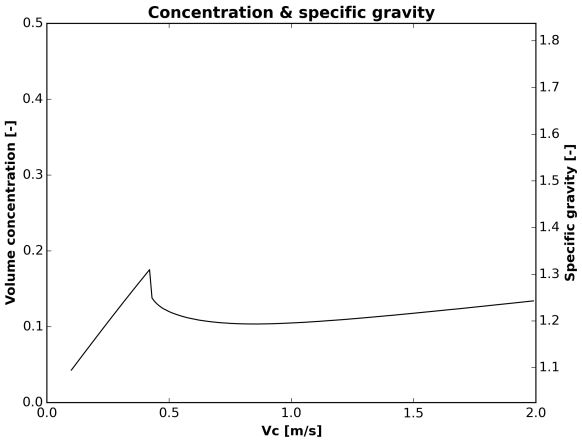

Figure 7.27: The concentrations and specific gravity for a production with a reduced dilatation

The shape of the production graph in figure 7.26 for a 20 percent reduction of the dilatation is quite similar to the reference graph. The linear increase ends at a higher trailing speed than it does for the reference production. This can be seen in table 7.16. The overall magnitude of the production is on the low side of the common production range.

Table 7.16: The trailing speed and production for the reference points with the quasi cloud model

Point	Trailing speed $[m/s]$	Production $[m^3/min]$
1.5 Knots	0.77	31.48
End linear increase	0.42	54.01

7.6.2 Production for $\epsilon = 0.192$

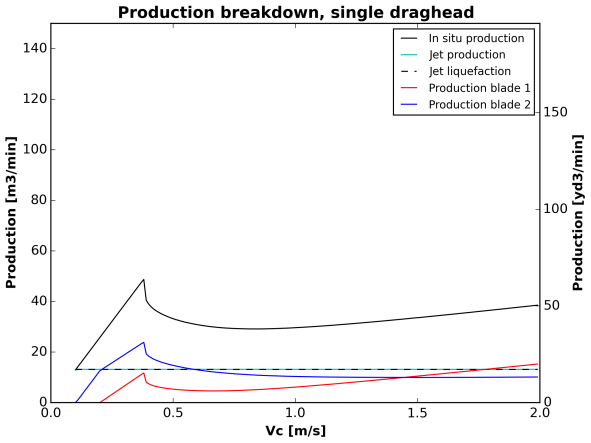

Figure 7.28: The production breakdown for a production with an increased dilatation

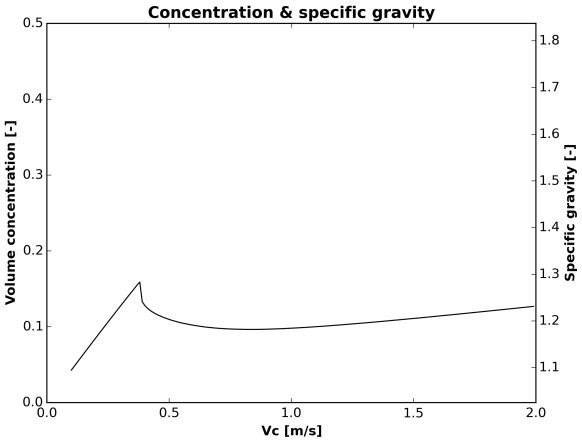

Figure 7.29: The concentrations and specific gravity for a production with an increased dilatation

The shape of the production graph in figure 7.28 for a 20 percent increase of the dilatation is quite similar to the reference graph. The linear increase ends at a lower trailing speed than it does for the reference production. This can be seen in table 7.17. The overall magnitude of the production is on the low side of the common production range.

Table 7.17: The trailing speed and production for the reference points with the quasi cloud model

Point	Trailing speed $[m/s]$	Production $[m^3/min]$
1.5 Knots	0.77	29.21
End linear increase	0.37	47.58

7.7 Permeability

In this paragraph the results of the sensitivity analysis for the variations in permeability are shown. Since the general course of the production graph has already been discussed in for the reference production, only notable differences will be discussed.

7.7.1 Production for $k_i = 0.000020m/s$ & $k_{max} = 0.0000473m/s$

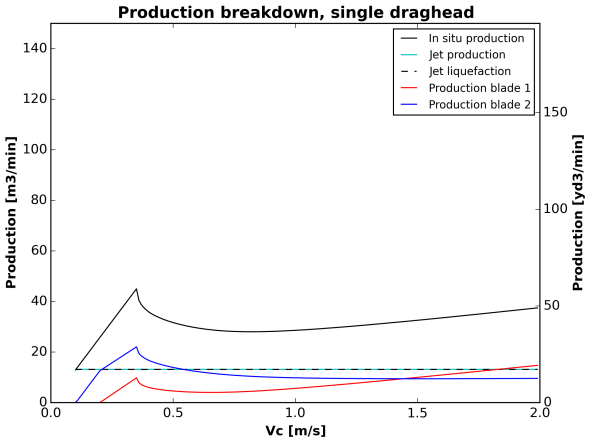

Figure 7.30: The production breakdown for a production with a reduced permeability

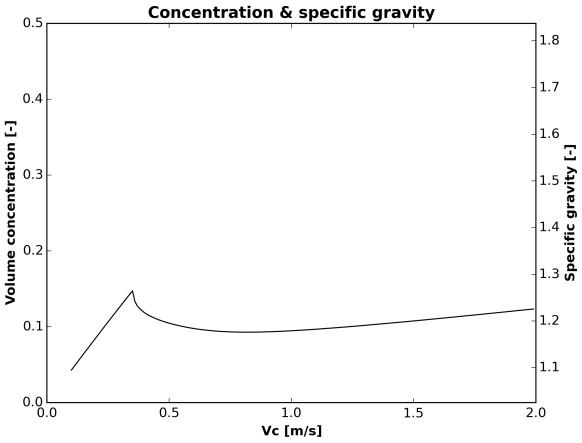

Figure 7.31: The concentrations and specific gravity for a production with a reduced permeability

The shape of the production graph in figure 7.30 for a 20 percent decrease of the permeability is quite similar to the reference graph. The linear increase ends at a lower trailing speed than it does for the reference production. This can be seen in table 7.18. Also, the drop in production after the linear increase is not as steep as for the reference production. The overall magnitude of the production is on the low side of the common production range.

Table 7.18: The trailing speed and production for the reference points with the quasi cloud model

Point	Trailing speed $[m/s]$	Production $[m^3/min]$
1.5 Knots	0.77	28.08
End linear increase	0.35	45.01

7.7.2 Production for $k_i = 0.000030 m/s$ & $k_{max} = 0.0000710 m/s$

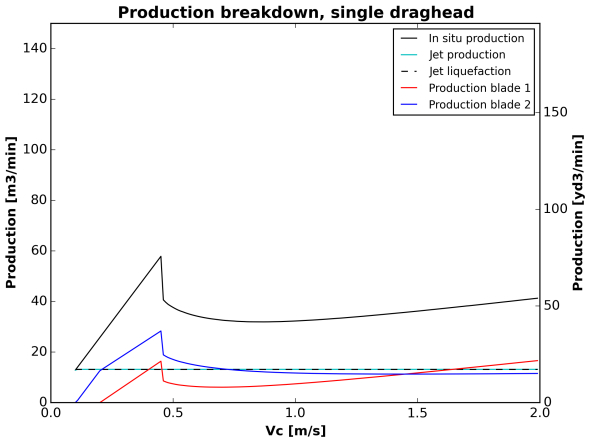

Figure 7.32: The production breakdown for a production with an increased permeability

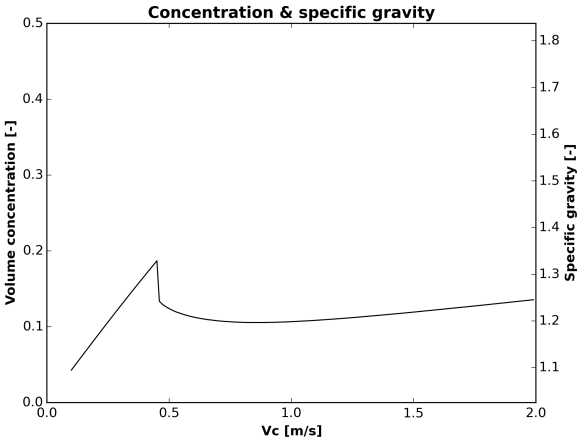

Figure 7.33: The concentrations and specific gravity for a production with an increased permeability

The shape of the production graph in figure 7.32 for a 20 percent increase of the permeability is quite similar to the reference graph. The linear increase ends at a higher trailing speed than it does for the reference production. This can be seen in table 7.19. Also, the drop in production after the linear increase is more severe than that of the reference production. The overall magnitude of the production is on the low side of the common production range but slightly higher than the reference production.

Table 7.19: The trailing speed and production for the reference points with the quasi cloud model

Point	Trailing speed $[m/s]$	Production $[m^3/min]$
1.5 Knots	0.77	32.16
End linear increase	0.45	57.86

7.8 Water depth

In this paragraph the results of the sensitivity analysis for the variations in water depth are shown. Since the general course of the production graph has already been discussed in for the reference production, only notable differences will be discussed.

7.8.1 Production for $z = 12m$

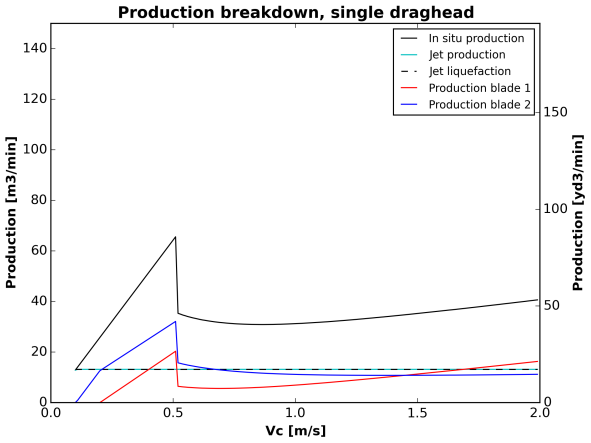

Figure 7.34: The production breakdown for a production with a reduced water depth

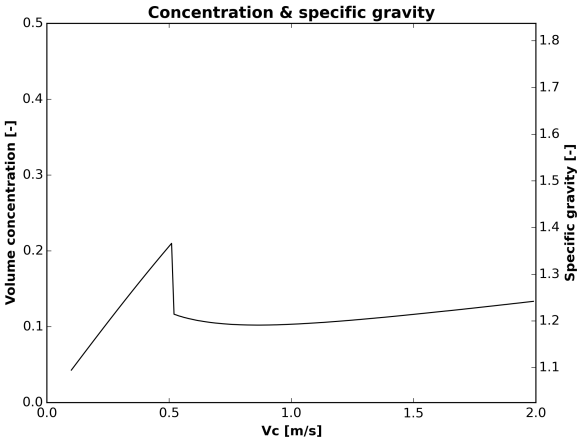

Figure 7.35: The concentrations and specific gravity for a production with a reduced water depth

The shape of the production graph in figure 7.34 for a 20 percent decrease of the water depth is quite similar to the reference graph. The linear increase ends at a higher trailing speed than it does for the reference production. This can be seen in table 7.20. The drop in production after the linear increase is very steep and large compared to that of the reference production. The production on the low side of the operation range fits nicely within the common production range. This is however the part of the linear increase. The magnitude of the production in the rest of the operational range is on the low side of the common production range.

Table 7.20: The trailing speed and production for the reference points with the quasi cloud model

Point	Trailing speed $[m/s]$	Production $[m^3/min]$
1.5 Knots	0.77	31.14
End linear increase	0.51	65.58

7.8.2 Production for $z = 18m$

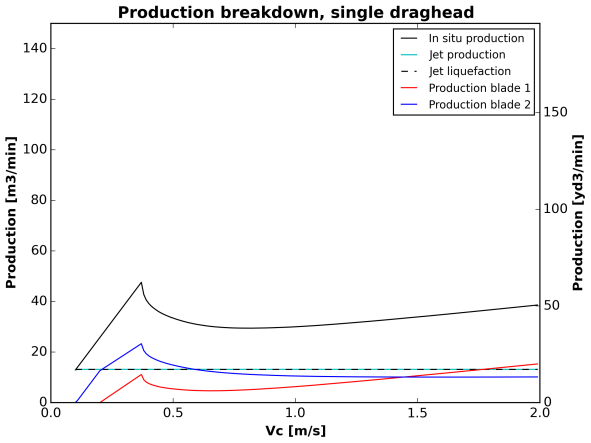

Figure 7.36: The production breakdown for a production with an increased water depth

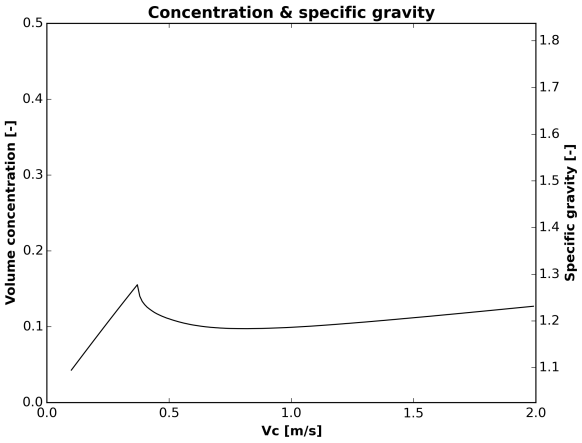

Figure 7.37: The concentrations and specific gravity for a production with an increased water depth

The shape of the production graph in figure 7.36 for a 20 percent increase of the water depth is quite similar to the reference graph. The linear increase ends at a lower trailing speed than it does for the reference production. This can be seen in table 7.21. The drop in production after the linear increase is smaller and less steep compared to that of the reference production. The overall magnitude of the production in the entire plotted range is on the low side of the common production range.

Table 7.21: The trailing speed and production for the reference points with the quasi cloud model

Point	Trailing speed $[m/s]$	Production $[m^3/min]$
1.5 Knots	0.77	29.40
End linear increase	0.37	47.58

7.9 Cylinder pressure

In this paragraph the results of the sensitivity analysis for the variations in cylinder pressure are shown. Since the general course of the production graph has already been discussed in for the reference production, only notable differences will be discussed.

7.9.1 Production for $p_{Cylinder} = 20 \cdot 10^5 Pa$

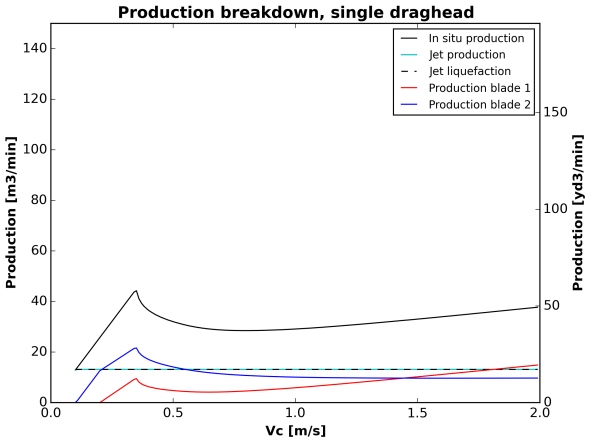

Figure 7.38: The production breakdown for a production with a reduced cylinder pressure

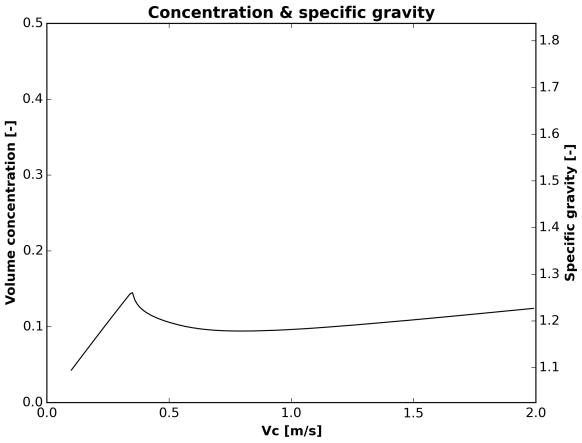

Figure 7.39: The concentrations and specific gravity for a production with a reduced cylinder pressure

The shape of the production graph in figure 7.38 for a 20 percent decrease of the hydraulic cylinder pressure is quite similar to the reference graph. The linear increase ends at a somewhat lower trailing speed than it does for the reference production. This can be seen in table 7.22. The drop in production after the linear increase is not as steep as that of the reference production. The overall magnitude of the production is on the low side of the common production range.

Table 7.22: The trailing speed and production for the reference points with the quasi cloud model

Point	Trailing speed $[m/s]$	Production $[m^3/min]$
1.5 Knots	0.77	28.46
End linear increase	0.34	43.72

7.9.2 Production for $p_{Cylinder} = 30 \cdot 10^5 Pa$

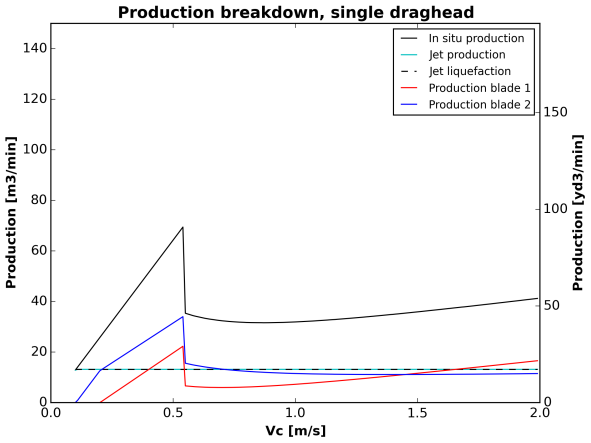

Figure 7.40: The production breakdown for a production with an increased cylinder pressure

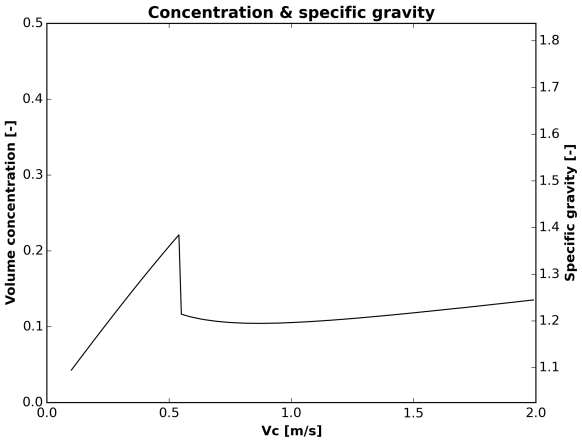

Figure 7.41: The concentrations and specific gravity for a production with an increased cylinder pressure

The shape of the production graph in figure 7.40 for a 20 percent increase of the hydraulic cylinder pressure is quite similar to the reference graph. The linear increase ends at a higher trailing speed than it does for the reference production. This can be seen in table 7.23. The drop in production after the linear increase is very steep and larger than that of the reference production. Again the part of the linear increase that is within the operational range fits nicely within the common range of production. The overall magnitude of the production is on the low side of the common production range but higher than that of the reference production.

Table 7.23: The trailing speed and production for the reference points with the quasi cloud model

Point	Trailing speed $[m/s]$	Production $[m^3/min]$
1.5 Knots	0.77	31.98
End linear increase	0.54	69.44

7.10 Heel jet flow

In this paragraph the results of the sensitivity analysis for the variations in heel jet flow are shown. Since the general course of the production graph has already been discussed in for the reference production, only notable differences will be discussed.

7.10.1 Production for $Q_{heel} = 0.008374 m^3/s$

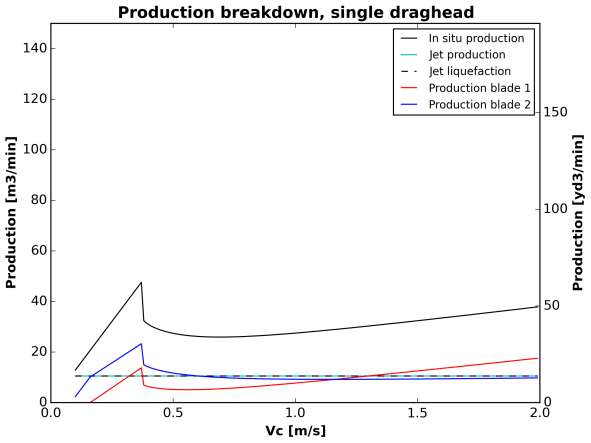

Figure 7.42: The production breakdown for a production with a reduced heel jet flow

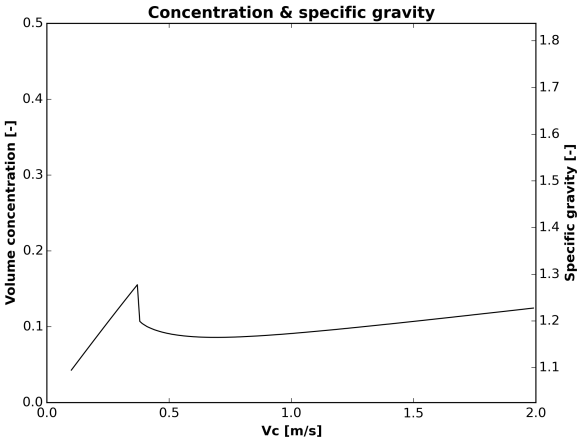

Figure 7.43: The concentrations and specific gravity for a production with a reduced heel jet flow

The shape of the production graph in figure 7.42 for a 20 percent decrease of the hydraulic cylinder pressure is quite similar to the reference graph. The linear increase ends at a somewhat lower trailing speed than it does for the reference production. This can be seen in table 7.24. The drop in production after the linear increase is steeper than that of the reference production. The overall magnitude of the production is on the low side of the common production range and is somewhat lower than the reference production. The heel jet production and heel jet liquefaction lines are lower than in the reference production graph, since the heel jet flow is reduced by 20 percent in this case.

Table 7.24: The trailing speed and production for the reference points with the quasi cloud model

Point	Trailing speed $[m/s]$	Production $[m^3/min]$
1.5 Knots	0.77	26.06
End linear increase	0.37	47.58

7.10.2 Production for $Q_{heel} = 0.012562 m^3/s$

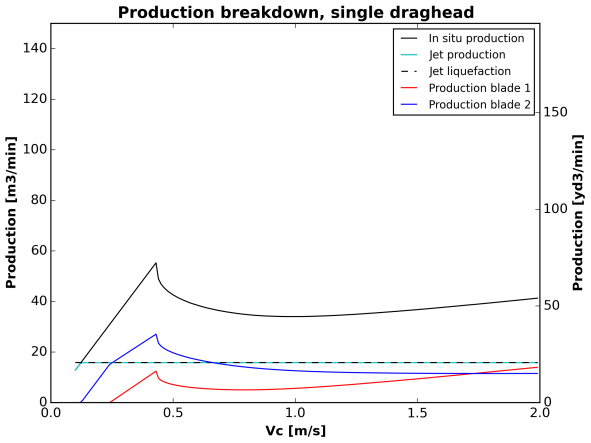

Figure 7.44: The production breakdown for a production with an increased heel jet flow

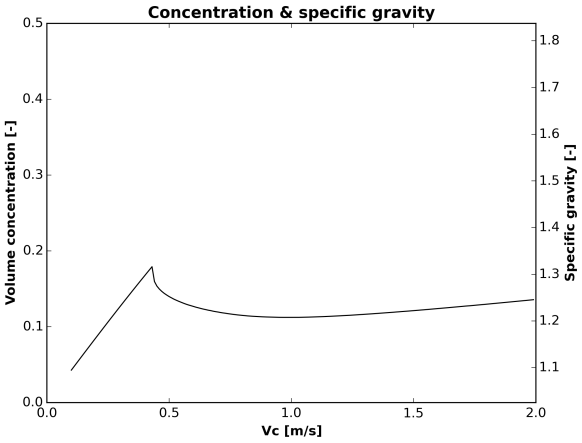

Figure 7.45: The concentrations and specific gravity for a production with an increased heel jet flow

The shape of the production graph in figure 7.44 for a 20 percent decrease of the hydraulic cylinder pressure is quite similar to the reference graph. The linear increase ends at a somewhat higher trailing speed than it does for the reference production. This can be seen in table 7.25. The drop in production after the linear increase is less steep than that of the reference production. The overall magnitude of the production is on the low side of the common production range but is within the common production range. The heel jet production and heel jet liquefaction lines are higher than in the reference production graph, since the heel jet flow is increased by 20 percent in this case.

Table 7.25: The trailing speed and production for the reference points with the quasi cloud model

Point	Trailing speed $[m/s]$	Production $[m^3/min]$
1.5 Knots	0.77	35.18
End linear increase	0.43	55.29

7.11 Lower arm angle

In this paragraph the results of the sensitivity analysis for the variations in lower arm angle. Since the general course of the production graph has already been discussed in for the reference production, only notable differences will be discussed.

7.11.1 Production for $\Gamma = -5.0°$

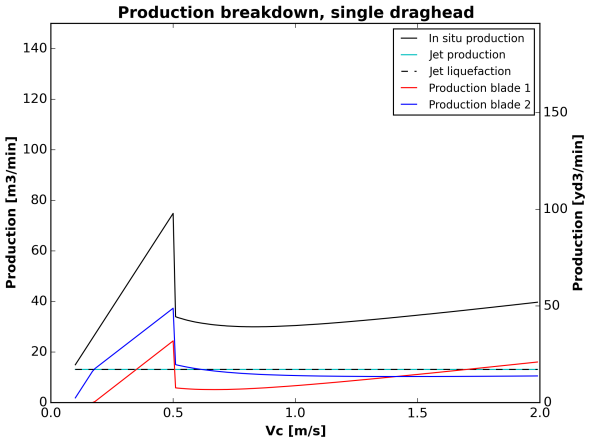

Figure 7.46: The production breakdown for a production with a reduced lower arm angle

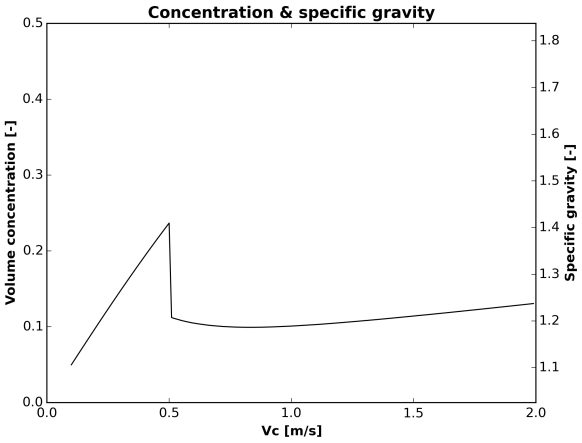

Figure 7.47: The concentrations and specific gravity for a production with a reduced lower arm angle

The shape of the production graph in figure 7.46 for a 20 percent decrease of the lower arm angle is quite similar to the reference graph. The linear increase ends at a somewhat higher trailing speed than it does for the reference production. This can be seen in table 7.26. The drop in production after the linear increase is steeper and larger than that of the reference production. The overall magnitude of the production is on the low side of the common production range and is somewhat higher than the reference production. The part of the linear increase that is within the operating range yields a production well within the common production range. Note that the linear increase of this graph is steeper than that of the reference graph. This is because a reduction of Γ increases the maximum slice thickness that can be cut.

Table 7.26: The trailing speed and production for the reference points with the quasi cloud model

Point	Trailing speed $[m/s]$	Production $[m^3/min]$
1.5 Knots	0.77	30.02
End linear increase	0.50	74.76

7.11.2 Production for $\Gamma = +5.0°$

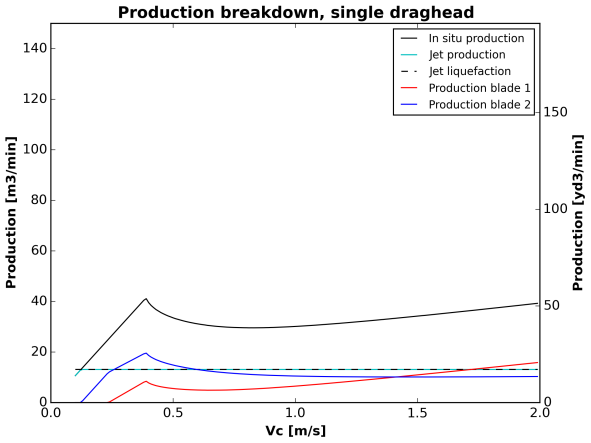

Figure 7.48: The production breakdown for a production with an increased lower arm angle

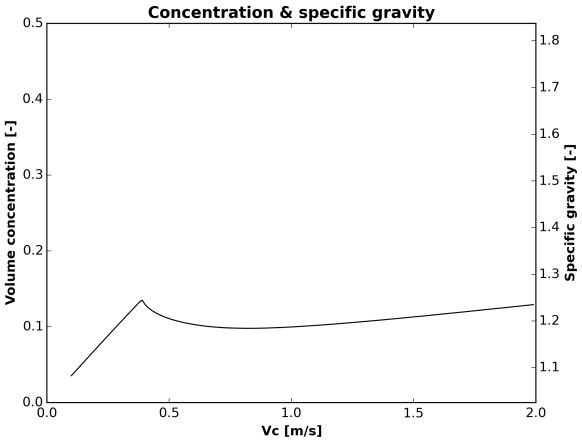

Figure 7.49: The concentrations and specific gravity for a production with an increased lower arm angle

The shape of the production graph in figure 7.48 for a 20 percent increase of the lower arm angle is quite similar to the reference graph. The linear increase ends at a somewhat lower trailing speed than it does for the reference production. This can be seen in table 7.27. The drop in production after the linear increase is less steep and smaller than that of the reference production. The overall magnitude of the production is comparable to that of the reference production and thus on the low side of the common production range. Note that the linear increase of this graph is less steep than that of the reference graph. This is because an increase of Γ decreases the maximum slice thickness that can be cut.

Table 7.27: The trailing speed and production for the reference points with the quasi cloud model

Point	Trailing speed $[m/s]$	Production $[m^3/min]$
1.5 Knots	0.77	29.63
End linear increase	0.38	40.40

7.12 Sensitivity analysis summary

In this paragraph the results of the sensitivity analysis that was carried out in paragraph 7.3 trough 7.11 are summarized and discussed. In the first section the results of the analysis of the production at a trailing speed of 1.5 knots are summarized and discussed. In the second section the results of the production at the end of the linear increase are summarized and discussed. In the last section the results for both data points are compared and discussed.

7.12.1 Summary 1.5 knots results

The results of the sensitivity analysis are shown in table 7.28. In addition to the plain results also the percentage difference with the reference value has been calculated. This is shown in the fourth column of the table.

Table 7.28: Summary of the production results of the sensitivity analysis at 1.5 knots trailing speed

Parameter	Trailing speed $[m/s]$	Production $[m^3/min]$	Percentage difference [%]
Reference	0.77	29.99	0.00
Angle of internal friction -20%	0.77	99.01	+230.10
Angle of internal friction +20%	0.77	24.38	-18.71
Dilatation -20%	0.77	31.48	+4.97
Dilatation +20%	0.77	29.21	-2.60
Permeability -20%	0.77	28.08	-6.37
Permeability +20%	0.77	32.16	+7.21
Water depth -20%	0.77	31.14	+3.82
Water depth +20%	0.77	29.40	-1.96
Cylinder pressure -20%	0.77	28.46	-5.10
Cylinder pressure +20%	0.77	31.98	+6.63
Heel jet flow -20%	0.77	26.06	-13.10
Heel jet flow +20%	0.77	35.18	+17.28
Lower arm angle -20%	0.77	30.02	+0.10
Lower arm angle +20%	0.77	29.63	-1.20

Most notable in the table is the +230.10 percent difference of the production between the reference production and the situation in which the angle of internal friction is reduced by 20 percent. It stands out because for all other changes of 20 percent the production does not even change 20 percent. This large difference is caused by the fact that the graph of the reduced angle of internal friction (figure 7.22) is linear over the entire range of trailing speed whilst in the other graphs the linear increase always ends before the trailing speed of 0.77 m/s. This makes a kind of unfair comparison since now two regimes are compared: the situation in which the visor is in the lowest possible position and the situation in which the visor has already rotated. In general there is no moment balance in the first regime, whilst in the second regime there always is a moment balance.
If the result for the reduction of the angle of internal friction is ignored then the largest difference is caused by the increase of the angle of internal friction. The increase of the angle of internal friction is 20 percent and the production reduction is 18.71 percent. Based on these number for this trailing speed the production seems to be almost linearly proportional to the angle of internal friction. This can however not be checked, since the results of a reduced angle of internal friction are in a different

regime.
After the increase of the angle of internal friction the largest production difference is achieved by increasing the heel jet flow. For an increase of heel jet flow of 20 percent the production increases with 17.28 percent. The decrease of the heel jet flow by 20 percent also leads to a relatively large reduction of the production of 13.10 percent. This does make it clear that change of production is not linearly proportional to the change in heel jet flow. It does show that of the controllable parameters (the dredging parameters) in this regime, the heel jet flow and thus the heel jet penetration has the largest influence on the in situ production.
The soil parameter that has the second largest influence on the production, after the angle of internal friction, is the permeability. For an increase and decrease of 20 percent the production changes respectively with +7.21 and -6.37 percent. It must however be kept in mind that the range of possible permeabilities spans several orders of magnitudes. If the reference permeability would have been chosen in a different order of magnitude then the results might different from what is presented in the table.
The soil parameter that has the smallest influence on the production is the dilatation. For an increase and decrease of 20 percent the production changes with respectively -2.60 and +4.97 percent. Since the sensitivity analysis for the dilatation almost completely covers the entire common range of dilatations (0.10 to 0.20) it seems that for this regime the dilatation has a relatively small influence on the in situ production.
The second largest controllable parameter in this regime is the pressure in the hydraulic cylinder. With an increase and decrease of 20 percent respectively a difference of +6.63 and -5.10 percent are achieved. This is however, more than a factor of 2.5 less than what the changes in heel jet flow achieved.
The dredging parameter that has the largest influence after the aforementioned parameters is the dredging depth. It is questionable whether this parameter can be called controllable since the only variations in water depth for a location are under the influence of the weather and the tides. However, whether dredging operations are carried out under certain weather conditions or tides is decided by a human. Hence, the water depth might be considered to be slightly controllable. Nevertheless an increase and a decrease of the water depth of 20 percent only leads to a change of respectively -1.96 and + 3.82 percent in in situ production.
The dredging parameter with the lowest influence on the production for this regime is the lower arm angle. For an increase and decrease of 20 percent the changes in production were respectively -1.20 and +0.10 percent. It should be noted that in this model the lower arm angle is independent of the water depth whilst in reality a certain dependence does exist.
When the magnitude of the calculated productions is compared with the common range range of production according to Great Lakes (36 to 125 m^3/min, 15th to 85th percentile, assuming 15 percent overflow losses) it is clear that all productions with the exception of the reduction of the angle of internal friction are lower than 36 m^3/min. This is odd because the trailing has been chosen in the middle of the operational range and thus a production in the order of magnitude of roughly the middle of the common production range (80.5 m^3/min, assuming a symmetrical distribution) might be expected. The only parameter that is in this order of magnitude is the reduced angle of internal friction, which is still in the linear regime.

7.12.2 Summary end of linear increase results

The results of the sensitivity analysis are shown in table 7.29. In addition to the plain results also the percentage difference with the reference value has been calculated. This is shown in the fourth column of the table. Good to note is that the percentage difference in production is the same as the percentage difference in trailing speeds since the production in this regime is linearly proportional to the trailing speed. This is with the exception of the changes in lower arm angle because changes in this angle change the maximum total slice thickness at the lowest possible visor angle.

Table 7.29: Summary of the production results of the sensitivity analysis for the end of the linear increase

Parameter	Trailing speed $[m/s]$	Production $[m^3/min]$	Percentage difference [%]
Reference	0.39	50.15	0.00
Angle of internal friction -20%	-	-	-
Angle of internal friction +20%	0.24	30.86	-38.46
Dilatation -20%	0.42	54.01	+7.69
Dilatation +20%	0.37	47.58	-5.13
Permeability -20%	0.35	45.01	-10.26
Permeability +20%	0.45	57.86	+15.38
Water depth -20%	0.51	65.58	+30.77
Water depth +20%	0.37	47.58	-5.13
Cylinder pressure -20%	0.34	43.72	-12.82
Cylinder pressure +20%	0.54	69.44	+38.46
Heel jet flow -20%	0.37	47.58	-5.13
Heel jet flow +20%	0.43	55.29	+10.26
Lower arm angle -20%	0.50	74.76	+49.08
Lower arm angle +20%	0.38	40.40	-19.44

The data shown the table shows the production and the trailing speed at which the linear increase of the production as a function of the trailing speeds ends. In other words, the production for an increment of the shown trailing speed (in this case the increment is 0.01 m/s) does not follow the linear increase anymore.
As was mentioned before there is no data available for the production for a reduction of 20 percent of the angle of internal friction because for the plotted range of trailing speeds the linear increase did not end.
The largest increase in production, 49.08 percent, is found for a decrease of the lower arm angle by 20 percent. For an increase of the lower arm angle of 20 percent a decrease of 19.44 percent in production is found. This is a large decrease albeit considerably lower than the increase of 49.08 percent.
After the decrease of the lower arm angle the largest increase of the production, 38.46 percent, is achieved by increasing the hydraulic cylinder pressure by 20 percent. However, when the cylinder pressure is reduced by 20 percent the production decrease is only 12.82 percent. The largest decrease in production, also 38.46 percent, is found for an increase of the angle of internal friction.
After the increase of cylinder pressure the largest increase of production is found for a decrease of the water depth. For a decrease of 20 percent an increase of the in situ production of 30.77 percent is found. Meanwhile for an increase of 20 percent only a decrease of 5.13 percent is found.
The remaining dredging parameter is the heel jet flow. For an increase and decrease of 20 percent of the reference flow the production respectively increases by 10.26 percent and decreases with 5.13

percent. Hence, in the linear production regime the the heel jet flow seems to have the least influence on the in situ production.
The remaining soil parameters are the dilatation and the permeability. Of these parameters the dilatation seems to have the least influence on the production in the linear regime since a 20 percent increase and decrease respectively on lead to a 5.13 percent decrease and an 7.69 percent increase of the in situ production.
The permeability seems to have more influence on the in situ production. An increase and decrease of 20 percent respectively lead to a 15.38 percent increase and a 10.26 percent decrease. It must however again be kept in mind that the permeability ranges over a span of several orders of magnitude. Thus, if the reference value would have been chosen differently the increases and decreases would possibly be different as well.
All parameters, with the exception of the 20 percent increase of the angle of internal friction yield a production that lies within the common range of production (36 to 125 m^3/min). However, most of the trailing speeds related to the productions lie below the operational range of trailing speeds. Although most productions lie within the common range, they do lie in the lower half (below 80.5 m^3/min) if a symmetric distribution is assumed.

7.12.3 Comparison of the reference points

All production results that were found for a trailing speed of 1.5 knots with the exception of one, lie in the production regime in which the visor has already moved to a new equilibrium position. The production results for the end of the linear increase are still in the regime where the visor is still in the lowest position. This means that the actuator moment is likely to be larger than the cutting moment. It is possible though that there is equilibrium between the two moments in this point.
The overall production magnitude for the end of the linear increase points is larger than that of the points of 1.5 knots. Furthermore the results of the end of the linear increase point lie in the expected or right order of magnitude whilst the 1.5 knots points do not. This is surprising since the end of the linear increase points generally lie at trailing speeds below the operational range, whilst the other points are measures in the middle of the operational range. Therefore it would be expected that especially the points in the middle of the operational range would at least yield productions in the right order of magnitude.
The difference between the production magnitude of the two types of points can clearly be seen in the production graphs since the end of the linear increase is usually marked by a steep drop in production. Although production does increase again after the drop, this does not happen at a rate nearly as fast as the rate of the linear increase. This is however to be expected since the maximum production increase is when the cut slice thickness is at a maximum, which is when the visor still is at the lowest possible angle.

7.13 Validation of calculated tooth jet cutting forces

Up until this paragraph the results shown were all for a draghead with the geometry of the Wild Dragon but without the use of tooth jets. This is how most modern dragheads operate. With an actuator, cutting teeth and heel jets. However, what the Wild Dragon distinguishes from the other dragheads is the application of water jets in the cutting teeth. Therefore it is interesting to see what the effect of the tooth jets on the production is.
In chapter 3 it was explained that no cutting theory for cutting with tooth jets yet existed and that therefore an extension to the cutting theory of Miedema has been made by the author. In contrast to the cutting theory of Miedema, which has been validated with measurements, there is no data publicly available on the cutting forces of teeth with tooth jets. This makes it challenging to validate the cutting forces that are calculated using the tooth jet model.
In this paragraph it is attempted to validate the cutting forces with of the tooth jet model. In the next section the approach of the validation is explained. The section after that shows the actual validation.

7.13.1 Specific energy approximation of cutting force reduction

The validation of the calculated cutting forces of the tooth jet model will be done by using the fact that in general water jets cut a certain volume of soil more efficiently than teeth. In other words, in general the specific energy of a soil for cutting with water jets is lower than the specific energy of that same soil for cutting with teeth. A rule of thumb exists that states that the specific energy of jetting is about 70 percent of that of cutting with teeth. This rule of thumb is demonstrated in the following equation.

$$E_{sp-jet} \approx 0.70 \cdot E_{sp-blade} \tag{7.13.1}$$

Specific energy is defined as the amount of energy required to cut a volume of soil. Hence the SI unit of specific energy is $\frac{J}{m^3}$. Trailing power is defined as energy per unit of time and in situ production is defined as unit of volume per unit of time. Since both have a unit that consist of a unit per time the specific energy for a blade can also be expressed in terms of trailing power and production.

$$E_{sp-blade} = \frac{P_{cutting}}{Production} = \frac{F_h \cdot v_c}{W \cdot v_c \cdot h_i} \tag{7.13.2}$$

Equation (7.13.2) shows that when the parameters needed to calculate the horizontal cutting force are known the specific energy can be calculated (since the other parameters in the equation are also needed to calculate the horizontal cutting force).
The power of water jets can be expressed in terms of the total jet flow and the pressure difference over the jet nozzle. If this power is divided by the production then the specific energy for the jetting process can be defined.

$$E_{sp-jet} = \frac{P_{jetting}}{Production} = \frac{Q_{jet} \cdot \Delta p_{jet}}{W \cdot v_c \cdot h_i} \tag{7.13.3}$$

Since from equation (7.13.1) the relationship between jetting specific energy and cutting specific energy is described a blade cutting equivalent specific jetting energy can be derived. This is shown in the following equation.

$$E_{sp-equivalent} = \frac{E_{sp-jet}}{0.70} = \frac{\frac{Q_{jet} \cdot \Delta p_{jet}}{0.70}}{W \cdot v_c \cdot h_i} \tag{7.13.4}$$

If a situation A is observed in which only a blade is cutting the soil then if all inputs needed to calculate the cutting force are known then the specific cutting energy can be calculated. Now a situation B is observed with a blade under the same cutting conditions, hence the soil parameters are the same, the cut layer thickness, the trailing speed et cetera. The only difference is that now the teeth have tooth jets. Since the cutting conditions are the same for situation A and B the specific cutting energy of situation A must be the equal to the cutting equivalent specific energy of situation B. This is shown in the following equation.

$$E_{sp-cutting,A} = \frac{F_{h,A} \cdot v_c}{W \cdot v_c \cdot h_i} = \frac{F_{h,B} \cdot v_c + \frac{Q_{jet} \cdot \Delta p_{jet}}{0.70}}{W \cdot v_c \cdot h_i} \tag{7.13.5}$$

The difference between the cutting force in situation A and B is now defined as ΔF_h. This is the difference in horizontal cutting force between a situation without tooth jets and a situation with tooth jets. An expression for ΔF_h can be found by rewriting equation (7.13.5).

$$\Delta F_h = F_{h,A} - F_{h,B} = \frac{Q_{jet} \cdot \Delta p_{jet}}{0.70 \cdot v_c} \tag{7.13.6}$$

Equation (7.13.6) shows that if for a certain trailing speed the jet pressure and flow are known or simply the jet power is known then the difference in horizontal cutting force between a situation without jets and a situation with jets for the same cutting conditions can be calculated.
Since the jet pressure is an input for the tooth jet model and the total jet flow is calculated based on the soil resistance and the jet pressure and expected cutting force difference can be calculated based on the specific energy rule of thumb. This cutting force difference can then be compared to the cutting force difference that the tooth jet model actually calculates. The difference between these two cutting force differences might give an indication of how valid the cutting forces of the tooth jet model are.

7.13.2 Comparison of cutting force reductions

In the previous section it was shown that when the jet power and the trailing speed are known then an expected reduction of the horizontal cutting force can be calculated. When this expected reduction is subtracted from the horizontal cutting force without tooth jets (for equal cutting conditions) then an expected tooth jet horizontal cutting force can be calculated. This expected tooth jet horizontal cutting force can then be compared to the actual tooth jet horizontal cutting force of the tooth jet model. If it is assumed that the cutting force reduction calculated with the rule of thumb approach gives a reasonable estimate of the cutting force reduction then the difference between the expected reduced cutting force and the actual reduced cutting force can say something about the performance of the tooth jet model. However, only the difference between the two reduced cutting forces does not say much about the actual performance of the tooth jet model. It should therefore be put in perspective by dividing the difference between the two reduced cutting forces by the non-reduced horizontal cutting force. This can be expressed in the following equation.

$$\%Difference_{model,E_{sp}} = \frac{F_{h,B_{E_{sp}}} - F_{h,B_{model}}}{F_{h,A}} \tag{7.13.7}$$

In equation (7.13.7) $F_{h,B_{E_{sp}}}$ is the reduced horizontal cutting force calculated by the specific energy approach and $F_{h,B_{model}}$ is the reduced horizontal cutting force calculated by the tooth jet model.
For the comparison different trailing speeds in the operating range are used: 0.5 knot, 1.0 knot, 1.5

knots and 2 knots. In SI units these trailing speeds are respectively: $0.2572m/s$, $0.5144m/s$, $0.7716m/s$ and $1.0228m/s$. From a manual iteration for the Liberty Island jet water system (see appendix K) a jet pressure of about 0.5 bar was found. This seems to be very low, considering that the maximum pressure that the pump can deliver is 10.0 bar. However, the pressure of 10.0 bar is at zero flow. Also, losses in the piping are expected. Therefore the three jet pressures chosen for the comparison are considerably lower than 10.0 bar: 1.0 bar, 3.0 bar and 5.0 bar.
The conditions for the comparison are the same as the conditions when the production results are calculated: the same draghead geometry, the same heel jet model, the same soil parameters et cetera. Furthermore the flow that can flow through the tooth jets will not be limited to a maximum. The pressure source of the jets lies at a distance of 30 percent of the total blade length from the tip. The same will be done with the production calculations with tooth jets.
For both blades of the Wild Dragon draghead the percentages of difference will be plotted for different jet pressures and trailing speed combinations. The percentages of difference will be plotted against the visor angle. The percentages difference will only be plotted for the visor angles for which the blade is actually cutting. This means that as soon as the blade starts cutting in the liquefied layer of the heel jets the line stops. Furthermore when the cutting force reduction of both approaches is such that the horizontal cutting forces is completely reduced to zero then there is no difference in reduction (since the tooth jets do not cause a negative cutting force) and thus no line is plotted either. Due to these reasons the lines in the graphs will end at different visor angles.
For both blade 1 and blade 2 of the Wild dragon draghead the difference between the tooth jet model and the specific energy approximation relative to the original cutting force are plotted for a range of visor angles in respectively figure 7.50 and 7.51. Each graph consists of four series, each belonging to a different trailing speed and each consisting of three data sets for different jet pressures. Each series is distinguished with a different line marker.
What is clearly noticeable in both graphs is that all peaks of the lines lie above zero and that the lines in general hardly go below zero. Based on equation (7.13.7) this means that with respect to the specific energy approximation, the tooth jet model in general is more likely to overestimate the cutting force reduction. This means that for the cutting conditions at a given peak the tooth jet model calculates a lower cutting force than the specific energy approximation. When comparing the graph of blade 1 with the graph of blade 2 it seems that all peaks of blade 2 have shifted to the right. This is due to the influence of the heel jets. For all four trailing speeds that are used the heel jets only penetrate the layer in reach of blade 1. This means that for any trailing speed blade 2 has to cut a thicker layer of sand than blade 1. This indicates that the peaks might be related to smaller cut slice thicknesses. Another indication that the peaks in the graphs might be related to the smaller cut slice thicknesses is that in the graph of blade 1 the peaks for one series (one trailing speed) seem to be clustered together. The left-most cluster is the series with the lowest trailing speed and hence the highest heel jet penetration. The clusters move right for increasing trailing speed. Right means higher visor angles an thus smaller cut slice thicknesses.
It can also be noticed that once a maximum has been reached, the line steeply drops to zero. Zero in this case means that both the model and the approximation completely remove any horizontal cutting force. For a cluster the line of the highest jet pressure always seems to go to zero first. This is to be expected since a higher jet pressure means a greater reduction of the original cutting force.
The explanation for the peaks of difference is that as the visor angle increases the cut slice thickness decreases. As a result of this decrease and an increase of the shear angle, the length of the shear plane ($\frac{h_i}{sin(\beta)}$) decreases at an even greater rate. Therefore the flow resistance of resistor R_5 decreases at a great rate which results in an increase of jet flow and a decrease of the cutting force. The force reduction of the approximation increases linearly proportional to the increase of the jet flow (see equation (7.13.6)) whilst the reduction calculated by the tooth jet model increases with a proportionality greater than linear. This creates an increase of the difference. However, at some point the tooth jet

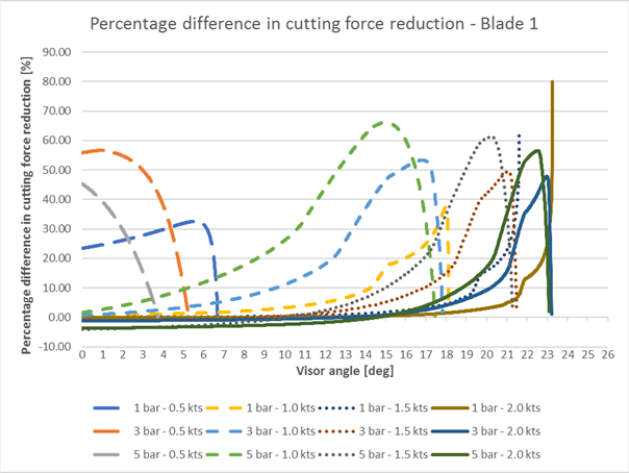

Figure 7.50: The differences in cutting force reduction between the tooth jet model and the specific energy approximation for blade 1

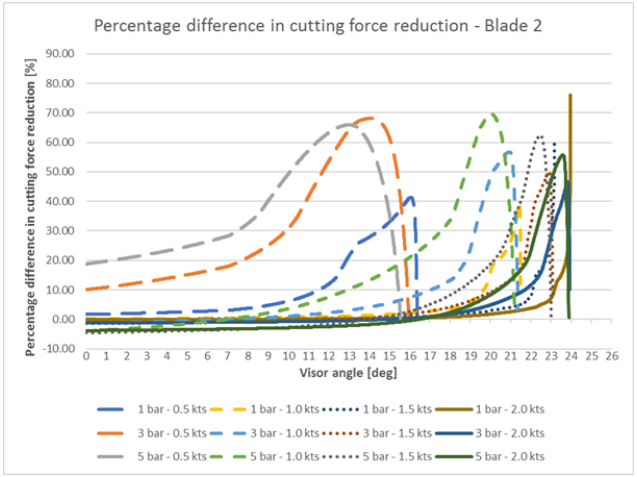

Figure 7.51: The differences in cutting force reduction between the tooth jet model and the specific energy approximation for blade 2

cutting force reduction reaches a maximum, the original cutting force is completely reduced to zero. Since an increase in visor angle only leads to a decrease of the original cutting force the difference between the approximation and the model can only get smaller. Hence, eventually the approximation catches up with the model and the difference becomes zero.

7.13.3 Usability of the tooth jet model

In the previous section the cause of the peaks in the difference plots was explained. Most of these peaks lie in a range of 40 and 70 percent cutting force reduction with respect to the original cutting force. This makes the tooth jet model to seem performing poorly and raises the question whether the tooth jet model is suitable to use in the production model. However, until now only the position and maximum of the peaks have been observed and no attention has been paid to the overall course of the difference or the performance of the tooth jet model in relation to the production model.
If the graphs in figures 7.50 and 7.51 are observed it can be seen that the higher the trailing speed the longer the the cutting force reduction difference stays within the margin of plus and minus 20 percent. This margin has however been chosen arbitrarily as an acceptable margin. It can be seen that the higher the trailing speed the longer the force reduction difference stays close to zero percent. This is partially caused by the fact that the influence of the water jets reduces at the higher trailing speeds which leads to small force reductions relative to the original cutting force. This is however in line with the specific energy approximation as can be seen in equation (7.13.6) where the trailing speed is in the denominator.
To answer the question whether the tooth jet model is still usable in the production model, the general course of the production as a function of the trailing speeds must be observed. This was already done in section 7.4.4 for the reference production with the quasi-cloud model. In this production course the visor angle stays at the lowest possible angle starting at $0.1m/s$ until roughly $0.3m/s$. This means that the cutting forces are not big enough to generate moments that can push the visor up. Since adding the tooth jet model would only make these cutting forces smaller the moments that are generated get even smaller and thus the visor stays in the lowest possible angle until at least the same trailing speed. However, it is likely that the visor will stay in the lowest position for higher speeds when tooth jets are used compared to when no tooth jets are used. For the production at low trailing speeds (in the

range of 0.5 knots) the difference in force reduction does not have any effect. However, the difference or error does affect the calculated cutting forces which are therefore likely to be too low. This would lead to a calculated required cutting force that is too low for those speeds.
After further increase of the trailing speed, the cutting forces will eventually be large enough to generate a moment that will push the visor out of the soil to a new equilibrium position. As was established earlier, this will not happen until at least a trailing speed of $0.3m/s$ but it is more likely that it will happen somewhere between the 1 and 1.5 knots (0.5144 and 0.7716 m/s) since the tooth jets reduce the cutting forces. When looking at the force difference graphs it can be seen that the lines for 1 and 1.5 knots all stay within the margin of plus and minus 20 percent until at least a visor angle of 8.5 degrees for blade 1 and at least 15.5 degrees for blade 2. This means that for these trailing speeds the difference between the model and the approximation is still within the acceptable margin for a large range of visor angles. The fact that blade 2 is performing better in terms of the cutting force difference is an advantage because blade 2 has the largest moment arms and will thus deliver the largest moment against the actuators which means that the total cutting moment and hence production are still calculated at a reasonable accuracy.
Whether the calculated difference in cutting force reduction is still acceptable at the higher end of the operating range (2.0 knots and up) is again very much dependent on the visor angle. In the reference production graph without tooth jets the visor angle is about 20 degrees at a speed of 1 knot. This would mean that the visor angle with tooth jets would be lower and thus the cutting force difference is still within the acceptable margin for both blades.
Overall it can be concluded that if the approximation of section 7.13.1 is considered to be accurate then for the operating range of trailing speeds the calculated production can also be considered to be reasonably accurate. The calculated cutting forces will in general be lower than what they in reality would be, albeit within an acceptable margin. The exception here is the calculated cutting forces at the lower end of the operating range since here the difference between the approximation and the model can be as large as 55 percent of the original cutting force, these do however not affect the production.

7.14 Sensitivity analysis with tooth jets

In this paragraph a sensitivity analysis will be done for the production model with the tooth jet model included. Since much of this sensitivity analysis is done the same way as the previous sensitivity analysis only the highlights will be shown instead of the whole process. Therefore this analysis will be covered in one paragraph instead of multiple.
In the first section a new parameter, the tooth jet pressure, will be introduced. The section after that the reference production for the production model with a reference tooth jet pressure will be shown. In the third section the results of the sensitivity analysis for a trailing speed of 1.5 knots will be discussed. The last section will cover the results of the sensitivity analysis for the end of the linear increase.

7.14.1 Tooth jet pressure reference

When the tooth jet model is added to the production model there is need for a new input parameter, the tooth jet pressure. This pressure is defined as the pressure drop over a tooth jet nozzle. In contrast to the heel jets the pressure in this case is not directly interchangeable with the jet flow according to the relationship shown in equation 7.3.4, because in the tooth jet model the jets are not assumed to be free-flowing.

The magnitude of the tooth jet pressure in reality is hard to predict since it is likely to be dependent on the permeability of the soil that the teeth are cutting. In order find a reasonable magnitude of the pressure a manual iteration with a parallel resistor model was done (see appendix K). However, the result of this, about 45 kPa, seems very low. Therefore the heel jet pressure is used as a reference. This pressure, in the reference case, is $3.89 \cdot 10^5 Pa$. The tooth jets however, have more flow resistance due to more piping and the soil that they are cutting and therefore a lower jet pressure must be expected. For the reference value of the tooth jet pressure therefore a pressure of $3.0 \cdot 10^5 Pa$ is chosen. This reference parameter together with the plus and minus 20 percent variations is shown in table 7.30.

Table 7.30: The parameters changing when the tooth jet pressure is changed

Parameter	-20%	Reference	+20%	Unit
Δp_{jet}	$2.4 \cdot 10^5$	$3.0 \cdot 10^5$	$3.6 \cdot 10^5$	Pa

7.14.2 Reference production - Tooth jets

In this section the reference production and concentration for the production model with the quasi-cloud model and the tooth jet model are discussed. The tooth jet model in the sensitivity analysis will be run without any restrictions on the maximum tooth jet flow and thus this will also be the case when the reference production is calculated.
The general model settings used during the sensitivity analysis with tooth jets will be the same as those of the sensitivity analysis without tooth jets and can be found in section 7.4.2. The reference parameters are the same too with the exception of the new tooth jet pressure. The reference parameters are summarized below.

- $\phi = 36°$
- $\delta = 24°$
- $\epsilon = 0.16$
- $n_i = 0.4$
- $n_{max} = 0.483$
- $k_i = 0.000025 m/s$
- $k_{max} = 0.0000591 m/s$
- $z = 15m$
- $p_{Cylinder} = 25 \cdot 10^5 Pa$
- $Q_{heel} = 0.010468 m^3/s$
- $p_{heel} = 3.89 \cdot 10^5 Pa$
- $\Gamma = 0°$
- $\Delta p_{jet} = 3.0 \cdot 10^5 Pa$

The course of the production for increasing trailing speed is generally the same for all variations of the sensitivity analysis, as was the case with the sensitivity analysis without the tooth jets. Therefore the general features will only be discussed in this section. Furthermore a description per variation as

was done in the analysis without tooth jets will not be done for this analysis. This is because the analysis in paragraphs 7.5 through 7.11 have shown that most differences are only slight differences in the production which can also be noted when simply summarized in a table. The production and concentration graph per variation can however still be found in appendix L. The auxiliary graphs showing the cutting forces, moments and cutting parameters are also, just as was the case without tooth jets, only shown in this section.

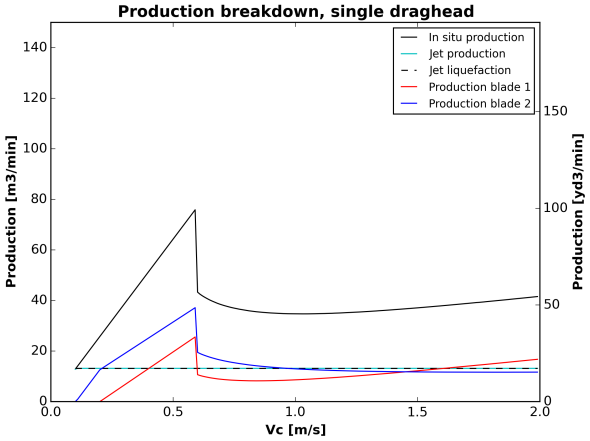

Figure 7.52: The production breakdown of the reference production with the quasi-cloud model and tooth jet model

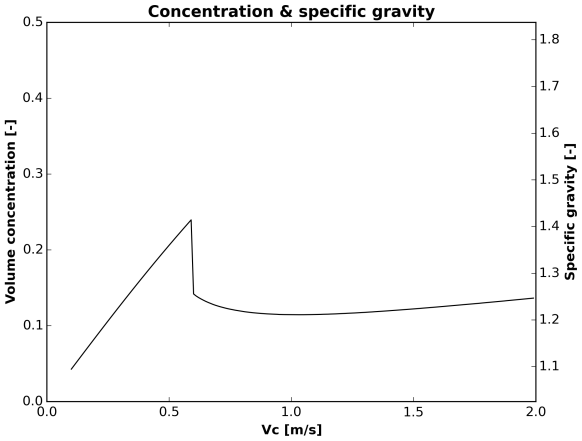

Figure 7.53: The concentrations and specific gravity of the reference production with the quasi-cloud model and tooth jet model

The description of the course of the in situ production graph of figure 7.52 starts at the lower speeds on the left and will move to the higher speeds on the right.
Starting at 0.1 m/s a linear increase of the production can be seen that ends at roughly 0.6 m/s. This linear increase means that the visor angle and thus the total slice thickness remains constant. In this case at the lowest possible position is a visor angle of zero degrees ($\Psi = 0°$), this can be seen in the second graph of figure 7.56. The black line of the third graph shows the constant slice thickness. When the visor is in the lowest possible position the actuator moments at that trailing speed and visor angle are larger than the combined cutting moments. This can be seen in the second graph of figure 7.54. In this graph it can be seen that the cutting moment of blade 2 during the linear increase is actually negative and thus helping the actuator.
What also can be noted in the range of the linear increase is a small jump in the moment arms at roughly 0.2 m/s for the moment arms of blade 2 and at roughly 0.25 m/s for the moment arms of blade 1 in figure 7.55. This jump occurs when pore under pressures appear or disappear on the blade. In this situation for the increase of the trailing speed the tooth jets are not able anymore to fully remove any under pressures at the tip of the blade and therefore pore under pressure start to exist on the blade. The acting point of a force is calculated using the pore under pressure distribution on the blade. When there is no under pressure on the blade then the acting point lies at the tip of the blade. When a pore under pressure starts to exist on the blade this acting point will move up the blade and this changes the moment arms hence causing the jumps in the moment arms. The jumps in the moment arms can also be seen in the separate cutting moments in the form of a small bend.
Eventually as the trailing speed increases the cutting moment at the lowest visor angle becomes larger than the actuator moment and thus the visor will move up to find a new moment equilibrium. This equilibrium is found at roughly 13 degrees. This change of about 13 degrees for a speed increment

of 0.01 m/s does however cause a large drop in the production, which can be seen at about 0.6 m/s. More about the change in visor angle in relation to the production can be found in appendix I.

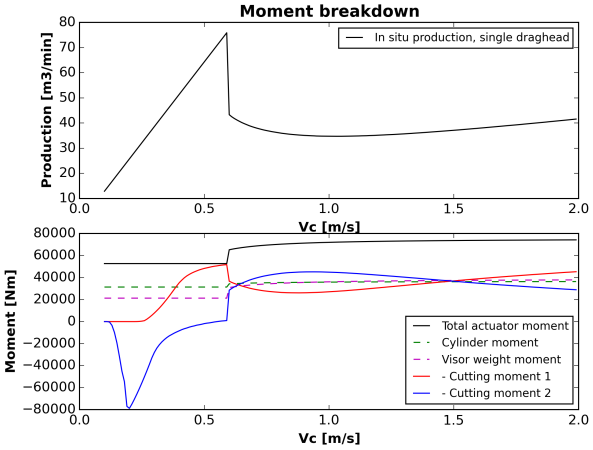

Figure 7.54: The moment breakdown of the reference production with the quasi-cloud model and the tooth jet model

After the large drop the production continues to decrease until a trailing speed of roughly 1.1 m/s is reached. The production then starts to increase again. This increase might seem linear but is in fact non-linear. This is caused by the non-linear decrease of the penetration depth of the heel jets and the non-linear increase of the actuator moment as a function of the visor angle.
When looking at the magnitude of the in situ production in the range of operational speeds (about 0.5 to 1.0 m/s) it can be seen that the production always lies in the range of common productions (36 to 125 m^3/min). After the drop of production at roughly 0.6 m/s the production is at the lower side of the production range though. Over the entire plotted range the calculated concentrations lie nicely within the range of common concentrations (1.1 to 1.5 specific gravity).
In the previous paragraph it was shown that the cutting forces calculated using the tooth jet model can show large differences with cutting forces calculated using a specific energy type of approach. It is therefore interesting to check how large the percentage of difference is at different trailing speeds of the reference production. To do this the graphs of section 7.13.2 are used in combination with the graph in figure 7.56. At the trailing speed of half a knot (roughly 0.25 m/s) the visor angle is zero degrees. For a jet pressure of 3 bar this leads to a difference for blade 1 and 2 of respectively 56 and 10 percent. For a trailing speed of 1 knot (roughly 0.5 m/s) the visor angle is still zero degrees, which leads to percentages difference of both blades which are approximately 1 percent. For a trailing speed of 1.5 knots (roughly 0.75 m/s) the visor angle is approximately 13 degrees. This leads to a percentage difference for blade 1 and 2 of respectively 4 and 1 percent. The last trailing speed is a speed of 2 knots (roughly 1.0 m/s) for which the visor angle is approximately 20 degrees. This leads to a percentage difference for blade 1 and 2 of respectively 9 and 5 percent. The differences at a low trailing speed are very big. They do however not lie within the operational range of trailing speeds and are therefore not really an issue. Within the range of operational trailing speeds a maximum difference of only 9 percent is found which is very acceptable.

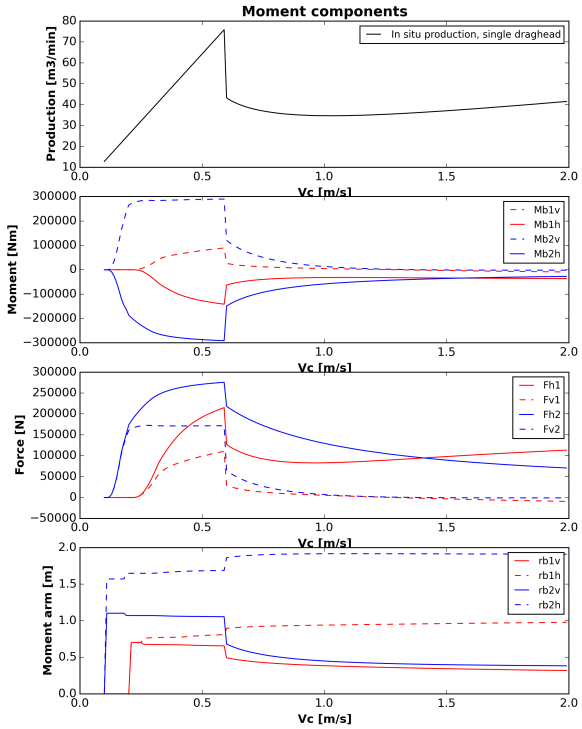

Figure 7.55: The moment components of the reference production with the quasi-cloud model and the tooth jet model

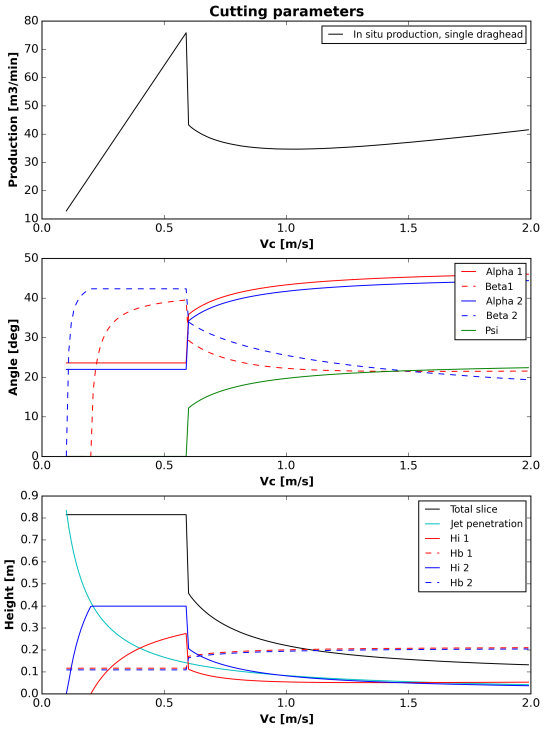

Figure 7.56: The cutting parameters of the reference production with the quasi-cloud model and the tooth jet model

7.14.3 Summary 1.5 knots results - Tooth jets

The results of the sensitivity analysis are shown in table 7.31. As was mentioned before the description of the production per variation has been left away because usually only slight differences between the variations can be noted. In addition to the plain results also the percentage difference with the reference value has been calculated. This is shown in the fourth column of the table.
The most notable parameters in the table are the parameters that lead to a percentage difference of 170.81 percent with respect to the reference production. These parameters are: the angle of internal friction increased by 20 percent, the water depth decreased with 20 percent, an increase of 20 percent of the hydraulic cylinder pressure and a decrease of the lower arm angle of 20 percent. For all these parameters the production is 99.01 m^3/min, which lies well within the range of common productions. The fact that these parameters have the same production for the same trailing speed indicates that for these parameters at 1.5 knots the linear increase is still present. This again makes comparing the performance for these parameters with the rest of the parameters unfair since in the linear increase regime there is likely no moment balance whilst in the other regime there must be a moment balance. When the order of magnitude of the production of the linear increase parameters is compared to the production for the other parameters it can be seen that the linear increase production is roughly a factor 3 larger. This is not surprising since after most linear increases a large drop in production can be seen.
When the parameters that lead to a linear production at 1.5 knots are neglected then the largest difference, a decrease of 18.07 percent, is found for an increase of the angle of internal friction of 20

percent. After this parameter an increase of 20 percent of the permeability leads to an increase of production of 17.31 percent. Meanwhile a decrease of the permeability of 20 percent leads to the second largest decrease of production, a decrease of 12.80 percent.

Table 7.31: Summary of the production results of the sensitivity analysis at 1.5 knots trailing speed with tooth jets

Parameter	Trailing speed $[m/s]$	Production $[m^3/min]$	Percentage difference [%]
Reference	0.77	36.56	0.00
Angle of internal friction -20%	0.77	99.01	+170.81
Angle of internal friction +20%	0.77	29.96	-18.07
Dilatation -20%	0.77	39.80	+8.85
Dilatation +20%	0.77	34.89	-4.58
Permeability -20%	0.77	31.88	-12.80
Permeability +20%	0.77	42.89	+17.31
Water depth -20%	0.77	99.01	+170.81
Water depth +20%	0.77	35.90	-1.82
Cylinder pressure -20%	0.77	34.33	-6.11
Cylinder pressure +20%	0.77	99.01	+170.81
Heel jet flow -20%	0.77	32.09	-12.23
Heel jet flow +20%	0.77	41.91	+14.64
Lower arm angle -20%	0.77	99.01	+170.81
Lower arm angle +20%	0.77	35.96	-1.65
Tooth jet pressure -20%	0.77	34.73	-5.02
Tooth jet pressure +20%	0.77	38.66	+5.73

After the aforementioned parameters the parameter with the largest decrease and increase is the heel jet flow. For a decrease and increase of 20 percent respectively a decrease of 12.23 percent and an increase of 14.64 percent of the in situ production are found.
A decrease and increase of 20 percent of the dilatation respectively lead to an increase of production of 8.85 percent and a decrease of production of 4.58 percent.
Decreasing and increasing the tooth jet pressure with 20 percent leads to respectively a decrease of 5.02 percent and an increase of 5.73 percent in production.
A decrease of the cylinder pressure of 20 percent leads to a decrease of production of 6.11 percent.
What is striking is that the increased counterparts of the parameters with the two smallest decreases both are still in the linear regime at 1.5 knots. These two parameters are an increase of the water depth and an increase of the lower arm angle by 20 percent. Their respective decreases of the production are 1.82 and 1.65 percent.
The overall magnitude of the production for the parameters that are not in the linear production regime at 1.5 knots is quite low. Most productions of these parameters lie around the 15th percentile of the production of 36 m^3/min. This is odd because the trailing speed of 1.5 knots has been chosen because it lies in the middle of the normal operating range. Therefore also a production that is roughly in the middle of the normal production range would be expected (about 80.5 m^3/min).
The parameters that do have a linear increase at 1.5 knots yield a production that lies well within the common range of production (15th and 85th percentile, 36 to 125 m^3/min) with a production of 99.01 m^3/min.

7.14.4 Summary end of linear increase results - Tooth jets

The results of the sensitivity analysis are shown in table 7.32. In addition to the plain results also the percentage difference with the reference value has been calculated. This is shown in the fourth column of the table. Good to note is that the percentage difference in production is the same as the percentage difference in trailing speeds since the production in this regime is linearly proportional to the trailing speed. This is with the exception of the changes in lower arm angle because changes in this angle change the maximum total slice thickness at the lowest possible visor angle.

Table 7.32: Summary of the production results of the sensitivity analysis for the end of the linear increase with tooth jets

Parameter	Trailing speed $[m/s]$	Production $[m^3/min]$	Percentage difference [%]
Reference	0.59	75.87	0.00
Angle of internal friction -20%	-	-	-
Angle of internal friction +20%	0.35	45.01	-40.68
Dilatation -20%	0.65	83.58	+10.17
Dilatation +20%	0.55	70.72	-6.78
Permeability -20%	0.47	60.44	-20.34
Permeability +20%	0.71	91.30	+20.34
Water depth -20%	0.83	106.73	+40.68
Water depth +20%	0.53	68.15	-10.17
Cylinder pressure -20%	0.49	63.01	-16.95
Cylinder pressure +20%	0.85	109.30	+44.07
Heel jet flow -20%	0.59	75.87	0.00
Heel jet flow +20%	0.59	75.87	0.00
Lower arm angle -20%	0.82	105.44	+38.98
Lower arm angle +20%	0.52	66.87	-11.86
Tooth jet pressure -20%	0.54	66.87	-8.47
Tooth jet pressure +20%	0.63	81.01	+6.78

The data shown in the table shows the production and the trailing speed at which the linear increase of the production as a function of the trailing speed ends. In other words, the production for an increment of the shown trailing speed (in this case the increment is 0.01 m/s) does not follow the linear increase anymore.
As was the case for the end of the linear increase results for a draghead without tooth jets, there is no data available for the production and trailing speed for the reduction of the angle of internal friction by 20 percent. This is due to the fact that the linear increase does not end in the plotted range.
The largest increase, an increase of 44.07 percent with respect to the reference value, is found for an increase of the cylinder pressure by 20 percent. A decrease of the cylinder pressure with 20 percent does however not lead to a decrease nearly as large. A decrease of only 16.95 percent is found.
After the increase of the cylinder pressure the largest change found is 40.68 percent. An increase of the angle of internal friction leads to a decrease of the in situ production of 40.68 percent. An increase of 40.68 percent is found for a decrease of the water depth of 20 percent. Again, an increase of the parameter by 20 percent does not lead to a change nearly as large. When the water depth is increased with 20 percent then the in situ production only decreases with 10.17 percent.
After the aforementioned parameters a reduction of the lower arm angle with 20 percent leads to the largest increase of production, an increase of 38.98 percent. The change in production for a reduction

of the lower arm angle with 20 percent is a decrease of 11.86 percent.
The decrease and increase of 20 percent of the permeability respectively lead to a decrease and increase of the production of 20.34 percent. This is interesting to see since both the increase and decrease lead to the same percentage of difference, albeit in opposite signs. Furthermore the percentage is nearly 20 percent which basically means that for these input conditions the production seems to be linear proportional to the permeability.
Decreasing and increasing the dilatation by 20 percent respectively leads to an increase of 10.17 and a decrease of 6.78 percent.
Changing the tooth jet pressure also does not lead to large changes in production. For an increase of the jet pressure of 20 percent the production only increases with 6.78 percent. A decrease of 20 percent leads to a decrease in production of 8.47 percent.
For a decrease and increase of 20 percent of the heel jet flow no change is seen in the production. This does not necessarilly mean that there is no change, but the change is at least smaller than the change in linear production for a change of 0.01 m/s in trailing speed.
All calculated productions for the varied parameters lie within the range of common productions (36 to 125 m^3/min). However, some of the trailing speeds lie below the operational range of trailing speeds of 1 to 2 knots (roughly 0.5 to 1.0 m/s).

7.14.5 Comparison of the reference points - Tooth jets

The production results for a trailing speed of 1.5 knots show that for most parameter variations, at this speed, the visor is no longer in the lowest possible position. This means that the visor has already moved to find a new moment balance. Only four parameter variations were still in the linear increase regime. The productions for these four variations also lie nicely within the common production range. The other productions lie on the low side or below the common production range. This is odd since the trailing speed is in the middle of the operational range.
The production results for the end of the linear increase all lie within the common production range. However their associated trailing speeds do not all lie within the operation range.
It is odd to see that productions in the middle of the operational range of trailing speeds lie on the low side of the expected production range or even lie below this range whilst for the linear increase the magnitude of the production might be right but the trailing speed is below the operation range. This clearly shows that there are two production regimes. The linear regime in which there not necessarily a balance between the actuator moments and the cutting moments and the other regime where the visor has moved and where there is a moment balance.

8 Discussion of Results

8.1 Introduction

In this chapter various aspects of the draghead production model are evaluated. The first aspects that will be discussed are the inputs that the model requires. This is followed by a discussion about the cutting forces that are calculated by the model and the influences of the cavitation cloud and the tooth jet model. The last paragraph will focus on the production that is calculated by the model. This means that there is looked at the influence of the tooth jets and how the model results compare to reality. It also includes the slurry concentration that is calculated.

8.2 Model inputs

8.2.1 Soil mechanical inputs

As can be seen in this report there are quite a number of soil parameters needed as an input for the production model: The angles of internal and external friction, the initial and maximum porosity, the initial and maximum permeability and the density of the sand grains. Another parameter that can be calculated using the porosities is the dilatation. Of all these parameters the easiest one to obtain is probably the density of the sand grains since this is usually simply assumed to be the density of pure quartz.
The other parameters are harder to obtain since they are usually not measured for a dredging job. For a dredging job usually only a grain size distribution is known. This does however not mean that the other soil parameters cannot be measured. Laboratory experiments exist in which the angle of internal, the angle of external friction, the initial permeability or the initial porosity can be measured. However, measuring the porosity or permeability after shearing will still be a challenge since the soil sample somehow has to be sheared while it is in the test setup. Another problem with laboratory experiments is that it is (near) impossible to get a soil sample without disturbing it. Therefore it is always the question how well the laboratory results of a disturbed soil sample match with the in situ conditions of the soil. Besides the question how well the laboratory results match reality other downsides of the laboratory tests are that they can be very time consuming and expensive (due to both equipment costs and the time consumption).
An alternative to laboratory experiments is using the grain size distribution, if it is known, to calculate the soil mechanical inputs. In appendix F equations are shown that use (parts of) the grain size distribution to calculate the permeability and other parameters of the soil. However, especially for the permeability many different papers with equations exist that try to predict the permeability based on the grain size distribution and the results of these papers do not necessarily match well for the same inputs. Equations that for instance only use a d_{10} as an input will yield the same result for two distributions as long as these two distributions have the same d_{10}. However, if the distributions are not the same then different results will be obtained when using equations that use the whole grain size distribution. Assuming that comparable things can happen for equations that try to predict other soil mechanical parameters again raises the question how well the outcomes of these calculations match the in situ conditions.

Even if the soil parameters obtained from a laboratory measurement or the grain size distribution reliably represent the in situ conditions of a soil then it is still possible that these results are only representative for the conditions in that particular part of the soil. On other locations in the same borrowing area different soil parameters might be found for soil samples. This would mean that it might be needed to take several samples and find average soil parameters for the entire area.
Until now the discussion was only about which method will yield soil parameters that come closest to the in situ soil parameters. However, a question that must be asked is whether a deviation of an input parameter with respect to the real in situ condition leads to large differences between the calculated and the real production. To answer this question the results of the sensitivity analysis must be analyzed.
In the sensitivity analysis the soil parameters that are varied are: the angle of internal friction, the dilatation and the permeability. When the angle of internal friction is varied then also the angle of external friction changes since it is assumed that it is two-thirds of the angle of internal friction. The dilatation is calculated using the initial and the maximum porosity. Furthermore the initial and the maximum porosity influence the initial and maximum permeability. When the permeability is varied in the sensitivity analysis only the permeability changes.
Out of all four analyses (two times at 1.5 knots, with and without tooth jets and two times the end of the linear increase, with and without tooth jets) the same ranking of the three soil mechanical parameters follows. Production changes the most for changes in the angle of internal friction. Reductions of the angle of internal friction even lead to a production that is linear (read optimal) for the entire range of operational trailing speeds. After the angle of internal friction the production changes the most for changes in the permeability. The production model is the least sensitive for changes in dilatation.
Because the production model seems to be very sensitive for the angle of internal friction it is important to have a good estimate of the magnitude of this parameter. Many methods exist to measure the angle of internal friction using a soil sample. The equipment needed for these measurements can however be very costly. Alternatively it is shown that the angle of internal friction can be calculated using a particle size distribution (PSD) in appendix F. Another commonly known parameter of the soil of the borrowing area is the SPT value (Standard Penetration Test) in blows per foot. Using equations of Miedema [4] the angle of internal friction can also be calculated based on this value. Combining the results of a PSD-based and a SPT-based method might lead to a reasonable estimate of the angle of internal friction and would thus prevent the need of expensive measuring equipment. If this equipment is already available then the measured angles of internal friction should be preferred over the calculated angles.
The permeability also has a relatively large influence on the production, albeit not nearly as large as the influence of the angle of internal friction. When tooth jets are used the production model seems to be the most sensitive to the permeability. This can be explained by the fact that the permeability is used to calculate the flow resistance of the jet flow lines and thus has a direct influence on the flow of jet water that flows to the shear zone. Even though the change in production for the change in permeability is not nearly as large as that of the angle of internal friction it must be kept in mind that contrary to the angle of internal friction a variation of plus and minus 20 percent does not nearly cover the entire range of possible permeabilities since the range of permeabilities for sand spans several orders of magnitude. This means that a chosen initial permeability can have a magnitude that is not uncommon for sands and that the production model using this permeability still yields productions that show a large deviation from the actual production. The maximum permeability can be calculated (estimated) based on the initial permeability and the dilatation. The sensitivity analyses show that the influence of the dilatation on the production is relatively small since the maximum change of production that is seen, for a change of dilatation of 20 percent, is 10.17 percent. Also, the sensitivity analysis for the dilatation almost covers the entire range of dilatation (roughly 0.10 to 0.20). It therefore seems that it is most important to accurately estimate or measure the initial permeability.

The maximum permeability can then simply be calculated based on the initial permeability and the dilatation. However, obtaining a correct value for the in situ permeability might be challenging due to the various reasons that were discussed earlier in this paragraph.
Concerning the dilatation, it seems that if no data on the dilatation is available then choosing a dilatation in the middle of the range might still yield reasonably accurate productions because the change of the production over the range of dilatations is relatively small. This said, measuring the porosity of a densified soil sample and then measuring the porosity of the same sample but loosely poured is relatively easy and might already give an estimate of the dilatation that is closer to reality than simply using the middle value. However, it is also possible that this approach is on the conservative side since it leads to a high value of the dilatation which leads to large cutting forces and therefore a lower production compared to situations with a smaller dilatation. Furthermore choosing a low initial porosity (dense soil) leads to a smaller jet penetration when using the equations of Vlasblom or Weegenaar compared to jet penetration of soil with a higher initial porosity, which will also contribute to the lower production for the low porosity case.

8.2.2 Equipment inputs

The equipment inputs of the production model can be split up in roughly three groups: the draghead geometry, the actuator parameters and the jet parameters. Using polar coordinates the relevant geometry of a draghead with two sets of teeth can be described by only 16 parameters. Most of these can simply be measured in the technical drawings of a draghead. The exceptions are the polar coordinates of the center of gravity of the visor. If the center of gravity is not indicated in a drawing then its position might be found by looking at the mass properties of a 3D model of the draghead in a CAD program. Alternatively an estimate of the position of the center of gravity might be made using the technical drawings of the draghead. This can however be a time consuming process, dependent on the desired accuracy of the estimate.
The actuator parameters for the Wild Dragon draghead are simply the mass of the visor, the diameter of the hydraulic cylinder and the operating pressure of the hydraulic cylinder. Both the mass and the cylinder diameters are easy to obtain since they both are indicated in technical drawings. The operating pressure(s) of the hydraulic cylinder should also not be problematic to obtain since these are indicated in the specifications of the draghead.
Of the equipment inputs the jet parameters are the most difficult to obtain. The nozzle diameters and the amount of nozzles can simply be found in the technical drawings. However, the pressure drop over the jet nozzle or jet pressure is dependent on the flow of jet water, which is dependent on the flow resistance of the entire jet water system and the pressure delivered by the pump, which is also dependent on the flow of jet water. If jet pressures are given then these pressures are likely the jet pressures for free flowing water jets. In the free flowing situation there is no contribution to the total flow resistance from a soil package at the jet nozzle. Therefore the pressure drop over the nozzle will be different than in the situation in which this contribution is taken into account. For the heel jets this is probably not problematic since it is likely that the jet penetration equations are calibrated using a free flowing jet pressure.
For the tooth jets it is harder to say whether using a free flowing jet pressure will work well. When the pore pressures are calculated with the influence of the tooth jets it is basically assumed that the jet flow is a laminar flow because Darcy's law is used. However, based on the flow speeds and the long pipe system that the water has flowed through, it is very unlikely that the jet flow is even near the laminar regime. A turbulent flow going back to a laminar flow in an instant is not possible. It is shown by the manual iteration in appendix K that this sudden transition from turbulent theories to laminar theory leads to an estimate of the tooth jet pressure that seems to be very low. The large simplifications of the flow system might also have contributed to the low calculated jet pressure.

Because trying to estimate the tooth jet pressure based on a combination of laminar and turbulent theory does not seem to work very well the simplest solutions seems to be just to use the free flowing jet pressure. In reality the jet pressure will probably lie somewhere between the free flowing pressure and the pressure calculated with laminar theory.

8.2.3 Dredging inputs

The remaining inputs, the dredging inputs, are basically the dredging depth and the lower arm angle. In the production model these two inputs can be chosen independently of each other. However, in reality the lower arm angle is dependent on the dredging depth through the geometry of the drag arm. Therefore it is possible to chose combinations of these inputs for the model that are not possible in reality. This can lead to both over- as underestimations of the calculated production with respect to the actual production.
The results of the sensitivity analysis for variation of the lower arm angle are mixed. When the visor has already moved from the lowest possible position then the visor angle hardly seems to influence the production. However, in the linear production regime, when the visor is still in the lowest possible position the lower arm angle seems to have a large influence on the production. Especially a decrease of the lower arm angle, which due to the definition made in this thesis is an increase of the angle between the lower arm and the seabed, seems to have a large influence on the production. This makes sense because when the visor is still in the lowest possible position decreasing the lower arm angle makes it possible to cut a larger total slice thicknesses and thus production increases. It is therefore important to use a lower arm angle that matches the dredging depth especially when the dredging depth is deeper than the standard depth of 15 meters. This is said assuming that the draghead is in standard position ($\Gamma = 0°$) at a depth of 15 meters.
Meanwhile the sensitivity analysis for the water depth also shows mixed results. Again the largest influence is seen when the visor is still the lowest position and again a decrease of the parameter leads to an increase in production and an increase leads to a decrease of production. However, due to the definition of the lower arm angle, an increase of the water depth will lead to a decrease of the lower arm angle. This means that a possible increase of production due to the decrease of the water depth is (partially) counteracted by the increase of the lower arm angle. How much the production increase is counteracted is dependent on the other inputs and at which regime is looked at.

8.3 Cutting forces

8.3.1 Calculated cutting forces and reality

As has been explained before, the cutting theory of Miedema that is used in the production model assumes that the mechanism that causes the cutting forces is the dilatation of the sand package due to the shearing of this package. The dilatation eventually causes pore under pressures to exist in the shear zone and on the blade. Using these pore under pressures the cutting forces can be calculated. Because in this theory it is assumed that the only mechanism is the under pressures due to dilatation, the influence of gravity and inertial forces, both forces related to the mass of the cut soil slice, are neglected.
A factor that is accounted for in the cutting model is that in reality the tip of the blade is not perfectly sharp due to wear. This allows for more water to flow from the back of the blade to the sand that is traveling up the blade, which reduces the pore under pressure on the blade. This effect, called the tip effect, has been discussed in chapter 3.

The cutting theory of Miedema has been verified with experiments in which sand is cut by a blade for different blade angles, cutting speeds and different ratios of the blade height over the cut slice thickness. These verifications show that the calculated cutting forces agree very reasonably with the measured cutting forces, despite the fact that the theory neglects the influences of the gravitational and inertial forces.
Besides the gravitational and inertial forces there are other factors that can cause a difference between the calculated and real cutting forces. One of these factors is that in the production model it is assumed that liquefied soil does not have any cutting force. This makes sense because if the soil has been jetted there are no pore under pressures that could cause a cutting force. The liquefied soil does have a mass and thus inertial and gravitational forces do play a role in reality. However, since experiments had already shown that neglecting the inertial and gravitational forces still leads to a very reasonable estimate of the cutting forces it is assumed that this is also true for cutting the liquefied soil. Furthermore the liquefied soil is likely to have a concentration lower than that of the cut soil on the blade. This means that the mass of the cut liquefied sand is also lower than that of the cut soil slice and that the relative influence of the inertial and gravitational forces is even smaller. Theoretically it is true that, when only looking at neglecting the cutting forces of the liquefied sand, it would mean that the calculated total cutting force is lower than the real cutting force. The difference would however be negligible compared to the total cutting force.
Another factor that causes the calculated cutting force to be different than the real cutting force is that in the production model a row of teeth of the draghead is modeled as a single blade. In reality the cutting teeth have some space between them. These spaces, or gaps, between the teeth allow water to flow from the back of the teeth to the shear zone. This leads to lower pore pressures in the shear zone and on the blade and thus to lower cutting forces. Modeling the cutting teeth as a single blade thus leads to an overestimation of the cutting forces, when only looking at this factor. Even when a blade is actually a single blade in reality then the cutting force is still overestimated because the cutting model does not account for water flows from the sides of the blade. Corrections for this side effect are however described in the *Delft Sand, Clay & Rock Cutting Model*. An alternative to modeling the teeth as a single blade would be modeling one tooth with the side effect and then multiplying its cutting forces with the number of teeth in a row.
A simplification in the production model that also leads to a difference between the calculated and the real cutting force is that the shear angle is always calculated as if the cutting process is fully cavitating. Depending on the cutting conditions this might not always actually be the case. Whether this simplification leads to an overestimation or underestimation of the cutting forces cannot be told right away because this is dependent on the cutting inputs. Based on tables in the *Delft Sand, Clay & Rock Cutting Model* the maximum difference in shear angle that the simplification causes is roughly three degrees. This makes it likely that the calculated cutting forces with the simplifications still match the real cutting forces very reasonably.

8.3.2 Cavitation cloud models

For the sensitivity analysis the reference production was calculated three times in paragraph 7.4: Without any cavitation cloud model, with the normal cavitation cloud model and with the quasi-cloud model. This allows for a comparison between the different cloud models and having no cloud model at all.
When the three reference productions are compared (figures 7.7, 7.12 and 7.17) it can be seen that in the operation range of trailing speeds (roughly 0.5 to 1.0 m/s) the production model without a cloud model performs best. Over the entire plotted range of speeds the production is linear, which means that the draghead is cutting the maximum possible slice thickness (for that lower arm angle). Furthermore the production calculated in the operational range of trailing speeds is in the right order of magnitude

whilst the productions of the other two models seem to be too low in this range. However, to draw the conclusion that using no cloud model therefore leads to the most realistic cutting forces, moments and production would be wrong. This is because the cavitation cloud model has been developed after high pore under pressures on large parts of the blade were observed during experiments. Thus in reality, for certain cutting conditions, a cavitation cloud will be present on the blade. In fact, even at the low trailing speeds for which all models yield the same linear production and thus have the same cutting conditions, it can be seen in figures 7.9, 7.15 and 7.19 that the calculated cutting forces are not necessarily the same. This shows that according to the cloud models the cutting conditions are such that a cavitation cloud is present. It also shows that although the productions are the same, the calculated cutting forces without a cloud model are not necessarily correct. When the cutting forces of blade 2 are compared for the no cloud production and the quasi cloud production it can be seen that the cutting forces are the same up until the sharp bend. From that point on especially the horizontal cutting force is larger for the quasi could model than that of the no cloud model. The sharp bend indicates the point at which the cavitation reaches the tip of the blade, which means that for the no cloud model the pore under pressures on the blade will not change anymore. The cutting forces do however still increase after the bent. This is due to the cavitation that is still expanding to the outside (the break point) of the shear layer. From this point differences in the cutting forces can be observed because the cavitation needs to reach the tip of the blade in order to model the effects of the cavitation cloud. Therefore the horizontal cutting forces of blade 2 for the quasi cloud model can be seen to increase more than those of the cloudless model. However, only a greater increase of the cutting forces for the quasi cloud model does not entirely explain why the cloudless model stays in the linear regime and why the quasi cloud model does change to a moment balance at a certain speed. It is rather a changing difference between the moments due to the horizontal cutting forces and the moments due to the vertical cutting forces that eventually cause a moment that is large enough to move the visor. Logically, these cutting moments are dependent on the cutting forces and the moment arms, both of which are (partially) dependent on the pore pressures on the blade. This is can be seen when the cutting forces and moments for the normal and the quasi cloud model are compared before the point that the visor moves. The magnitude of the cutting forces of blade 2 as well as the magnitude of the moment arms for both models are very comparable. However, the small differences between the cutting forces and moment arms are apparently enough to have the visor move for the normal cloud model at a lower trailing speed than that of the quasi cloud model. The introduction of a cavitation cloud above a blade thus seems to increase the difference between the horizontal and the vertical cutting moments or in other words, it increases the total cutting moment that is counteracting the actuator moments.

The need for the quasi cloud model to have the cavitation reach the tip of the blade in order to model the effects of a cloud shows the difference between the normal cloud model and the quasi cloud model. For the normal cloud model having cavitation anywhere in the shear layer, means that there is a potential for a cavitation cloud to exist. It does not matter what the distance between the cloud and the blade is and as soon as the cloud is above the blade, that part of the blade will be subject to the cavitation pressure. Given that cavitation in the shear layer does not start at the tip of the blade it is likely that for the same conditions the normal cloud model will have a cloud earlier than the quasi cloud model. This is demonstrated by the fact that the visor moves earlier for the normal cloud model than for the quasi cloud model (see figure 7.20 and 7.16).

To answer the question which cloud model, if any, helps modeling the cutting forces the best for the production model it will not suffice to only look at the cutting forces. This is because the cutting forces seem to be in quite the same order of magnitude when the visor is still in the lowest possible position. Whether the total cutting moment will be great enough to counteract the actuator moment is thus dependent on subtle differences. Therefore it must also be taken into account what the different models do after the visor has moved. In other words, what happens to the production, especially in

the operating range of trailing speeds and how does this compare to reality. For this performance assessment of the different cloud models also the factors that cause a difference between the calculated and the real cutting forces that were discussed in the previous section should be taken into account.
As was mentioned before, of the three variations the best production for the entire operational range was achieved when no cloud model was used. In figure 7.9 it can be seen that at the end of the plot the cutting moments of both blades have (nearly) become constant, which indicates that there is cavitation in (nearly) the entire shear zone. Because at the end of the plotted range there is still no moment balance found and because the moments are constant it can be concluded that the trailing speed can be increased indefinitely and that the visor will remain in the lowest position, meaning that the production increase will always be linear. Even if the calculated pore pressures would match reality this would not happen due to the gravitational and especially the inertial forces that play a role at high cutting speeds. Even with the gravitational and inertial effects modeled the model without a cloud would perform better than the other models because these would also be subject to these effects.
The model that performs worst, production wise, is the normal cloud model. After a very short linear production increase the production almost flattens out and within the plotted range the production never reaches the common range of productions. Apparently the normal cavitation cloud model quickly leads to a large buildup of pore pressures on the blade which causes the cutting moment to be large enough to counteract the actuator moment very quickly. It is however unlikely that this would happen with a draghead in reality because a draghead does not have a blade but a row of teeth. The gaps between the teeth would allow water to flow into the cavitation cloud which would diminish its size and thus influence. Therefore the normal cavitation cloud model likely overestimates the pore pressures on the blade and thus wrongly estimates the magnitude and direction of the cutting force with a disappointing production as the result. Another objection to this cloud model is that regardless of the height of the cloud above the blade, the under pressure on the blade is the cavitation pressure. In reality the higher the cloud would be above the blade the more water from different directions can flow to the cloud (due to the larger area on the sides) and thus reduce the clouds influence.
When the quasi-cloud model is used the linear production increase lasts longer than when using the normal cloud model. This is partially due to the fact that a cloud is only modeled after cavitation reaches the tip and thus the occurrence of the a cloud starts later than for the normal cloud model. However, when cavitation reaches the tip of the blade (indicated by the sharp bend in the cutting force) the cutting force can still be seen to increase for a while before the visor moves. This indicates that the cavitation cloud progresses more slowly over the blade compared to the normal cloud model. It can be argued that the quasi-cloud model progression of the cavitation cloud comes closer to reality than that of the normal cloud model because for the same cutting conditions the influence of the cloud is smaller. It can therefore be argued that the quasi cloud model models a cloud that comes closer to what the cavitation cloud would be in reality with gaps between the teeth than the normal model. However, since the precise influence of the gaps between the teeth is not known it cannot be stated how much better the quasi cloud model actually performs. A downside of the quasi cloud model is that the model simply works through a pore under pressure surplus and does not have, contrary to the normal cloud model, a real physical basis.
Nevertheless the quasi-cloud model seems to be the most suitable cloud model because it has a smooth progression of the cloud onto the blade, it does allow for a cloud to exist above the blade (which is observed during measurements) and because it is not as likely to overestimate the cloud its influence on the cutting force unlike the normal cloud model.

8.3.3 Tooth jet model

As has been mentioned before, what sets the Wild Dragon draghead apart from other dragheads is the application of water jets in the cutting teeth. In the production model the influence of these tooth

jets has been added by modeling the tooth jets as a pressure source in the pore pressure model. Under influence of this pressure difference water flows from the jet (a point on the blade) into the shear zone and thus (partially) reduces the effects caused by dilatation. In paragraph 7.13 it was shown that the reduction of the horizontal cutting force by application of this tooth jet model was very reasonably in correspondence with a cutting force reduction based on a specific energy-based approach in the operational range of trailing speeds. However, in this comparison the tooth jet pressure, the trailing speed, the soil conditions and the dredging conditions were kept constant. For the changing visor angle the blade angle, height and slice thickness thus change. This means that also the length of the flow lines of the tooth jet change and thus the (total) resistance of the flow lines changes. Given that the jet pressure is kept constant this means that the total tooth jet flow will change for changing visor angle. This also means that the jet power changes for changing visor angles because jet power is defined as the jet pressure times the jet flow. For the cutting force reduction comparison this did not pose a problem because the jet power per visor angle has been used to calculate the specific energy-based cutting force reduction. It is however questionable whether the tooth jet power and thus the pump power really notably changes under influence of the changing visor angle in reality. In other words, it is questionable whether using Darcy's Law to model the influence of the tooth jets leads to realistic jet flows (and powers).
In appendix K a manual iteration to find flows and pressures for the jet water system was done. Here also results were found that lead to the question whether the Darcy flow accurately models the influence of the tooth jets. The results from the iteration showed a large tooth jet flow for a rather small jet pressure (pressure drop over the nozzle). Part of this low jet pressure might have been caused by an overestimation of the pressure losses in the draghead but the large flow for a small pressure drop is partially caused by using Darcy's Law. In the iteration not the total area of the tooth jet nozzles is used but the total area of the shear zone to which the jet water flows. This is because this area is also used in the tooth jet model for the pore pressures, albeit maybe not that obvious. Because the shear zone area is very large compared to the area of the tooth jet nozzles also a large flow should be expected. If the total area of the tooth jets would have been used instead, then the total flow and thus the cutting force reduction would both be reduced significantly.
Because the calculated tooth jet pressure in the iteration was smaller than commonly observed in practice a higher tooth jet pressure for the sensitivity analysis was chosen which is closer to that of a free flowing jet as was also explained in section 7.14.1. This did however yield good results according to the specific energy approach. Therefore the results of this method of modeling the tooth jets seem to be very ambiguous. When modeling the tooth jets with Darcy's law in the total flow scheme (the iteration) the calculated tooth jet pressure seems to be too low and the tooth jet flow too big. If then because of this low pressure a higher tooth jet pressure, that would be expected for a free flowing jet (which follows Bernoulli's Law), is used in the tooth jet pore pressure model (which uses Darcy's Law) then the calculated cutting force reductions seem to be in line with cutting force reduction calculations based on specific energy. It therefore seems that the Darcy flow from the tooth jets to the shear zone is not an accurate representation of the actual physical processes. This is not surprising because if this would be the actual physical process then the jet water flow would be required to suddenly go from a turbulent flow to a laminar flow, which is not possible.
That the tooth jet model does not represent the actual physical jetting process properly does not necessarily mean that the model is not usable. When a certain jet pressure is used, a certain amount of water will flow to the shear zone, which means that the whole process is associated with a certain jet power. It has been shown that when this power is used to calculate a cutting force reduction based on the specific cutting energy this cutting force reduction matches the reduction based on the pore under pressure reduction (using the same flow) fairly well. At least for the tested (see section 7.4.1) cutting conditions and geometry. Even when both cutting force reductions do agree there is still the problem that the associated jet power might not be of a realistic order of magnitude at all. However, if

the jet power and pressure are known and the calculated cutting force reductions do reasonably agree with these and each other then, assuming that the normal cutting force calculation is close enough to reality (see previous section), the calculated cutting forces using the tooth jet model might be fairly close to the real cutting forces.

8.4 Production

8.4.1 General course of production

In the results chapter many different results have been shown in the form of an in situ production (and concentration) as a function of the trailing speed. For the sensitivity analyses many different inputs have been used. Furthermore results for different and no cavitation cloud models have been shown as well as results for when tooth jets are applied. Even though this many variations of the production model have been tested, the courses of the production results can be categorized in just two categories. In the first category the production is linear for all trailing speeds. This also includes all trailing speeds that were are not plotted. In the second category the production is characterized by a linear increase at first after which a less steep increase or even a temporary decline in in situ production is observed. For the sensitivity analyses the end of the linear production increase is usually marked by a temporary steep decline of in situ production. However, as can be seen in appendix I this is purely dependent on the draghead geometry, trailing speed and visor angle and thus a continued increase, albeit less steep than the linear increase is also possible.
As was discussed in section 8.3.2, an indefinite linear production increase and the cutting forces associated with it are not realistic. This production was only observed for the production model without application of a cavitation cloud model.
A linear production is however desirable in this production model because it is the maximum production possible for a given draghead geometry at a certain speed. Because erosion due to suction is neglected in this model the maximum layer thickness that can be removed by the draghead, and thus is responsible for the production, is simply the layer that can be removed by the cutting teeth. These teeth can cut the thickest layer when the visor is in the lowest possible position.
In the production courses of the second category that were seen in the sensitivity analyses this desired linear production usually only lasts until somewhere in the beginning of the operational range (0.5 to 1.0 m/s). The exact speed at which the linear increase ends is dependent on two things. First there must exist a visor angle for which moment equilibrium exists between the cutting and the actuator moments. Second the cutting moment at the lowest possible visor angle must be greater than the actuator moment. This is needed to move the visor upwards in the first place. The steep decline in production that is seen after the linear increase, which is not seen in reality, is solely caused by an increase of the visor angle that is too large to sustain an increasing production (see appendix I). This sudden (too) large increase of the visor angle is caused by the fact that the cutting moment does not have its maximum at the the lowest visor angle (normally $\Psi = 0°$) but at a larger angle (see figure 6.2). This means that for a given cutting condition the cutting moment at the lowest visor angle can still be smaller than the actuator moment but that at higher visor angles equilibrium might already be possible. The visor then still will not move because at the angle at which the visor is, the cutting moment is still smaller than the actuator moment. When through increasing the trailing speed the cutting moment at the lowest possible visor angle finally becomes larger than the actuator moments, the visor will move to the first possible angle at which equilibrium is found, hence causing a jump from the lowest possible angle to the new equilibrium angle. If the maximum cutting moment would have been at the lowest possible angle then much smaller changes in visor angle would have been expected because no equilibrium points will exist for any visor angle until the cutting moment at the lowest

possible angle is at least as large as the actuator moment.
The drop in production, caused by the jump in the visor angle can thus be attributed to the fact that the cutting moment is not maximum at the lowest possible visor angle but at a higher visor angle. In other words, it is caused by the shape of the cutting moment curve as a function of the visor angle. Because a moment consists of an arm times a force the combination of these is in the end responsible for the jump in the visor angle. This raises the question whether one of these is not modeled correctly because the visor angle jumps have not been observed in reality. In section 8.3.1 it was established that the cutting forces calculated in the production model using Miedema his theory, despite a number of simplifications are likely to reasonably agree with the real cutting forces for the same conditions. This means that the moment arms might be modeled incorrectly. However, the moment arms basically consist of two parts, the geometry-based part and the modification due to the force acting point. As has been explained before the force acting point can move between the tip and the middle of the blade based on the pore under pressure distribution on the blade. This changes the moment arm of the cutting forces slightly. The change of the magnitude of the moment arms as a result of the shifting force acting point is however not very significant compared to the magnitude of the moment arms in general. What is mainly causing the shape of the cutting moment curve to be as it is in figure 6.2 is, as has also been explained before, the large change of the vertical moment arms under the influence of visor rotation with respect to the relative small change of the horizontal moment arms under that same influence.
What this shows is that, assuming that the cutting forces match reality sufficiently well and assuming that the moving force acting point barely has any influence, the jump in the visor angle is ultimately caused by the geometry of the draghead. In other words, the visor angle jump is to be expected due to the design of the draghead. Especially the rapid decline of the vertical moment arm of blade 2 for a changing visor angle causes the shape of the cutting moment curve. This can also be seen in figure 6.2, where the moment curve of blade 1 is relatively flat but the moment curve of blade 2 still increases a lot after the lowest visor angle.
As was mentioned before, in reality the visor has not been observed to suddenly move up. One possible explanation for this could simply be that the behavior of the constant force mechanism of the actuator is not correctly modeled. In reality the hydraulic cylinder is not a closed system because this would mean that a small displacement of the piston would compress the hydraulic fluid and thus lead to a large increase of the cylinder force. Which means that there would be no constant force. Instead, the constant force mechanism relies on a control system to keep the cylinder force (relatively) constant for displacements of the piston. Because the exact way how this control system in reality works is proprietary information of the manufacturer this is not known. Thus the authors interpretation of the constant force mechanism is used, which means that it can differ from reality.
Another explanation for why the visor has not been observed to suddenly move up is that the conditions in reality are not such that the visor needs to move up. As has been seen during the sensitivity analyses the point at which the visor moves up is dependent on the inputs and also the application of tooth jets or not. Usually this point lies somewhere in the range of operational trailing speeds (between roughly 0.5 and 1.0 m/s). When the tooth jets are applied it can be seen that the point moves more towards the higher speeds of that range. Maybe this point in reality lies outside of the range of operational speeds for the soil conditions that are encountered. If this is the case it would mean that the production model does overestimate the cutting forces. This was however already discussed as a possibility in section 8.3.1.
If the point at which the visor moves in reality lies at higher trailing speeds than at which is operated then this would mean that the visor is in the lowest position for the operational trailing speeds. This also means that the draghead production is simply a linear function of the trailing speed. Although a linear function almost seems to be a too simple outcome of the production model, support for it can be found in the production distribution graphs in appendix J. As was mentioned before the 15th

and 85th percentile of this distribution are respectively a production of 36 and 125 m^3/min. If now the productions according to this linear relation are calculated for the boundaries of the operational range of trailing speeds, 1 to 2 knots (0.5144 and 1.0289 m/s to be more precise), then productions of respectively 66.15 and 132.30 m^3/min are found. Of this production range about 89 percent lies within the 15th to 85th percentile production of the production distribution. The part that does not lie within this range is still of a magnitude that is observed within the remaining 15 percent. If a trailing speed of 1 knot would be assumed to be the lowest trailing speed at which is trailed then the model seems to overestimate the production at low speeds because the 15th percentile lies a lot lower then the 66.15 m^3/min that was calculated. There can however be multiple explanations for an overestimation. The first is that the 15th and 85th percentile productions were calculated using an overflow loss of 15 percent. This was the average of 10 and 20 percent, the range of overflow losses commonly observed. Thus, if a higher overflow loss was chosen the difference between the production at 1 knot and the 15th percentile would already be smaller. Another explanation is that the model assumes that all soil jetted by the heel jets is sucked up by the draghead. However, especially at lower trailing speeds, which have a high jet penetration, there is a chance that the jetted soil is blown out of the reach of the draghead. This would count as a production loss. To more accurately model this more should be known about the shape of the jetted volume as a function of the trailing speed. At least it is very likely that this shape is not a perfect rectangle, as how it is modeled in the production model. As the sensitivity analyses showed the lower arm angle does have an influence on the production because it influences the maximum slice thickness that can be cut. As was explained before in reality the lower arm angle is dependent on the water depth. Thus, the production in reality for a certain trailing speed is also dependent on the water depth. Good to note is that both the overflow loss and the water depth can work in both ways. In other words, they can lead to a higher production than shown as well as a lower production than shown at a given trailing speed.

Concerning the relatively high production at low trailing speeds for the production model compared to the 15th percentile, it is of course also possible that in reality simply trailing speeds below 1 knot do occur.

If in reality the visor does not move for common cutting conditions, as the results of the production model seem to suggest, then the question should be asked what the use of the hydraulic cylinder is. Assuming that the linear production is true, the hydraulic cylinder could simply be replaced by a solid steel bar and the production would still be the same. A possible explanation for the use of the hydraulic cylinder is that is ensures production while it keeps the helmet at the ground when the cutting conditions do (temporarily) not allow for cutting the maximum slice thickness with regard to the drag arm moment. If at trailing speed the soil conditions change in such a way that the (horizontal) cutting forces increase then at some point the moments due to these cutting forces will become too large and a new drag arm moment equilibrium must be found. This new equilibrium can only be found by reducing the cutting forces or in other words, by reducing the cut slice thickness. If a draghead is not equipped with a visor that can move the the only option is to move the entire lower arm and draghead combination up. If the harder cutting conditions would only occur now and then then this could lead to a lower arm and draghead that slam into the seabed now and then. This could damage the equipment. This slamming can be prevented by having a movable visor since now only the visor has to move to reduce the cutting force.

This however still not explains the use of a hydraulic cylinder to move the visor because moving visors with other actuators like a spring or weights do also exist. The main reason for choosing the hydraulic cylinder over the other actuators is that its 'behavior' can still be adjusted during trailing by changing the operating pressure whilst other actuators required the drag arms to be lifted up in order to change any actuator settings.

Although the linear production of the draghead seems likely due to the order of magnitude of the calculated production, there is still the possibility that in reality the visor would move up more slowly

than shown in the production model and that thus a non-linear production in the right order of magnitude can be achieved. If this is the case then it is possible that the constant force mechanism is not modeled correctly, as was already discussed before. Another cause could be that the cutting moment as a function of the visor angle is not calculated correctly. As was discussed before a smoother visor movement for increasing trailing speed is expected when the cutting moment is maximum at the lowest visor angle. This is however not the case for the current production model. Because the moment arms are mostly geometry-based it is likely that the cause of this lies at the calculated cutting forces. One possible cause can be the fact that the cutting teeth are not modeled separately and that the effects of the sides of a tooth on the cutting forces are not modeled. Another possibility is that at the lowest visor angles the blade angles are so small that the cutting theory of Miedema deviates too much from reality. Of course a combination of both is also a possibility. It does however remain questionable whether these two would have a significant effect on the moment curve compared to the effect of the reducing vertical moment arm.
Up to this moment the linear production seems to be the simplest and most logical course of production. The fact that the sudden changes of the visor angle and thus production that are predicted by the model have not been observed can most likely be explained by this point of movement lying outside the range of trailing speeds in reality. It is possible that due to inhomogeneities of the soil the visor in reality does shortly move up but it might then move back to the lowest possible position just as fast.

8.4.2 Sensitivity without tooth jets

When looking at the influence of specific parameters on the calculated production (table 7.28 and 7.29), in other words the sensitivity of the production model for certain parameters, a distinction must be made between the sensitivity for the linear increase part and the sensitivity for the other non-linear part. During the linear increase there is no equilibrium between the cutting moments and the actuator moments until just before the visor will move and the transition is made to the non-linear part. Due to the lack of (need for) equilibrium in the linear part some sensitivities of the model for some parameters might be different compared to the sensitivities of the model for the non-linear part. In this section first the sensitivities for the non-linear part will be discussed, after this the sensitivities for the linear part will be discussed. Good to note is that these sensitivities are for a draghead without tooth jets.
The sensitivity analysis shows that the biggest influence on the production is the angle of internal friction. As has been explained, in the production model the angle of internal friction directly influences the angle of external friction. Both friction angles can be seen as (partially) responsible for eventually 'transmitting' the water pressure forces onto the blade. This is mostly done through the resulting force K_2. The equation for the sum of the horizontal forces (3.3.15 for cutting) shows that all terms contain sines. This means that for inputs of a normal magnitude, for a larger angle of internal (and external) friction a larger fraction of the water pressure forces is transmitted onto the blade. The horizontal cutting force is responsible for the moment that will push the visor upwards. Thus it makes sense that a decrease of the internal friction angle leads to an increase of production because a smaller fraction of the water pressure forces is transmitted onto the blade and thus the horizontal cutting force is smaller. Through the same reasoning it also makes sense that an increase of the friction angle leads to a decrease in production.
What is interesting to see is that the other two soil parameters, the dilatation and the permeability, have a much smaller influence on the production than the angle of internal friction. This is kind of odd since all three soil parameters are needed to calculate the cutting forces. This difference can however be explained by the fact that the friction angle is simply responsible for transmitting a fraction of the calculated water pressure forces onto the blade while the dilatation and the permeability are more re-

sponsible for the magnitude of these water pressure forces. At the trailing speed of the measurements, which is 1.5 knots, it is likely that the shear zone is already fully cavitating. This means that a large part of the cutting forces (with small exceptions due to different shear angles) is already fixed. The relatively small variance of the production that is left for the different dilatations and permeabilities can be attributed to the progression of the cavitation cloud onto the blade. The fact that a decrease of the dilatation leads to an increase in production makes sense because a decrease of the dilatation also decreases the cutting forces. A decrease of the permeability leads to an increase of the pore under pressures and thus the cutting forces and hence leads to a decrease in production.
Assuming that at the trailing speed of 1.5 knots the cutting forces are more or less the same for different parameter variations because the shear zone is already fully cavitating would suggest that the model might be more sensitive for variations in the water depth. This is because changing the water depth changes the under pressure that occurs during cavitation. This eventually influences the cutting forces and moments. However, the results of the sensitivity analysis show that the water depth barely influences the production. An explanation for this is that in order to move the visor a certain cutting moment and thus a certain cutting force is needed. Since the visor has already moved at the trailing speed of 1.5 knot for both depth variations as well as the reference production this means that this certain cutting force has already been reached. Thus even at the shallowest water depth the under pressures are low enough to produce a cutting force that is capable of moving the visor. When the visor has rotated the cutting forces reduce significantly and so does the influence of the cutting forces and factors responsible for the cutting forces. The fact that production drops for an increase of the water depth can be explained by the larger under pressures that can be achieved during cavitation. These lead to larger cutting forces an thus the visor will move sooner for larger water depths hence causing a larger drop in production.
The production increases for an increase of the cylinder pressure and vice versa. This makes sense because an increase in cylinder pressure eventually means an increase of the actuator moment. However, due to the fact that the cylinder moment is roughly only about the half of the total actuator moment the influence of changes in the cylinder pressure is limited.
The heel jet flow has the second largest influence on the production after the angle of internal friction. The flow of the heel jets is eventually translated into a certain layer thickness that is removed before the sand is cut by the teeth. When the cutting process is fully cavitational the cutting force is linearly proportional to the cut slice thickness. The fact that the production does not reflect this proportionality could indicate that the cutting process is not fully cavitating. However, another more likely explanation is that this is caused by non-linearities as the result of changing visor angles.
The parameter with the smallest influence on the production is the lower arm angle. This makes sense because the lower arm angle predominantly determines the maximum slice thickness that can be cut. This maximum slice thickness can only be achieved when the visor is in the lowest possible position. However, at 1.5 knots the visor has already moved to a new equilibrium position. The only small influence that the lower arms angle than still has is the influence on the position of the actuator attachment and thus on the actuator moment.
The discussed results above were for a trailing speed of 1.5 knots. When the results for the end of the linear increase are observed it seems that the overall the sensitivity for the parameters has increased with respect to the results for a trailing speed of 1.5 knots.
Again the angle of internal friction seems to have the largest influence on the production. For the decrease of 20 percent the linear increase does not end in the observed range of trailing speeds which is basically what has been proposed in the previous section as what might be happening with the production in reality.
Although the influence of the dilatation and the permeability on the production has increased it is still small compared to the influence of the angle of internal friction. The reason for this has already been given in the first part of this section.

The influence of the water depth on the production has increased a lot compared to the results at 1.5 knots. The explanation for this large influence has also somewhat been explained in the first part of this section. As has been explained before, the water depth eventually determines the maximum cutting force during cavitational cutting. It was also stated that a certain minimum cutting force (and thus moment) is needed to move the visor. Once this has happened the influence of the water depth diminishes. The results of the end of the linear increase represent the production at the moment just before the visor first starts moving and thus the water depth still has a large influence. Increasing the water depth shifts the point of visor movement to lower trailing speeds, which leads to a lower production and vice versa.
Compared to the results of the production at 1.5 knots the influence of the cylinder pressure has increased. When the cylinder pressure is changed the cylinder force and thus also the cylinder moment change linear proportionally. Since the end of the linear increase is observed it might be expected that the production also simply changes 20 percent because the cutting moment does this. This is however not the case. The cutting moment (as a function of the visor angle) does change with 20 percent but the cutting moment does not change linearly with the trailing speeds and therefore different percentages are seen.
While the influence of most parameters has increased the influence of the heel jet flow has actually decreased. The most likely explanation for this is however that this is caused by the large drop in production after the visor has moved. At the end of the linear decrease the total in situ production is considerably higher than at the speed of 1.5 knots while the production of the heel jets has remained constant. Therefore in percentages the contribution of the heel jet production with respect to the total production is greater at 1.5 knots than at the end of the linear increase.
The influence of the lower arm angle has changed tremendously with respect to the influence at 1.5 knots. At 1.5 knots there was barely any influence and at the end of the linear increase the lower arm angle has the second largest influence on the production, after the angle of internal friction. The explanation for this is simple. During the linear increase the visor is in the lowest possible position. The slice thickness that is cut at the lowest possible position is dependent on the lower arm angle. Therefore in the linear regime the lower arm angle is of importance. The non-linearities can be explained that the trigonometry involved in calculating the cut slice thickness, at the angles used, are far from linear.
As has been shown the sensitivities greatly differ for the situation in which the end of the linear production increase is monitored and the situation in which the production at 1.5 knots is monitored. Most of the parameters show the same trends for variations for both situations. However, which sensitivity comes closest to reality is dependent on which production regime is considered to be closest to reality. More on this will be discussed in section 8.4.5.

8.4.3 Sensitivity with tooth jets

In the previous section the results of a sensitivity analysis were discussed for a draghead without tooth jets. In this section the results of the sensitivity analysis with tooth jets are discussed (table 7.31 and 7.32). Again first the sensitivities for the non-linear part will be discussed. A difference with the previous section will be that also specifically the influence of the tooth jets will be discussed. For this the discussion in the previous section is used as a reference.
For the sensitivities at 1.5 knots without tooth jets there was only one parameter for which a reduction of 20 percent lead to a still linear production at 1.5 knots. This parameter was the angle of internal friction. It was therefore denoted as the parameters with the greatest influence on the production. For the sensitivities at 1.5 knots with tooth jets four parameters still have a linear production increase. These parameters are the angle of internal friction, the water depth, the cylinder pressure and the lower arm angle. This increase from one to four parameters shows at least that the tooth jet model

does its work. The cutting forces at a given trailing speed are reduced compared to the cutting forces without tooth jets. This means that with tooth jets the visor starts moving at higher trailing speeds which means prolonged maximum production.
Which of these four parameters has the greatest influence on production can be seen by looking at the other value of a parameter, this the value for a 20 percent change in the other direction. Doing this it still seems that the angle of internal friction has the largest influence on the production. After this the cylinder pressure has the largest influence on the production, then the water depth and then the lower arm angle. When comparing the other values to those of the results without tooth jets at 1.5 knots only tiny differences can be seen. This indicates that if it were not for the linear increase to be still present at 1.5 knots then little production increase would have been seen for the introduction of the tooth jets for these parameters. This raises the question whether it is fair to regard these parameters to have a large influence in the non-linear regime whilst at 1.5 knots they are not in the non-linear regime. Because the goal of this discussion is to discuss the sensitivities for the linear and the non-linear regime separately it seems more fair to disregard the linear data in this case.
Nevertheless the angle of internal friction still has the largest influence on the production just like is the case for the situation without jets. As was mentioned before little difference in percentages is seen when the two cases are compared. This is however no surprise since the tooth jet model acts during the pore pressure calculations. The angle of internal friction is only used to transmit the forces due to the pore pressures onto the blade. This is explained in more detailed in the previous section.
Because the pore pressure model acts during the pore pressure calculations an increase of influence should be expected for the dilatation and the permeability. When the sensitivities with tooth jets are compared with the sensitivities without tooth jets both the influence of the dilatation and the permeability roughly double. Although the influence of the dilatation stays quite small with respect to the influence of the angle of internal friction it does become more important compared to the influence of the other parameters. The influence of the permeability becomes the second largest influence, nearly as large as that of the angle of internal friction. It thus seems that in a production model in which all cutting forces are solely pore under pressure-based the parameters used to calculate these under pressures become more important when measures are introduced to reduce the pore under pressures.
Based on the percentage that is not in the linear increase, the influence of the water depth, which was already very small, actually seems to be slightly reduced. This makes sense because the water depth determines the under pressure at cavitation and thus eventually the maximum cutting force. Due to the introduction of the tooth jets water is provided to counteract the effect of dilatation and thus pore pressures in the shear layer and on the blade might not even be near the maximum under pressure.
The influence of the cylinder pressure has barely changed after the introduction of the tooth jets. This makes sense because the cylinder pressure does not directly influence the calculation of the cutting forces.
The heel jets do directly influence the calculated cutting forces because they remove a certain layer thickness which then does not have to be cut. Therefore a (slight) change in influence is seen for the heel jet flow. With the introduction of the tooth jets the influence of the heel jets is slightly reduced. The reduction of the influence of the heel jet flow can be explained through the fact that the total production is greater when cutting with tooth jets, yet the production of the heel jet is the same as before the introduction of the tooth jets. Therefore the percentage of the contribution of the heel jets to the total production is reduced.
The influence of the lower arm angle has barely changed and is again the smallest influence of all parameters in the sensitivity analysis. Again the lack of change after introduction of the tooth jets and the small influence can be explained by the fact that the lower arm angle does not directly influence the cutting forces when the visor has already moved from the lowest possible position.
The last parameter that was observed in the sensitivity analysis is the tooth jet pressure. What is

interesting to note is that its influence on the production is not that big and that the percentage of change in both directions is nearly the same. The latter can be explained by the fact that the tooth jet flow, for the same flow resistance, is linearly proportional to the jet pressure. The flow resistance during the measurements of the variation for an increase and a decrease of the jet pressure is however not the same because the visor angle is slightly different, which in its term also eventually causes the difference in production.
The sensitivity analysis at 1.5 knots with tooth jets shows that if the visor has already moved the introduction of tooth jets leads to an increase of the influence of the parameters that are associated with the working method of these jets while the influence of the rest of the parameters more or less stays the same. The slight differences in influence that are seen can be explained by the fact that the visor angles at 1.5 knots is different for the situation with and without jets. This is caused by the fact that the point at which the visor starts moving shifts to higher trailing speeds due to the cutting force reduction of the tooth jets.
When the sensitivities of the end of the linear increase are compared with the sensitivities at 1.5 knots then, just like in the previous section, overall the sensitivity is seen to increase. This is if the linear increase results at 1.5 knots are neglected.
Again the angle of internal friction has the largest influence on the production, partially because for a 20 percent reduction of this angle the linear increase does not stop in the plotted area. However, in contrast to the 1.5 knots results the sensitivity of the angle of internal friction has actually slightly increased after the introduction of the tooth jets. This can be explained by the fact that this is a result in the linear regime where there is likely no equilibrium between the actuator and the cutting moments. In order to move the visor a certain maximum cutting force (and moment) is needed. This cutting force is dependent on the pore pressures through the water pressure forces and is dependent on the angle of internal friction to transmit these forces onto the blade. Because the introduction of the tooth jets slightly hinders the development of the pore pressures and thus the water pressure forces, maximizing the cutting force is achieved by as efficiently transmitting the forces onto the blade as possible, which is done through the angle of external friction. Therefore in this regime the sensitivity of the angle of internal friction is actually increased by introduction of the tooth jets.
The influence of the dilatation and the permeability have also increased. As was discussed earlier in this section this is to be expected because these two parameters are related to the calculation of the pore under pressures, which is also on which the tooth jet model acts.
The second largest influence on the production is the cylinder pressure. The influence of this parameter has also increased since the introduction of the tooth jets. This can again be explained through the fact that this regime and its production exists as long as there is no moment equilibrium. The introduction of the tooth jet model reduces the cutting forces and cutting moments. Thus for a given trailing speed in the linear regime the magnitude of the cutting moment is reduced while the actuator moment stays the same. Thus a higher trailing speed can be reached before a moment balance is achieved and thus the influence of the cylinder pressure is greater when tooth jets are introduced.
As was the case without tooth jets the influence of the water depth in the linear regime is much larger than the influence in the non-linear regime. Again this can be explained by the fact that the water depth determines the maximum under pressure and thus the maximum cutting force. The fact that the influence of the water depth has increased whilst the results for 1.5 knots show that the influence decreases seem odd. The most likely explanation is that at the trailing speed at the end of the linear increase the influence of the tooth jets has more or less diminished and cavitation does begin to start to play a role again.
It is remarkable to see that after the introduction of the tooth jets the heel jet flow does not have any influence on the production, or better put, the trailing speed at which the visor will move because the heel jets still contribute to the total production. Apparently at this trailing speed the heel jet penetration, or the layer removed by the heel jets, is already so small that its cutting force reducing

effect is negligible compared to the magnitude of the cutting forces. The fact that this speed can be reached before the visor moves can therefore be (almost) fully attributed to the cutting force reduction of the tooth jets.
Together with the heel jet flow the lower arm angle is the only parameter of which the influence has reduced after the introduction of the tooth jets. Nevertheless the lower arm angle still has got a large influence on the production in the linear regime because it determines the maximum slice thickness that can be cut. The influence is however slightly reduced, which is likely caused by the reference value already being taken at a higher speed, due to the cutting force reduction of the tooth jets.
The tooth jet pressure has a relatively small influence on the production, this was also the case in the non-linear regime. The explanation for this was already given earlier in this section.
With the introduction of the tooth jets a clear difference between the sensitivities for the linear and the non-linear regime can be seen. In the non-linear regime, where there is moment balance between the cutting and the actuator moments, the introduction of tooth jets only really seems to change the influence on the production of parameters directly related to the working method of the tooth jets. In other words, parameters directly used in calculating the pore under pressures.
In the linear regime it can be seen that the cutting force reduction due to the introduction of the tooth jets shifts the point of visor movement to higher trailing speeds and thus increases production. In this regime the pore pressure related parameters also see an increase of influence, which partially might be attributed to the introduction of the tooth jets. However, parameters that have a large influence on the magnitude of the actuator and cutting moment at the lowest possible visor angle seem to be dominant. This is because eventually the point at which this regime ends is determined by which of the two moments is greater.

8.4.4 Concentration

In addition to the in situ production also the slurry concentration in the drag arm is calculated. As has been explained before, in order to calculate the concentration it is assumed that the volume that is sucked in by the suction mouth is greater than the in situ volume that is cut by the draghead. The flow entering the suction mouth is then dictated by the flow of the dredge pump. Because this flow is dependent on the concentration of the pumped slurry, a root-finding algorithm must be used to find the final concentration. The pump flow of the dredge pump as a function of the slurry concentration is the most important part of this method of calculating the slurry concentration. By changing the shape of this function the model can be tuned to only yield concentration outputs that are of a plausible order of magnitude. The upside of this method is that very few inputs are needed and that it yields a result that is likely to be somewhat close to the real concentration for that production. The downside is that for a given in situ production and porosity always the same concentration is obtained. Hence, other influences on the pump flow, like the grain size distribution and the water depth are ignored. An option is to make the function of the pump flow and the concentration also dependent on the water depth. This does however require that data of the water depth, the slurry concentration and the pump flow is available. However, even then there is no guarantee that the calculated concentration would match the actual concentration because this method is does not use any calculations based on flow resistance and pressure losses.
The latter does not mean that this method of calculating the slurry concentration cannot be useful. It does simply mean that due to the many influences that are ignored there might be a limit to how well the concentration can be predicted. This has however not been researched for this thesis. If the concentration can be calculated sufficiently well then this method can be a very powerful method thanks to its simplicity and the small number of required inputs.

8.4.5 Model and reality

In the previous sections a total of four possible sensitivities have been discussed: sensitivities with and without tooth jets and sensitivities for different regimes. This raises the question which set of sensitivities is the most representative for the sensitivity in reality.
Whether the sensitivity with or without tooth jets must be chosen in simply dependent on whether the draghead is equipped with tooth jets. Thus, in the case of the Wild Dragon draghead, the sensitivities with tooth jets should be chosen. However, the choice of the production regime is more difficult. The main working principle of the production model is finding equilibrium between the cutting moments and the actuator moments and thus the most logical choice at first seems to be to use the sensitivities for the non-linear regime. The production in the non-linear regimes within the range of operating trailing speeds can however be considered to be very low compared to what is a normal production and this is the case for all variations that were made. In contrast, the linear production regime actually shows productions that are in the right order of magnitude for trailing speeds in the operational range. The problem with the linear regime is that it usually ends somewhere in the range of operational trailing speeds and that the transition of the linear regime to the non-linear regime is marked by a large drop in in situ production. This has never been observed in practice.
Introduction of the tooth jet model reduced the cutting forces and cutting moments and thereby extended the duration of the linear regime further into the range of operational trailing speeds. However, the large drop in production is still present for all variations.
Because a decrease of the cutting forces and moments leads to an extension of the linear regime into the operation range of trailing speeds two things are possible regarding the production in reality, both of which have already slightly been discussed. The first possibility is that in reality the production is linear with the trailing speed, at least, at the operating trailing speeds. Outside the operating trailing speeds the drop of production might happen but this is never observed because these speeds are never trailed at. This would also imply that the production model overestimates the cutting forces, but this has also already been discussed as a possibility. The most likely explanation for the overestimation is that the cutting teeth are modeled as a single blade. This neglects the side effects in which more water flows from the sides of the blade to the shear zone, hence reducing the pore under pressures and cutting forces.
The other possibility is that in reality, after an initial linear regime there will be a transition to the non-linear regime. If this is true then this would mean that the model calculates the production after the linear increase incorrectly because the drop in production has never been observed in reality and the production in the non-linear regime that is calculated is too low. For the production to not drop after the linear regime it is required that the visor does not rotate too much when moving from the lowest possible position (linear regime) to the new equilibrium. As has already been discussed this requires the cutting moment as a function of the visor angle to have a different shape. A shape in which the largest cutting moment is achieved at the lowest possible visor angle. Changing the cutting moment as a function of the visor angle can be achieved by changing the calculated cutting forces, the moment arms or both. However, because the moment arms are mainly obtained from the geometry of the draghead (technical drawings) it is likely that the change should be made in the calculated cutting forces. This would however imply that the calculated cutting forces are incorrect or at least not realistic enough. This would be odd because real measurements show that cutting forces calculated using Miedema's cutting theory match reality pretty well.
It seems that the arguments mostly favor the first possibility, that the production in reality is a linear function of the trailing speed, especially the order of magnitude of the production and the likeliness that the production model overestimates the cutting forces. It therefore seems that the best option is to choose the sensitivities obtained for the situation with tooth jets at the end of the linear regime as most representative for the sensitivities in reality.

If this situation is chosen then the parameter with the largest influence is the angle of internal friction. This is however the case for every situation. The downside of the angle of internal friction being the largest influence on the production is that it cannot be adjusted since it is a property of the soil.
The second largest influence on the production is the pressure of the hydraulic cylinder. This is a parameter that can be controlled by the dredger. The pressure should however not be chosen to be as large as possible. Instead the pressure should be chosen in such a way that the production is still linear at the chosen trailing speed. Choosing a pressure higher than this pressure is simply a waste of energy since production in the linear regime can only be increased by increasing the trailing speed or by changing the cut slice thickness (the lower arm angle).
After the angle of internal friction and the cylinder pressure the parameters with the largest influence are respectively the water depth and the lower arm angle. These two parameters have however been varied independently in the sensitivity analysis. In reality the lower arm angle is (partially) dependent on the water depth and the effects on the production of both parameters counteract each other. It is therefore likely that in reality the influence of the water depth on the production is much smaller than shown in the sensitivity analysis.
The permeability, a parameter that is also a soil property and thus cannot be changed, still has a relatively large influence on the production. It must however be kept in mind that the permeabilities found for sands can span several orders of magnitude. Therefore the influence of the permeability might actually be different than the influence found in the sensitivity analysis when a sand with a different permeability is chosen.
The dilatation also cannot be chosen in reality because it also is a soil property. Its influence on the production is however relatively small.
Although tooth jets make a big difference in terms of production compared to a situation in which no tooth jets are applied, the increase of the tooth jet pressure itself does not have a large influence on the production. It therefore seems that a certain pressure is needed to sufficiently reduce the cutting forces but that once this pressure is reached, it is not that useful to further increase this pressure.
The sensitivity analysis showed that a change in the heel jet flow does not influence the production. This situation is comparable to that of the tooth jet pressure. A certain minimum heel jet flow is needed to allow for production in the linear regime, but once this has been reached increasing the flow further does not lead to better productions. In reality it would be a challenge to find this point. But finding this point could save energy (and costs) by not using a larger flow than needed.
Of all controllable parameters the cylinder pressure seems to be the most important parameter. However, if it would be possible to influence the lower arm angle regardless of the water depth then it would be possible to increase the production for a given trailing speed. What must be kept in mind is that all sensitivities and suggestions discussed above are based on the production model. As was discussed in paragraph 6.11 the model neglects a number of limiting factors. It is therefore possible that the production calculated by the model for a certain trailing speed cannot be reached in reality. An example would be that the cylinder pressure is set in such a way that linear production at a given trailing speed is ensured according to the model. However, for these cutting conditions in reality the moment balance of the drag arm cannot be achieved and thus the whole lower arm will move up and push the draghead out of the soil. Such a situation demonstrates the restrictions of the production model.

9 Conclusion

9.1 Introduction

The previous chapters of this thesis showed the theory behind, the working principle, the main components and the results of the draghead production model. In this chapter the findings of modeling a draghead production model and the findings based on the outputs of the model will be repeated. Furthermore there will be reflected on whether the production model is capable of delivering the required outputs.
The ultimate goal of making a draghead production model was to obtain a slurry concentration that would then serve as an input for a pumping model and a hopper sedimentation model. This can help project estimators to estimate the required time and costs of a project because they do not have to solely rely on slurry concentrations that were recorded on previous comparable projects.
The available inputs for the model were the mechanical design of the dredge (this includes the availability of jetwater), the soil mechanical properties, the dredging depth (water depth) and the trailing speed. The required outputs for the model were the draghead cutting production (the in situ production), the cut slice thickness, the slurry concentration, the propulsion resistance and the required downpressure. All of these outputs were expected to be presented per either material strength or per trailing speed. The choice has been made to go for the latter because sand do not have a strength.
The chosen approach for modeling the draghead production was to focus on the draghead. The draghead, or more particularly the helmet, was assumed to be fixed above the seabed just barely touching it. This way, the influence of the drag arm and the vessel is neglected. In order to find the slice thickness cut by the draghead, which is used to calculate the in situ production, a moment balance was sought between the moments caused by actuators and the moments caused by cutting the soil. Eventually the model then uses the in situ production and the dredge pump flow as a function of the slurry concentration to find the slurry concentration. As an example draghead the Wild Dragon draghead was used, this is the draghead used on the dredge Liberty Island.
The next three paragraphs in this chapter will respectively cover the findings found by modeling the draghead production, the findings found by doing the sensitivity analysis and the reflection on the required outputs.

9.2 Model

As was mentioned before this paragraph will cover the findings found whilst modeling the production model.

9.2.1 Geometry

It has been shown that the complex geometry of a draghead can be reduced to a small number of points and lengths which is eventually enough to use to calculate an in situ production. The choice to represent these points in polar coordinates might make obtaining these points from a technical drawing slightly more difficult because it requires to also measure angles instead of only distances. This small disadvantage of using polar coordinates is however greatly outweighed by the ease the polar

coordinates bring when it comes to rotating one or a group of points around the origin. This allowed the rotation of the draghead visor (including teeth) to be modeled as well as changes in the lower arm angle whilst the important geometry points could still be captured in a pair of coordinates.

9.2.2 Heel jets

The study into jet penetration equations showed that traditional jet scour equations are not suitable to model the cutting process of the heel jets. The main reason for this is that all these equations assumed that the water jet is suspended above the bed at a nonzero distance whilst the heel jets are directly on the sand bed. Another impractical side of the traditional jet scour equations is that most of these equations calculate a final scour depth for a stationary jet. The heel jets are not stationary and due to this non-stationary nature it is questionable whether a final scour depth could ever be reached. A last objection to the traditional jet scour equations was that the jet water speeds at which these experiments were conducted are much lower than the jet water speeds of the heel jets.
The equations that were found to be suitable for application in the production model all rely on one specific principle. First a cut or liquefied volume is calculated, after which this volume is divided by a certain width (the draghead width in this case) and the trailing speed. This type of equation is easy to implement but it means that the heel jet production is assumed to be constant over a range of trailing speeds (with the exception of very low trailing speeds). The downside of using this type of equation is that for low trailing speeds the jet penetration becomes unrealistic since it will go to infinity when approaching a trailing speed of zero. This is not directly a problem for the calculated production but it will lead to wrong cutting forces. Another reason why this approach can lead to wrongly calculated cutting forces is that it neglects the shape of the liquefied jet volume by assuming an evenly distributed volume under the entire width of the draghead. This neglects the possibility of the existence of sand pillars between the jets which could lead to higher cutting forces. This shows the importance of understanding the shape of the volume liquefied by a jet. Therefore further research is recommended, which can be read in paragraph 10.2.

9.2.3 Cutting theory

Application of only the basic cutting theory of Miedema for water saturated sand led to cutting forces that were at no speed capable of generating moments that could move the visor. This is a direct consequence of the fact that the theory neglects the inertial forces and the fact that the basic theory does not allow for cavitation to move up the blade. The latter could be solved by implementing Miedema's cavitation cloud theory (more on this in paragraph 3.6).
Because the cutting theory is based on pore under pressures it allowed for and led to the development of a pore under pressure-based approach on modeling the tooth jets (more on this in paragraph 3.5).
A challenge of implementing Miedema's cutting theory for water saturated sand in the production model is that quite a few soil mechanical properties are needed that are commonly not known by dredging companies. This does not mean that the properties cannot be measured, although commonly only a particle size distribution is known. As has been shown, theory on calculating certain soil mechanical properties based on the PSD does exist. It would therefore make an interesting research to see how well the needed soil mechanical properties can be calculated based on the PSD, more on this can be found in paragraph 10.6.

9.2.4 Cavitation cloud models

Introduction of a cavitation cloud model in the cutting model allows for a higher average pore under pressure on the blade by allowing cavitation to move up on the blade. This higher average pore under pressure in its turn causes higher water pressure forces and thus higher cutting forces. This also slightly changes the direction of the total cutting force.
The introduction of a cavitation cloud favors the horizontal cutting force more than the vertical cutting force and therefore the horizontal cutting moment (counteracting the actuator moments) more than the vertical cutting moment (helping the actuator moments). When comparing production model with and without the cloud model this can be noticed by the visor starting to move at lower speeds or the visor moving in the first place when the cloud is present.
Of the two cloud models tested the quasi-cloud model yielded better results. This can mostly be attributed to its smooth progression of the cloud onto the blade. Although the normal cloud model has a better physical basis its progression of the cloud onto the blade is very sudden which eventually causes large visor movements and low productions.

9.2.5 Tooth jet model

Introduction of a pore pressure-based tooth jet model in the cutting model has lead to lower cutting forces and higher productions. The cutting force reduction achieved by the introduction of the tooth jets matches well, especially at operating trailing speeds, with the cutting force reduction calculated using an energy-based approach. However, due to the fact that no limit is set to the flow of jet water provided, the jet power is not limited either. This means that the tooth jet model potentially can calculate cutting force reductions whose corresponding jet power is too large to be realistic. During normal operating conditions this has however not been observed.

9.2.6 Concentration model

Requiring very few inputs the concentration model is a simple way to come up with an estimate of the slurry concentration. Having an equation describing the pump flow as a function of the slurry concentration in the model is the models greatest advantage and disadvantage at the same time. On one hand this allows for a function to be used that is based on actual flow data. On the other hand the function can be chosen in such a way that for every in situ production a seemingly plausible concentration can be calculated. Thus when using the concentration model a lot of attention must be spent to generate a pump system-specific pump flow equation. If this is done there is however still no guarantee that the calculated concentrations are correct because this model does neglect many influences on the slurry flow, one of the more important parameters being the particle size.

9.2.7 Simplifications and limitations

In the production model a number of assumptions and simplifications were made that influence the calculated cutting forces. Modeling the cutting teeth as a single blade neglects the gaps between the teeth and therefore the 'side effect' which allows more water to flow to the blade. Therefore the cutting force might be overestimated. On the other hand the inertial forces are neglected which might mean that the cutting forces are underestimated. Which of the two effects eventually dominates is hard to tell without actually modeling the effect, however the findings in section 8.4.5 do suggest that the cutting forces might actually be overestimated by the production model.

The limiting factors described in paragraph 6.11 are not implemented in the model. Therefore there is a risk that the model calculates the production for a situation that could not even exist in reality.

9.3 Sensitivity analysis

As was mentioned before this paragraph will cover the findings found by performing a sensitivity analysis on the production model.

9.3.1 Production as a function of the trailing speed

In general, according to the production model, the in situ production as a function of the trailing speed is characterized by a linear increase at first. This linear increase is then then followed by a steep drop in production, after which the production will start to rise again albeit not nearly as fast as during the linear increase. The production rise can seem linear but is actually hyperbolic due to the way the heel jets are modeled. The production is only of a realistic magnitude at operating speed when the linear increase is still present.
The steep drop in production after the linear increase, which is when the visor first starts moving, is mostly caused by the draghead geometry rather than the way the cutting forces are calculated.

9.3.2 Linear production in reality

Based on a number of findings and presumptions from the production model (results) it seems most likely that production by the Wild Dragon draghead in reality can be characterized as a linear function of the trailing speed. The first of the findings supporting this is that production only seems to be in the right order of magnitude, at operating speeds, when the production is still linearly increasing. Another finding supporting this is that the linear increase usually seems to end somewhere in the range of operating trailing speeds whilst the drop associated with the end of this increase is not noticed in practice. Another support is the presumption that the cutting forces are overestimated due to neglecting the side effects of the separate cutting teeth. Together with the observed trend that the linear production ends at higher trailing speeds when the cutting forces for a given speed are reduced it leads to the presumption that in reality the linear increase ends at trailing speeds higher than the operating speeds and that the drop in production therefore is not observed.
The aforementioned is just a theory and should be tested to see whether it holds. Therefore a follow-up research is suggested in paragraph 10.4.

9.3.3 Sensitivity of the production model

The sensitivity analyses have shown that the influence of parameters tends to change dependent on the application of tooth jets and the cutting regime observed. However, all analyses showed that of the parameters tested, the angle of internal friction of the sand has the largest influence on the production.
If it is assumed that the presumption mentioned in the previous section is true than another soil parameter that has a large influence on the production is the permeability. Of the parameters that can be controlled the pressure in the hydraulic cylinder has the largest influence on the production.
Another interesting finding is that the lower arm angle and the water depth both seem to have a large influence on the production when they are independent of each other. In reality there is a

dependence between both in which both parameters counteract each other effects. Therefore it would be interesting to add this dependence to the model. More on this can be found in paragraph 10.3.
Good to note is that no percentages are stated. This is because if other values were chosen as reference values then other percentages would likely be the result. Therefore it is hard to rate the influence of a parameter on an absolute scale and thus the influence was only observed relative to the influence of other parameters.

9.4 Required outputs

In this last paragraph there is reflected on whether the required outputs of the model are actually delivered by the model. As was mentioned before the choice has been made to present all outputs as a function of the trailing speed.
The first required output was the draghead cutting production. This has been the main output delivered by the model. To get to this the cut slice thickness, which is another required output is multiplied with the draghead width and the trailing speed. The resultant slurry concentration is calculated based on the in situ production and is thus also delivered.
The propulsion resistance and the resulting downpressure are not directly calculated by the production model. However, the cutting forces needed to calculate both are delivered by the production model.

10 Recommendations

10.1 Introduction

In this chapter various recommendations related to the production model are presented. Some of these recommendations might have already been announced in the conclusion, others are new. The recommendations vary from suggestions for additions to the production model to suggestions for experiments that can lead to new additions to the production model to experiments to verify the production models outcomes.

10.2 Jetted volume shape and size

As the study into the different jetting theories has shown, all (publicly) available jetting equations that are suitable for application in the production model perform poorly at low trailing speeds. This mostly leads to a wrong estimation of the cutting forces. Furthermore, when using a row of jets, it is assumed that the liquefied area below the jets is rectangular and that the entire area is liquefied. This can also lead to wrong estimates of the cutting forces.
In order to obtain better jetting equations, experiments should be conducted in which at least the maximum width and depth of a liquefied soil area are measured for a trailing jet. However, if there is a way to get a more detailed measurement of the liquefied area then this is preferred. This way the liquefied volume of sand can be measured as well as a maximum penetration depth and width. The maximum penetration width can be used to evaluate whether jets in a row cover the entire area between the jets. The parameters that should be varied during the experiments are at least the jet pressure, the nozzle diameter (jet flow) and the trailing speed but the jet power and soil permeability would also be interesting.
Since a trailing jet experiment can relatively easily be converted into a stationary jet experiment it is recommended to combine the trailing jet experiments with stationary jet experiments. In these experiments it would be interesting to monitor the liquefied volume development over time. For this at least the penetration depth and the diameter of the jetted volume should be measured. However, if a more precise way of measuring the jetted volume is available then this is preferred. The parameters that should be varied are the same as for the trailing jet experiments, with the exception of the trailing speed.
The knowledge gained from these experiments would be very valuable because especially the jetted volume equations would have a wider application range than only dragheads. It could be applied to virtually any cutting tool that utilizes water jets. The results of the stationary jet experiments can be used to improve the hopper fluidization process.

10.3 Water depth dependent lower arm angle

On several occasions it has been mentioned that in reality the lower arm angle is dependent on the water depth. It is recommended to add a relationship describing the lower arm angle as a function of the water depth to the production model. This prevents productions to be calculated under conditions

that are not possible in reality. It will also result in a more realistic representation of the influence of the water depth on the production since it will be (partially) counteracted by the changing lower arm angle.
Because the drag arm consists of two rotating parts there can be many combinations of angles that will lead to the same dredging depth. Technical drawings of the vessel do however sometimes contain sketches of the drag arm at multiple dredging depths (water depths). These drawings could be used to derive a function for the lower arm angle.

10.4 Linear draghead production

One of the main findings presented in the conclusion was that the model results suggest that draghead production in reality might be characterized as a linear function of the trailing speed. To check this the loading distribution graph as shown in appendix J can be used. This graph has been made by using the average productions of many dredging jobs. A requirement for checking whether the production is linear is that for all these jobs the average water depth and trailing speed must be known. Another requirement is that there is a relationship available describing the lower arm angle as a function of the water depth.
Now for every job the average water depth should be used to calculate the average lower arm angle, which in its turn should be used with the draghead geometry to calculate the average slice thickness when the visor is in the lowest possible position. This should then be multiplied with the average trailing speed and the draghead width to obtain an average in situ production. Because the loading graph does not display in situ production there should still be accounted for overflow losses (around 15 percent) to get the loading production. Using all these new loading productions a new distribution graph can be made.
Comparing the newly made graph with the original graph could give a better indicating about whether the production in reality can be characterized as linear. Of course differences between the graphs are to be expected, if only because an average overflow loss is assumed.

10.5 Modeling separate cutting teeth

As has been mentioned before it is likely that the cutting forces are overestimated due to the cutting teeth being modeled as one large blade. In order to calculate better cutting forces it might therefore be better to model the teeth separately whilst also implementing the 'side effects' as described in *The Delft Sand, Clay & Rock Cutting Model* to account for the effects of the spaces between the teeth.
For the width of a tooth the width of the draghead should be divided by the number of teeth, instead of using the actual width of a tooth. This is because the sand in between two teeth is also cut.
Implementing a model for separate cutting teeth in the production model would probably lead to a cutting force reduction due to the side effect, which will lead to a prolonged linear production.

10.6 Particle size distribution based soil parameters

The draghead production model requires a number of soil mechanical properties that are usually not measured: the porosity, the permeability, the dilatation and the angles of internal and external friction. Normally for a dredging job one or a small number of soil samples are available and of these samples a particle size distribution is generated. Collecting these samples and measuring the aforementioned

parameters in a laboratory would be time consuming and expensive (due to time and equipment costs). Furthermore it is questionable whether the measured parameters in the laboratory are representative for the conditions in situ. Also it is the question if samples from a few locations are representative for the entire borrowing area. This last point will however always be a problem because soil conditions can be different from meter to meter.
Due to the high measurement costs it would be nice if the required soil mechanical properties can be calculated based on the particle size distribution. This is possible and for a few parameters there has already been referred to appendix F. For the remaining parameters also a small overview is given in appendix F and an example code for Python utilizing all these theories is given in appendix D.
The fact that these properties can be calculated does not mean that the theories actually do a good job in predicting the soil properties. Therefore it would be interesting to compare actual measurements of a sand with the predicted properties based on the PSD of that sand, preferably for different types of sand. Calculation of soil properties based on the PSD will allow the draghead production model and future models utilizing the cutting theory to be tested using data of previous projects for which a PSD is available.

10.7 Implementation of production limits

The draghead production model in its current state produces results but does not check whether these results are possible in reality. It would therefore be nice if the production model after running would indicate until which speed the plotted results are not in conflict with one of the limiting factors that were described in paragraph 6.11. A number of parameters needed to do this, the cutting forces, are already calculated by the model.
Another interesting addition to the model, regarding a limiting factor, is to add a moment balance for the lower arm around the current moment balance of the visor. If the linear production theory does not hold then it would be interesting to see what kind of production result this implementation gives.

10.8 Test heel jet production

The sensitivity analyses showed that introducing tooth jets to the production model decreased the influence of the heel jets on the production significantly. In the production model the heel jet production is constant for varying speeds which means that in the linear production regime the heel jets relative contribution reduces for increasing speed. This eventually led to a situation in which increasing the heel jet production with 20 percent did not even lead to a total production increase of a percent. This limited production contribution raises the question if the heel jet power, delivered by the pump, cannot be used more efficiently. A possibility for this might be to plug the heel jets which forces more flow to the visor jets but also the tooth jets. Thus by blocking the heel jets more power is available for the tooth jets.
It is hard to predict the change in production, if any, because the tooth jet model is jet pressure-based while more power available probably means an increase of pressure as well as flow. Nevertheless it would still be interesting to see the performance of a draghead with only tooth jets. Results of such experiments could influence future draghead choices or future jet water allocations.

10.9 Cutting model for cohesive materials

As was mentioned in the introduction of this thesis, the original scope of this research was to create a draghead production model for cohesive and non-cohesive materials. However, for this thesis the choice was made to focus on the non-cohesive materials. Adding the option to calculate the production for cohesive materials (clays) would however not be that difficult. This would require to write a clay cutting module which calculates cutting forces for cutting clay. The advantage of clay cutting with respect to sand cutting is that it is assumed that pore pressures do not play a role. Hence, no pore pressure module is required. What is required is that the cohesion and adhesion of the clay are known, thus these must somehow be measured. A way to measure these parameters has already been developed at Great Lakes by T.A.A. Combe and is described in his thesis [17].
The influence of heel and tooth jets on the clay cutting production is rather hard to predict. However, a good first approach might be to neglect their influence.

A Cutting theory addendum

In the first paragraph a cutting model for the cutting of dry sand will be covered. Although this model is not used in the production model, it has been used during debugging and is therefore still described.
The paragraph that follows describes saturated sand cutting with a soil wedge. This theory is currently not used in the production model, although it is described how it can be implemented.
The last paragraph of this chapter covers cutting force calculations in the case that the blade is not perpendicular to the cutting direction. Again, this theory is not used in the draghead production code but its possible implementation is described.

A.1 Dry sand cutting

In dredging there are few occasions where sand that is being cut can actually be defined as dry sand. However, by adjusting the input densities the dry sand model can also be used to calculate cutting forces for water saturated sand. These calculated cutting forces can the give insight in the contribution of gravitational and inertial forces with respect to the total cutting force. How the input density has to be adjusted will be shown in section A.1.2. The first section will explain how the cutting forces can be calculated using a force equilibrium.

A.1.1 Equilibrium of forces

The cutting model for dry sand assumes that the cutting process is continuous and stationary. This means that all forces in the same direction, including the cutting forces, are in equilibrium.
Furthermore it is assumed that there is no adhesion nor cohesion since the material being cut is dry sand and that there are no under pressures due to dilatation (for more information see section 3.3.1) because the permeability of the sand for air is high.
Not taking adhesion, cohesion and the under pressures into account reduces the amount of forces acting on the layer of soil that is cut. The remaining acting forces can be seen figure A.1 and are explained below.

Acting forces:

- G: Gravitational force, due to the weight of the slice
- I: Inertial force, due to acceleration of the sand from standstill to v_c
- N_1: Normal force on shear surface, due to effective grain stresses
- S_1: Shear force on shear plane, due to internal friction $(N_1 \cdot tan(\phi))$
- N_2: Normal force on blade surface, due to effective grain stresses
- S_2: Shear force on blade surface, due to external friction between sand and steel $(N_2 \cdot tan(\delta))$

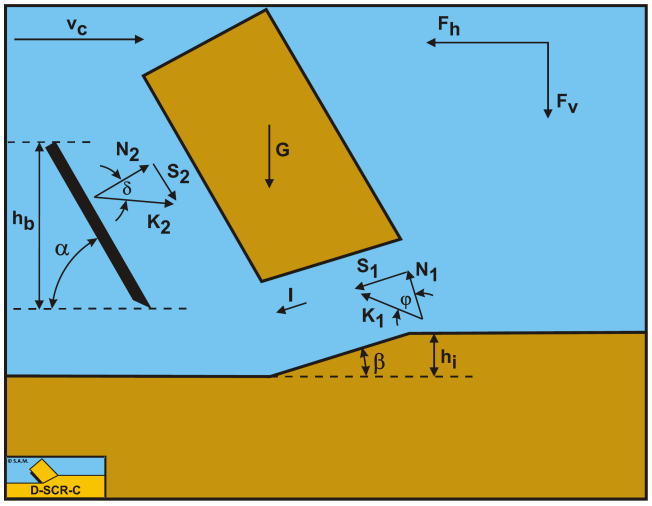

Figure A.1: Forces acting on the cut slice

It is important to notice that due to Newton's third law the forces acting on the blade are equal to N_2 and S_2 but in opposite direction.

The normal force N_1 and the shear force S_1 can be combined into a resulting force K_1:

$$K_1 = \sqrt{N_1^2 + S_1^2} \tag{A.1.1}$$

The same can be done with N_2 and S_2, resulting in K_2:

$$K_2 = \sqrt{N_2^2 + S_2^2} \tag{A.1.2}$$

Because the cutting process is assumed to be continuous and stationary there must be an equilibrium in both the horizontal forces and the vertical forces:

$$\sum F_h = K_1 \cdot sin(\beta + \phi) + I \cdot cos(\beta) - K_2 \cdot sin(\alpha + \delta) = 0 \tag{A.1.3}$$

$$\sum F_v = -K_1 \cdot cos(\beta + \phi) + I \cdot sin(\beta) + G - K_2 \cdot cos(\alpha + \delta) = 0 \tag{A.1.4}$$

Since equation (A.1.3) and equation (A.1.4) have the same two unknowns the system of equations is solvable (see Appendix B). Solving the equations yields new expressions for K_1 and K_2:

$$K_1 = \frac{G \cdot sin(\alpha + \delta) - I \cdot cos(\alpha + \beta + \delta)}{sin(\alpha + \beta + \delta + \phi)} \tag{A.1.5}$$

$$K_2 = \frac{G \cdot sin(\beta + \phi) + I \cdot cos(\phi)}{sin(\alpha + \beta + \delta + \phi)} \tag{A.1.6}$$

The inertia forces can be calculated by an equation derived by Wismer and Luth [18],[19]:

$$I = \rho_s \cdot v_c^2 \cdot \frac{sin(\alpha)}{sin(\alpha + \beta)} \cdot h_i \cdot w \tag{A.1.7}$$

The gravitational force can be derived based on the geometry of the layer cut. For the layer in figure 3.1 the gravitational force is defined as follows:

$$G = \rho_s \cdot g \cdot h_i \cdot w \cdot \frac{sin(\alpha + \beta)}{sin(\beta)} \cdot \left\{ \frac{(h_b + h_i \cdot sin(\alpha))}{sin(\alpha)} + \frac{h_i \cdot cos(\alpha + \beta)}{2 \cdot sin(\beta)} \right\} \tag{A.1.8}$$

In figure A.1 it can be seen that the blade exerts a force K_2 onto the cut slice. This means that the slide exerts a force of the same magnitude onto the blade. Using trigonometry force K_2 can be decomposed into a horizontal and a vertical cutting force:

$$F_h = K_2 \cdot sin(\alpha + \delta) \tag{A.1.9}$$

$$F_v = K_2 \cdot cos(\alpha + \delta) \tag{A.1.10}$$

A.1.2 Submerged dry sand cutting

As mentioned before the soil density ρ_{soil} in the dry sand cutting theory can be altered to study the contribution of inertia and gravitational forces in cutting water saturated sand.
The soil density is present in both the inertia part, equation (A.1.7) and the gravitational part, equation (A.1.8). However, the soil density has to be altered differently for each part.

For the inertia part the effects of the water in the pores has to be taken into account since this water adds mass to the sand bed. What fraction of the water saturated soil is water is dependent on what fraction of the soil is pore. Hence, the porosity is needed to calculate a new soil density as well as the density of pure quartz, ρ_q and the density of (sea)water, ρ_w:

$$\rho_{soil} = n_{max} \cdot \rho_w + (1 - n_{max}) \cdot \rho_q \tag{A.1.11}$$

Substituting equation (A.1.11) into equation (A.1.7) yields the following equation:

$$I = (n_{max} \cdot \rho_w + (1 - n_{max}) \cdot \rho_q) \cdot v_c^2 \cdot \frac{sin(\alpha)}{sin(\alpha + \beta)} \cdot h_i \cdot w \tag{A.1.12}$$

The gravity part has to be changed to account for the buoyancy force, since the sand grains are submerged:

$$\rho_{soil} = n_{max} \cdot (\rho_q - \rho_w) \tag{A.1.13}$$

Substituting equation (A.1.13) into equation (A.1.8) yields the following equation:

$$G = (n_{max} \cdot (\rho_q - \rho_w)) \cdot g \cdot h_i \cdot w \cdot \frac{sin(\alpha + \beta)}{sin(\beta)} \cdot \left\{ \frac{(h_b + h_i \cdot sin(\alpha))}{sin(\alpha)} + \frac{h_i \cdot cos(\alpha + \beta)}{2 \cdot sin(\beta)} \right\} \tag{A.1.14}$$

Using equation (A.1.12) and equation (A.1.14) in equation (A.1.6) gives the inertia and gravitation dominated cutting forces.

A.1.3 The shear angle

In the previous sections it has been assumed that the shear angle β is known but actually the shear angle has to be calculated. According to Miedema the shear angle can analytically be derived for the inertial forces:

$$\beta = \frac{\pi}{2} - \frac{2 \cdot \alpha \ + \delta + \phi}{2} \tag{A.1.15}$$

For the production model the use of the submerged dry sand cutting model is only optional since the contribution of inertial and gravitational forces is negligible compared to the water under pressure forces. The main cutting forces are calculated using the saturated sand cutting model. This model also requires a shear angle β. How this shear angle is calculated is explained in section 3.3.4. This shear angle can then also be used in the submerged dry sand model and equation (A.1.15) has not to be used.

A.2 Saturated sand cutting with a wedge

The wedge cutting model can be used in the production model on two occasions. The first occasion is when the draghead is bulldozing through the soil and the bulldozing forces have to be calculated. The second occasion is when the cutting forces have to be calculated when the draghead is equipped with a turtle exclusion device.
In principle the wedge cutting model is similar to the saturated sand cutting model. Both models are governed by the effects of dilatation (see section 3.3.1) and the cutting forces are calculated using a force equilibrium. The main difference is the geometry since the sand is now cut using a sand wedge. Definitions regarding the sand wedge will be given in section A.2.1. A sand wedge is formed when the sum of the angles α, β, δ and ϕ approaches 180°. At this point the regular saturated sand cutting mechanism is no longer the mechanism that does the minimal amount of cutting work, so the cutting mechanism changes to the mechanism that does, which is the wedge cutting mechanism.

A.2.1 Definitions

In this paragraph the definitions for the saturated wedge cutting model are given. The definitions are shown in figure A.2 and are described below.

Definitions:

A: Tip of the wedge

B: End of the shear plane

C: Top of the blade

D: Tip of the blade

A-B: Shear plane

A-C: Wedge surface

A-D: Wedge bottom

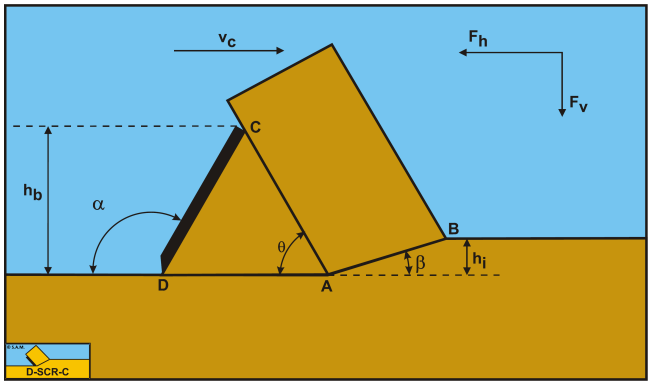

Figure A.2: Definitions concerning cutting with a wedge

D-C: Blade surface

h_b: Blade height

h_i: Thickness of the layer cut

v_c: Cutting velocity or trailing speed

α: Blade angle

β: Shear angle

θ: Wedge angle

F_h: Horizontal force, positive in direction of arrow

F_v: Vertical force, positive in direction of arrow

A.2.2 Force equilibrium

The cutting model for water saturated sand with a wedge assumes that the cutting process is continuous and stationary. This means that all forces in the same direction, including the cutting forces, are in equilibrium.
As with the normal saturated sand cutting model it is assumed that there is no adhesion nor cohesion since the material being cut is sand. The contributions of gravitational and inertial forces are again omitted because their magnitude is negligible compared to the magnitude of the pore under pressure forces that are the result of dilatation. What dilatation is and why it leads to pore under pressures is explained in section 3.3.1 and section 3.3.2. The numerical calculation of the pore pressure forces is explained in paragraph 3.4.
The forces acting on the cutting soil wedge are shown in figure A.4 and are explained below.

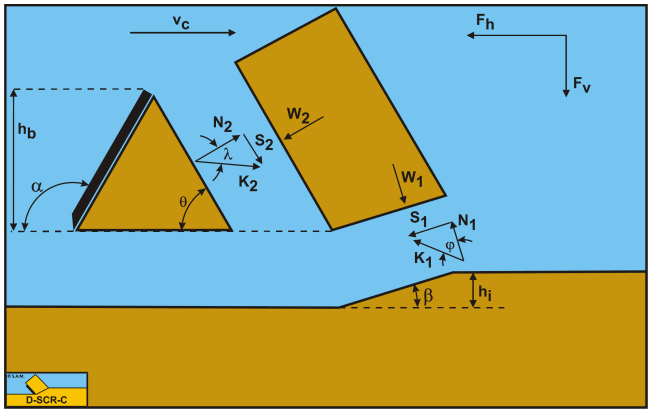

Figure A.3: Forces acting on the saturated cut slice

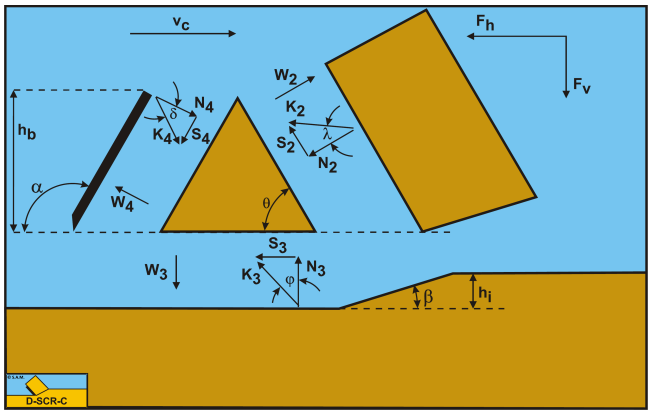

Figure A.4: Forces acting on the saturated soil wedge

Acting forces:

W_1: Force due to water under pressure in the shear zone

W_2: Force due to water under pressure on the wedge

W_3: Force due to water under pressure on the wedge bottom

W_4: Force due to water under pressure on the blade

N_1: Normal force on shear surface, due to effective grain stresses

S_1: Shear force on shear plane, due to internal friction $(N_1 \cdot tan(\phi))$

N_2: Normal force on the pseudo blade, due to effective grain stresses

S_2: Shear force on pseudo blade, due to soil/soil friction $(N_2 \cdot tan(\lambda))$. λ because the friction angle of the pseudo blade is not necessarily equal to ϕ since the soil already has been deformed.

N_3: Normal force on the bottom of the wedge, due to effective grain stresses

S_3: Shear force on bottom of wedge, due to soil/soil friction $(N_3 \cdot tan(\phi))$

N_4: Normal force on blade, due to effective grain stresses

S_4: Shear force on blade, due to external friction between soil and steel $(N_4 \cdot tan(\delta))$

It is important to notice that due to Newton's third law the forces acting on the blade are equal to N_4, S_4 and W_4 but in opposite direction.
Before the cutting forces on the blade can be determined first the cutting forces on the pseudo blade have to be determined. This is also done through force equilibria.

The horizontal force equilibrium:

$$\sum F_h = K_1 \cdot sin(\beta + \phi) - W_1 \cdot sin(\beta) + W_2 \cdot sin(\theta) - K_2 \cdot sin(\theta + \lambda) = 0 \tag{A.2.1}$$

The vertical force equilibrium:

$$\sum F_v = -K_1 \cdot cos(\beta + \phi) + W_1 \cdot cos(\beta) + W_2 \cdot cos(\theta) - K_2 \cdot cos(\theta + \lambda) = 0 \tag{A.2.2}$$

The resulting force on the shear plane is now:

$$K_1 = \frac{W_2 \cdot sin(\lambda) + W_1 \cdot sin(\theta + \beta + \lambda)}{sin(\theta + \beta + \lambda + \phi)} \tag{A.2.3}$$

The resulting force on the pseudo blade is now:

$$K_2 = \frac{W_2 \cdot sin(\theta + \beta + \phi) + W_1 \cdot sin(\phi)}{sin(\theta + \beta + \lambda + \phi)} \tag{A.2.4}$$

In equation (A.2.3) and (A.2.4) W_1 and W_2 are the water pressure forces on the shear plane and on the pseudo blade:

$$W_1 = p_{1m} \cdot L_1 \cdot W \tag{A.2.5}$$

$$W_2 = p_{2m} \cdot L_2 \cdot W \tag{A.2.6}$$

Where p_{1m} and p_{2m} are calculated as described in section A.2.5, W is the width of the blade and L_1 and L_2 are respectively the length of the shear zone and the length of the pseudo blade:

$$L_1 = \frac{h_i}{sin(\beta)} \tag{A.2.7}$$

$$L_2 = \frac{h_b}{sin(\theta)} \tag{A.2.8}$$

Using equation (A.2.4) the cutting forces on the pseudo blade can now be derived:

$$F_h = -W_2 \cdot sin(\theta) + K_2 \cdot sin(\theta + \lambda) \tag{A.2.9}$$

$$F_v = -W_2 \cdot cos(\theta) + K_2 \cdot cos(\theta + \lambda) \tag{A.2.10}$$

Note that λ is introduced here as the internal friction angle for the soil in the wedge. Since the soil in the wedge is moving it does not necessarily have the same properties as the soil in the layer cut. The

friction angle of the soil in the wedge will likely be somewhat lower than the friction angle of the soil in the layer cut. However, the friction angle will likely not be lower than the external friction angle between soil and steel.
Assuming that λ will be the average of the internal friction angle ϕ and the external friction angle δ and assuming that $\delta = \frac{2}{3} \cdot \phi$ (see the experiments of Potyondy [20]) leads to the following expression for λ:

$$\lambda = \frac{5}{6} \cdot \phi \tag{A.2.11}$$

To get the cutting forces on the blade first the horizontal and vertical force equilibrium on the wedge must be solved. Note that δ_e in the equations is the mobilized external friction angle. The mobilized external friction angle is not necessarily equal to δ because the sand in the wedge is moving.

The horizontal force equilibrium:

$$\begin{aligned} \sum F_h = &+ W_4 \cdot sin(\alpha) - K_4 \cdot sin(\alpha + \delta_e) + K_3 \cdot sin(\phi) \\ &- W_2 \cdot sin(\theta) + K_2 \cdot sin(\theta + \lambda) = 0 \end{aligned} \tag{A.2.12}$$

The vertical force equilibrium:

$$\begin{aligned} \sum F_v = &+ W_4 \cdot cos(\alpha) - K_4 \cdot cos(\alpha + \delta_e) + W_3 - K_3 \cdot cos(\phi) \\ &- W_2 \cdot cos(\theta) + K_2 \cdot cos(\theta + \lambda) = 0 \end{aligned} \tag{A.2.13}$$

The grain force on the bottom of the wedge is now:

$$\begin{aligned} K_3 = &\frac{-W_2 \cdot sin(\alpha + \delta_e - \theta) + K_2 \cdot sin(\alpha + \delta_e - \theta - \lambda)}{sin(\alpha + \delta_e + \phi)} \\ &+ \frac{W_3 \cdot sin(\alpha + \delta_e) + W_4 \cdot sin(\delta_e)}{sin(\alpha + \delta_e + \phi)} \end{aligned} \tag{A.2.14}$$

The grain force on the blade is now:

$$\begin{aligned} K_4 = &\frac{-W_2 \cdot sin(\theta + \phi) + K_2 \cdot sin(\theta + \lambda + \phi)}{sin(\alpha + \delta_e + \phi)} \\ &+ \frac{W_3 \cdot sin(\phi) + W_4 \cdot sin(\alpha + \phi)}{sin(\alpha + \delta_e + \phi)} \end{aligned} \tag{A.2.15}$$

In equation (A.2.14) and (A.2.15) W_3 and W_4 are the water pressure forces on the bottom of the wedge and on the blade:

$$W_3 = p_{3m} \cdot L_3 \cdot W \tag{A.2.16}$$

$$W_4 = p_{4m} \cdot L_4 \cdot W \tag{A.2.17}$$

Where p_{3m} and p_{4m} are calculated as described in section A.2.5, W is the width of the blade and L_3 and L_4 are respectively the length of the bottom of the wedge and the length of the blade:

$$L_3 = h_b \cdot \left(\frac{1}{tan(\theta)} - \frac{1}{tan(\alpha)} \right) \tag{A.2.18}$$

$$L_4 = \frac{h_b}{sin(\alpha)} \tag{A.2.19}$$

Using equation (A.2.15) the horizontal and vertical cutting forces on the blade can be derived:

$$F_h = -W_4 \cdot sin(\alpha) + K_4 \cdot sin(\alpha + \delta_e) \tag{A.2.20}$$

$$F_v = -W_4 \cdot cos(\alpha) + K_4 \cdot cos(\alpha + \delta_e) \tag{A.2.21}$$

A.2.3 The shear angle

Calculating the shear angle when cutting with a saturated wedge follows the same procedure as calculating the shear angle when cutting water saturated sand with a blade. Basically finding the shear angle through iteration for which the cutting work is minimal. For more details see section 3.3.4. The difference in the shear angle calculations comes from the difference in 'blade' angle and material. Instead of using the blade angle α the pseudo blade angle θ must be used. The angle of external friction of sand and steel δ is changed to friction angle between sand and mobilized sand λ. These two changes lead to the following equation:

$$\begin{aligned} \frac{\partial F'_h}{\partial \beta} = &- h_i \cdot \frac{sin(\phi) \cdot sin(\theta + 2 \cdot \beta + \lambda + \phi) \cdot sin(\theta + \lambda)}{sin^2(\beta) \cdot sin(\theta + \beta + \lambda + \phi)^2} \\ &+ h_b \cdot \frac{sin(\lambda) \cdot sin(\theta + \lambda)}{sin(\theta) \cdot sin(\theta + \beta + \lambda + \phi)^2} = 0 \end{aligned} \tag{A.2.22}$$

The equation above can also be solved using an iterative method.

A.2.4 The wedge angle

In order to calculate the wedge cutting forces the wedge angle or pseudo blade angle θ must be known. Using the calculations of Hatamura & Chijiiwa and many others Miedema has found an empirical equation for θ:

$$\theta = (90 - \phi) \cdot \left(0.73 + 0.0788 \cdot \frac{h_b}{h_i}\right) \tag{A.2.23}$$

A.2.5 Parallel resistor method for wedge cutting

The parallel resistor method for saturated sand cutting with a wedge is based on the same principles as those of the parallel resistor method, which is described in section 3.4.1. Again, water flows only perpendicular into the shear zone and again four flow lines can be identified, which can be seen in figure A.5. Two of these flow lines go through soil that has not (yet) been deformed. Hence, the soil had a permeability k_i and a porosity n_i. The other two flow lines go through soil that has been deformed and thus the soil there has a permeability k_{max} and a porosity n_{max}. A difference with the other parallel resistor model is that next to the pore vacuum pressure on the blade and in the shear zone also the pore vacuum pressures on the pseudo blade and on the bottom of the wedge will be

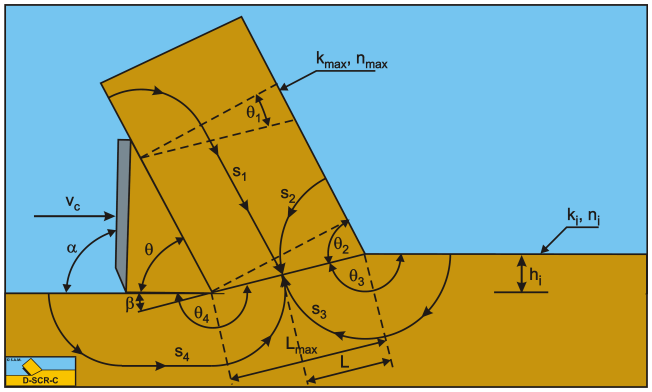

Figure A.5: Flow lines in the analytical method for saturated wedge cutting

calculated.
The definitions of figure A.5 are given below.

Definitions:

s_1: Flow line from top of blade through deformed sand package

s_2: Flow line from free surface through deformed sand package

s_3: Flow line from front of blade through initial sand package

s_4: Flow line from back of blade through initial sand package

θ_1: Angle between a line perpendicular to blade and the shear zone

θ_2: Angle between the free surface and the shear zone

θ_3: Angle between the initial sand bed and the shear zone

θ_4: Angle between the sand bed after cutting and the shear zone

L_{max}: Length of the shear zone, $h_i/sin(\beta)$

L: Variable distance between the free surface and the current soil element in the shear zone

h_i: Thickness of the layer cut

v_c: Cutting velocity or trailing speed

α: Blade angle

β: Shear angle

θ: Wedge angle

In section 3.3.2 Darcy's Law was used to find the specific flow q in equation (3.3.5). This equation however, assumed infinitesimal small changes in pressure and distance. To make the equation suitable for numerical calculations the infinitesimal small pressure changes and distance changes are changed to pressure and distance differences:

$$q = k \cdot i = k \cdot \frac{\Delta p}{\rho_w \cdot g \cdot \Delta s} \tag{A.2.24}$$

Using equation (A.2.24) an expression for the total specific flow through the four flow lines as result of dilatation can be found:

$$\begin{aligned} q &= \epsilon \cdot v_c \cdot sin(\beta) \\ &= k_{max} \cdot \frac{\Delta p}{\rho_w \cdot g \cdot s_1} + k_{max} \cdot \frac{\Delta p}{\rho_w \cdot g \cdot s_2} + k_i \cdot \frac{\Delta p}{\rho_w \cdot g \cdot s_3} + k_i \cdot \frac{\Delta p}{\rho_w \cdot g \cdot s_4} \end{aligned} \tag{A.2.25}$$

In equation (A.2.25) the length of flow line s_1 is defined as:

$$\begin{aligned} &s_1 = (L_{max} - L) \cdot \theta_1 + L_2 \\ &\text{With: } \theta_1 = \pi - \theta - \beta \text{ and } L_2 = h_b / sin(\theta) \end{aligned} \tag{A.2.26}$$

The length of flow line s_2 is:

$$\begin{aligned} &s_2 = L \cdot \theta_2 \\ &\text{With: } \theta_2 = \theta + \beta \end{aligned} \tag{A.2.27}$$

The length of flow line s_3 is:

$$\begin{aligned} &s_3 = L \cdot \theta_3 \\ &\text{With: } \theta_3 = \pi - \beta \end{aligned} \tag{A.2.28}$$

The length of flow line s_4 is:

$$\begin{aligned} &s_4 = (L_{max} - L) \cdot \theta_4 + L_5 \\ &\text{With: } \theta_4 = \pi + \beta \text{ and } L_5 = 0.2 \cdot h_i / sin(\theta) \end{aligned} \tag{A.2.29}$$

The factors of 0.8 and 0.2 for the lengths s_2, s_3 and L_5 are correction factors and are calibrated on experiments. Length L_2 is the length of the pseudo-blade and L_5 is 0.2 times the pseudo-blade height. The total specific flow can be rewritten as follows:

$$\begin{aligned} \rho_w \cdot g \cdot q &= \rho_w \cdot g \cdot \epsilon \cdot v_c \cdot sin(\beta) \\ &= \frac{\Delta p}{\left(\frac{s_1}{k_{max}}\right)} + \frac{\Delta p}{\left(\frac{s_2}{k_{max}}\right)} + \frac{\Delta p}{\left(\frac{s_3}{k_i}\right)} + \frac{\Delta p}{\left(\frac{s_4}{k_i}\right)} = \frac{\Delta p}{R_1} + \frac{\Delta p}{R_2} + \frac{\Delta p}{R_3} + \frac{\Delta p}{R_4} = \frac{\Delta p}{R_t} \end{aligned} \tag{A.2.30}$$

In equation (A.2.30) it can be seen that the resistance of a flow line is defined as the length of the flow line divided by the permeability of the soil in which the flow line is located. The equations for the resistance of the four flow lines are given below:

$$R_1 = \frac{s_1}{k_{max}} \tag{A.2.31}$$

$$R_2 = \frac{s_2}{k_{max}} \tag{A.2.32}$$

$$R_3 = \frac{s_3}{k_i} \tag{A.2.33}$$

$$R_4 = \frac{s_4}{k_i} \tag{A.2.34}$$

Since all four flow lines have the same pressure difference Δp they can be seen as four parallel resistors in an electrical circuit. In an electrical circuit the equivalent resistor R_t can be calculated for parallel resistors. Using the same equation this can also be done for the flow resistance in the soil:

$$\frac{1}{R_t} = \frac{1}{R_1} + \frac{1}{R_2} + \frac{1}{R_3} + \frac{1}{R_4} \tag{A.2.35}$$

Rewriting equation (A.2.30) now yields an equation for the pressure difference between a point (or element) in the shear zone and the hydrostatic pressure (pore vacuum pressure):

$$\Delta p = \rho_w \cdot g \cdot v_c \cdot \epsilon \cdot sin(\beta) \cdot R_t \tag{A.2.36}$$

However, the results of equation (A.2.36) are corrected to better match data from experiments:

$$\Delta p = (\rho_w \cdot g \cdot v_c \cdot \epsilon \cdot sin(\beta) \cdot R_t) \cdot sin(\theta)^{0.2} \tag{A.2.37}$$

The average pore vacuum pressure in the shear zone can now be found by integration for infinitesimal small elements or by summation for a finite amount of elements, as is shown below:

$$p_{1m} = \frac{1}{n} \cdot \sum_{i=0}^{n} \Delta p_i \tag{A.2.38}$$

Now the average pore vacuum pressure on the pseudo-blade can be calculated using the pressure difference at the tip of the blade:

$$\begin{aligned} &p_{2m} = p_{tip} \cdot f \cdot \left(1 + \left(\frac{k_i}{k_{max}}\right)^2 \cdot sin(\theta)\right) \\ &\text{With: } p_{tip} = \Delta p_{i=N} \end{aligned} \tag{A.2.39}$$

The factor f is calibrated on experiments and is, for the non-cavitating case, defined as follows:

$$f_{non-cav} = \frac{\left(\frac{h_i}{h_b}\right)^{(\frac{\pi}{2} - 1.35 \cdot \theta)} \cdot sin(\theta + \beta) \cdot sin(\theta)^{0.5}}{0.5 \cdot sin(\beta)} \tag{A.2.40}$$

If cavitation does occur in the shear zone the factor f changes:

$$\begin{aligned} &f = f_{non-cav} \cdot \mathrm{e}^A + (1 - \mathrm{e}^A) \\ &\text{With: } A = -2 \cdot f_{non-cav} \cdot (p_0 - p_{1m})/p_{1m} \end{aligned} \tag{A.2.41}$$

In equation (A.2.41) the pressure p_0 is the average unrestricted pore vacuum pressure. This is the average pore vacuum pressure p_{1m} in case the pressure drops are not restricted by the saturated water vapor pressure. Meaning that $\rho_w \cdot g \cdot (z + 10)$ is not the limit. However, for the end result p_{2m} it is.

The average pore vacuum pressure on the bottom of the wedge can be calculated using the following equation:

$$p_{3m} = 0.5 \cdot \left(\frac{p_{max} \cdot L_5}{(L_3 + L_5)} + p_{max} \right) \cdot sin(\theta)^{1.5}$$
$$\text{With: } L_3 = h_b \cdot (1/tan(\theta)) - 1/tan(\alpha) \tag{A.2.42}$$

In equation (A.2.42) the length L_3 is the length of the bottom of the wedge. The pressure p_{max} is the maximum unrestricted pore vacuum pressure found in the shear zone. Again, the average pore vacuum pressure p_{3m} is limited to the saturated water vapor pressure.
The average pore vacuum pressure on the blade can be calculated using the following equation:

$$p_{4m} = p_{2m} \cdot \left(\frac{h_b}{(h_b + L_3)} \right)^{0.8} \tag{A.2.43}$$

If the maximum unrestricted pore vacuum pressure p_{max} is larger than the saturated water vapor pressure the average pore vacuum pressure on the blade has to be compensated:

$$p_{4m} = p_{4m} + (\Delta p_{max} - p_{4m}) \cdot \left(1 - \mathrm{e}^{-(\frac{p_{max} - \Delta p_{max}}{\Delta p_{max}/3})} \right) \tag{A.2.44}$$

In equation (A.2.44) Δp_{max} is the saturated water vapor pressure, which is still the upper limit.
When p_{1m}, p_{3m}, p_{3m} and p_{4m} are calculated they serve as inputs for the cutting force calculations, as is explained in section A.2.2.

A.3 The snowplow effect

In this paragraph the snowplow effect will be discussed. The snowplow effect is what happens when the blade is not perpendicular to the cutting direction. An extra force will be added due to the soil being deviated sideways. The only time that the snowplow effect model is needed in the production model is when the cutting force of a turtle exclusion device (TED) must be calculated. Furthermore in the production model there is only need for the horizontal cutting force of the TED (the force in the cutting direction). Therefore the description of the snowplow effect in this paragraph will only focus on calculating the cutting force in trailing direction. A detailed description of the calculations in the other directions as well as in the trailing direction is given in S.A. Miedema's *The Delft Sand, Clay & Rock Cutting Model*, [4],[5].
The first section of this paragraph covers cutting forces that serve as an input for the snowplow effect calculations. The second section covers the actual calculations of the snowplow cutting force in trailing direction.

A.3.1 Input cutting forces

Calculations of the cutting force due to the snowplow effect start with a horizontal cutting force F_h and a vertical cutting force F_v as an input. These cutting force can be obtained by using one of the cutting models described in paragraph A.1, 3.3 and A.2. In the case of the production model the snowplow effect model is only used when cutting with TEDs. The TED cutting force calculations use the saturated wedge cutting model.
It is important that F_h and F_v are calculated as if the blade is cutting in a normal way. Hence the normal trailing speed v_c and blade width W are used. There is no compensation for the blade actually being at a deviation angle yet. This will be described in the next section.

A.3.2 The snowplow cutting force

As mentioned at the beginning of this paragraph only the cutting force in trailing direction is of importance. This force consists of two major components: the horizontal cutting force F_h and the deviation force that tries to push the blade sideways F_{d2}. The snowplow cutting force in trailing direction can be calculated using the following equation:

$$F_{x2} = F_h \cdot cos(\iota) + F_{d2} \cdot sin(\iota) \tag{A.3.1}$$

In equation (A.3.1) x is the trailing direction and the subscript 2 denotes that it is a force acting on the blade. The angle ι is defined as the angle between the trailing direction and a line perpendicular to the blade, see figure A.6.

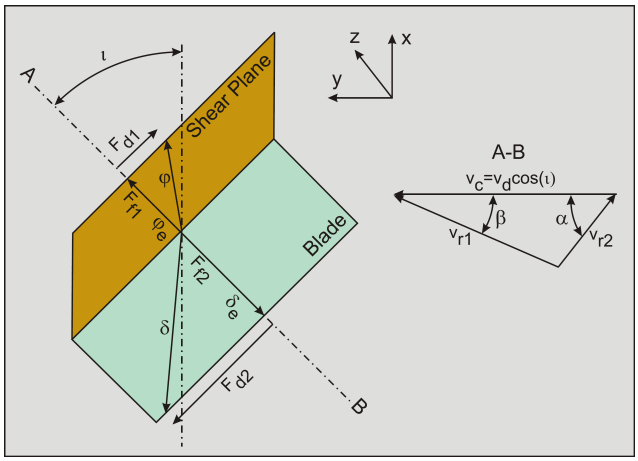

Figure A.6: The snowplow force directions

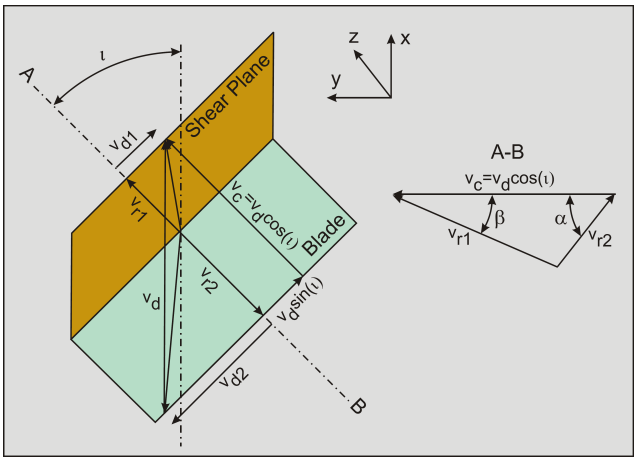

Figure A.7: The snowplow velocities and directions

In section A.3.1 it was explained that the horizontal cutting force F_h is an input. However the deviation force is still unknown and can be calculated using the following equation:

$$F_{d2} = F_{f2} \cdot \frac{v_{d2}}{v_{r2}} \tag{A.3.2}$$

In equation (A.3.2) F_{f2} is the friction force on the blade, see figure A.6, which can be calculated as follows:

$$F_{f2} = F_h \cdot cos(\alpha) - F_v \cdot sin(\alpha) \tag{A.3.3}$$

In equation (A.3.2) v_{r2} is the relative velocity of the sand grains with respect to the blade, perpendicular to the edge (see figure A.7) and can be calculated as follows:

$$v_{r2} = v_c \cdot \frac{sin(\beta)}{sin(\alpha + \beta)} \tag{A.3.4}$$

The velocity component of the deviation velocity on the blade v_{d2} can be calculated using the following equation:

$$v_{d2} = v_d \cdot \frac{sin(\iota)}{(1 + \lambda)} \tag{A.3.5}$$

In which the deviation velocity v_d is defined as follows:

$$v_d = \frac{v_c}{cos(\iota)} \tag{A.3.6}$$

The λ in equation (A.3.5) is the ratio between the deviation velocity component in the shear zone and the deviation velocity component on the blade and can be calculated using the following equation:

$$\lambda = \left(\frac{F_h \cdot cos(\alpha) - F_v \cdot sin(\alpha)}{F_h \cdot cos(\beta) + F_v \cdot sin(\beta)} \right) \cdot \left(\frac{sin(\alpha)}{sin(\beta)} \right) \tag{A.3.7}$$

With the equations described above the snowplow cutting force can be calculated. How these equations can be applied in a TED cutting model can be found in paragraph H.2.

B Finding K_1 and K_2

In this appendix is shown how a system of two equations and two unknowns is solved in order to obtain expressions for K_1 and K_2. Although solving a system of two equations and two unknowns is pretty straightforward in general, in the case of K_1 and K_2 some trigonometric actions are applied in order to get $sin(\alpha+\beta+\delta+\phi)$ in the denominator. These trigonometric actions might not be obvious at first and are therefore shown.
There are multiple occasions in chapter 3 where expressions for K_1 and K_2 have to be found. Since all these calculations are similar only the calculation of K_1 for dry sand cutting is shown as an example. The trigonometric addition equations below play an important role in the calculations.

$$sin(x+y) = sin(x)\cdot cos(y) + cos(x)\cdot sin(y) \tag{B.0.1}$$

$$cos(x+y) = cos(x)\cdot cos(y) - sin(x)\cdot sin(y) \tag{B.0.2}$$

The actual calculations start with the sum of the horizontal and vertical cutting forces:

$$\sum F_h = K_1\cdot sin(\beta+\phi) + I\cdot cos(\beta) - K_2\cdot sin(\alpha+\delta) = 0 \tag{B.0.3}$$

$$\sum F_v = -K_1\cdot cos(\beta+\phi) + I\cdot sin(\beta) + G - K_2\cdot cos(\alpha+\delta) = 0 \tag{B.0.4}$$

By rewriting equation (B.0.3) an expression for K_2 in terms of K_1 is found:

$$\begin{aligned} &K_1\cdot sin(\beta+\phi) + I\cdot cos(\beta) - K_2\cdot sin(\alpha+\delta) = 0 \\ &K_1\cdot sin(\beta+\phi) + I\cdot cos(\beta) = K_2\cdot sin(\alpha+\delta) \\ &K_2 = \frac{K_1\cdot sin(\beta+\phi) + I\cdot cos(\beta)}{sin(\alpha+\delta)} \end{aligned} \tag{B.0.5}$$

Substituting equation (B.0.5) in equation (B.0.4) yields the following expression:

$$\begin{aligned} &-K_1\cdot cos(\beta+\phi) + I\cdot sin(\beta) + G - K_2\cdot cos(\alpha+\delta) = 0 \\ &-K_1\cdot cos(\beta+\phi) + I\cdot sin(\beta) + G - cos(\alpha+\delta)\cdot\left(\frac{K_1\cdot sin(\beta+\phi) + I\cdot cos(\beta)}{sin(\alpha+\delta)}\right) = 0 \\ &-K_1\cdot cos(\beta+\phi) + I\cdot sin(\beta) + G - \frac{K_1\cdot sin(\beta+\phi)\cdot cos(\alpha+\delta) + I\cdot cos(\beta)\cdot cos(\alpha+\delta)}{sin(\alpha+\delta)} = 0 \end{aligned} \tag{B.0.6}$$

Equation (B.0.6) can be further simplified as follows:

$$\begin{aligned} &-K_1\cdot cos(\beta+\phi) + I\cdot sin(\beta) + G - \frac{K_1\cdot sin(\beta+\phi)\cdot cos(\alpha+\delta) + I\cdot cos(\beta)\cdot cos(\alpha+\delta)}{sin(\alpha+\delta)} = 0 \\ &-K_1\cdot cos(\beta+\phi)\cdot sin(\alpha+\delta) + I\cdot sin(\beta)\cdot sin(\alpha+\delta) + G\cdot sin(\alpha+\delta) \\ &-K_1\cdot cos(\beta+\phi)\cdot cos(\alpha+\delta) - I\cdot cos(\beta)\cdot cos(\alpha+\delta) = 0 \\ &-K_1\cdot(sin(\alpha+\delta)\cdot cos(\beta+\phi) + cos(\alpha+\delta)\cdot sin(\beta+\phi)) + \\ &I\cdot(sin(\alpha+\delta)\cdot sin(\beta) - cos(\alpha+\delta)\cdot cos(\beta)) + G\cdot sin(\alpha+\delta) = 0 \end{aligned}$$

(B.0.7)

Now using the trigonometric addition equations (B.0.1) and (B.0.2), equation (B.0.7) can be further simplified to the following expression:

$$-K_1 \cdot sin(\alpha + \beta + \delta + \phi) - I \cdot cos(\alpha + \beta + \delta) + G \cdot sin(\alpha + \delta) = 0 \tag{B.0.8}$$

Equation (B.0.8) can now rewritten as follows:

$$\begin{aligned}
&- K_1 \cdot sin(\alpha + \beta + \delta + \phi) - I \cdot cos(\alpha + \beta + \delta) + G \cdot sin(\alpha + \delta) = 0 \\
&- K_1 \cdot sin(\alpha + \beta + \delta + \phi) - I \cdot cos(\alpha + \beta + \delta) = -G \cdot sin(\alpha + \delta) \\
&- K_1 \cdot sin(\alpha + \beta + \delta + \phi) = -G \cdot sin(\alpha + \delta) + I \cdot cos(\alpha + \beta + \delta) \\
&K_1 \cdot sin(\alpha + \beta + \delta + \phi) = G \cdot sin(\alpha + \delta) - I \cdot cos(\alpha + \beta + \delta) \\
&K_1 = \frac{G \cdot sin(\alpha + \delta) - I \cdot cos(\alpha + \beta + \delta)}{sin(\alpha + \beta + \delta + \phi)}
\end{aligned} \tag{B.0.9}$$

The same process can be repeated to obtain K_2. Alternatively equation (B.0.9) can be substituted for K_1 in equation (B.0.5) to obtain an expression for K_2.

C Root finding in Python

One of the most important steps in the production calculations is finding a visor angle for which a moment balance exists. For this angle the moments caused by the cutting forces cancel out the moment of the actuator. This is the point where a cumulative graph of all visor moments would go through zero.
For a range of visor angles multiple of these zero-points or roots can exist. The ScipPy library of Python [21] has multiple functions that can find the roots of a function. Each of these functions uses a different root-finding algorithm. The available root-finding algorithms are the Brent's quadratic method, Brent's hyperbolic method, Ridders' method, the bisection method and the Newton-Raphson method. All of these methods require the function of which the roots must be found as an input and require this input function to be continuous. For all except the Newton-Raphson method the other required input is an interval $[a, b]$ in which the root must be found. This interval must be chosen such that the sign of $f(a)$ is opposite to that of $f(b)$. Instead of an interval the Newton-Raphson method required an estimate x_0 of the position of the root. This is a disadvantage because a bad estimate of the root position might lead to another root being found instead. Another disadvantage is that it is not possible to define a range. Therefore it is possible that roots are found that lie outside of the range of possible visor angles. For these reasons the Newton-Raphson method is not used to find the moment balance.
The interval $[a, b]$ in the other methods is defined in the production model when the rough location of the right-most intersection (see section 6.6) has been found. This intersection point has been found by increasing the visor angle step-by-step until the sign of the cumulative graph of moments changes. The visor angle for which the sign has changed becomes b. The visor angle that is one step back becomes a.
Besides the same required inputs the Brent's quadratic method, Brent's hyperbolic method, Ridders' method and the bisection method also have the same optional inputs. This means that all of these methods can have the same maximum number of iterations or the same required iteration tolerance. Therefore all of these methods would be able to find the same number for a required tolerance. The only difference is the speed at which this happens or the speed of convergence. However, the calculations for the operational range of trailing speeds between 0 and 1 meters per second do not take long enough for the converge speed to be of any importance. Therefore any of the aforementioned methods can be used in the production method except for the Newton-Raphson method.

D The Production Model in Python

The Python code of the production model is property of Great Lakes Dredge & Dock Company.

For questions or more information please contact Robert Ramsdell.

Email: rcramsdell@gldd.com

E Smoothstep function

A smoothstep function is an interpolation function that allows for a smooth transition between two output values over a given range of input values. In general a smoothstep function yields a value of zero when the input value x is smaller than or equal to zero and a value of 1 when x is equal to or greater than 1. Values for x between 0 and 1 yield an interpolated value according to a third or higher order polynomial. This polynomial is designed in such a way that it yields 0 and 1 for x respectively equal to 0 and 1. The derivative of the polynomial is 0 for both x is 0 and x is 1.
In the production model the smoothstep function is used to make a smooth transition between the case when the pore pressures on the blade are subject to the tip effect and the case when the pore pressures are not subject to the tip effect anymore. The other application of the smoothstep function is to model the cavitation cloud in the normal cloud model. The smoothstep function used in the production model is a third order polynomial and is shown in equation E.0.1.

$$\begin{aligned} &\text{For: } x \leq 0,\ smoothstep(x) = 0 \\ &\text{For: } 0 < x < 1,\ smoothstep(x) = 3x^2 - 2x^3 \\ &\text{For: } x \geq 1,\ smoothstep(x) = 1 \end{aligned} \tag{E.0.1}$$

In the production model the values used with the smoothstep function do usually not range between 0 and 1. The smoothstep function can therefore be modified to yield outputs between o_{min} and o_{max} for input values between i_{min} and i_{max}. First a value for a between 0 and 1 is calculated based on input i between i_{min} and i_{max}.

$$a = \frac{i - i_{min}}{i_{max} - i_{min}} \tag{E.0.2}$$

Using this a, an output between o_{min} and o_{max} can be calculated using a modified smoothstep function.

$$\begin{aligned} &\text{For: } i \leq i_{min},\ smoothstep(i) = o_{min} \\ &\text{For: } i_{min} < i < i_{max},\ smoothstep(i) = (o_{max} - o_{min}) \cdot (3a^2 - 2a^3) + o_{min} \\ &\text{For: } i \geq i_{max},\ smoothstep(i) = o_{max} \end{aligned} \tag{E.0.3}$$

F Soil parameter and particle size distribution relations

F.1 Introduction

For dredging jobs commonly the particle size distribution (PSD) or sieve curves are the only soil data available. It would therefore be nice if soil mechanical parameters could be derived of the PSD so that these can be used as inputs in the production model and other models. Theories that aim to predict a certain parameter based on the PSD do exist. Most widely known are theories aimed at predicting the permeability since this parameter is hard to measure in reality. However, theories aimed at predicting the porosity and the angle of internal friction do also exist. In the following paragraphs of this appendix a number of theories aimed at predicting the aforementioned parameters are summarized. An example code has been created utilizing these theories. It can be found in appendix D.

F.2 Kozeny-Carman

The Kozeny-Carman equation was first introduced by Josef Kozeny in 1927 [10] and later edited and revisited by Phillip Carman in 1937 [11] and 1956 [12], hence the name Kozeny-Carman. In the course of years there have been many variants of the Kozeny-Carman equation. The equation below has been chosen because it expresses the permeability as a function of the particle size.

$$k = \frac{\rho_w \cdot g}{\mu_w} \cdot \frac{n^3}{180 \cdot (1-n)^2} \cdot d_m^2 \tag{F.2.1}$$

In this equation ρ_w is the density of water, g is the gravitational constant, μ_w is the dynamic viscosity of water, n is the porosity of the soil and d_m is the mean particle diameter. The mean particle diameter is defined as follows:

$$d_m = \frac{d_{10} + d_{20} + d_{30} + d_{40} + d_{50} + d_{60} + d_{70} + d_{80} + d_{90}}{9} \tag{F.2.2}$$

The porosity of the soil based on the particle size distribution can be estimated using the equation of Istomina in paragraph F.4.

F.3 Shepherd

The equations of Shepherd [13] were obtained by performing statistical power regression analyses on 19 sets of published data on grain size and permeability of unconsolidated sediments. Shepherd states that previous theoretical and empirical studies have shown that permeability relates to particle diameter by a relationship in the following form:

$$k = c \cdot d^2 \tag{F.3.1}$$

In this equation c is a dimensionless coefficient and d is the particle diameter. Although the exponent in equation (F.3.1)is equal to 2, this exponent might change as the result of a power regression analysis.

After Shepherd performed the power regression analyses, different coefficients and exponents were found for different classes of sand. The three classes relevant to dredging are river sands, beach sands and dune sands. The equations for each class are given below.
River sands:

$$k = 800 \cdot d^{1.5} \tag{F.3.2}$$

Beach sands:

$$k = 3500 \cdot d^{1.65} \tag{F.3.3}$$

Dune sands:

$$k = 12000 \cdot d^{1.75} \tag{F.3.4}$$

In the equations above d is in millimeters. However, it is unclear what d should be in the case of non-mono-sized sand. The mean particle diameter d_m from equation (F.2.2) could yield good results. Important to note is that the unit of the permeability of the equations above is expressed in gallon per day per square foot (GPD/ft^2). To convert this unit to meters per second (m/s) the permeability has to be multiplied with $4.7160 \cdot 10^{-7}$.

F.4 Istomina

Based on experimental results V.S. Istomina [22] found the following relationship between the porosity and the coefficient of uniformity:

$$n = 0.255 \cdot (1 + 0.83^{C_u}) \tag{F.4.1}$$

In this equation C_u is the coefficient of uniformity and is defined as follows:

$$C_u = \frac{d_{60}}{d_{10}} \tag{F.4.2}$$

F.5 Ouchiyama

Ouchiyama describes an analytic method to calculate the porosity of a randomly packed bed of spherical particles. However, because the complexity of the method no equations will be given in this paragraph. Instead these equation can be found in the article of Ouchiyama [23].
The application of the method of Ouchiyama can be found in appendix D.

F.6 Mosfeta

Through experiments Mosfeta et al [24] found a correlation between the particle sizes of a sand an its peak angle of internal friction. The peak angle of internal friction ϕ^p is the angle of internal friction found at the moment that the soil actually starts shearing.
A particle size distribution consists of multiple particle size ranges and a percentage (or fraction)

which indicates how much of the total weight falls in a certain range. For a single particle size range the peak angle of internal friction ϕ_i^p can be calculated using the smallest particle diameter of the range d_i using the following relation:

$$\phi_i^p = 34 + 10 \cdot d_i \tag{F.6.1}$$

The angle of internal friction calculated using the previous equation is the angle for a single range of particle diameters. In order to get an angle for the whole range of particle diameters a weighed particle diameter d_w can be used in equation F.6.1. To obtain this weighed particle diameter the smallest diameter of a range should be multiplied with the corresponding weight fraction p_i. This must be done for all ranges and then all these results must be added. This is shown in the following equation.

$$d_w = \sum_i p_i \cdot d_i \tag{F.6.2}$$

G Production model flowchart

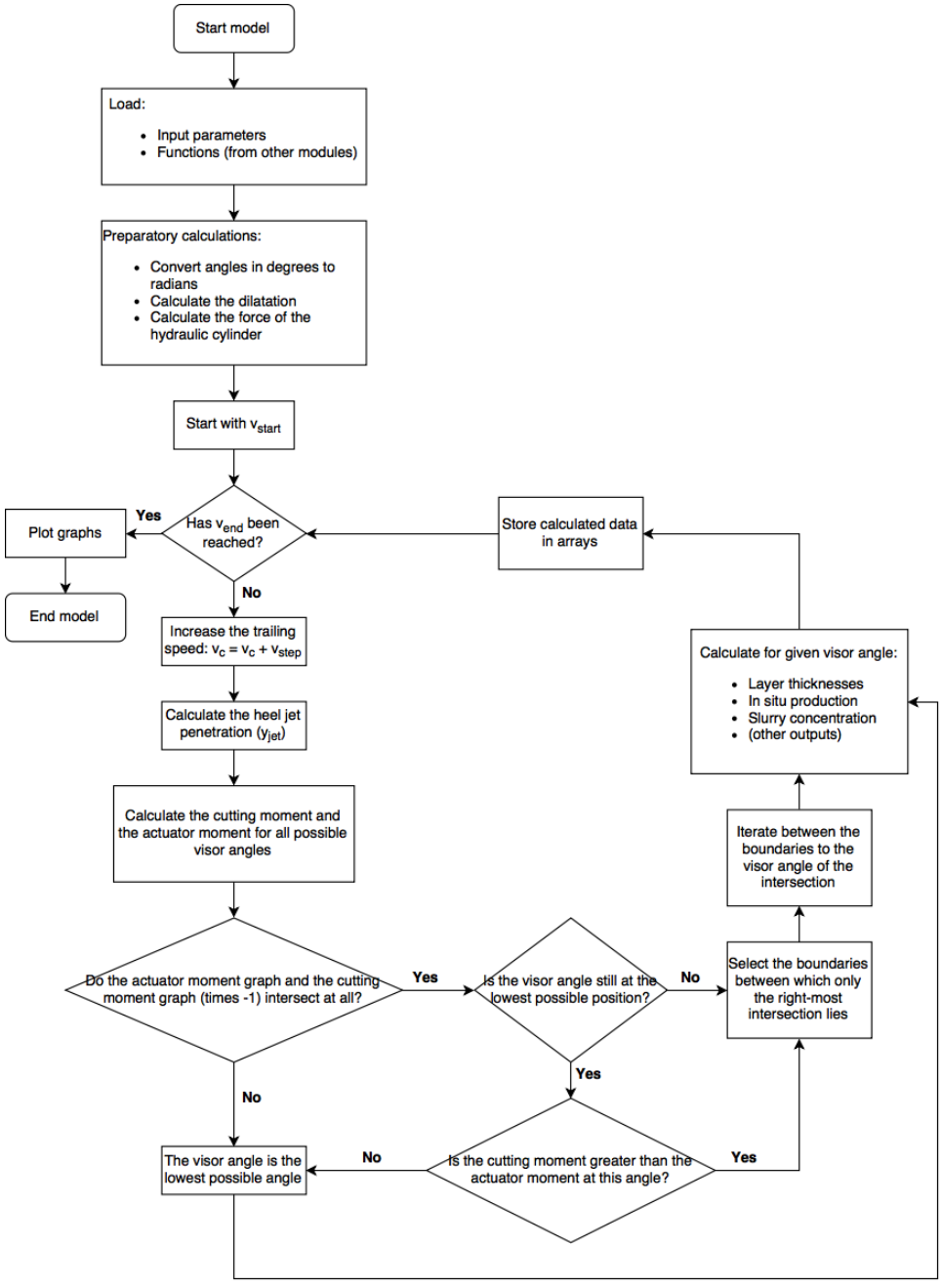

Figure G.1: A flowchart of the main processes in the production model in correspondence with the model discussed in chapter 6 (*ResetAngle* is set to *False*)

H Implementation of bulldozing & the TED

H.1 Bulldozing

The bulldozing calculations have not been been added to the main code that is used to produce the results in chapter 7. However, for possible future references the implementation of the theory used to calculate bulldozing forces and production is described in this appendix.

H.1.1 Bulldozing forces

The calculations of the bulldozing forces are done within the trailing speed loop since the bulldozing forces change with changing trailing speeds. The part of the draghead that would be bulldozing, the heel and up, is assumed to be vertical when the draghead is in standard position ($\Gamma = 0$). This leads to the following equation that is used to calculate the blade angle.

$$\alpha_{Bulldoze} = 90 - \Gamma \tag{H.1.1}$$

In equation H.1.1 both angles are in degrees. Hence for further calculations the blade angle must be converted to radians. Since the blade angle usually is 90 degrees or at least in that order of magnitude, the cutting process is assumed to be the cutting process of a water saturated wedge. Therefore the wedge angle must also be calculated. For this, equation (A.2.23) is used with the assumption that the blade height h_b is equal to the slice thickness h_i. This leads to the following equation.

$$\theta = 0.8088 \cdot (90 - \phi) \tag{H.1.2}$$

Again, the angles are in degrees and have to be converted to radians to used them in cutting force calculations.
The bulldozing force calculations start with calculating the shear angle β. The shear angle is calculated by iteratively solving the following equation.

$$\begin{aligned} \frac{\partial F'_h}{\partial \beta} = &- h_i \cdot \frac{sin(\phi) \cdot sin(\theta + 2 \cdot \beta + \lambda + \phi) \cdot sin(\theta + \lambda)}{sin^2(\beta) \cdot sin(\theta + \beta + \lambda + \phi)^2} \\ &+ h_b \cdot \frac{sin(\lambda) \cdot sin(\theta + \lambda)}{sin(\theta) \cdot sin(\theta + \beta + \lambda + \phi)^2} = 0 \end{aligned} \tag{H.1.3}$$

Again, the equation for the fully cavitational situation is used since this greatly simplifies and speeds up the iteration. In equation (H.1.3) the initial cut height h_i is defined as the distance between the lowest part of the heel and the soil surface. As was mentioned before the blade height h_b is assumed to be equal to h_i. The mobilized internal friction of the wedge λ can be calculated using the following equation.

$$\lambda = \frac{5}{6} \cdot \phi \tag{H.1.4}$$

The next step is to calculate the pore under pressures in the shear layer p_{1m}, on the pseudo blade p_{2m}, on the bottom of the wedge p_{3m} and on the blade p_{4m}. This is done using the parallel resistor

method, which is explained in paragraph A.2.5 and therefore skipped in this explanation.
When the pore under pressures are calculated the water pressure forces on the shear layer, the pseudo blade, the bottom of the wedge and the blade are calculated using the following equations.

$$W_1 = \frac{p_{1m} \cdot h_i \cdot W}{sin(\beta)} \tag{H.1.5}$$

$$W_2 = \frac{p_{2m} \cdot h_b \cdot W}{sin(\theta)} \tag{H.1.6}$$

$$W_3 = p_{3m} \cdot h_b \cdot \left(\frac{1}{tan(\theta)} - \frac{1}{tan(\alpha)} \right) \cdot W \tag{H.1.7}$$

$$W_4 = \frac{p_{4m} \cdot h_b \cdot W}{sin(\alpha)} \tag{H.1.8}$$

Good to note is that W is still equal to the width of the draghead. Next the resulting force on the shear plane and on the pseudo blade are calculated.

$$K_1 = \frac{W_2 \cdot sin(\lambda) + W_1 \cdot sin(\theta + \beta + \lambda)}{sin(\theta + \beta + \lambda + \phi)} \tag{H.1.9}$$

$$K_2 = \frac{W_2 \cdot sin(\theta + \beta + \phi) + W_1 \cdot sin(\phi)}{sin(\theta + \beta + \lambda + \phi)} \tag{H.1.10}$$

After this the grain force on the bottom of the wedge and the grain force on the blade are calculated.

$$\begin{aligned} K_3 = & \frac{-W_2 \cdot sin(\alpha + \delta_e - \theta) + K_2 \cdot sin(\alpha + \delta_e - \theta - \lambda)}{sin(\alpha + \delta_e + \phi)} \\ & + \frac{W_3 \cdot sin(\alpha + \delta_e) + W_4 \cdot sin(\delta_e)}{sin(\alpha + \delta_e + \phi)} \end{aligned} \tag{H.1.11}$$

$$\begin{aligned} K_4 = & \frac{-W_2 \cdot sin(\theta + \phi) + K_2 \cdot sin(\theta + \lambda + \phi)}{sin(\alpha + \delta_e + \phi)} \\ & + \frac{W_3 \cdot sin(\phi) + W_4 \cdot sin(\alpha + \phi)}{sin(\alpha + \delta_e + \phi)} \end{aligned} \tag{H.1.12}$$

When the grain forces have been calculated the cutting (or bulldozing) forces on the draghead can be calculated using the following equations.

$$F_h = -W_4 \cdot sin(\alpha) + K_4 \cdot sin(\alpha + \delta_e) \tag{H.1.13}$$

$$F_v = -W_4 \cdot cos(\alpha) + K_4 \cdot cos(\alpha + \delta_e) \tag{H.1.14}$$

For simplicity the mobilized angle of external friction δ_e in equations (H.1.13) and (H.1.14) can be chosen as equal to δ.

H.1.2 Bulldozing production

The bulldozing process in the previous section can be described as cutting a layer of sand with the draghead and a sand wedge. The sand that is cut is eventually pushed to the sides of the draghead. Here it is not sucked into the drag arm since it is not moved to the suction mouth by the blades. This means that the bulldozing process does not contribute to production in the sense that it does not bring sand in the hopper. However, if with production is meant the volume of soil that is simply removed from the path of the draghead then the bulldozing process does contribute to production. The production by bulldozing is then simply defined as follows.

$$Production_{Bulldoze} = h_i \cdot W \cdot v_c \tag{H.1.15}$$

As was mentioned before, in equation (H.1.15) the initial cut height h_i is the distance between the bottom of the heel and the soil surface.
Although the bulldozing effect does not bring any sand into the hopper it does affect the production through the bulldozing forces. The bulldozing forces contribute to the total horizontal and vertical force and therefore affect the maximum trailing speed for which production is possible before it is limited by either propulsion force, propulsion power or downforce.

H.2 Turtle exclusion device

Just like the bulldozing calculations the calculations for cutting with a turtle exclusion device have not been added to the main code. This means that these calculations have not been used to produce the results in chapter 7. However, for possible future references the implementation of the theory used to calculate TED forces and production is described in this appendix.

H.2.1 Forces when using a TED

A turtle exclusion device prevents sea turtles from being sucked into the draghead by pushing the turtles out of the way of the draghead. When the turtles are pushed out of the way there is no direct contact between the TED and the turtle, instead the TED is designed to create a sand wave that pushes the turtle aside.
Given the fact that the TED generates a sand wave and the fact that the blade angle of the TED

Figure H.1: A turtle exclusion device (bright red) mounted on a draghead

is nearly 90 degrees (as can be seen in figure H.1) the cutting process of the TED is assumed to be

saturated sand cutting with a wedge. However, the TED can be seen as two blades which are at an angle with respect to the cutting direction. Therefore also the snowplow theory is used to calculate the TED cutting forces.
Due to legislation, the penetration depth and angle of the TED are specified and hence are fixed. The initial cut height h_i is fixed at 6 inches or 152 mm (0.152 m). The TED makes an angle of about 15 degrees with the horizon, which results in a blade angle of about 105 degrees. The TED used on the Wild Dragon draghead has a height h_{TED} of 14 inches (0.35 m). Together with the blade angle this can be used to calculate the blade height using the following equation.

$$h_b = h_{TED} \cdot cos(\alpha - 90) \tag{H.2.1}$$

Due to the shape of the TED, the TED only partially penetrates the seabed. Furthermore the only point where the penetration depth is equal to 6 inches is at the tip of the TED. To account for this, the TED is modeled as a blade with a initial cut height of 6 inches and a width of $\frac{1}{4}W$. The factor of $\frac{1}{4}$ consist of a factor $\frac{1}{2}$ for the fact that only roughly the half of the width of the TED (which is equal to the width of the draghead) actually penetrates the soil and another factor of $\frac{1}{2}$ since the average slice thickness of the part that is penetrating is only 3 inches.
The cutting force calculations now start with calculating the wedge angle θ using the following equation from paragraph A.2.

$$\theta = (90 - \phi) \cdot \left(0.73 + 0.0788 \cdot \frac{h_b}{h_i}\right) \tag{H.2.2}$$

Note that the angles in equation (H.2.2) are in degrees and have to be converted to radians in order to use them in calculations in Python.
The cutting force calculations for the TED start with calculating the shear angle β. The shear angle is calculated by iteratively solving the following equation.

$$\begin{aligned}\frac{\partial F_h'}{\partial \beta} =& - h_i \cdot \frac{sin(\phi) \cdot sin(\theta + 2 \cdot \beta + \lambda + \phi) \cdot sin(\theta + \lambda)}{sin^2(\beta) \cdot sin(\theta + \beta + \lambda + \phi)^2} \\ &+ h_b \cdot \frac{sin(\lambda) \cdot sin(\theta + \lambda)}{sin(\theta) \cdot sin(\theta + \beta + \lambda + \phi)^2} = 0\end{aligned} \tag{H.2.3}$$

Equation (H.2.3) is the equation for a fully cavitational situation. The equation for a fully cavitational situation is used because it greatly simplifies and speeds up the iteration. As was explained before, the mobilized internal friction of the wedge λ can be calculated using the following equation.

$$\lambda = \frac{5}{6} \cdot \phi \tag{H.2.4}$$

The next step is to calculate the pore under pressures in the shear layer p_{1m}, on the pseudo blade p_{2m}, on the bottom of the wedge p_{3m} and on the blade p_{4m}. This is done using the parallel resistor method, which is explained in paragraph A.2.5 and therefore skipped in this explanation.
When the pore under pressures are calculated the water pressure forces on the shear layer, the pseudo blade, the bottom of the wedge and the blade are calculated using the following equations.

$$W_1 = \frac{p_{1m} \cdot h_i \cdot \frac{1}{4}W}{sin(\beta)} \tag{H.2.5}$$

$$W_2 = \frac{p_{2m} \cdot h_b \cdot \frac{1}{4}W}{sin(\theta)} \tag{H.2.6}$$

$$W_3 = p_{3m} \cdot h_b \cdot \left(\frac{1}{tan(\theta)} - \frac{1}{tan(\alpha)} \right) \cdot \frac{1}{4} W \tag{H.2.7}$$

$$W_4 = \frac{p_{4m} \cdot h_b \cdot \frac{1}{4} W}{sin(\alpha)} \tag{H.2.8}$$

Good to note is that W is still equal to the width of the draghead and that a factor of $\frac{1}{4}$ has been added for the reason discussed earlier in this section. Next the resulting force on the shear plane and on the pseudo blade are calculated.

$$K_1 = \frac{W_2 \cdot sin(\lambda) + W_1 \cdot sin(\theta + \beta + \lambda)}{sin(\theta + \beta + \lambda + \phi)} \tag{H.2.9}$$

$$K_2 = \frac{W_2 \cdot sin(\theta + \beta + \phi) + W_1 \cdot sin(\phi)}{sin(\theta + \beta + \lambda + \phi)} \tag{H.2.10}$$

After this the grain force on the bottom of the wedge and the grain force on the blade are calculated.

$$\begin{aligned} K_3 = & \frac{-W_2 \cdot sin(\alpha + \delta_e - \theta) + K_2 \cdot sin(\alpha + \delta_e - \theta - \lambda)}{sin(\alpha + \delta_e + \phi)} \\ & + \frac{W_3 \cdot sin(\alpha + \delta_e) + W_4 \cdot sin(\delta_e)}{sin(\alpha + \delta_e + \phi)} \end{aligned} \tag{H.2.11}$$

$$\begin{aligned} K_4 = & \frac{-W_2 \cdot sin(\theta + \phi) + K_2 \cdot sin(\theta + \lambda + \phi)}{sin(\alpha + \delta_e + \phi)} \\ & + \frac{W_3 \cdot sin(\phi) + W_4 \cdot sin(\alpha + \phi)}{sin(\alpha + \delta_e + \phi)} \end{aligned} \tag{H.2.12}$$

When the grain forces have been calculated the cutting forces of the TED can be calculated using the following equations.

$$F_h = -W_4 \cdot sin(\alpha) + K_4 \cdot sin(\alpha + \delta_e) \tag{H.2.13}$$

$$F_v = -W_4 \cdot cos(\alpha) + K_4 \cdot cos(\alpha + \delta_e) \tag{H.2.14}$$

For simplicity the mobilized angle of external friction δ_e in equations (H.1.13) and (H.1.14) can be chosen as equal to δ.
Until now the cutting process of the TED has simply been cutting with a wedge and has almost been identical to the process described in paragraph H.1. These calculations might already give a reasonable estimate of the order of magnitude of the cutting forces of the TED. However, since the TED deflects the sand to the sides also the snowplow theory from paragraph A.3 is used to calculate the horizontal cutting force.
The calculations of the horizontal cutting force of the TED due to the snowplow effect start by

calculating Λ. This uppercase Λ represents the ratio between the deviation velocity in the shear zone and the deviation velocity components on the blade and should not be confused with the lowercase λ, which represents the mobilized internal friction angle. The ratio between the deviation velocity components is calculated using equation (A.3.7), however since in the situation of the TED the pseudo blade is actually cutting the blade angle α should be replaced with the wedge angle θ.

$$\lambda = \left(\frac{F_h \cdot cos(\theta) - F_v \cdot sin(\theta)}{F_h \cdot cos(\beta) + F_v \cdot sin(\beta)} \right) \cdot \left(\frac{sin(\theta)}{sin(\beta)} \right) \tag{H.2.15}$$

Note that the shear angle β also is the shear angle of the wedge cutting process.
The next step is to calculate the deviation velocity v_d using the following equation.

$$v_d = \frac{v_c}{cos(\iota)} \tag{H.2.16}$$

In equation (H.2.16) the angle ι is the deviation angle. For the TED of the Wild Dragon draghead the deviation angle is about 40 degrees.
The deviation velocity is used to calculate the deviation velocity component that is in the direction of the trailing speed v_{d2}.

$$v_{d2} = v_d \cdot \frac{sin(\iota)}{(1 + \Lambda)} \tag{H.2.17}$$

The next step is to calculate the velocity of the sand grains relative to the pseudo blade and the friction force on the pseudo blade.

$$v_{r2} = v_c \cdot \frac{sin(\beta)}{sin(\alpha + \beta)} \tag{H.2.18}$$

$$F_{f2} = F_h \cdot cos(\theta) - F_v \cdot sin(\theta) \tag{H.2.19}$$

Now the deviation force can be calculated using the following equation.

$$F_{d2} = F_{f2} \cdot \frac{v_{d2}}{v_{r2}} \tag{H.2.20}$$

The final step is to calculate the new horizontal cutting force of the TED.

$$F_{x2} = F_h \cdot cos(\iota) + F_{d2} \cdot sin(\iota) \tag{H.2.21}$$

Note that the vertical cutting force that was calculated using the wedge cutting theory is still assumed to be the vertical cutting force.

H.2.2 Production when using a TED

As was explained before, the TED pushes sea turtles out of the way of the draghead by creating a sand wave. By law it is required that the tip of the TED is 6 inches below the heel. Since in a normal situation for a draghead it is assumed that the heel is at the surface of the soil whilst cutting this means that the TED pushes sand aside that could potentially be sucked up by the draghead. This

differs from a draghead that is bulldozing since in that situation the draghead is assumed to be sunken into the soil. Which means that the heel is below the soil surface. The soil that is above the heel is bulldozed by the draghead and pushed aside, but since this sand could not be sucked up anyway it is not considered as a production loss. Since the TED pushes sand aside that is below the heel, the TED causes a production loss. This production loss can be calculated as follows.

$$Loss_{TED} = h_i \cdot \frac{1}{4} W \cdot v_c \tag{H.2.22}$$

In equation (H.2.22) h_i is the penetration depth of the tip of the TED and W is the width of the draghead. The factor of $\frac{1}{4}$ is again due to the fact that the TED only penetrates the soil for the half of its width and the fact that only the tip of the TED penetrates the soil at the depth of h_i. This method might however underestimate the losses caused by the TED since it does not account for the geometry of the sand wedge. In reality this sand wedge could possibly push sand aside at a greater width and a greater depth.
Since the TED removes sand that would otherwise be cut by the blades, adding the model of the TED influences the cutting forces and hence the moment balance. The layer removed by the TED must therefore be accounted for within the moment loop. This can be done in a similar way as is done with the jetted layer. This approach does mean that there is a gap between the heel jets and the new soil surface or in other words, the jets are suspended above the sand bed. How suspending a jet does affect the jetted volume of soil is not known and therefore ignored.
The calculation of the cutting forces of the TED do not necessarily have to be done within the moment loop since they are not used in this loop. Since these forces do change per trailing speed, they should be done within the trailing speed loop.
The TED also influences production indirectly since the cutting forces contribute to the total horizontal and vertical force. Therefore they affect the maximum trailing speed for which production is possible before it is limited by either propulsion force, propulsion power or downforce.

I Change in production rate

This appendix consists of two sections. The first section discusses how the production rate can be calculated. The second section discusses what the maximum visor movement is allowed to be to ensure an increasing production for increasing trailing speeds.
Good to note is that what is called 'production' actually already is a production rate since the unit is a unit of volume per unit of time. However, in this appendix and in the rest of the report with production the actual production rate is meant. In this appendix and the rest of the report with production rate the change of the actual production rate for a change of trailing speed is meant. The unit of this production rate is a unit of volume per unit of time per unit of velocity. In SI units this would be cubic meters per second per meters per second ($\frac{m^3/s}{m/s}$).

I.1 Production rate

For a certain trailing speed, the maximum production possible is achieved by having the visor in the lowest possible position. If the lower arm angle is not adjusted ($\Gamma = 0°$) then the lowest possible visor angle is 0°.
In general the production is defined as the thickness of the layer removed between the heel and tip of the lowest blade times the trailing speed and the width of the draghead. Hence, for the Wild Dragon draghead the total production for a draghead can be calculated using the following equation.

$$Production_{Total} = W \cdot v_c \cdot (r_6 \cdot sin(\angle r_6 - \Psi) - r_{heel}) \tag{I.1.1}$$

In order to find out how the production is affected by an increase of the trailing speed the derivative of the total production is taken with respect to the trailing speed.

$$\frac{\partial Production_{Total}}{\partial v_c} = W \cdot (r_6 \cdot sin(\angle r_6 - \Psi) - r_{heel}) - \frac{\partial \Psi}{\partial v_c} \cdot W \cdot v_c \cdot r_6 \cdot cos(\angle r_6 - \Psi) \tag{I.1.2}$$

In equation I.1.2 it can be seen that it is not possible to simply calculate the production rate by only using the production model inputs. In addition to some of the production model inputs also the visor angle Ψ and the rate of change of the visor angle as a function of the trailing speed $\frac{\partial \Psi}{\partial v_c}$ is needed. This does make sense since the production is dependent on the total slice thickness that is cut and this slice thickness is dependent on the visor angle. However, since the visor angle must be found through iteration there is no expression that can simply substitute Ψ. The same is true for the rate of change of the visor angle.
For these reasons it is not possible to predict the production rate unless the visor angle and the rate of change of the visor angle are known. When the visor angles per trailing speed have been calculated then an approximation of the production rate can be made. It is an approximation because the calculated visor angles are always a finite set of points. The rate of change of the visor angle is then approximated as follows.

$$\frac{\partial \Psi}{\partial v_c} \approx \frac{\Delta \Psi}{\Delta v_c} = \frac{\Psi_{new} - \Psi_{old}}{v_{c-new} - v_{c-old}} \tag{I.1.3}$$

The approximation of the production rate can then be written as follows.

$$\frac{\partial Production_{Total}}{\partial v_c} \approx W \cdot (r_6 \cdot sin(\angle r_6 - \Psi_{old}) - r_{heel}) - \frac{\Delta\Psi}{\Delta v_c} \cdot W \cdot v_{c-new} \cdot r_6 \cdot cos(\angle r_6 - \Psi_{old}) \quad \text{(I.1.4)}$$

When the visor angle per trailing speeds is known this means that the production model has been run. Therefore also the production per trailing speed is known. This can also be used to calculate the production rate. Equation I.1.4 can then be used to verify the calculated result.

I.2 Threshold of production increase

What is interesting to know is how many degrees a visor is allowed to move up for an increase of trailing speed in order to still increase the production. If this is known then it is also known if for certain conditions increasing the trailing speed will actually lead to an increase of production. Knowing how many degrees the visor is allowed to rotate for an increase of trailing speed can also explain drops (or peaks) in the production as a function of the trailing speed.
In order to calculate the threshold value of the visor angle change per trailing speed change ($\frac{\partial\Psi}{\partial v_c}$) the situation is observed in which an increase of the trailing speed does not lead to a change in the production. In other words, the situation in which $\frac{\partial Production_{Total}}{\partial v_c} = 0$. For this condition equation I.1.2 can then be written as follows.

$$\frac{\partial Production_{Total}}{\partial v_c} = W \cdot (r_6 \cdot sin(\angle r_6 - \Psi) - r_{heel}) - \frac{\partial\Psi}{\partial v_c} \cdot W \cdot v_c \cdot r_6 \cdot cos(\angle r_6 - \Psi) = 0 \quad \text{(I.2.1)}$$

Next equation I.2.1 can be rewritten into the following expression for $\frac{\partial\Psi}{\partial v_c}$.

$$\frac{\partial\Psi}{\partial v_c} = \frac{tan(\angle r_6 - \Psi)}{v_c} - \frac{r_{heel}}{v_c \cdot r_6 \cdot cos(\angle r_6 - \Psi)} \quad \text{(I.2.2)}$$

The outcome of equation I.2.2 can be interpreted as how many radians per meter per second increase the visor is allowed to increase in order to stay at the same production. If the increase of the visor angle is more than that number then the production will decrease. If the increase of the visor angle is below that number the production will still increase for increasing trailing speed.
The value of $\frac{\partial\Psi}{\partial v_c}$ is dependent on the trailing speed as well as the visor angle at which the visor is at that trailing speed. In figure I.1 this value, converted to degrees per step in trailing speed, is plotted for a range trailing speeds and a range of visor angles. The size of the step in trailing speeds is chosen to be 0.01 meters per second. The range of trailing speeds is 0.1 to 1.0 meters per second and the range of visor angles is 0 to 26 degrees.

It can be seen that the maximum allowable change of the visor angle to ensure no decrease of the production is only roughly three degrees at best. It should also be noted that this margin only gets smaller for increasing trailing speeds and visor angles.

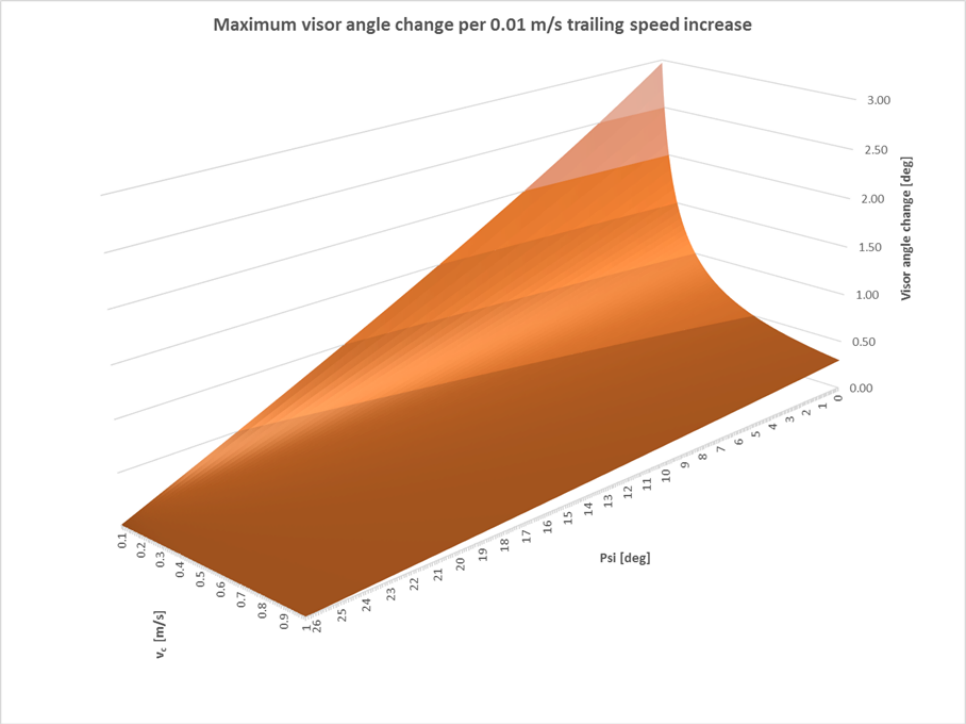

Figure I.1: The maximum visor angle change for a trailing speed increase of 0.01 m/s to ensure that the production does not decrease

J Liberty Island loading graphs

In the graphs below the observed loading rates and observed loading densities of the trailing suction hopper dredge Liberty Island are displayed in histograms. In the histograms also a curve displaying the cumulative percentage of the observations is drawn.
The loading rate of a TSHD is usually not the same as the in situ production. This would only be the case if the overflow losses were zero. In this thesis an overflow loss of 15 percent is assumed and thus the loading rate should be divided by 0.85 to obtain the in situ production. To convert the loading rate from cubic yards per minute to cubic meters per minute the loading rate has to be multiplied with 0.765.

Figure J.1: Loading rate histogram of the Liberty Island

Figure J.2: Loading density histogram of the Liberty Island

In the histograms the average loading rates and the average specific gravities that lie between the 15th and the 85th percentile of the distribution can be regarded as normal or common loading rates and specific gravities. For the observed loading rates the 15th and the 85th percentile respectively are 40 and 140 yd^3/min. When these numbers are converted to cubic meters per minute and are compensated for overflow losses using the methods described above then values of 36 and 125 m^3/min for in situ production are obtained. These values are used as a reference to assess the model performance. For the loading density the 15th and 85th percentile values are respectively 1.1 and 1.5.

K Tooth jet iteration example

In this appendix the results of a manual iteration (with the help of Excel) aimed to find the flows and pressures for the jet water system of the Liberty Island are shown. The iteration is done according to the described procedure of section 3.5.2 and is done to see what the orders of magnitude of the different pressures and flows are. Because the calculation procedure has been discussed in section 3.5.2 only the inputs and the results will be shown and discussed in this appendix.

Table K.1: The inputs for the jet water iteration

Parameter	Magnitude	Unit
A	-425348	$\frac{kg}{m^7}$
B	44766	$\frac{kg}{m^4 s}$
B	1000000	Pa
f_1	0.0135	$-$
f_2	0.0154	$-$
f_3	0.0150	$-$
D_1	0.334	m
D_2	0.394	m
D_3	0.210	m
L_{Total1}	392	m
L_{Total2}	127	m
L_{Total3}	1227	m
A_{heel}	0.0038	m^2
A_{visor}	0.00737	m^2
A_{soil}	1.30	m^2
$R_{5-Total}$	23.3	s

The parameters A, B and C are the coefficients that are used to model the pump curve with a parabolic equation. The f inputs are the friction factors for the different sections of pipe. The model consists of three large sections of pipe because the equivalent length method is used to account for all the minor losses. This does mean that in reality within the length of one pipe actually more different diameters of pipe can exist and thus differences with reality can be expected. The three different pipe sections also have a different diameter D and a length L_{Total}.
The parameter A_{heel} is the total area of all heel jets, the area A_{visor} is the total area of the visor jets above one row of teeth and the area A_{soil} is an estimate of the total area of the shear zone of a blade. The flow resistance $R_{5-Total}$ is the total flow resistance of the flow lines from the tooth jet to the shear layer.
As was explained in section 3.5.2 the main goal of the iteration is to find the flow conditions for which the flow through the tooth jets according to the Darcy theory is the same as that according to the parallel resistor scheme (because the system is over defined). For the conditions above matching flows were found, which are presented in table K.2. The pressure delivered by the pump and the pressure losses over resistors 1 and 2 as well as their corresponding flows seem very plausible. There is a large pressure loss due between the pump and the draghead (resistor 1) but this makes sense because the

Table K.2: The results for the jet water iteration

Pressure	Pa
Δp_{pump}	850828.2
Δp_1	443021.6
Δp_2	407806.5
$\Delta p_{3,1}$	362725.3
$\Delta p_{3,2}$	45081.3
$\Delta p_{3,3}$	45081.3
Flow	m^3/s
Q_{pump}	0.64716
Q_1	0.64716
Q_2	0.087756
Q_3	0.27970
$Q_{3,2}$	0.029594
$Q_{3,3}$	0.250108
$Q_{3,3}(Darcy)$	0.250144

real distance is fairly large and has multiple sharp 90 degrees bends which cause great losses. The pressure loss and corresponding flow over the heel jets (resistor 2) seems to be in accordance with the flows that have been found by AFT Fathom [25] (0.087756 m^3/s for the iteration versus 0.10468 m^3/s for Fathom).
The pressure losses inside the draghead (resistor 3,1) are tremendous which raises the question whether the equivalent length L_{Total3} has not been greatly overestimated. Due to the great pressure loss the pressure losses over the heel and tooth jets are very small. Despite the small pressure difference over the tooth jet nozzles there is a very large flow. This can be explained by the fact that the tooth jet nozzles are modeled with the laminar Darcy flow. Because a laminar flow has smaller pressure losses than a turbulent flow modeling the jets as a laminar flow will lead to a greater flow for a given pressure difference than modeling the jets with a turbulent flow. Therefore the flow through the tooth jets is likely to be highly overestimated. In reality the pressure difference over the tooth jet nozzles will probably lie closer to that of the heel jets.

L Production graphs sensitivity analysis with tooth jets

L.1 Angle of internal friction

L.1.1 Production for $\phi = 28.8°$

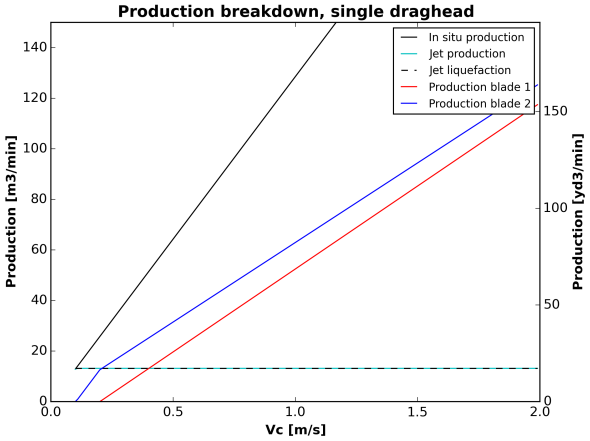

Figure L.1: The production breakdown for a production with a reduced angle of internal friction

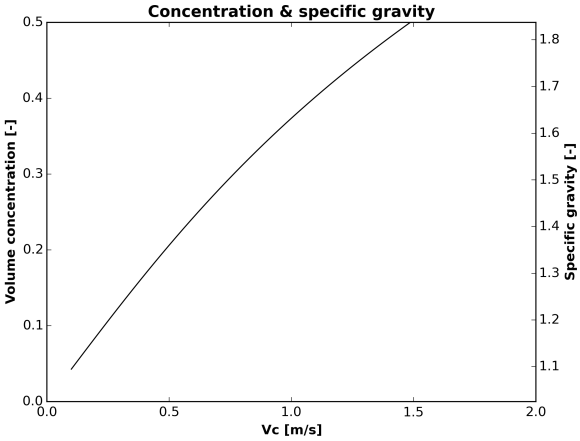

Figure L.2: The concentrations and specific gravity for a production with a reduced angle of internal friction

L.1.2 Production for $\phi = 43.2°$

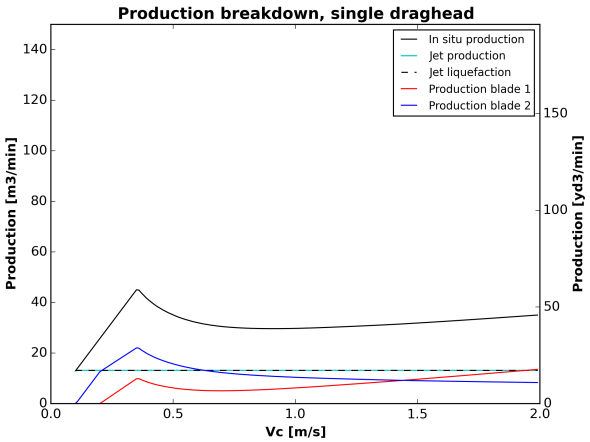

Figure L.3: The production breakdown for a production with an increased angle of internal friction

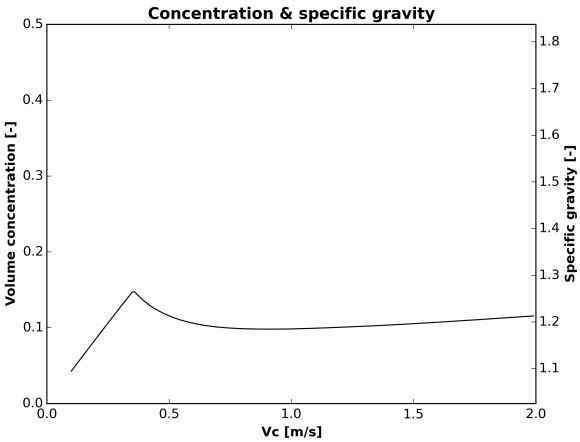

Figure L.4: The concentrations and specific gravity for a production with an increased angle of internal friction

L.2 Dilatation

L.2.1 Production for $\epsilon = 0.128$

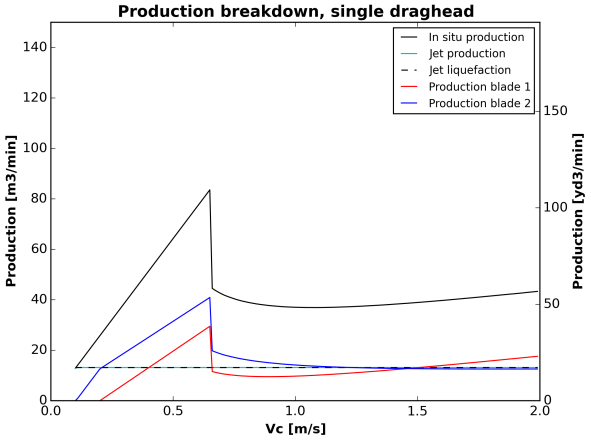

Figure L.5: The production breakdown for a production with a reduced dilatation

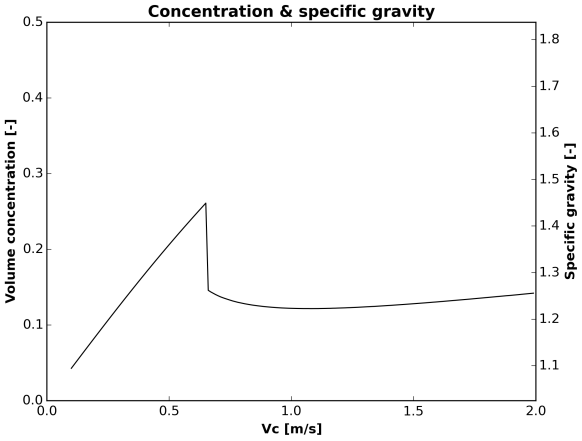

Figure L.6: The concentrations and specific gravity for a production with a reduced dilatation

L.2.2 Production for $\epsilon = 0.192$

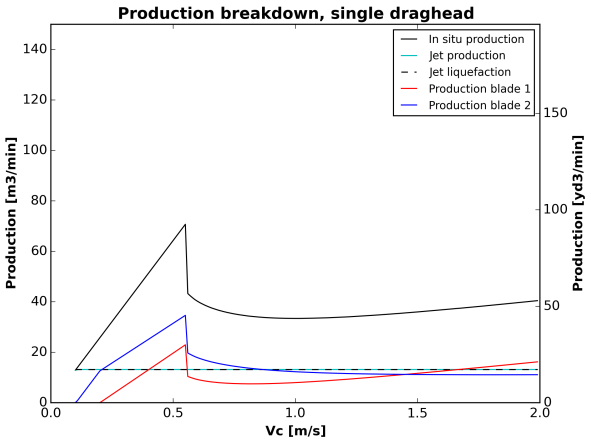

Figure L.7: The production breakdown for a production with an increased dilatation

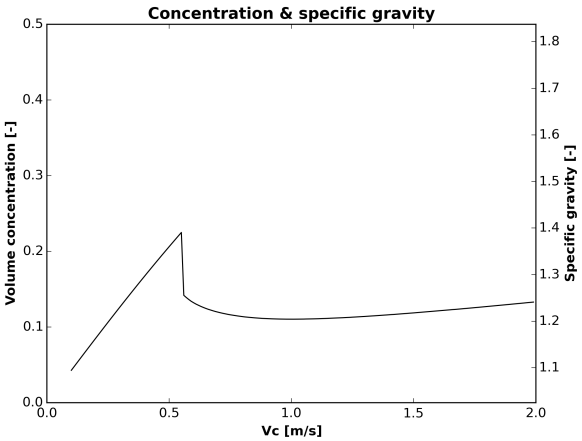

Figure L.8: The concentrations and specific gravity for a production with an increased dilatation

L.3 Permeability

L.3.1 Production for $k_i = 0.000020m/s$ & $k_{max} = 0.0000473m/s$

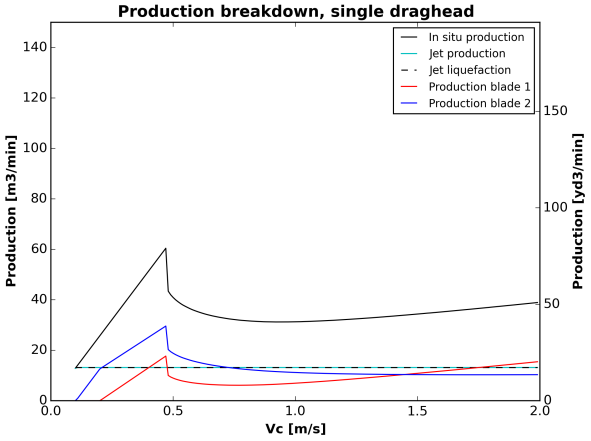

Figure L.9: The production breakdown for a production with a reduced permeability

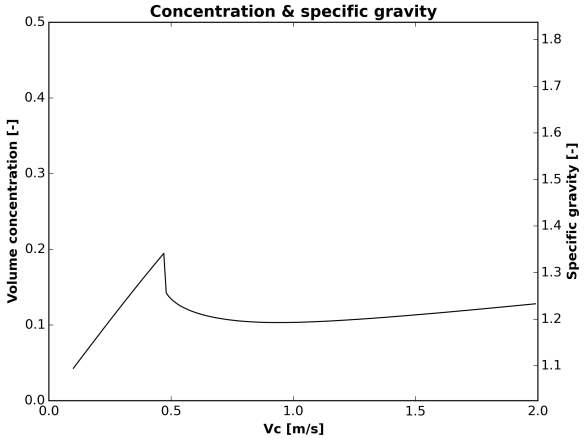

Figure L.10: The concentrations and specific gravity for a production with a reduced permeability

L.3.2 Production for $k_i = 0.000030m/s$ & $k_{max} = 0.0000710m/s$

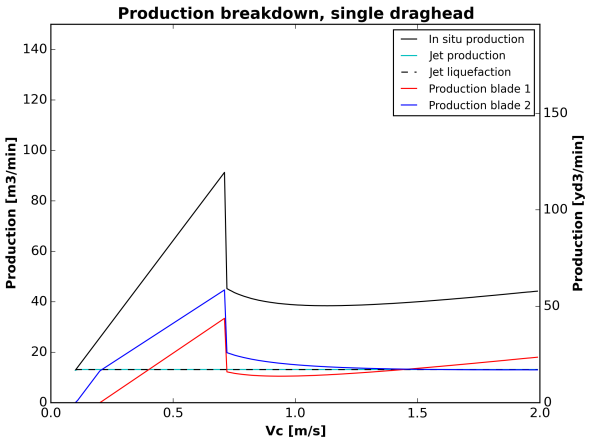

Figure L.11: The production breakdown for a production with an increased permeability

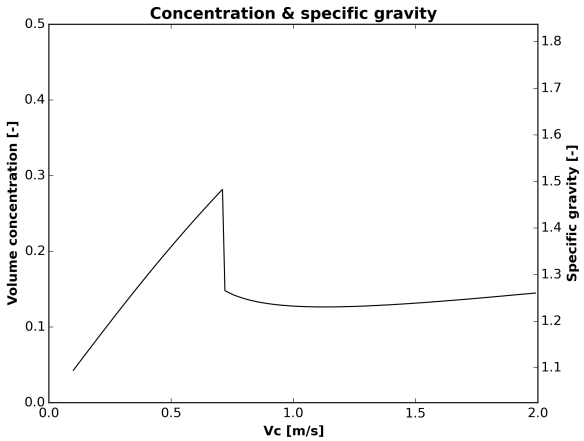

Figure L.12: The concentrations and specific gravity for a production with an increased permeability

L.4 Water depth

L.4.1 Production for $z = 12m$

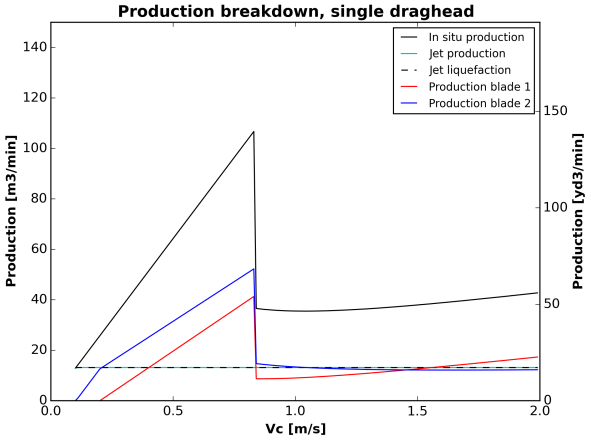

Figure L.13: The production breakdown for a production with a reduced water depth

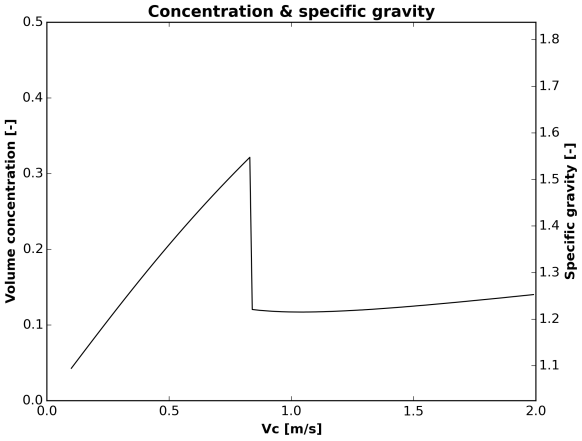

Figure L.14: The concentrations and specific gravity for a production with a reduced water depth

L.4.2 Production for $z = 18m$

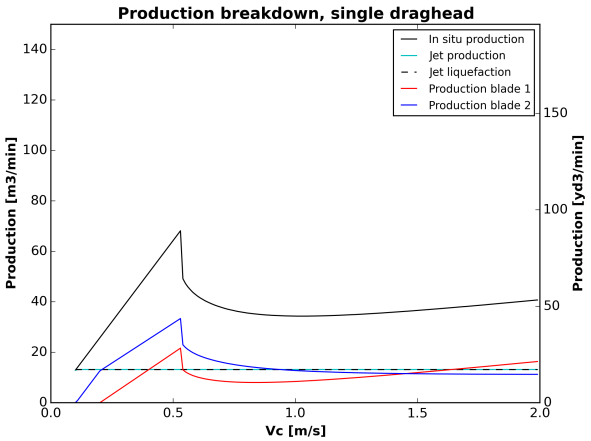

Figure L.15: The production breakdown for a production with an increased water depth

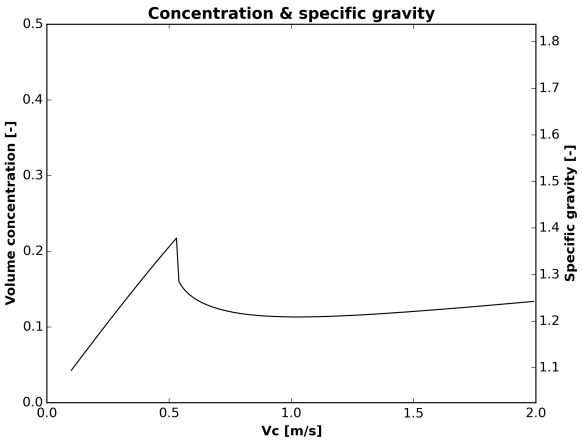

Figure L.16: The concentrations and specific gravity for a production with an increased water depth

L.5 Cylinder pressure

L.5.1 Production for $p_{Cylinder} = 20 \cdot 10^5 Pa$

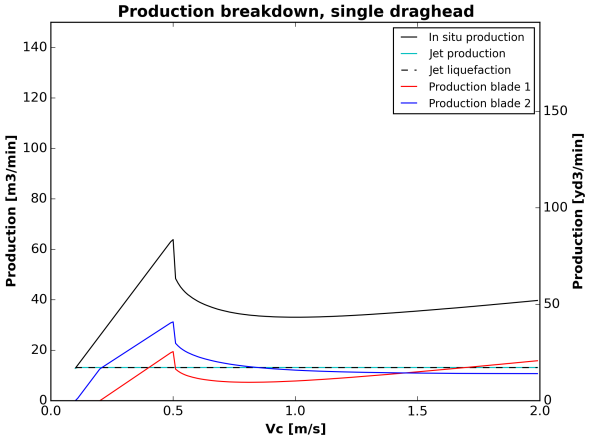

Figure L.17: The production breakdown for a production with a reduced cylinder pressure

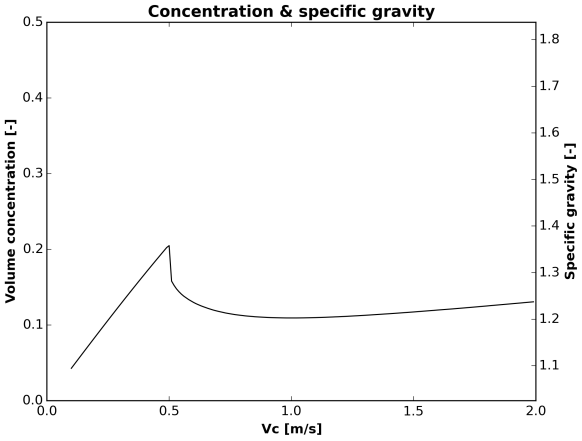

Figure L.18: The concentrations and specific gravity for a production with a reduced cylinder pressure

L.5.2 Production for $p_{Cylinder} = 30 \cdot 10^5 Pa$

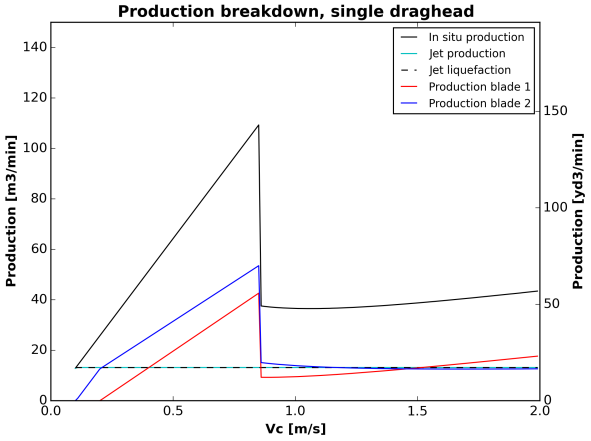

Figure L.19: The production breakdown for a production with an increased cylinder pressure

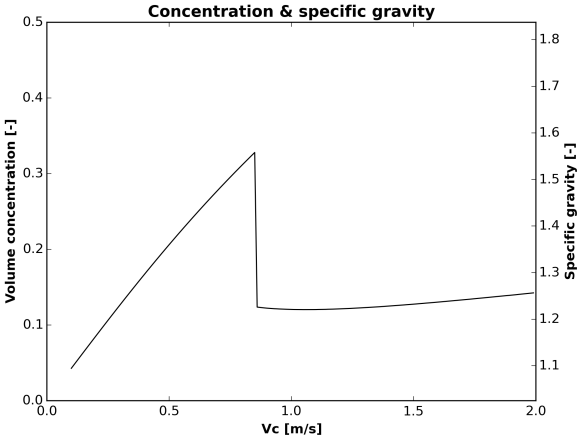

Figure L.20: The concentrations and specific gravity for a production with an increased cylinder pressure

L.6 Heel jet flow

L.6.1 Production for $Q_{heel} = 0.008374 m^3/s$

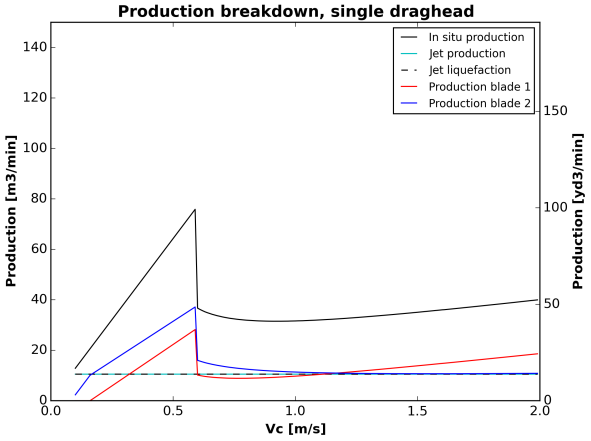

Figure L.21: The production breakdown for a production with a reduced heel jet flow

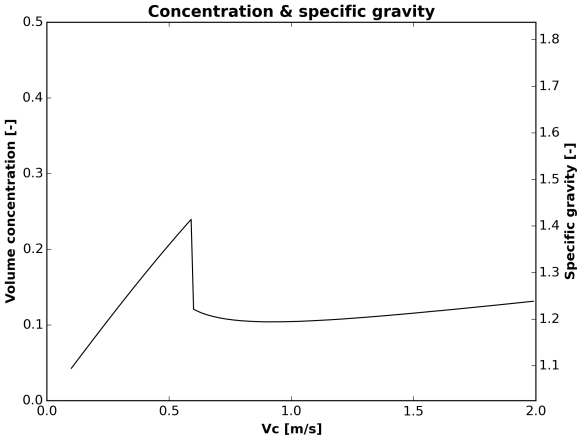

Figure L.22: The concentrations and specific gravity for a production with a reduced heel jet flow

L.6.2 Production for $Q_{heel} = 0.012562 m^3/s$

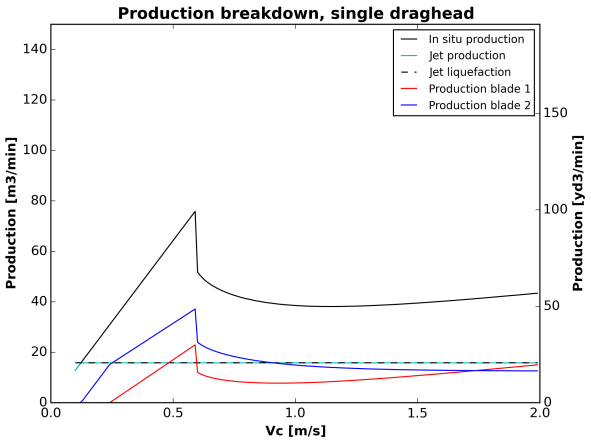

Figure L.23: The production breakdown for a production with an increased heel jet flow

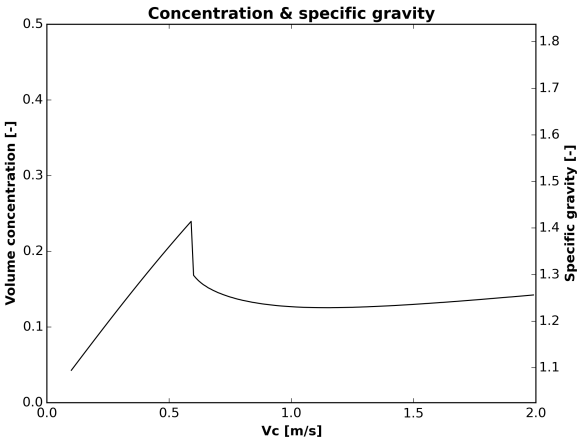

Figure L.24: The concentrations and specific gravity for a production with an increased heel jet flow

L.7 Lower arm angle

L.7.1 Production for $\Gamma = -5.0°$

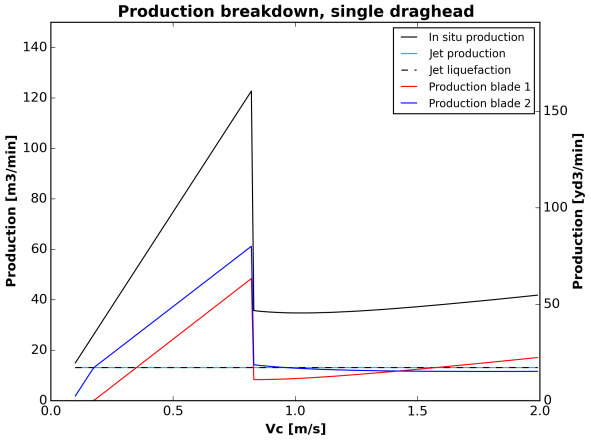

Figure L.25: The production breakdown for a production with a reduced lower arm angle

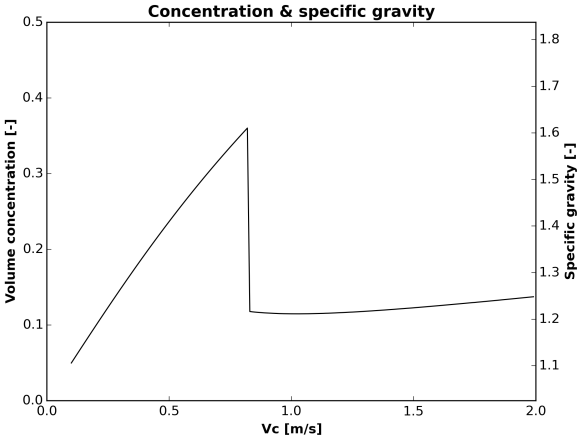

Figure L.26: The concentrations and specific gravity for a production with a reduced lower arm angle

L.7.2 Production for $\Gamma = +5.0°$

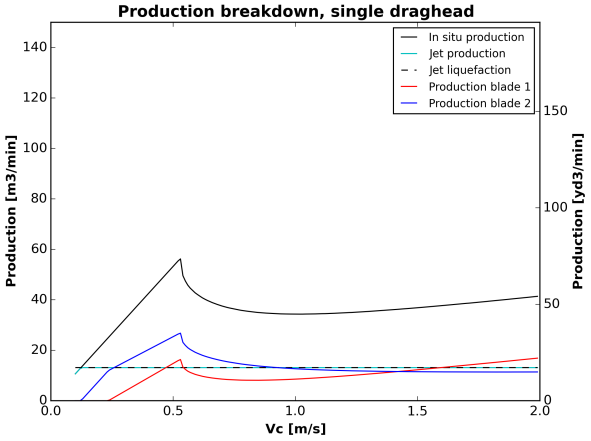

Figure L.27: The production breakdown for a production with an increased lower arm angle

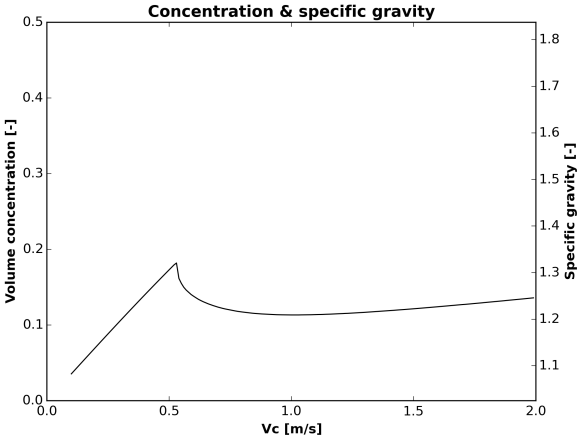

Figure L.28: The concentrations and specific gravity for a production with an increased lower arm angle

L.8 Tooth jet pressure

L.8.1 Production for $\Delta p_{jet} = 2.4 \cdot 10^5 Pa$

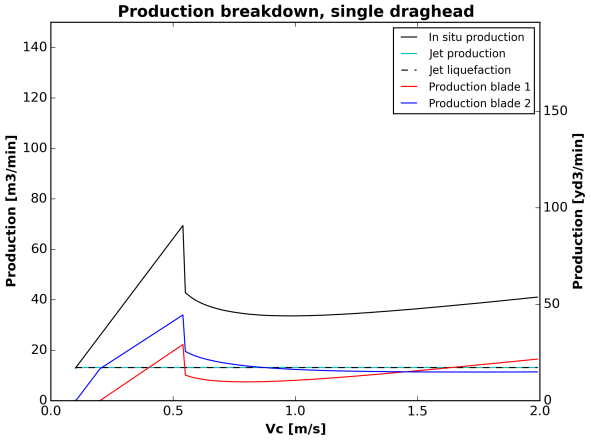

Figure L.29: The production breakdown for a production with a reduced tooth jet pressure

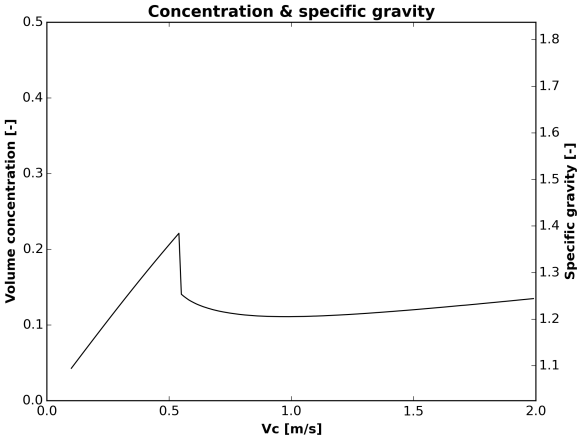

Figure L.30: The concentrations and specific gravity for a production with a reduced tooth jet pressure

L.8.2 Production for $\Delta p_{jet} = 3.6 \cdot 10^5 Pa$

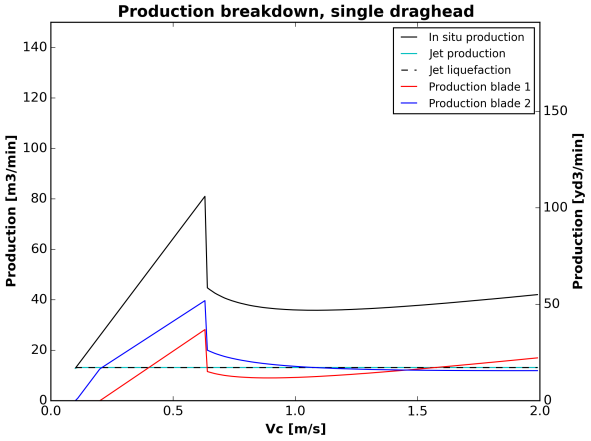

Figure L.31: The production breakdown for a production with an increased tooth jet pressure

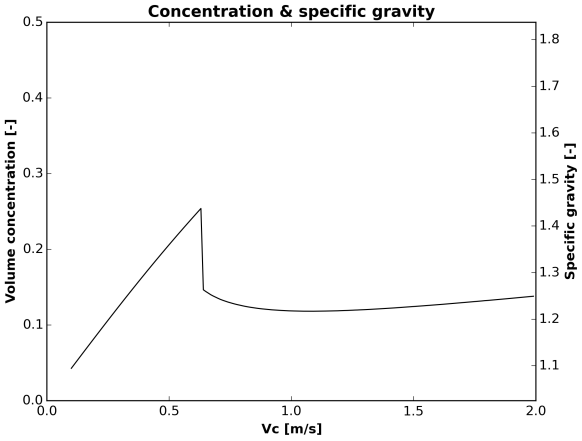

Figure L.32: The concentrations and specific gravity for a production with an increased tooth jet pressure

Bibliography

[1] IHC Merwede wild dragon draghead information. http://www.ihcdredgers.com/research-development/research-development/wild-dragon/. Accessed: 01-06-2016.

[2] W.J. Vlasblom. Designing dredging equipment. Lecture notes (WB3408b) at Delft University of Technology. See: http://www.dredgingengineering.com/dredging/media%5CLectureNotes%5CVlasblom%5C02%20TSHD.pdf Accessed: 03-08-16.

[3] PM van den Bergh, J Osnabrugge, and C de Keizer. An optimal dredging process by using new draghead control concepts. In *CEDA Dredging Days 2015: Innovative dredging solutions for ports, Rotterdam, the Netherlands - Proceedings*. CEDA.

[4] Sape A Miedema. *The Delft Sand, Clay and Rock Cutting Model*. IOS Press, first edition, 2014.

[5] Sape A Miedema. *The Delft Sand, Clay and Rock Cutting Model*. IOS Press, third edition, 2015.

[6] Srinivasa Ramanujan. Modular equations and approximations to π. *Quart. J. Math*, 45:350–372, 1914.

[7] OO Aderibigbe and N Rajaratnam. Erosion of loose beds by submerged circular impinging vertical turbulent jets. *Journal of hydraulic research*, 34(1):19–33, 1996.

[8] Po-Hung Yeh, Kuang-An Chang, John Henriksen, Billy Edge, Peter Chang, Andrew Silver, and Abel Vargas. Large-scale laboratory experiment on erosion of sand beds by moving circular vertical jets. *Ocean Engineering*, 36(3):248–255, 2009.

[9] Irandokht Dehghani, Babak Lashkar-Ara, Mohamad Zakermoshfegh, and Mohamad Hossein Ghotbi. Experimental study of the dynamic scour plunging pool under submerged circular jet.

[10] Josef Kozeny. *Über kapillare Leitung des Wassers im Boden:(Aufstieg, Versickerung und Anwendung auf die Bewässerung)*. Hölder-Pichler-Tempsky, 1927.

[11] Phillip C Carman. Fluid flow through granular beds. *Transactions-Institution of Chemical Engineeres*, 15:150–166, 1937.

[12] Philip Crosbie Carman. *Flow of gases through porous media*. Academic press, 1956.

[13] Russell G Shepherd. Correlations of permeability and grain size. *Ground Water*, 27(5):633–638, 1989.

[14] Robert A Weegenaar, Geert H Keetels, Mark O Winkelman, and Cees van Rhee. Sand erosion with a traversing circular jet. In *Proceedings of the Institution of Civil Engineers-Maritime Engineering*, volume 168, pages 76–83. Thomas Telford Ltd, 2015.

[15] Pieter de Jong. De uitvoering van een lab. onderzoek naar de mogelijkheden van gecombineerd snijden en spuiten in zand. Master's thesis, Delft University of Technology, 1988.

[16] Sape Andries Miedema. Calculation of the cutting forces when cutting water saturated sand. *Doctor thesis, Delft, Netherlands*, 1987.

[17] TAA Combe and SA Miedema. The influence of adhesion on cutting processes in dredging. 2015.

[18] RD Wismer and HJ Luth. Rate effects in soil cutting. *Journal of Terramechanics*, 8(3):11–21, 1972.

[19] Robert D Wismer and Harold J Luth. Performance of plane soil cutting blades in clay. *Transactions of the ASAE*, 15(2):211–0216, 1972.

[20] J Gl Potyondy. Skin friction between various soils and construction materials. *Geotechnique*, 11(4):339–353, 1961.

[21] SciPy python-based software for science, mathematics and engineering. `https://www.scipy.org/`. Accessed: 11-07-2017.

[22] VS Istomina. Seepage stability of the soil. *Translated from Russian, Moscow*, 1957.

[23] Norio Ouchiyama and Tatsuo Tanaka. Porosity estimation from particle size distribution. *Industrial & engineering chemistry fundamentals*, 25(1):125–129, 1986.

[24] E Mostefa Kara, Mourad Meghachou, and Nabil Aboubekr. Contribution of particles size ranges to sand friction. *Engineering, Technology & Applied Science Research*, 3(4):pp–497, 2013.

[25] AFT Fathom flow simulation software. `http://www.aft.com/products/fathom`. Accessed: 11-07-2017.